Growth and characterization of nanostructured wide band gap semiconductors for optoelectronic applications

Thesis submitted to

COCHIN UNIVERSITY OF SCIENCE AND TECHNOLOGY

in partial fulfillment of the requirements

for the award of the degree of

DOCTOR OF PHILOSOPHY

Aneesh P. M.

Department of Physics
Cochin University of Science and Technology
Cochin - 682 022, Kerala, India

November 2010

Growth and characterization of nanostructured wide band gap semiconductors for optoelectronic applications

Ph.D. thesis in the field of Materials Science

Author:
Aneesh P.M.
Optoelectronic Devices Laboratory
Department of Physics
Cochin University of Science and Technology
Cochin - 682 022, Kerala, India.
Email: aneeshpm@gmail.com

Supervisor:
Dr. M.K. Jayaraj
Professor
Optoelectronic Devices Laboratory
Department of Physics
Cochin University of Science and Technology
Cochin - 682 022, Kerala, India.
Email: mkj@cusat.ac.in

Front cover: SEM image of ZnO nanorods grown by hydrothermal method
Back cover: Schematic of ZnMgO/ZnO/ZnMgO symmetric MQW structures

November 2010

.

Dedicated to the caring hands

Dr. M. K. Jayaraj
Professor
Department of Physics
Cochin University of Science and Technology
Cochin 682 022, India.

6th November 2010

Certificate

Certified that the work presented in this thesis entitled "Growth and characterization of nanostructured wide band gap semiconductors for optoelectronic applications "is based on the authentic record of research carried out by Aneesh P. M. under my guidance in the Department of Physics, Cochin University of Science and Technology, Cochin 682 022 and has not been included in any other thesis submitted for the award of any degree.

Dr. M. K. Jayaraj
(Supervising Guide)

Phone : +91 484 2577404 extn 33 Fax: 91 484 2577595 Email: mkj@cusat.ac.in

Declaration

Certified that the work presented in this thesis entitled "Growth and characterization of nanostructured wide band gap semiconductors for optoelectronic applications "is based on the original research work done by me under the supervision and guidance of Dr. M. K. Jayaraj, Professor, Department of Physics, Cochin University of Science and Technology, Cochin-682 022 and has not been included in any other thesis submitted previously for the award of any degree.

<div align="right">Aneesh P. M.</div>

Cochin-22
6th November 2010

Acknowledgments

This thesis arose in part out of years of research that has been done since I came to CUSAT. When I look back, I realize that I have worked with a great number of people whose contribution in assorted ways to the research and the making of the thesis deserved special mention. It is a pleasure to convey my gratitude to them all in my humble acknowledgment.

I would like to express my overwhelming gratitude to my research guide, Dr. M. K. Jayaraj, for his expertise shown in guiding my work and the willingness to share his knowledge and experience. He has given immense freedom for us in developing ideas and he is always willing to hear and acknowledge sincere efforts. His profound practical skills, immense knowledge and critical but valuable remarks led me to do a good research. I especially thank him for his prompt reading and careful critique of my thesis. Throughout my life I will benefit from the experience and knowledge I gained working with Dr. M. K.Jayaraj.

I express my sincere thanks to Prof. M.R.Anantharaman, Head, Department of Physics and all the former Heads of the Department - Prof. V. C. Kuriakose, Prof. T. Ramesh Babu, Prof. Godfrey Louis - for permitting me to use the research facilities in the Department. I would like to thank my doctoral committee member Prof. B. Pradeep and all the other teachers in Department of Physics. I gratefully acknowledge the help and inspiration from Jayalekshmi teacher who has inspired me in both academic and personal development.

I express my sincere thanks to Dr. K Rajeev Kumar and Prof. Tamio Endo for their support during my PhD work. I would like to extend my thanks to Prof. T. Pradeep, IIT Madras for TEM measurements. I thank

Contents

i

List of Figures

Preface

Nanotechnology deals with materials or structures in nanometer scales (10^{-9} m), typically ranging from sub nanometers to several hundreds of nanometers. Earlier people believed that material properties can be changed only by varying the chemical composition. But later it has been found that the material properties can be tuned by varying the size of the material without changing the chemical composition. The transition from micron sized particles to nanoparticles leads to a number of changes in their physical properties. The major change is the increase in the surface area to volume ratio, as the size of the particle moves to a regime where quantum confinement effects are predominant. These new properties or phenomena will not only satisfy everlasting human curiosity, but also promise a new advancement in technology. Another very important aspect of nanotechnology is the miniaturization of current and new instruments, sensors and machines that will have great impact on the world we live in. Nanotechnology has an extremely broad range of potential applications from nanoscale electronics and optics, to nanobiological systems.

The band gap of the semiconductors increases compared to their bulk value and the density of states will also be modified as the size of the particles reduces. The luminescent properties of these nanostructures are quite interesting. The luminescence emission and absorption edge can be tuned by changing the particle size. Phosphors are the solid material that emits light when it is exposed to some radiation such as ultraviolet light or an electron beam. Efficient phosphors for lighting applications, flat panel displays, radioactive light sources etc have always been a goal for researchers. The particle size of conventional phosphors are in micrometer scale, hence light scattering at grain boundaries is strong and it decreases the light output. Nanophosphors can be synthesized from tens to hundreds of nanometers that are smaller than the light wavelength and can reduce the scattering, thereby enhancing the luminescence efficiency. The objective of the present study is the synthesis of nanophosphors and tuning of its emission by doping of rare earth material. The growth of various nanostructures by physical and chemical methods for luminescent, magnetic and biological applications have also been investigated. Synthesis of nanostructures of wide band gap semiconductors are discussed in this thesis. Nanostructures of zinc oxide (ZnO), zinc sulfide (ZnS) and zinc gallium oxide (ZnGa$_2$O$_4$) are synthesized by hydrothermal, liquid phase pulsed laser ablation (LP-PLA) and pulsed laser deposition (PLD) techniques. These nanostructures were characterized for luminescent, magnetic and biological applications.

Chapter 1 gives an introduction to nanotechnology. This chapter discusses the different types of quantum confined systems and corresponding density of states. Various properties and applications of these nanostructures are discussed in this chapter. A brief review of oxide and sulfide nanostructures is presented.

Chapter 2 describes in detail the techniques for the growth of various nanostructures and characterization tools employed in the present work. The nanostructures were synthesized by hydrothermal method, liquid phase pulsed laser ablation (LP-PLA) and pulsed laser deposition (PLD) techniques. X-ray diffraction (XRD), high resolution transmission electron microscopy (HRTEM), selected area electron diffraction (SAED) and scanning electron microscopy (SEM) are used for the structural characterization. Compositional analysis has been carried out by energy dispersive x-ray (EDX) technique and inductively coupled plasma atomic emission spectroscopic (ICP- AES) studies. Thickness of the films was measured using stylus profiler. Band gap of the materials in thin film form and bulk were estimated from the optical transmittance and diffuse reflectance spectroscopy respectively using a UV-Vis-NIR spectrophotometer. In order to determine the changes with temperature during the formation of nanostructures, thermogravimetric analysis (TGA) was carried out. The room temperature photoluminescence (PL) emission were recorded using the flourimeter and the emission color is quantified by the CIE coordinates. The basic operation of FT-IR (Thermo Nicolet) and Raman spectrometer used for the present investigation are also briefly discussed in this chapter.

Chapter 3 describes the low temperature hydrothermal synthesis of oxide phosphors like $ZnGa_2O_4$. Undoped and Eu doped $ZnGa_2O_4$ nanoparticles were synthesized by hydrothermal method by varying the process parameters such as temperature, time of growth, volume ratio of Zn/Ga precursor solutions. $ZnGa_2O_4$ spinel powders synthesized by other methods require heat treatment at higher temperatures for several hours and subsequent grinding. This may damage the phosphor surfaces, resulting in

the loss of emission intensity. The hydrothermally synthesized nanoparticles were structurally characterized by x-ray diffraction and high resolution transmission electron microscopy. The PL emission of doped and undoped $ZnGa_2O_4$ nanoparticles shows that $ZnGa_2O_4$ is a good host material and Eu doped $ZnGa_2O_4$ may find application as blue to red phosphor converter.

Chapter 4 describes the growth of various nanostructures of zinc oxide (ZnO) by hydrothermal method. The objective of the present work is to grow ZnO nanoparticles and nanorods by varying the precursors for various possible optoelectronic and biological applications. The hydrothermal synthesis of stable ZnO nanoparticles by varying the growth temperature, time and concentration of the precursors are discussed in the first part of the chapter. The dependance of temperature, time of growth and precursor concentration on the structure, morphology, optical properties were investigated in detail. The hydrothermal growth of ZnO nanorods is an interesting area of study especially for sensor applications. The second part of the chapter explains the synthesis route for the growth of ZnO nanorods. The white luminescence from these nanorods originating from the intrinsic defects can be utilized for white light solid state lighting applications.

Chapter 5 describes growth of ZnO nanostructures doped with luminescent and magnetic impurities for optoelectronic and possible spintronic applications. The hydrothermal growth conditions were optimized for Co doped ZnO nanostructures by varying the parameters like temperature, time of growth and dopant concentration. The electron paramagnetic resonance and diffuse reflectance spectra confirms the incorporation of Co^{2+} in the ZnO lattice. The magnetic properties investigated by SQUID measurements shows paramagnetism in Co doped ZnO nanostructures. Second

part of the chapter deals with the growth of europium doped ZnO nanostructures by hydrothermal method by varying the process parameters and dopant concentration. These nanoparticles were characterized structurally by XRD and HRTEM. The photoluminescent emission shows the Eu doped ZnO nanostructures are good phosphors. The red emission can be effectively obtained either by exciting with UV (397 nm) or by blue (466 nm) light.

Highly transparent, luminescent, chemically pure and biocompatible ZnO nanoparticles without any surfactant were synthesized by liquid phase-pulsed laser ablation (LP- PLA) from ZnO and Zn target. The dependence of laser fluence, time of ablation, oxygen and nitrogen bubbling during ablation and pH of the medium on the properties of the ZnO nanoparticles were investigated. The growth of these nanoparticles by LP-PLA in acidic, neutral and basic medium give some inference on the stability of these colloidal solution and the formation of passivation layer on the surface of these particles. The formation of these nanoparticles were confirmed by HRTEM, SAED patterns. The nanoparticles grown under oxygen and nitrogen bubbling during LP-PLA indicate that oxygen defects plays a major role in the yellow luminescence emission of these ZnO colloids. ZnS and Mn doped ZnS nanoparticles were also synthesized by LP-PLA technique. The blue and yellow luminescence from ZnS and ZnS:Mn nanoparticles were discussed. These luminescent, nontoxic ZnO and ZnS nanoparticles will find applications in biomedical imaging and cancer detections. The growth and characterization of LP-PLA grown nanoparticles are summerised in chapter 6.

The growth of symmetric (ZnMgO/ZnO/ ZnMgO) and asymmetric ($CuGaO_2$/ZnO/ZnMgO) multiple quantum well (MQW) structures by pulsed

laser ablation technique with varying confinement layer thickness is described in chapter 7. The blue shift in the photoluminescence (PL)emission can be related to the reduction in the confinement layer thickness. Efficient room temperature PL was observed from these MQWs, which was found to be blue shifted as compared to the room temperature near band edge PL from ZnO thin film grown at same experimental conditions.

Chapter 8 summarizes the major contributions of the present investigations and recommends the scope for future works.

Part of the work presented in the thesis has been published in various journals

Journal Papers

1. Growth of ZnS:Mn nanoparticles by liquid phase pulsed laser ablation, **P. M. Aneesh**, R. Reshmi and M. K. Jayaraj (Submitted to J. Phys. Chem. C)

2. Red luminescence from hydrothermally synthesized Eu doped ZnO nanoparticles under visible excitation, **P. M. Aneesh** and M. K. Jayaraj, Bull. Mater. Sci., **33**, 227 (2010)

3. Co^{2+} Doped ZnO Nanoflowers Grown by Hydrothermal Method, **P. M. Aneesh**, Christie Thomas Cherian, M. K. Jayaraj and T. Endo, Journal of the Ceramic Society of Japan, **118**, 333 (2010)

4. Dependence of Size of Liquid Phase Pulsed Laser Ablated ZnO Nanoparticles on pH of the Medium, **P. M. Aneesh**, Arun Aravind, R. Reshmi, R. S. Ajimsha and M. K. Jayaraj, Transactions of Materials Research Society of Japan, **34**, 759 (2009)

5. Hydrothermal synthesis and characterization of undoped and Eu doped $ZnGa_2O_4$ nanoparticles, **P. M. Aneesh**, K. Mini Krishna and M. K. Jayaraj, Journal of Electrochemical society **156(3)**, K33 (2009)

6. Synthesis of ZnO nanoparticles by hydrothermal method, **P. M. Aneesh**, K.A. Vanaja and M.K. Jayaraj, Proc. SPIE **6639**, 66390J (2007)

Conference Papers

1. ZnO quantum wells and quantum dots for optoelectronic applications, M. K. Jayaraj and **P. M. Aneesh**, National Seminar on Nanostrctured Materials and Nanophotonics, Kochi, India

2. White emission from ZnO nanostructures for solid state lighting applications, **P. M. Aneesh** and M.K. Jayaraj, 22nd Kerala Science Congress, Peechi, India

3. White luminescence from hydrothermally synthesized ZnO nanostructures, **P. M. Aneesh** and M. K. Jayaraj, International Conference on Electroceramics (ICE-2009), Delhi, India

4. Growth of various nanostructures of ZnO by LPPLA and hydrothermal method, **P. M. Aneesh**, Arun Aravind and M. K. Jayaraj, DAE-BRNS 5th National Symposium on Pulsed Laser Deposition of Thin Films and Nanostructured Materials (PLD-2009), Chennai, India

5. Room temperature photoluminescence from symmetric and asymmetric ZnO quantum wells grown by pulsed laser deposition, **P. M. Aneesh**, R. S. Ajimsha, M. K. Jayaraj, P. Misra and L. M. Kukreja,

Second International Conference on Frontiers in Nanoscience and Technology (Cochin Nano-2009), Kochi, India

6. Various nanostructures of ZnO grown by LP-PLA and chemical methods, **P. M. Aneesh**, Arun Aravind, R. Reshmi and M. K. Jayaraj, 2nd International conference Bangalore Nano 08, Bangalore, India

7. The Growth of Surfactant Free of ZnO Nanoparticles by Liquid Phase Pulsed Laser Ablation, Madambi K Jayaraj, Reshmi Raman, Ajimsha Sreedharan, **Aneesh P Madathil**, Anoop Gopinadhan, Arun Aravind, IUMRS- ICEM 2008, Australia

8. Growth of ZnO nanostructures by pulsed laser ablation, M. K. Jayaraj, R. S. Ajimsha, R. Reshmi, R. Sreeja, **P. M. Aneesh**, National Conference, Pondicherry University, Pondicherry, India

9. Hydrothermal Synthesis and Characterization of $ZnGa_2O_4$ Nanophosphor, K. Mini Krishna, K. Manzoor, **P. M. Aneesh** and M. K. Jayaraj (CTMS-07)

Other publication to which author has contributed

Journal Papers

1. Linear and Nonlinear Optical Properties of Gold Nanoparticle Attached MWCNTs, R.Sreeja, **P. M. Aneesh** and M.K.Jayaraj (Submitted to Carbon)

2. Liquid phase pulsed laser ablation of metal nanoparticles for nonlinear optical applications, R. Sreeja, R. Reshmi, **P. M. Aneesh** and M.K.Jayaraj (Submitted to J. Phys. Chem. C)

3. Vertically aligned ZnO nanorods on various substrates by hydrothermal method, **P. M. Aneesh**, P. P. Subha, L. S. Vikas, Sonima Mohan and M. K. Jayaraj Proc. SPIE, **7766**, 776606 (2010)

4. Linear and nonlinear optical properties of luminescent ZnO nanoparticles embedded in PMMA matrix, R Sreeja, Jobina John, **P. M. Aneesh** and M. K. Jayaraj, Optics communications **283**, 2908 (2010)

5. Growth of ITO thin films on polyamide substrate by bias sputtering, M. Nisha, K. A. Vanaja, K. C. Sanal, K. J. Saji, **P. M. Aneesh** and M. K. Jayaraj, Materials Science in Semiconductor Processing **13**, 64 (2010)

6. Violet luminescence from ZnO nanorods grown by room temperature Pulsed Laser Deposition, R. S. Ajimsha, R. Manoj, **P. M. Aneesh** and M. K. Jayaraj, Current Applied Physics **10**, 693 (2010)

7. Size dependent optical nonlinearity of Au nanocrystals, R. Sreeja, **P. M. Aneesh**, Arun Aravind, R. Reshmi, Reji Philip and M.K.Jayaraj, Journal of Electrochemical society, **156 (10)**, K167 (2009)

8. Synthesis of Highly Luminescent, Bio-Compatible ZnO Quantum Dots Doped with Na, B. Vineetha, K. Manzoor, R. S. Ajimsha, **P. M. Aneesh** and M. K. Jayaraj, Journal of Synthesis, Reactivity in Inorganic and Nanometal Chemistry **38**, 126 (2008)

Conference Papers

1. Vertically aligned zinc oxide nanorods on glass substrate by hydrothermal method, **P. M. Aneesh**, Sonima Mohan and M. K. Jayaraj,

International Conference On Materials for the Millennium (Matcon-2010), Kochi, India

2. Bonding of gold nanoparticles on ZnO nanostructures, **P. M. Aneesh**, K. A. Vanaja and M. K. Jayaraj, 5th International Conference on Materials for Advanced Technologies (ICMAT 2009) and International Union of Materials Research Societies (IUMRS-ICA 2009), Singapore

3. Synthesis of gold nanoparticles by laser ablation in liquid media, **P. M. Aneesh**, Arun Aravind, R. Sreeja, R. Reshmi and M. K. Jayaraj, Second International Conference on Frontiers in Nanoscience and Technology (Cochin Nano-2009), Kochi, India

4. Gold nanoparticles by liquid phase pulsed laser ablation for biological and optical limiting applications, **P. M. Aneesh**, R. Sreeja, Arun Aravind, R. Reshmi and M. K. Jayaraj, 2nd International conference Bangalore Nano 08, Bangalore, India

5. Size dependent optical absorptive nonlinearity of Au nano clusters in water, **P. M. Aneesh**, R.Sreeja, Arun Aravind, R Reshmi, M.K.Jayaraj, Photonics 2008, Delhi, India

6. Synthesis and Characterization of Luminescent Sodium doped ZnO quantum dots, B. Vineetha, K. Manzoor, R. S. Ajimsha, **P. M. Aneesh**, M. K. Jayaraj (CTMS-07)

7. Spatial study of RF magnetron plasma using Langmuir probe, Joshy. N. V, **P. M. Aneesh**, K.J. Saji, Johney Isaac, M. K. Jayaraj, 20th National Symposium on Plasma and Technology, PLASMA - 2005

Chapter 1

Introduction to nanotechnology

1.1 Introduction

Nanoscience and nanotechnology includes the synthesis, characterization, exploration and utilization of nanostructured materials. The application of nanomaterials can be historically traced back to even before the generation of modern science and technology. Nanoparticles were used as dye materials in ceramics by ancient people [1]; colloidal gold was used in medical treatment for cure of dipsomania, arthritis etc, as early as from 19th century; systematic experiments conducted on nanomaterials had also been started from the days of well known Faraday experiments [2] in the 1857. In 1959, Richard Feynman gave a lecture titled "there's plenty of room at the bottom", suggesting the possibility of manipulating things at atomic level [3]. This is generally considered to be the foreseeing of nanotechnology. However, the real burst of nanotechnology didn't come until

the early 1990s. In the past decades, sophisticated instruments such as scanning electron microscopy, transmission electron microscopy and scanning probe microscopy for characterization and manipulation became more available for researchers to approach the nanoworld. Device miniaturization in semiconductor industry is also a significant factor for the development of nanotechnology. The Moore's law predicted the performance of transistor and density double every 24 months. Nanoelectronic devices based on new nanomaterials systems and new device structures will contribute to the development of next generation of microelectronics. For example, single electron transistor [4, 5] and field effect transistor [6–8] based on single wall carbon nanotubes are already on the way.

The developments in quantum physics and the emergence of new fields like soft condensed matter physics all gave a new dimension to the wide area of materials science. The earlier notion of change in material properties by change in composition or mixing of different materials remained no more isolated and a radically different approach emerged in which, material properties are engineered by changing the size by keeping the chemical composition intact [9, 10]. The methodology of varying the material characteristics with size is feasible only in a specific size regime, namely nano meter (10^{-9} meter), where a quantum swapping of classical phenomena can be observed. This gave birth to a new branch of science and technology called 'nanoscience' and 'nanotechnology'.

Nanotechnology deals with materials or structures in nanometer scales, typically ranging from sub nanometers to several hundred nanometers. One nanometer is 10^{-3} micrometer or 10^{-9} meter. Nanotechnology is the design, fabrication and application of nanostructures or nanomaterials, and the

fundamental understanding of the relationships between physical properties or phenomena and material dimensions. Nanotechnology is a new field or a new scientific domain. Similar to quantum mechanics, on nanometer scale, materials or structures may possess new physical properties or exhibit new physical phenomena. Some of these properties are already known. For example, band gap of semiconductors can be tuned by varying material dimension. There may be many more unique physical properties not known to us yet. These new physical properties or phenomena will not only satisfy everlasting human curiosity, but also promise new advancement in technology. Another very important aspect of nanotechnology is the miniaturization of current and new instruments, sensors and machines that will greatly impact the world we live in. Examples of possible miniaturization are: computers with infinitely great power that compute algorithms to mimic human brains, biosensors that warn us at the early stage of the onset of disease and preferably at the molecular level and target specific drugs that automatically attack the diseased cells on site, nanorobots that can repair internal damage and remove chemical toxins in human bodies, and nanoscaled electronics that constantly monitor our local environment.

Further, nanotechnology was also expanded extensively to other fields due to the novel properties of nanomaterials discovered and to be discovered. For example, nanowires can be potentially used in nanophotonics, laser [11], nanoelectronics [12], solar cells [13], resonators [14] and high sensitivity sensors [15]. Nanoparticles can be potentially used in catalysts [16], functional coatings, nanoelectronics [17], energy storage [18], drug delivery [19] and biomedicines [20]. Nanostructured thin films can be used in light emitting devices, displays and high efficiency photovoltaics. These are only a limited part of the fast developing nanotechnology, yet numerous of other

potential applications of nanomaterials have already been or will be discovered. Nanotechnology is an interdisciplinary research field in which many physicists, chemists, biologists, materials scientist and other specialists are involved.

The term of nanomaterials covers various types of nanosturctured materials which posses at least one dimension in the nanometer range. Various nanostructures which include zero dimension nanostructures such as metallic, semiconducting and ceramic nanoparticles; one dimension nanostructures such nanowires, nanotubes and nanorods; two dimension nanostructures such as quantum well structures. Besides this individual nanostructures, ensembles of these nanostructures form high dimension arrays, assemblies, and superlattices. The properties of materials with nanometer dimensions are significantly different from those of atoms and bulk materials. This is mainly due to the nanometer size of the materials which render them: (i) large fraction of surface atoms; (ii) high surface energy; (iii) spatial confinement; (iv) reduced imperfections, which do not exist in the corresponding bulk materials [21].

Due to their small dimensions, nanomaterials have extremely large surface area to volume ratio, which makes a large fraction of atoms of the materials to be on the surface or interfacial atoms, resulting in more surface dependent material properties. Especially when the sizes of nanomaterials are comparable to Debye length, the entire material will be affected by the surface properties of nanomaterials [22, 23]. This in turn may enhance or modify the properties of the bulk materials. For example, metallic nanoparticles can be used as very active catalysts. Chemical sensors from nanoparticles and nanowires enhanced the sensitivity and sensor selectivity. The quantum confinement of nanomaterials has profound effects on

the properties of nanomaterials. The energy band structure and charge carrier density in the materials can be modified quite differently from their bulk counter part and this in turn will modify the electronic and optical properties of the materials.

Nanotechnology has an extremely broad range of potential applications in nanoscale electronics, optics, nanobiological systems, nanomedicine etc. Therefore it requires formation and contribution from multidisciplinary teams of physicists, chemists, materials scientists, engineers, molecular biologists, pharmacologists and others to work together on (i) synthesis and processing of nanomaterials and nanostructures, (ii) understanding the physical properties related to the nanometer scale, (iii) design and fabrication of nano-devices or devices with nanomaterials as building blocks, and (iv) design and construction of novel tools for characterization of nanostructures and nanomaterials.

Synthesis and processing of nanomaterials and nanostructures are the essential aspect of nanotechnology. Studies on new physical properties and applications of nanomaterials and nanostructures are possible only when nanostructured materials are made available with desired size, morphology, crystal and microstructure and chemical composition. Work on the fabrication and processing of nanomaterials and nanostructures started long time ago, far earlier than nanotechnology emerged as a new scientific field. Such research has been drastically intensified in the last decade, resulting in overwhelming literatures in many journals across different disciplines. The research on nanotechnology is evolving and expanding very rapidly. There are two principal ways of manufacturing nanoscale materials; the top-down nanofabrication starts with a large structure and proceeds to

make it smaller through successive cuttings while the bottom-up nanofabrication starts with individual atoms and builds them up to a nanostructure. When we bring constituents of materials down to the nanoscale, the properties change. Some materials used for electrical insulations can become conductive and other materials can become transparent or soluble. For example gold nanoparticles have a different colour, melting point and chemical properties, due to the nature of the interactions among the atoms that make up the gold, as compared to a nugget of gold. Nano gold does not look like bulk gold, the nanoscale particles can be orange, purple, red or greenish depending on the size of the particle. All these new properties that open up when bringing the material down in scale is of great interest for the industry and society as it enables new applications and products.

Nanotechnology is considered by some to be the next industrial revolution and is believed to cause enormous impacts on the society, economy and life in general in the future. Nanotechnology have wide application in medicine, information technology, biotechnology, energy production and storage, material technology, manufacturing, instrumentation, environmental applications and security.

Lasers and light emitting diodes (LED) from both quantum dots and quantum wires are very promising in the future developments of optoelectronics. High density information storage using quantum dot devices is also a fast developing area. Reduced imperfections are also an important factor in determination of the properties of the nanomaterials. Nanosturctures and nanomaterials favours of a self-purification process in that the impurities and intrinsic material defects will move to near the surface upon thermal annealing. This increased materials perfection affects the properties of

nanomaterials. For example, the chemical stability for certain nanomaterials may be enhanced, the mechanical properties of nanomaterials will be better than the bulk materials.

1.2   Quantum confinement

The band gap of a semiconductor is, by definition [24], the energy necessary to create an electron and a hole, at rest with respect to the lattice and far enough apart so that their Coulomb attraction is negligible. If one carrier approaches the other, they may form a bound state (Wannier exciton) at an energy slightly below the band gap. For bulk semiconductor, the dimension of the exciton can be theoretically calculated by exciton Bohr radius [25, 26]

$$a_B = \frac{\hbar\epsilon}{\mu e^2} \tag{1.1}$$

where $\hbar$ is defined as Planck's constant, ϵ is the dielectric constant, μ is the exciton reduced mass [26]. However, if the radius of a semiconductor nanocrystal is reduced to less than its exciton Bohr radius, we can imagine that the exciton will be strongly confined in this limited volume and the electronic structure of the three-dimensionally confined electrons and holes will be drastically modified. The term quantum confinement, describes this confinement of the exciton within the physical boundaries of the semiconductor.

Quantum confinement is an inherent phenomenon for all the low- dimensional semiconductors, such as quantum well, quantum wire, and quantum dot, which describe confinement in 1, 2 and 3 dimensions respectively. The exciton Bohr radius (a_B) is often used to judge the extent of confinement in

a semiconductor nanocrystal with radius, a. In the analysis of experimental data, one needs to consider three different regimes: a>a_B, a∼a_B, and a<a_B, which are named as weak confinement, intermediate confinement and strong confinement regimes, respectively [25].

To build the theoretical models of electronic structure for quantum dots one uses quantum mechanics to describe the behavior of electrons in a semiconductor. In quantum mechanics electrons exhibit a wave-particle duality and can be described by a wave function. According to Heisenberg's uncertainty principle, position x and momentum p of an electron cannot be precisely determined simultaneously. For a plain wave, the position is unknown and can possibly be located at any position, but the momentum has a precisely defined value $\hbar$k, where k is the wave number or wave vector. However, for an electron confined in a limited space such as in a semiconductor crystal, the uncertainty in position decreases, but the momentum is no longer well defined and k has an uncertain value. Because the energy E is related to the momentum p or k vector, it will also have uncertain energy levels.

In a bulk semiconductor, carrier motion is unrestricted along all three spatial directions. However, a nanostructure has one or more of its dimensions reduced to a nanometre length scale and this produces a quantisation of the carrier energy corresponding to motion along these directions. If the quantum confinement is along one direction, the carriers can have free motion in other two directions. If the quantum confinement is in two directions, the carriers have free motion only in one direction. The carriers have no free motion if they are confined in all three directions. The total energy of electrons (or holes) will be the sum of allowed energies associated with

the motion of these carriers along the confined direction and the kinetic energy due to free motion in the remaining unconfined directions.

1.2.1 Confinement in one dimension: quantum wells

Quantum wells are structures in which a thin layer (confinement layer) of a smaller band gap semiconductor is sandwiched between two layers (barrier layer) of a wider band gap semiconductor. The heterojunction between the smaller and the wider band gap semiconductors forms a potential well confining the electrons and the holes in the smaller band gap material. This is the case of a type I quantum well. In a type II quantum well, the electrons and the holes are confined in different layers. Thus the motions of the electrons and the holes are restricted in one dimension (along the thickness direction). This system represents a two-dimensional electron gas (2DEG), when electrons are present in the conduction band.

Total energy of the electron is the sum of allowed energies associated with the motion of these carriers along one direction (say z direction) and the kinetic energy due to free motion of carriers in other two directions (say x, y directions)

$$E_{Total} = \frac{\hbar^2}{2m}[\frac{n_z \pi}{a}]^2 + \frac{\hbar^2}{2m}({k_x}^2 + {k_y}^2) \tag{1.2}$$

where 'a' is the thickness of the confinement layer, which corresponds to the width of the potential well, n_z = 1, 2, 3,..... and k_x and k_y are the wave vectors along x and y directions.

Lasers fabricated using single or multiple quantum wells based on wide band gap semiconductors as the active region have been extensively studied over the last two decades. Quantum well lasers offer improved performance

with lower threshold current and lower spectral width as compared to that of regular double heterostructure lasers. Quantum wells allow the possibility of independently varying barriers and confinement layer compositions and widths, and thus separate determination of optical confinement and electron injection. One of the main differences between the single quantum well and the multiple quantum well lasers is that the confinement factor of the optical mode is significantly smaller for the former. This results in higher threshold carrier and current densities for single quantum well lasers; however the confinement factor of single quantum well lasers can be significantly increased using a graded-index cladding structure [27]. The emission from the quantum well structures determine the quality of confinement and barrier layer and the interface between these layers. Growth of epitaxial layers will be beneficial for the device applications.

Epitaxy refers to the formation of a single crystal on the top of a single crystal structure and subsequent evolution of a specific crystallographic orientation between film and the substrate as growth commences. The specific orientation relationship is governed by crystal systems and lattice parameters of the two faces. There are two types of epitaxy: homoepitaxy and heteroepitaxy. Homoepitaxy refers to the state when both the film and the substrate are of same material. Si on Si wafer is the example of homoepitaxy. Heteroepitaxy is related to the situation when film and substrate are of different materials, e.g., metal film on alkali halide substrate. Heteroepitaxy is the most common form of epitaxy in various technological applications such as semiconductors, superconducting devices, ferroelectric memories, optoelectronic devices etc.

1.2.2 Confinement in two dimensions: quantum wires

The term nanowire is widely used to represent one-dimensional nanostructures that have a specific axial direction while their side surfaces are less well-defined [28, 29]. The wire- or rod-like shape of one-dimensional nanostructures has caused them to be the source of somewhat intensifying research of the past several years. In particular, their novel electrical and mechanical properties are the subject of intense research. Quantum wires represent two-dimensional confinement of electrons and holes. Such confinement permits free-electron behavior in only one direction, along the length of the wire (say the y direction). For this reason, the system of quantum wires describes a one-dimensional electron gas (IDEG) when electrons are present in the conduction band. The category of one-dimensional nanostructures consists of a wide variety of morphologies. These include whiskers, nanowires, nanorods, fibers, nanotubules, nanocables, and nanotubes, among others. Nanowires and nanorods are one-dimensional nanostructures whose width does not exceed 100 nanometers. Nanowires have been successfully synthesized out of a wide range of materials, including titanium oxide [30], indium oxide [31], indium-tin oxide [32], aluminum [33], tungsten oxide [34] and zinc oxide [35] etc.

Here, total energy of the electron is the sum of allowed energies associated with the motion of these carriers along two direction (say y, z direction) and the kinetic energy due to free motion of carriers in the other direction (say x direction)

$$E_{Total} = \frac{\hbar^2}{2m}[\frac{n_z\pi}{a}]^2 + \frac{\hbar^2}{2m}[\frac{n_y\pi}{b}]^2 + \frac{\hbar^2}{2m}(k_x{}^2) \qquad (1.3)$$

where n_y, n_z are integers and a, b are confined sizes of the materials along z and y directions.

Nanotubes

The term nanotubes represents two separate types of nanostructure. The first is any structure that appears to be like a nanowire with a hollow center. The side surfaces of the nanotube in this sense may be well-faceted. Many materials have been used to make these structures. The difference of nanowires and nanorods from nanotubes is the geometry of their cross-section. Nanotubes are hollow and have a cross-section resembling the perimeter of a circle or the outside of a rectangle. Nanowires and nanorods have solid cores. Their cross-section resembles a filled-in circle or hexagon. Research on one-dimensional nanostructures took-off recently with the publication in 1991 of Iijima's seminal paper outlining the discovery of carbon nanotubes, "helical microtubules of graphitic carbon"[36].

Carbon nanotubes are made up of a hexagonal network of carbon atoms forming a crystaline graphite sheet. This sheet is roled up to form a tubular structure. If the tube consists of only a single carbon sheet that meets end on end, then the carbon nanotube is referred to as a single walled carbon nanotube (SWCNT). However, if the nanotube consist of multiple sheets rolled up coaxially or if the nanotube roll up somewhat spirally, then the carbon nanotube is referred to as a multi walled carbon nanotube (MWCNT).

1.2.3   Confinement in three dimensions: quantum dots

Quantum dots represent the case of three-dimensional confinement, hence the case of an electron confined in a three-dimentional quantum box, typically of dimensions ranging from nanometers to tens of nanometers. These dimensions are smaller than the de Broglie wavelength of thermal electrons. A quantum dot is often described as an artificial atom because the electron is dimensionally confined just like in an atom (where an electron is confined near the nucleus) and similarly has only discrete energy levels. The electrons in a quantum dot represent a zero-dimensional electron gas (0DEG).

Here, total energy of the electron is the sum of allowed energies associated with the motion of these carriers along all three directions (say x, y, z direction)

$$E_{Total} = \frac{\hbar^2}{2m}[\frac{n_z\pi}{a}]^2 + \frac{\hbar^2}{2m}[\frac{n_y\pi}{b}]^2 + \frac{\hbar^2}{2m}[\frac{n_x\pi}{c}]^2 \qquad (1.4)$$

where n_x, n_y, n_z are integers and a, b, c are confined sizes of the materials along z, y and x directions.

Quantum dots are zero-dimensional nanostructures of semiconductors. Quantum dots were first theorized in the 1970s and initially synthesized in the early 1980s. If semiconductor particles are made small enough, quantum effects begin to assert themselves. These effects limit the energies at which electrons and holes can exist in the particles. Because energy is related to wavelength of the resulting photon, this means that the optical properties of the particle can be finely tuned depending on its size.

Quantum mechanics determines that only certain discrete energy levels are allowed in a single atom. If two identical atoms are held at large dis-

tances from each other, electrons in each level will have exactly the same energy. As those two atoms are brought closer to one another, they interact, and no two electrons with the same spin can have the same energy. This governing principle is called the Pauli exclusion principle. When a large number of atoms are brought together to form a solid, the discrete allowed energy levels of the individual atoms become a continuous energy band. In bulk structures, these properties can only be altered by adding constituents to create defects, interstitials, or substitutions in the material. The impressive phenomenon in QDs is that the optical and electronic properties can be precisely tuned by changing the size of the dots in addition to adding dopants. The electronic and optical properties that were thought to be inherent to a material can be transformed when the material was in a small enough (nanoscale) size.

Figure 1.1: Size dependent luminescent emission ranging from blue to red from CdSe quantum dots. On the left is the smaller size quantum dots having blue emission (Image Courtesy of M. S. Wong, Rice University)

As the dimensions of a material decrease in size, quantum confinement effects begin to occur. Quantum confinement occurs when material dimension is smaller than exciton Bohr radius [37]. This restricts carriers' movement, resulting in the above mentioned discrete energy levels and differences in material properties. Quantum confinement effects in QDs have a significant impact on the optical properties of the material. Figure 1.1 shows the size dependent luminescent properties of the CdSe QDs.

Quantum dots are often described in terms of the degree of confinement. The strong confinement regime is defined to represent the case when the size of the quantum dot (e.g., the radius R of a spherical dot) is smaller than the exciton Bohr radius a_B. In this case, the energy separation between the sub-bands (various quantized levels of electrons and holes) is much larger than the exciton binding energy. Hence, the electrons and holes are largely represented by the energy states of their respective sub-bands. As the quantum dot size increases, the energy separation between the various sub-bands becomes comparable to and eventually less than the exciton binding energy. The latter represents the case of a weak confinement regime where the size of the quantum dot is much larger than the exciton Bohr radius. The electron-hole binding energy in this case is nearly the same as in the bulk semiconductor.

Because of its unique properties, quantum dots have some promising potential applications. The more prolific research involves using quantum dots for biological imaging [38, 39] and computing [40] applications. Zinc sulfide has also plays an important role in quantum dot based nanosensors. Quantum computing makes use of the electronic properties of quantum dot.

1.3   Density of states
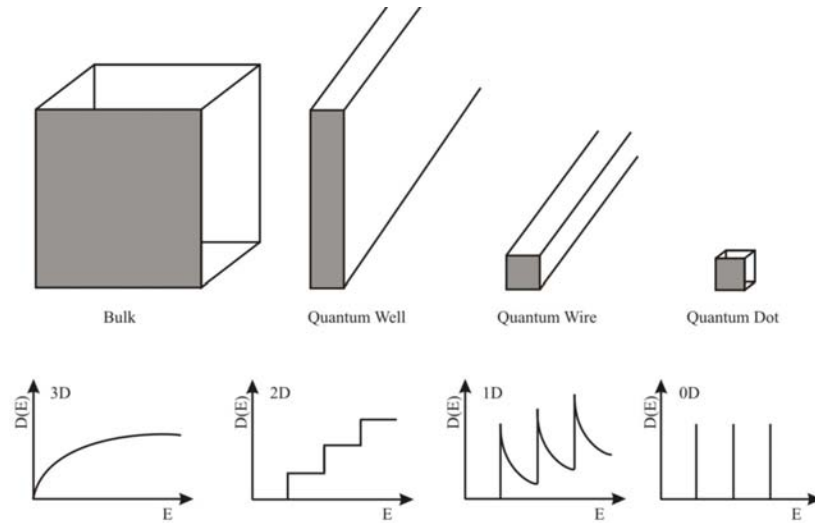
Figure 1.2: Schematic illustration of density of states of a semiconductor as a function of dimension

The density of states is defined as the number of energy states present in a unit energy interval per unit volume. Due to the quantization of energy levels, the relationship between the density of states and energy values is also dramatically modified as shown in figure 1.2 for low dimension semiconductors [41]. For bulk semiconductor, the density of states is proportional to $E^{1/2}$. However, this gradual increase in the density of states with energy increases in steps for quantum well due to quantum confinement. For quantum wire and dot, the confinement of electrons and holes in more than one dimension leads to further quantization of energy levels. The density of states profile turns to sharper curves with respect to energy. In the case

of three-dimensional confined quantum dot, the energy states are concentrated in a few sharp discrete energy levels.

The density of states of three dimensional electron gas (bulk semiconductor) is proportioanl to $E^{1/2}$. The density of states for a two dimensional structure is constant and does not depend on the energy due to free motion of electron. The density of states, D(E), for a quantum wire can be shown to have an inverse energy dependence ($E^{-1/2}$). The density of states of quantum dot is a delta funtion which is represented as δ[E - E(n_x, n_y, n_z)], where En_x, En_y and En_z are the quantized energy in the confined x, y and z directions.

1.4 Properties of nanomaterials

1.4.1 Mechanical properties

Due to the nanometer size, many of the mechanical properties of the nanomaterials are different from the bulk materials including the hardness, elastic modulus, fracture toughness, scratch resistance and fatigue strength etc. An enhancement of mechanical properties of nanomaterials can result due to this modification, which are generally resulting from structural perfection of the materials [21, 42]. The small size either renders them free of internal structural imperfections such as dislocations, micro twins, and impurity precipitates or the few defects or impurities present can not multiply sufficiently to cause mechanical failure. The imperfections within the nano dimension are highly energetic and will migrate to the surface to relax themselves under annealing, purifying the material and leaving perfect material structures inside the nanomaterials. Moreover, the external surfaces of nanomaterials also have less or free of defects compared to bulk

materials, serving to enhance the mechanical properties of nanomaterials [21]. The enhanced mechanical properties of the nanomaterials could have many potential applications both in nanoscale such as mechanical nano resonators, sensors, microscope probe tips and nanotweezers for nanoscale object manipulation, light weight high strength materials, flexible conductive coatings, wear resistance coatings, tougher and harder cutting tools etc.

Among many of the novel mechanical properties of nanomaterials, high hardness has been observed for many nanomaterials. A variety of superhard nanocomposites can be made of nitrides, borides and carbides by plasma-induced chemical and physical vapor deposition [43]. The excellent mechanical properties of nanomaterials could lead to many potential applications in all the nano, micro and macro scales. High frequency electro-mechanical resonators have been made from carbon nanotubes and nanowires. Nanostructured materials can also be used as nanoprobes or nanotwizzers to probe and manipulate nanomatierals in a nanometer range [44]. Due to their high aspect ratio and small dimensions, one-dimensional nano structures such as carbon nanotubes can also be used as nano probe tips.

The nanotweezers can be made from two individual carbon nanotubes. This nanotweezers operated under electrical stimulus was used to probe the electrical characteristics of nanostructures. It could be useful both in the nanostructure characterization and the manipulation. The nanotweezers could be used as a novel electromechanical sensor that can detect pressure or viscosity of media by measuring the change in resonance frequency and Q-factor of the device. They can also be explored into manipulation and modification of biological systems such as structures within a cell.

1.4.2   Thermal properties

By controlling the structures of materials at nanoscale dimensions, the properties of the nanostructures can be controlled and tailored in a very predictable manner to meet the needs for a variety of applications. The engineered nanostructures include metallic and non-metallic nanoparticles, nanotubes, quantum dots and superlattices, thin films, nano composites and nanoelectronic and optoelectronic devices which utilize the superior properties of the nanomaterials to fulfill the applications.

Many properties of the nanoscale materials have been well studied, including the optical electrical, magnetic and mechanical properties. However, the studies on thermal properties of nanomaterials have only seen slower progresses. This is partially due to the difficulties of experimentally measuring and controlling the thermal transport in nanoscale dimensions. Atomic force microscope (AFM) has been introduced to measure the thermal transport of nanostructures with nanometer-scale high spatial resolution, providing a promising way to probe the thermal properties with nanostructures [45]. Moreover, the theoretical simulations and analysis of thermal transport in nanostructures are still in infancy. As the dimensions go down into nanoscale, the availability of the definition of temperature is in question.

In non-metallic material system, the thermal energy is mainly carried by phonos, which have a wide variation in frequency and the mean free paths. The heat carrying phonons often have large wave vectors and mean free path in the order of nanometer range at room temperature, so that the dimensions of the nanostructures are comparable to the mean free path and wavelength of phonons. However the general definition of tempera-

ture is based on the average energy of a material system in equilibrium. For macroscopic systems, the dimension is large enough to define a local temperature in each region within the materials and this local temperature will vary from region to region, so that one can study the thermal transport properties of the materials based on certain temperature distributions of the materials. But for nanomaterial systems, the dimensions may be too small to define a local temperature. Moreover, it is also problematic to use the concept of temperature which is defined in equilibrium conditions, for the nonequilibrium processes of thermal transport in nanomaterials, posing difficulties for theoretical analysis of thermal transport in nanoscales [45].

In nanomaterials systems, several factors such as the small size, the special shape, the large interfaces modify the thermal properties of the nanomaterials, rendering them the quite different behavior as compared to the macroscopic materials. As the dimension goes down to nanoscales, the size of the nanomaterials is comparable to the wavelength and the mean free path of the phonons, so that the phonon transport within the materials will be changed significantly due the phonon confinement and quantization of phonon transport, resulting in modified thermal properties. The special structure of nanomaterials also affects the thermal properties. For example, because of the tubular structures of carbon nanotubes, they have extremely high thermal conductivity in axial directions, leaving high anisotropy in the heat transport in the materials [46]. The interfaces are also a very important factor for determining the thermal properties of nanomaterials.

The use of nanofluid to enhance the thermal transport is another promising application of the thermal properties of nanomaterials. Nanofluids are generally referred to the solid-liquid composite materials, which consist of

nanomaterials of size in the range 1-100nm suspended in a liquid. Nanofluids hold increasing attentions in both research and practical applications due to their greatly enhanced thermal properties compared to their base fluids. Many type of nanomaterials can be used in nanofluids including nanoparticles of oxides, nitrides, metals, metal carbides, and nanofibers such as single walled and multi walled carbon nanotubes, which can be dispersed in to a variety of base liquid depending on the possible applications, such as water, ethylene glycol, and oils. The most important features of nanofluids are the significant increase of thermal conductivity compared with liquids without nanomaterials.

1.4.3 Structural properties

The increase in surface area and surface energy with decreasing particle size leads to changes in interatomic spacings. For Cu metallic clusters the interatomic spacing is observed to be decreasing with decreasing cluster size. This is due to the compressive strain induced by the internal pressure arising from the small radius of curvature in the nanoparticle. Conversely, for semiconductors and metal oxides there is evidence that interatomic spacings increase with decreasing particle size.

A further effect is the apparent stability of metastable structures in small nanoparticles and clusters, such that all traces of the usual bulk atomic arrangement is lost. Metallic nanoparticles, such as gold, are known to adopt polyhedral shapes such as cubeoctahedra, multiply twinned icosahedra and multiply twinned decahedra. These nanoparticles may be regarded as multiply twinned crystalline particles (MTPs) in which the shapes can be understood in terms of the surface energies of various crystallographic planes, the growth rates along various crystallographic directions

and the energy required for the formation of defects such as twin bound-
aries. However, there is compelling evidence that such particles are not
crystals but are quasiperiodic crystals or crystalloids. These icosahedral
and decahedral quasicrystals form the basis for further growth of the nan-
ocluster, upto a size where they will switch into more regular crystalline
packing arrangements.

Crystalline solids are distinct from amorphous solids in that they possess
long-range periodic order and the patterns and symmetries which occur
correspond to those of the 230 space groups. Quasiperiodic crystals do
not possess such long-range periodic order and are distinct in that they
exhibit fivefold symmetry, which is forbidden in the 230 space groups. In
the cubic close-packed and hexagonal close-packed structures, exhibited by
many metals, each atom is coordinated by 12 neighbouring atoms. All
of the coordinating atoms are in contact, although not evenly distributed
around the central atom. However, there is an alternative arrangement in
which each coordinating atom is situated at the apex of an icosahedron and
in contact only with the central atom. If however we relax this rigid atomic
sphere model and allow the central atom to reduce in diameter by 10%,
the coordinating atoms come into contact and the body now has the shape
and symmetry of a regular icosahedron with point group symmetry 235,
indicating the presence of 30 two fold, 20 three fold and 12 five fold axes of
symmetry. This geometry represents the nucleus of a quasiperiodic crystal
which may grow in the forms of icosahedra or pentagonal dodecahedra.
These are dual solids with identical symmetry, the apices of one being
replaced by the faces of the other.

The size-related instability characteristics of quasiperiodic crystals are
not well understood. A frequently observed process appears to be that

of multiple twinning, such crystals being distinguished from quasiperiodic crystals by their electron diffraction patterns. Here the five triangular faces of the fivefold symmetric icosahedron can be mimicked by five twin-related tetrahedra (with a close-packed crystalline structure) through relatively small atomic movements.

1.4.4   Chemical properties

The change in structure as a function of particle size is intrinsically linked to the changes in electronic properties. The ionization potential (the energy required to remove an electron) is generally higher for small atomic clusters than for the corresponding bulk material. Furthermore, the ionization potential exhibits marked fluctuations as a function of cluster size. Such effects appear to be linked to chemical reactivity of the materials.

Nanoscale structures such as nanoparticles and nanolayers have very high surface area to volume ratios and potentially different crystallographic structures which may lead to a radical alteration in chemical reactivity. Catalysis using finely divided nanoscale systems can increase the rate, selectivity and efficiency of chemical reactions such as combustion or synthesis whilst simultaneously, significantly reducing waste and pollution. Nanoparticles often exhibit new chemistry as distinct from their larger particulate counterparts; for example, many new medicines are insoluble in water when in the form of micron-sized particles but will dissolve easily when in a nanostructured form.

1.4.5 Magnetic properties

Magnetic nanoparticles are used in a range of applications, including ferrofluids, colour imaging, bioprocessing, refrigeration as well as high storage density magnetic memory media. The large surface area to volume ratio results in a substantial proportion of atoms (those at the surface which have a different local environment) having a different magnetic coupling with neighbouring atoms, leading to differing magnetic properties.

Ferromagnetic particles become unstable when the particle size reduces below a certain size, since the surface energy provides a sufficient energy for domains to spontaneously switch polarization directions. As a result, ferromagnetics become paramagnetics. However, nanometer sized ferromagnetic turned to paramagnetic behaves differently from the conventional paramagnetic and is referred to as superparamagnetics. An operational definition of superparamagnetism would include at least two requirements. Firstly, the magnetization curve should not show hysteresis, since that is not a thermal equilibrium property. Secondly, the magnetization curve for an isotropic sample must be temperature dependent to the extent that curves taken at different temperatures must approximately superimpose when plotted against H/T after correction for the temperature dependence of the spontaneous magnetization.

Whilst bulk ferromagnetic materials usually form multiple magnetic domains, small magnetic nanoparticles often consist of only one domain and exhibit a phenomenon known as superparamagnetism. In this case the overall magnetic coercivity is then lowered: the magnetizations of the various particles are randomly distributed due to thermal fluctuations and only become aligned in the presence of an applied magnetic field.

Giant magnetoresistance (GMR) is a phenomenon observed in nanoscale multilayers [47] consisting of a strong ferromagnet (e.g., Fe, Co) and a weaker magnetic or non-magnetic buffer (e.g., Cr, Cu); it is usually employed in data storage and sensing. In the absence of a magnetic field the spins in alternating layers are oppositely aligned through antiferromagnetic coupling, which gives maximum scattering from the interlayer interface and hence a high resistance parallel to the layers. In an oriented external magnetic field the spins align with each other and this decreases scattering at the interface and hence resistance of the device.

1.4.6   Optical properties

The reduction of materials' dimension has pronounced effects on the optical properties. The size dependence can be generally classified into two groups. One is due to the increased energy level spacing as the system becomes more confined, and the other is related to surface plasmon resonance. The quantum size effect is most pronounced for semiconductor nanoparticles, where the band gap increases with a decreasing size, resulting in the interband transition shifting to higher frequencies [48, 49]. In a semiconductor, the energy separation, i.e. the energy difference between the completely filled valence band and the empty conduction band is of the order of a few electron volts and increases rapidly with a decreasing size [49]. Quantum confinement produces a blue shift in the band gap as well as appearance of discrete subbands corresponding to quantization along the direction of confinement. The optical properties of nanostructured semiconductors are highly size dependent and thus can be modified by varying the size alone, keeping the chemical composition in tact. The luminescent emission from the semiconductor nanostructures can be tuned by varying

the size of the nanoparticles. In the case of nanostructured semiconductor lasers, the carrier confinement and nature of electronic density of states of the nanostructures make it more efficient for devices operating at lower threshold currents than lasers with bulk materials. The size dependent emission spectra of quantum wells, quantum wires and quantum dots make them attractive lasing media. The performance of quantum dot lasers is less temperature dependent than conventional semiconductor lasers [50]. The same quantum size effect is also known for metal nanoparticles. However, in order to observe the localization of the energy levels, the size must be very small, as the level spacing has to exceed the thermal energy ($\sim$26 meV). Surface plasmon resonance is the coherent collective excitation of all the free electrons within the conduction band, leading to an in-phase oscillation [51, 52]. When the size of a metal nanocrystal is smaller than the wavelength of incident radiation, a surface plasmon resonance is generated [53]. The energy of the surface plasmon resonance depends on both the free electron density and the dielectric medium surrounding the nanoparticle. The width of the resonance varies with the characteristic time before electron scattering. For larger nanoparticle, the resonance sharpens as the scattering length increases. Noble metals have the resonance frequency in the visible range of electromagnetic spectrum.

1.4.7   Electronic properties

The changes which occur in electronic properties as the system length scale is reduced are related mainly to the increasing influence of the wave-like property of the electrons (quantum mechanical effects) and the scarcity of scattering centres. As the size of the system becomes comparable with the de Broglie wavelength of the electrons, the discrete nature of the energy

states becomes apparent once again, although a fully discrete energy spectrum is only observed in systems that are confined in all three dimensions. In certain cases, conducting materials become insulators below a critical length scale, as the energy bands cease to overlap. Owing to their intrinsic wave-like nature, electrons can tunnel quantum mechanically between two closely adjacent nanostructures, and if a voltage is applied between two nanostructures which aligns the discrete energy levels in the DOS, resonant tunneling occurs, which abruptly increases the tunneling current.

In macroscopic systems, electronic transport is determined primarily by scattering with phonons, impurities or other carriers or by scattering at rough interfaces. The path of each electron resembles a random walk, and transport is said to be diffusive. When the system dimensions are smaller than the electron mean free path for inelastic scattering, electrons can travel through the system without randomization of the phase of their wavefunctions. This gives rise to additional localization phenomena which are specifically related to phase interference. If the system is sufficiently small so that all scattering centres can be eliminated completely, and if the sample boundaries are smooth so that boundary reflections are purely specular, then electron transport becomes purely ballistic, with the sample acting as a waveguide for the electron wavefunction.

Conduction in highly confined structures, such as quantum dots, is very sensitive to the presence of other charge carriers and hence the charge state of the dot. These Coulomb blockade effects result in conduction processes involving single electrons and as a result they require only a small amount of energy to operate a switch, transistor or memory element. All these phenomena can be utilised to produce radically different types of components

for electronic, optoelectronic and information processing applications, such as resonant tunneling transistors and single-electron transistors.

1.4.8   Biological systems

Biological systems contain many examples of nanosized materials and nanoscale systems. Biomineralization of nanocrystallites in a protein matrix is highly important for the formation of bone and teeth, and is also used for chemical storage and transport mechanisms within organs. Biomineralization involves the operation of delicate biological control mechanisms to produce materials with well-defined characteristics such as particle size, crystallographic structure, morphology and architecture. Generally complex biological molecules such as DNA have the ability to undergo highly controlled and hierarchical self-assembly, which makes them ideal for the assembling of nanosized building blocks.

Biological cells have dimensions within the range 110 mm and contain many examples of extremely complex nano assemblies, including molecular motors, which are complexes embedded within membranes that are powered by natural biochemical processes.

1.5   Nanostructure fabrication methods

Nanostructures can be made in numerous ways. The broad classification divides methods into either those which build from the *bottom up*, atom by atom, or those which construct from the *top down* using processes that involve the removal or reformation of atoms to create the desired structure.

In the bottom-up approach, atoms, molecules and even nanoparticles themselves can be used as the building blocks for the creation of complex

nanostructures; the useful size of the building blocks depends on the properties to be engineered. By altering the size of the building blocks, controlling their surface and internal chemistry, and then controlling their organization and assembly, it is possible to engineer properties and functionalities of the overall nanostructured solid or system. These processes are essentially highly controlled, complex chemical synthesis. On the other hand, top-down approaches are inherently simpler and rely either on the removal or division of bulk material, or on the miniaturization of bulk to produce the desired structure with the appropriate properties. When controlled, both top-down and bottom-up methods may be viewed as essentially different forms of nanostructural engineering. Biological processes are essentially intermediate between top-down and bottom-up processes, however in reality they usually constitute complex bottom-up processes.

Milling, lithographic processes, machining etc are top down methods. Bottom-up processes effectively encompass chemical synthesis and/or the highly controlled deposition and growth of materials. Chemical synthesis may be carried out in either the solid, liquid or gaseous state. Vapour phase deposition methods, plasma-assisted deposition processes such as sputtering, dc glow discharge, molecular beam epitaxy (MBE), metal organic vapour phase epitaxy (MOVPE), colloidal methods, solgel methods etc are bottom up methods.

1.6 Phosphors and luminescence mechanisms

Phosphors are luminescent materials that emit light when excited, and are usually microcrystalline powders or thin-films designed to provide visible color emission. A phosphor usually comprises of a host crystal material

and one or more intentionally introduced impurities, called activators. The concentration of activators can be as low as tens of ppm, such as for donor-acceptors, or can be as high as 20% for rare earth dopants. The band gap of a phosphor host is generally larger than 3 eV to be transparent to visible light, and so either a wide-band-gap semiconductor or an insulator is used as the host.

Luminescence is the emission of electromagnetic radiation (photon) usually in the visible region which is not thermal in origin, involving a radiative transition. According to the types of excitation, the phenomena of luminescence can be classified as: photo-, cathodo-, electro-, and thermo-luminescence etc., which is excited by photons, electrons, current, and heat, respectively [54]. In addition to classification by excitation, two other terms are also often used and are related to the decay time (τ): fluorescence ($\tau < 10$ms) and phosphorescence ($\tau > 0.1$s) [54, 55].

The luminescence of phosphors can be traced to two mechanisms: luminescence in semiconductors and luminescence of localized centers. Luminescence of semiconductors normally occurs, after band-to-band excitation, between impurity states within the band gap, such as donor-acceptor pair luminescence. In the case of luminescent centers, the transitions occurs between energy levels of single ions. In the figure 1.3, left and middle diagram shows the excitation and emission can be both localized onto one center (called an activator) or separated from each other: excitation on the sensitizer (S) is followed by emission on the activator (A) [55]. The excitation and emission of semiconductors are shown in the right diagram of the figure 1.3. In semiconductors, most important impurities are donors and acceptors that dominate semiconductive properties, and they act as luminescence activators. In this unlocalized type of luminescence, the electrons

and holes of the host lattice, i.e., free electrons in the conduction band and free holes in the valance band, participate in the luminescence process. In figure 1.3, A and A* represents the ground and excited state of activator, S and S* represents the ground and excited state of sensitizer and D and A represents the donor and acceptor levels of semiconductor.
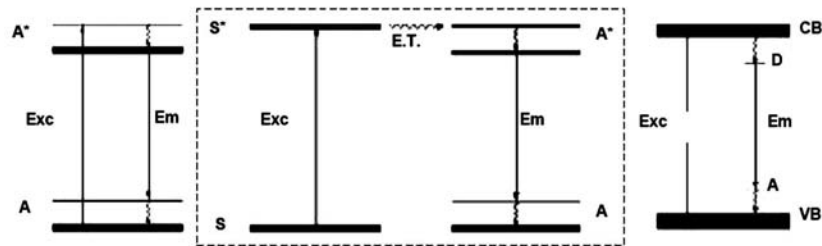
Figure 1.3: Schematic of luminescence mechanisms of phosphors: in localized centers (left, middle) and in semiconductors (right)

After decades of research and development, thousands of phosphors have been prepared and some of them are widely used in many areas [54]. In practical applications, phosphors are often excited by cathode rays, x-rays, or UV emission of a gas discharge, which corresponds to applications in displays, medical imaging and lighting, respectively, such as cathode-ray-tube (CRT) color television, x-ray fluorescent screens and fluorescent lamps.

Materials with nano dimensions such as quantum dots, nanowires, nanorods and nanotubes, have attracted a great deal of attention recently due to their interesting properties that cannot be obtained from the conventional macroscopic materials. Various technological applications require materials that are ordered on all length scales, from the molecular to nano. These novel

nanoscale materials are expected to have potential applications in areas such as optoelectronic devices, photo catalyst fabrication and drug delivery systems. Nanophosphor materials are of potential interest in non-linear optics and in fast optical switching. Quantum dots of II-VI semiconductors have attracted particular attention, because they are easy to synthesize within the size range required for quantum confinement. A reduction in the particle size strongly influences the crystallinity, melting point and structural stability. The unique characteristics of the nanomaterials are believed to have originated from the quantum confinement effects due to the change in the band structure into discrete quantum levels as a result of the smaller size of the nanoparticles.

Luminescent quantum dot is a new paradigm of phosphor known as quantum phosphor. Different from regular microcrystalline phosphors, these nanocrystals exhibit extremely small sizes of 1∼10nm in diameter and size dependent tunable emission from the same pure semiconductor material. The research on quantum dot technology was pioneered by Brus and others since the early 1980's, [56, 57] who demonstrated a wide range of size quantization effects that could be obtained as the size of a semiconductor was reduced to the nanoscale regime. This quantum dot technology enables great flexibility in tuning the optical properties of a material by controlling its physical size [56–58]. For example, the band gap of CdS was found to increase from 2.5 eV, the bulk value, to >3.5 eV as the particle diameter was decreased from 10nm to 1nm [58]. Concurrently, the spectral properties of the luminescence changed and the decay time became extremely fast, ∼ 1-10 ps. As the dot diameter becomes progressively smaller, the energy band shifts to larger values. This indicates that quantum dots can

be engineered to emit in selected spectral regions and in combinations, can cover the entire visible spectrum.

Quantum dots have been widely used as fluorescence tags and have many potential applications in optoelectronic devices such as photovoltaic cells, LEDs and nano-lasers [58]. By far the most common application is in fluorescence tagging to replace molecular dyes. For example, injecting a tagging substance into a biological cell makes it possible to identify that cell from its fluorescence amid other cells.

1.7 Wide band gap semiconductors

The nanostructures can be realized through different types of structures as well as through different materials. The focus of the present thesis is the growth and characterization of different nanostructures of wide band gap semiconductors.

1.7.1 Zinc oxide (ZnO)

ZnO is an oxide of the group II metal oxide, and belongs to the P6$_3$mc space group. Under most growth conditions, ZnO is an n-type semiconductor, though p-type conductivity of ZnO has also been reported for growth under certain conditions [59–62]. ZnO exhibits a wurtzite structure (hexagonal symmetry) or rock salt structure (cubic symmetry). However, ZnO crystals most commonly stabilize with the wurtzite structure (hexagonal symmetry), whereas the crystals exhibit the rock salt phase (cubic symmetry) at high pressure. The wurtzite crystal structure of ZnO is shown in figure 1.4. Even though it is tetrahedrally bonded, the bonds have a partial ionic character. The lattice parameters of ZnO are a = 0.32495 nm and c

= 0.52069 nm at 300K, with a c/a ratio of 1.602, which is close to the 1.633 ratio of an ideal hexagonal close-packed structure. In the direction parallel to the c-axis, the Zn-O distance is 0.1992 nm, and it is 0.1973 nm in all other three directions of the tetrahedral arrangement of nearest neighbors. In a unit cell, zinc occupies the (0, 0, 0.3825) and (0.6667, 0.3333, 0.8825) positions and oxygen occupies the (0, 0, 0) and (0.6667, 0.3333, 0.5) positions [63]. The wurtzite structure of ZnO has a direct energy bandgap of 3.37 eV at room temperature. The lowest conduction band of ZnO is predominantly s-type, and the valance band is p-type (sixfold degenerate).

The Zn-O bond is half ionic and half covalent. Doping in ZnO is much easier compared with other covalent-bond wide bandgap semiconductors, such as GaN. By appropriate doping, the electrical conductivity of ZnO can be tailored from semiconducting to semimetal, keeping high optical transparency to the visible and UV spectral regime. ZnO nanotips are attractive for field emission due to their low emission barrier, high saturation velocity, and high aspect ratio. ZnO is more resistant to radiation damage than Si, GaAs, and GaN [64], which is preferred for the long-term stability of field emission emitters in high electric fields. These make ZnO an ideal candidate among transparent conducting oxides (TCOs) for field emission displays.

ZnO is a wide band gap (3.37 eV) compound semiconductor that is suitable for short wavelength optoelectronic applications. The high exciton binding energy (60 meV) in ZnO crystal can ensure efficient excitonic emission at room temperature. Room temperature ultraviolet (UV) luminescence has been reported in nanoparticles and thin films of ZnO. ZnO is transparent to visible light and can be made highly conductive by doping.
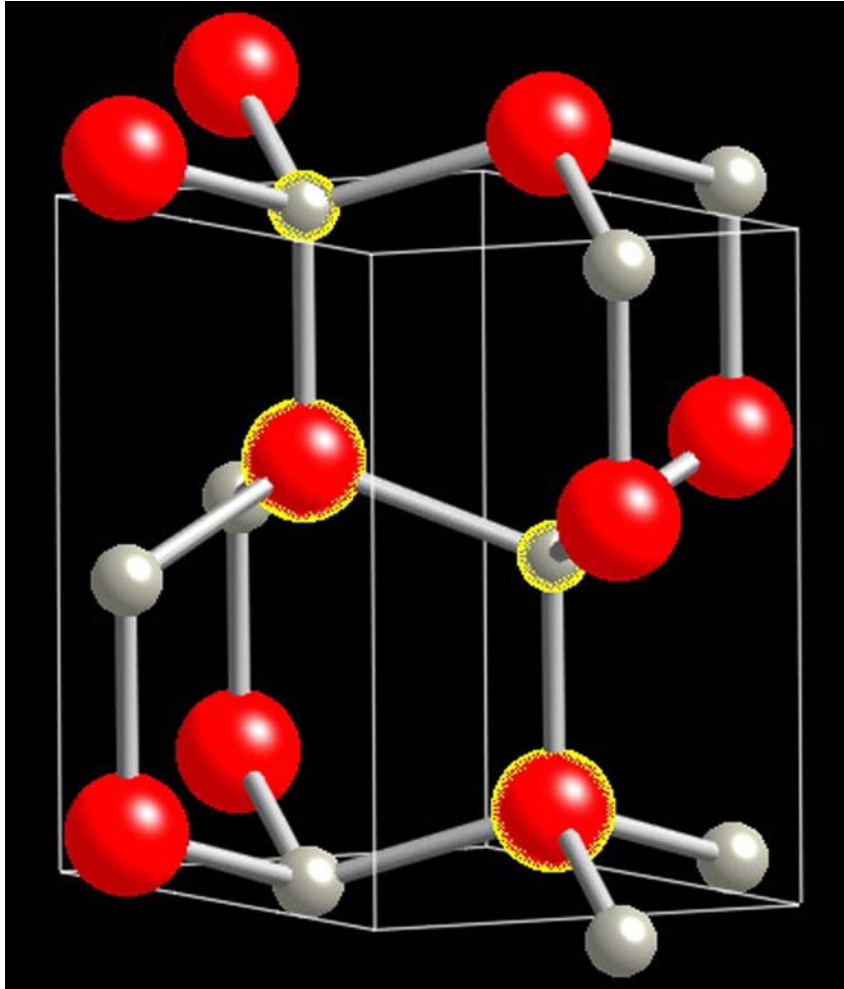
Figure 1.4: The wurtzite structure of ZnO (Zn white, O red; highlighted atoms are inside unit cell)

ZnO is a versatile functional material that has a diverse growth morphologies such as, nanoparticles [35], core/shell nanoparticles [65] nanowires and nanorods [66], nanocombs [67], nanorings [68], nanoloops and nanohe-

lices [69], nanobows [70], nanobelts [71] nanocages [72], nanocomposites [73] and quantum wells [74]. These structures have been successfully synthesized under specific growth conditions [75]. Nanostructures have attracted attention because of their unique physical, optical, and electrical properties resulting from their low dimensionality. ZnO has an effective electron mass of $\sim$0.24 m_e, and a large exciton binding energy of 60 meV. Thus bulk ZnO has a small exciton Bohr radius ($\sim$1.8 nm) [76, 77]. The quantum confinement effect in ZnO nanowires should be observable at the scale of an exciton Bohr radius. An example is the well-width-dependent blue shift in the PL spectra observed in both of ZnO/MgZnO MQWs and nanorods [78], with the ZnO well widths ranging from 1 to 5 nm. Blue shift of emission from free excitons was reported for ZnO nanorods with diameters smaller than 10 nm, which was ascribed to the quantum size effect [79]. Zeng et al [65] studied the tempertaure dependant blue emission from Zn/ZnO core/shell nanostructures synthesized by laser ablation in liquid medium. Au is commonly used as a catalyst for growing ZnO nanowires by vapor liquid solid process [80]. Nanobelts of ZnO are usually grown [81] by sublimation of ZnO powder without introducing a catalyst. Wang et. al reported the hydrothermal growth of ZnO nanoscrewdrivers and their gas sensing properties [82]. The dependance of confinement layer thickness on the PL emission of ZnMgO/ZnO/ZnMgO multiple quantum well structures were reported recently [74]. They also presented room temperature luminescence from this symmetric multiple quantum well structures. Rare earth and transition metals were doped in ZnO nanostructures for luminescent and magnetic applications [83, 84].

Nanostructured ZnO materials have received broad attention due to their distinguished performance in electronics, optics and photonics. From

1960s, synthesis of ZnO thin films has been an active field because of their applications as sensors, transducers and catalysts. In the last few decades, study of one dimensional (1D) materials has become a leading edge in nanoscience and nanotechnology. With reduction in size, novel electrical, mechanical, chemical and optical properties are introduced, which are largely believed to be the result of increased surface area and quantum confinement effects. Nanowire-like structures are the ideal system for studying the transport process in one-dimensionally (1D) confined objects, which are of benefit not only for understanding the fundamental phenomena in low dimensional systems, but also for developing new generation nanodevices with high performance.

ZnO nanostructures have a wide range of technological applications like surface acoustic wave filters [85], photonic crystals [86], photodetectors [87], light emitting diodes [88], photodiodes [89], gas sensors [90], optical modulator waveguides [91], solar cells [92] and varistors [93]. ZnO is also receiving a lot of attention because of its antibacterial property and its bactericidal efficacy has been reported to increase as the particle size decreases [94].

The studies presented in the thesis includes the synthesis of nanoparticles and nanorods of ZnO by low temperature methods like hydrothermal and liquid phase pulsed laser ablation techniques. Room temperature photoluminescent emission from ZnO based symmetric and asymmetric multiple quantum well structures grown by pulsed laser ablation is also discussed in the thesis. Rare earth and transition metal doped ZnO nanostructures grown by hydrothermal method and its magnetic and luminescent properties have been investigated.

1.7.2   Zinc sulfide (ZnS)

Wurtzite ZnS is a direct wide band gap semiconductor which is one of the most important material in photonics. This is because of its high transmittance in the visible range and high index of refraction (about 2.2). ZnS has been synthesized as nanowires, nanobelts, nanocombs, and, most recently, nanohelices [95–97]. All of these are one-dimensional nanostructures. Recently, ZnS nanobelts have been doped with manganese without changing their crystallography [98]. ZnS doped with manganese (Mn) exhibits attractive light-emitting properties with increased optically active sites for applications as efficient phosphors. Furthermore, single ZnS nanobelts have been shown to facilitate optically pumped lasing [99]. All of these properties make ZnS one dimensional nanostructures attractive candidates for use in devices and other technological applications.

Zinc sulfide has two types of crystal structures: hexagonal wurtzite ZnS (referred to as "hexagonal phase") and cubic zinc blende ZnS (referred to as "cubic phase"). Typically, the stable structure at room temperature is zinc blende, there are few reports of stable wurtzite ZnS. The cubic form has a band gap of 3.54 eV at 300 K whereas the hexagonal form has a band gap of 3.91 eV. The transition from the cubic form to the wurtzite form occurs at around 1020^0C. Figure 1.5 shows the cubic zinc blende structure of ZnS.

ZnS is also an important phosphor host lattice material used in electroluminescent devices (ELD), because of the band gap large enough to emit visible light without absorption and the efficient transport of high energy electrons [100].
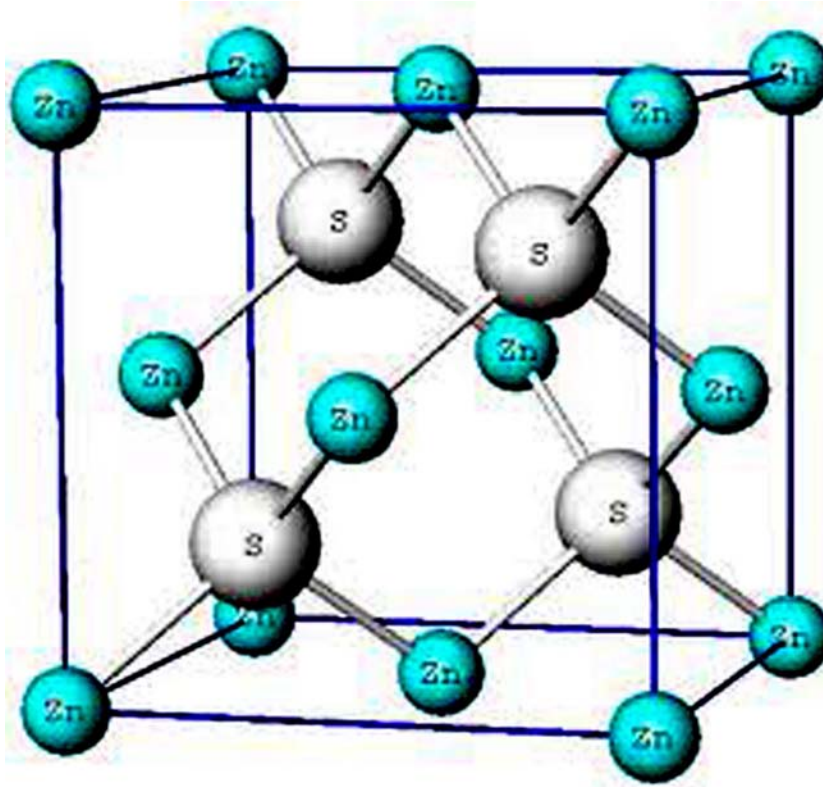
Figure 1.5: The cubic zinc blende structure of ZnS

Bhargava et al. [101] first reported luminescence properties of manganese doped ZnS nanocrystals prepared by a chemical process at room temperature, which initiated investigation on luminescent ZnS nanostructures. Recently, ZnS nanobelts doped with manganese were synthesized by hydrogen-assisted thermal evaporation and studied its lasing action [99]. ZnS nanostructures synthesized by chemical vapor deposition (CVD) have a large number of defects, perhaps due to oxygen incorporation [102]. Nath

et. al studied the green luminescence of ZnS and ZnS:Cu quantum dots embedded in zeolite matrix [103]. This study demonstrates the technological importance of semiconductor quantum dots prepared by low cost chemical route. Manzoor et. al [104] reported the growth of Cu^+-Al^{3+} and Cu^+-Al^{3+}-Mn^{2+} doped ZnS nanoparticles by wet chemical method for electroluminescent applications. The high fluorescent efficiency and dispersion in water makes ZnS:Mn nanoparticles an ideal candidate for biological labelling.

The study presented in the thesis includes the synthesis of ZnS and Mn doped ZnS nanoparticles by liquid phase pulsed laser abaltion technique and its luminescent properties are discussed.

1.7.3   Zinc gallium oxide ($ZnGa_2O_4$)

In 1991, Itoh et al. [105] was the first to report on a new spinel phosphor system - the $ZnGa_2O_4$. It is a ternary oxide compound of ZnO and Ga_2O_3 comprising of only the fourth row cations. The n-type semiconducting [106] $ZnGa_2O_4$ is unique, being a phosphor with cubic symmetry and having an optical band gap of 4.4 eV rendering the material transparency into the UV region of the electromagnetic spectrum.

Zinc gallium oxide crystallizes in the normal spinel structure (Figure 1.6) that has been interpreted as a combination of rock salt and zinc blende structures. The spinel unit cell belongs to the cubic space group Fd3m (Oh^7) [107] with eight formula units per cell and contains two kinds of cation sites. In this normal spinel, Zn^{2+} ions occupy tetrahedral sites and Ga^{3+} ions occupy octahedral sites with lattice constant a = 8.37 $\mathring{A}$. The oxygen ions are in face centered cubic closed packing. A subcell of this structure has four atoms, four octahedral interstices and eight tetrahedral

interstices. This makes a total of twelve interstices to be filled by three cations, one divalent (Zn^{2+}) and two trivalent (Ga^{3+}). In each elementary cell, one tetrahedral and two octahedral sites are filled. Eight of these elementary cells are arranged so as to form a unit cell containing 32 oxygen ions, 16 octahedral cations, and 8 tetrahedral cations. The spinel structure, hence, turns out to be a close packed cubic arrangement of anions with one-half of the octahedral holes and one-eighth of the tetrahedral holes filled with cations. The material exhibits excellent stability and cubic symmetry in spite of the fact that almost three fourth of the structure is vacant. This is because spinel structures have the ability to accept structural vacancies, thus forming a defect solid solution while remaining as single phase [108].
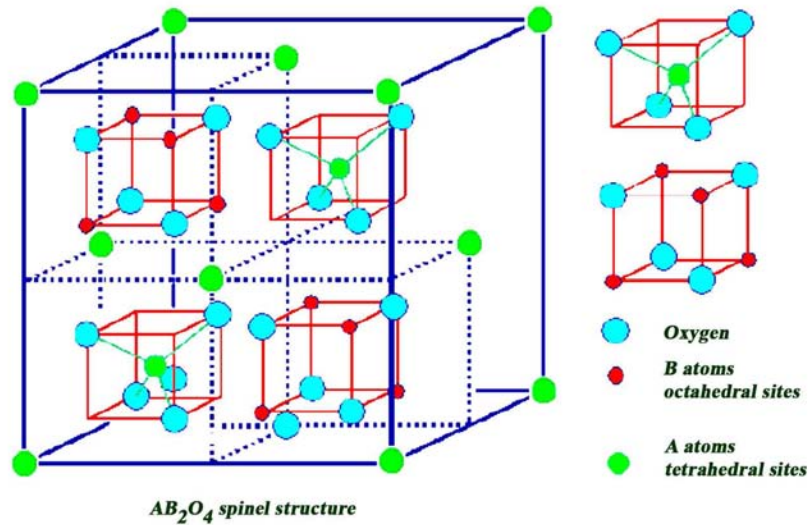
Figure 1.6: Spinel cubic crystal structure of $ZnGa_2O_4$

$ZnGa_2O_4$ exhibits an intrinsic blue luminescence under excitation by

both ultraviolet light and low voltage electrons via a self-activated optical center associated with the octahedral Ga-O group [109, 110]. The emission properties are relatively sensitive to preparation conditions and Ga/Zn ratio in $ZnGa_2O_4$ phosphor [111]. It is reported that the cathodoluminescence (CL) spectra of $ZnGa_2O_4$ has a peak at 457 [112] or 470 nm [113], while the photoluminescent (PL) peak is located at about 432 [110], 450 [114] or 470-490 nm [115].

$ZnGa_2O_4$ phosphor can emit in the different regions of the visible spectrum by suitably doping it with transition metals or rare-earth elements. Mn^{2+} activated $ZnGa_2O_4$ has been widely investigated as an efficient green emitting phosphor [114]. The material emits green when doped with Tb [116] or Tm. Activation with Co [117], Cr and Eu [118, 119] gives red and while Ce provides the blue emission. There are reports stating that a systematic tuning (usually, a redshift) of the luminescent properties of self-activated $ZnGa_2O_4$ phosphors is possible by Cd [120] or Si [121] substitution.

Growth of $ZnGa_2O_4$ and Eu doped $ZnGa_2O_4$ nanoparticles and the luminescent emission properties of these nanoparticles were investigated in the present study.

1.8   Device applications

Nanotechnology offers an extremely broad range of potential applications from electronics, optical communications and biological systems to new materials. Many possible applications have been explored and many devices and systems have been studied. Some of the applications of nanostructures are follows.

1.8.1 Optical devices

Nanowire laser

UV laser sources are of strong research interest because of their broad applications, including nonline-of-sight covert communication, bioagent detection, high-density optical storage, and UV photonics. ZnO has a high exciton binding energy of 60 meV, much greater than the thermal energy at room temperature (26 meV). Thus the exciton in ZnO could be stable even at room temperature, which facilitates efficient excitonic recombination. Nanowire UV lasers and laser arrays could serve as miniaturized light sources for optical interconnections, quantum computing, the microanalysis for biochemical and environmental applications toward the integration of lab-on-a-chip. It is still a technical challenge to achieve reliable and device quality p-type ZnO materials. Optically pumped ZnO nanowire laser arrays as well as single ZnO nanowire lasers have been demonstrated [122–124]. The nanowires with diameters ranging from 20 to 150 nm and lengths up to 40 μm are being used as the lasing medium. The samples are directly pumped by the fourth harmonic of an Nd:YAG laser at room temperature. Light emission was collected along the c-axis of the nanowire.

The single nanowire lasing behavior is further proved by using near-field scanning optical microscopy (NSOM) [124]. The nanowire was removed by sonication in an alcohol solvent and dispersed onto a quartz substrate. The emitted light was collected by the fiber probe of an NSOM. The emission spectrum shows that the single nanowire serves as an active Fabry-Perot optical cavity.

Light emitting diodes

Blue/green light-emitting diodes (LED) have been developed based on nanostructures of wide-band gap II-VI semiconductor nanomaterials [125]. Such devices take direct advantages of quantum well heterostructure configurations and direct energy band gap to achieve high internal radiative efficiency. Various LED at short visible wavelengths have been fabricated based on nanostructures or quantum well structures of ZnSe-based material [126, 127] and ZnTe-based materials [128].

Nanowire photodetector

ZnO is suitable material as a UV photodetector because of its direct wide bandgap and large photoconductivity. ZnO epitaxial film-based photoconductive and Schottky type UV photodetectors have been demonstrated [129]. Large photoconductivity has been reported for a single ZnO nanowire [130]. The ZnO nanowires with diameters ranging from 50 to 300nm were dispersed on prefabricated gold electrodes. Electrical resistivities without and with UV light irradiation were measured in a four-terminal configuration. The conductivity of ZnO nanowire under UV irradiation increases by 4 to 6 orders of magnitude compared with the dark current with a response time in the order of seconds. The photoresponse has a cut off wavelength of ~370 nm.

It is known that the photoresponse of ZnO consists of two parts: a fast response due to reversible solid-state processes, such as intrinsic interband transition, and a slow response mainly due to the oxygen adsorption-photodesorption and defect related recombination processes [130, 131]. A two-step process gives rise to the slow increase in photoconductivity: (1)

oxygen adsorps on the surface states as a negatively charged ion by capturing a free electron:

$$O_2 + e^- \rightarrow O_2^- \tag{1.5}$$

and (2) photodesorption of O_2 by capturing a photogenerated hole:

$$h^+ + O_2^- \rightarrow O_2 \tag{1.6}$$

Therefore, the photogenerated electrons increase the conductivity. The slow process can be suppressed by reducing the trap density and background carrier concentration. ZnO nanowires also show a reversible switching behavior between dark conductivity and photoconductivity when the UV lamp is turned on and off. These suggest that ZnO nanowires are good candidates for optoelectronic switches.

1.8.2   Solid state lighting and white LED

Over 125 years ago kerosene lanterns were used as the lighting source, until Edisons discovery of the incandescent light bulb in 1879. Following the invention of the fluorescent lamps, high pressure sodium lamps and so on, we are now living through another great revolution in lighting technology, known as solid state lighting. In the evolution of lighting technology, phosphors play an important role such as in fluorescent lamps, and will continue to affect greatly the cutting-edge technology, solid state lighting.

Solid state lighting refers to the lighting emission from solid state diodes, known as LEDs, which exhibit higher energy conversion efficiency, compact structure and longer life compared to conventional lamps [132–134]. Until recently, LEDs have been used primarily for low intensity monochromatic

lighting applications such as indicator lights or alphanumeric displays. Advances in materials research and device fabrication have increased the intensity of red, green and blue LEDs dramatically, so that the light intensity emitted at a particular wavelength can rival that from light bulbs with color filters.

White light emitters have attracted special interest recently for a number of potential applications in cars, traffic information signs, displays and general illumination [132–134]. White LEDs can be fabricated by several methods [133]. The first lies solely on combination of LEDs with the three primary colors to produce bright white light source which are significantly more efficient than incandescent bulbs and are more adaptable. Multiple semiconductor LEDs will not be competitive in the larger market for residential and commercial lighting. Moreover, the directional nature of LED output makes this approach not suitable for general illumination application.

Another more practical method for producing white LEDs has been developed using group III-nitride group nitride LEDs driving the downconverting phosphors [133]. Blue and Ultraviolet (UV) emission from (InAlGa)N LEDs can be used to excite phosphors. Upon absorption of blue or UV light, the phosphors convert the energy to visible radiation depending on the type of phosphors used. White light can be achieved through mixing red (R), green (G) and blue (B) color emitting phosphors. White light emission can also be achieved by using part of the blue emission of the exciting wavelength of LEDs and the blue to red and green down converter phosphors.

Solid state lighting and white LEDs offers new opportunities and challenges for the application of phosphors. Traditional phosphors, such as

YAG:Ce, have been commercialized for use on blue LEDs to produce white light by Nichia Corp [133]. However, to improve the performance of white LEDs, new phosphors which absorb strongly in the blue, near-UV region still need to be developed.

1.8.3 Electronic devices

Field emission devices

Field emission sources are widely used in flat-panel displays. In thermionic emission, electrons are emitted from a heated filament. Field emission is a cold-cathode emission, in which electrons are emitted from a conductor into vacuum through its surface barrier under the applied electric field even at room temperature. Compared with thermionic emission, field emission has the advantages of less thermal shift, low energy spread, and low operating voltage. Traditional field emission devices (FEDs) require complicated fabrication processes. An ideal field emitter should be highly conductive, very sharp at the tip, robust, and easy to fabricate. ZnO has a high melting point, low emission barrier, and high saturation velocity. Furthermore, ZnO is more resistant to radiation damage than Si, GaAs, and GaN, preferred for long-term stability for the field emitters in the high electrical field. As a widely studied transparent conductive oxide [135], ZnO can be made both highly conductive and optically transparent from the visible to near-UV range through proper doping. These properties make ZnO nanotips a promising candidate for FEDs. The field emission properties of ZnO nanowires were first studied by Lee's group in 2002 [136]. ZnO nanoneedle arrays with sharp-tips show improved field emission performance [137].

Field effect transistor

Field effect transistors (FETs) can be fabricated by contacting semiconducting one-dimensional nanostructures to metallic electrodes, allowing the exploration of the electrical properties of the structures. FETs have been fabricated with SnO_2 and ZnO nanobelts and with nanowires [138]. A ZnO nanobelt FET synthesized by thermal evaporation has showed a high threshold voltage of -15V, which is due to the high resistive contact resulting from simply depositing the ZnO nanobelt on top of the gold electrodes. It has a switching ratio of nearly 100 and a peak conductivity of 1.25 x $10^{-3}Scm^{-1}$. It also shows UV sensitivity. By placing these one-dimensional nanostructure based FETs in different environments, they can be shown to have excellent applications as nanoscale sensors. The high surface to volume ratio of one-dimensional nanostructures makes them potentially far superior than thin films. This allows higher sensitivity for sensors because the faces are more exposed and the small size is likely to produce a complete depletion of carriers into the nanobelt, which typically changes the electrical properties.

1.8.4   Biological applications of nanoparticles

One important branch of nanotechnology is nanobiotechnology. Nanobiotechnology includes (i) the use of nanostructures as highly sophisticated machines or materials in biology and medicine, and (ii) the use of biological molecules to assemble nanoscale structure [139]. One of the important biological application of colloidal nanocrystals is molecular recognition. But there are many more biological applications of nanotechnology [140, 141]. Nanocrystals conjugated with a receptor can be directed to bind to positions

where ligand molecules are present, which fit the molecular recognition of the receptor [139]. This facilitates a set of applications including molecular labeling. For example, when gold nanoparticles aggregate, a change of color from ruby-red to blue is observed, and this phenomenon has been exploited for the development of very sensitive colorimetric methods of deoxyribonucleic acid (DNA) analysis [142].

Chapter 2

Synthesis and characterization of nanostructures

2.1 Introduction

As particle size drops from microns to tens of nanometers, metallic nanoparticles cease to behave as bulk metal and begin exhibiting quantum mechanical behavior similar to that of individual atoms. Ten hydrogen atoms stacked side-by-side measure only a single nanometer. The lure of nanotechnology is not just making small devices; but to construct the smallest physical structures possible. A single atom is only a one tenth of a nanometer in diameter. Nanotechnology is, in a very literal sense, an opportunity to play with nature's own building blocks [143]. The realization of the full potential of nanosystems has so far been limited due to their difficulties in their synthesis and subsequent assembly into useful functional

structures and devices. The three steps in the development of nanoscience and technology include material preparation, characterization and device fabrication.

The synthesis of nanoscale particles has received considerable attention in view of the potential for new materials with novel properties and the design of catalysts with specific dimensions and composition. Nanoscale materials posses several unique properties such as large surface area, unusual adsorptive properties, surface defects, and fast diffusivities. This chapter discuss various techniques that were used in the growth of nanostructures. Nanoparticles, nanorods and quantum well structures were grown by hydrothermal method, liquid phase pulsed laser ablation and pulsed laser deposition techniques. Various characterization tools were used to study its structural, morphological, optical and magnetic properties.

2.2 Experimental techniques for the growth of nanostructures

Preparation of nanoparticle is being advanced by numerous physical and chemical techniques. Nanostructured materials are synthesized using a combination of approaches, for example melting and solidification process followed by thermodynamical treatments, or solution/vacuum deposition. In many cases however the final product is dictated by the kinetics of thermodynamics of systems. There are basically two broad areas of synthesis techniques for nanostructured materials namely (1) physical methods and (2) chemical methods.

2.2.1 Physical methods

Several physical methods are currently in use for the synthesis and commercial production of nanostructured materials. The first and the most widely used technique involve the synthesis of single-phase metals and ceramic oxides by the inert-gas evaporation technique [144]. The generation of atom clusters by gas phase condensation proceeds by evaporating a precursor material, either a single metal or a compound, in a gas maintained at a low pressure, usually below 1 atm. The evaporated atoms or molecules undergo a homogeneous condensation to form clusters via collisions with gas atoms or molecules in the vicinity of a cold-powder collection surface. The clusters once formed must be removed from the region of deposition to prevent further aggregation and coalescence of the clusters. These clusters are readily removed from the gas condensation chamber either by natural convection of the gas or by forced gas flow.

Sputtering is another technique used to produce nanostructured clusters as well as a variety of thin films [145, 146]. This method involves the ejection of atoms or clusters of designated materials by subjecting them to an accelerated and highly focused beam of inert gas such as argon or helium. Sputtering process produces films with better controlled composition, provides films with greater adhesion and homogeneity and permits better control of film thickness. The sputtering process involves the creation of gas plasma usually an inert gas such as argon by applying voltage between a cathode and anode. The target holder is used as cathode and the anode is the substrate holder. Source material is subjected to intense bombardment by ions. By momentum transfer, particles are ejected from the surface of the cathode and they diffuse away from it, depositing a thin

film of the material onto the substrate.

The third physical method involves the generation of nanostructured materials via severe mechanical deformation. In this method nanostructured materials are produced not by cluster assembly but rather by structural degradation of coarser-grained structures induced by the application of high mechanical energy. The nanometer-sized grains nucleate within the shear bands of the deformed materials converting a coarse-grained structure to an ultra fine powder. The heavy deformation of the coarser materials is effected by means of a high-energy ball mill or a high-energy shear process. Although this method is very useful in generating commercial quantities of the material, it suffers from the disadvantage of contamination problems resulting from the sources of the grinding media.

Chemical vapor deposition (CVD) is the process of depositing chemically reacting volatile compound of a material, with other gases, to produce a nonvolatile solid on a suitably placed substrate [147]. It differs from physical vapor deposition (PVD), which relies on material transfer from condensed-phase evaporant or sputter target sources. Because CVD processes do not require vacuum or unusual levels of electric power, they were practiced commercially prior to PVD. Because they are subject to thermodynamic and kinetic limitations and constrained by the flow of gaseous reactants and products, CVD processes are generally more complex than those involving PVD. Plasma-enhanced chemical vapor deposition (PECVD) is one of the modifications of the conventional CVD process. In the PECVD system, electric power is supplied to the reactor to generate the plasma. The power is supplied by an induction coil from outside the chamber, or directly by diode glow-discharge electrodes. In the plasma, the degree of

ionization is typically 10^{-4}, so the gas in the reactor consists mostly of neutrals. Ions and electrons travel through the neutrals and get energy from the electric field in the plasma.

Self-assembled quantum dots nucleate spontaneously under certain conditions during molecular beam epitaxy (MBE) and metallorganic vapour phase epitaxy (MOVPE), when a material is grown on a substrate to which it is not lattice matched. The resulting strain produces coherently strained islands on top of a two-dimensional "wetting layer". This growth mode is known as Stranski-Krastanov growth. The islands can be subsequently buried to form the quantum dot. This fabrication method has potential for applications in quantum cryptography (i.e. single photon sources) and quantum computation [144]. The main limitations of this method are the cost of fabrication and the lack of control over positioning of individual dots.

Liquid phase pulsed laser ablation (LP-PLA)

Laser ablation had been identified as a versatile technique for the preparation of nanostructures, mainly nanorods, quantum wells and quantum dots. Precise control over the size of the nanostructures could be attained by playing various deposition parameters like substrate temperature, substrate to target distance, gaseous atmosphere in the chamber and laser energy density during the pulsed laser deposition [148]. Recently liquid phase-pulsed laser ablation technique (LP-PLA) has been evolved as a synthesis technique for the preparation of nano particles [149]. In this method, the bulk target of the material is immersed in a liquid (for example water) and then the laser beam (from Nd:YAG or excimer laser) is allowed to focus through the liquid on to the target surface. A simple experimental setup of LP-PLA

technique is shown in figure 2.1. Plasma of the ejected species disperses directly to the liquid in which the target is immersed. By controlling the energy density of the laser beam and using liquids containing surfactants, size of the particle can be tuned. This LP-PLA is very simple, by product free and clear technique, because quantum dots can be directly dispersed in liquid medium without the play of much chemistry. Transparent and highly luminescent ZnO, Zn and ZnS nanoparticles dispersed in water have been prepared by this method using third (355 nm) and fourth (266 nm) harmonics of Nd:YAG laser.
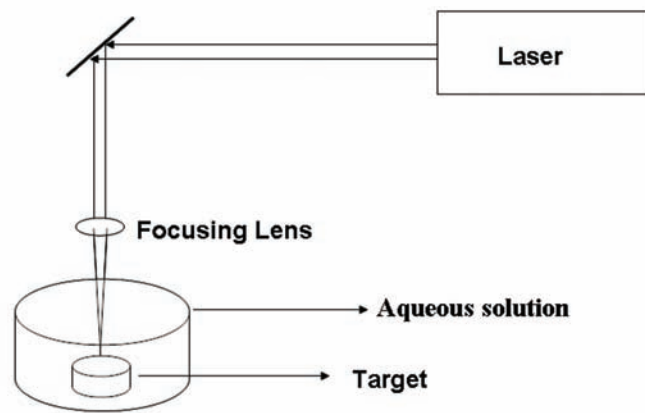
Figure 2.1: Experimental setup used for the growth of nanoparticles by LP- PLA technique

Pulsed laser deposition (PLD)

The laser is a source of energy in the form of monochromatic and coherent photons, enjoying ever increasing popularity in diverse and broad applications. In many areas such as metallurgy, medical technology and electronic industry, the laser has become an irreplaceable tool. In material science

also lasers play a significant role either as a passive component for process monitoring or as an active tool by coupling its radiation energy to the material being processed. The coupling of laser radiation with the processing material led to various applications such as localized melting during optical pulling, laser annealing of semiconductors, surface cleaning by desorption and ablation, laser induced rapid quench to improve surface hardening and most recently pulsed laser deposition for growing thin films [150].

Pulsed laser deposition (PLD) is clearly emerging as one of the premier thin film deposition technology. PLD has gained a great deal of attention in the past few years for its ease of use and success in depositing materials of complex stoichiometry. PLD was the first technique used to successfully deposit the superconducting $YBa_2Cu_3O_{7-x}$ thin film. Since then, many materials that are normally difficult to deposit by other methods, especially multi-element oxides, have been successfully deposited by PLD. In the case of multi-elemental compounds such as high temperature superconductors, ferroelectrics and electro optic materials, this technique is extremely successful. This technique offers many potential applications, from integrated circuits and optoelectronics to micro mechanics and medical implants [151].

The best quality films can be deposited by controlling the substrate temperature (T), the relative and absolute arrival rates of atoms (R) and the energy of the depositing flux (E). PLD offers the best control over these parameters than other vacuum deposition techniques [150]. A schematic diagram of a simple PLD technique is shown in figure 2.2. In its simplest configuration, a high-power laser situated outside the vacuum deposition chamber is focused by means of external lenses onto the target surface, which serves as the evaporation source. PLD relies on a photon interaction to create an ejected plume of material from any target. The vapor

(plume) is collected on a substrate placed at a short distance from the target. Though the actual physical processes of material removal are quite complex, one can consider the ejection of material to occur due to rapid explosion of the target surface due to superheating. Unlike thermal evaporation, which produces a vapor composition dependent on the vapor pressures of elements in the target material, the laser-induced expulsion produces a plume of material with stoichiometry similar to the target.
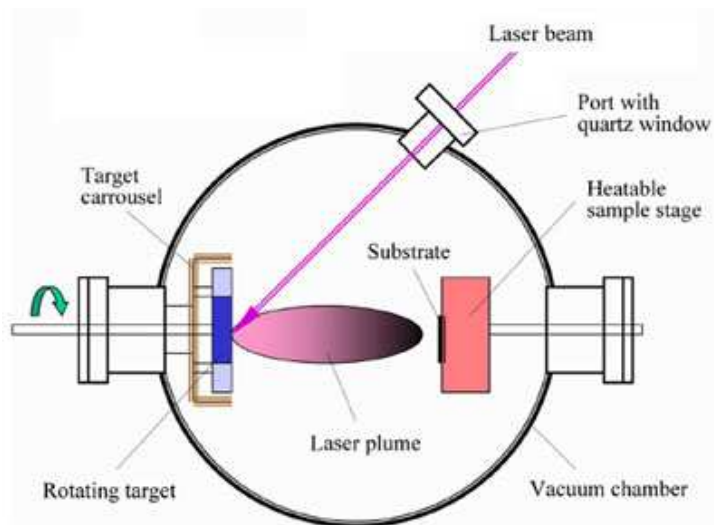
Figure 2.2: Schematic diagram of the PLD setup used for the present investigation

The main advantage of PLD derives from the laser material removal mechanism. It is generally easier to obtain the desired film stoichiometry for multi-element materials using PLD than with any other deposition techniques. Typical plasma temperature measured by emission spectroscopy during initial expansion is 10,000 K, which is well above the boiling point

of most materials (3000 K). Heating of the plasma to these temperatures is thought to occur by inverse-Bremsstrahlung absorption of the laser light in a free-free transition of electron ion pair. This high temperature would evaporate the surface layer of the target thereby replicating exact target composition in the thin films.

Mechanisms of PLD

Pulsed laser deposition is a very complex physical phenomenon involving laser-material interaction under the impact of high-power pulsed radiation on solid target, and formation of plasma plume with highly energetic species. The thin film formation process in PLD generally can be divided into the following four stages.

1. Interaction of laser radiation with the target material.

2. Dynamics of the ablated materials.

3. Deposition of the ablated materials on the substrate.

4. Nucleation and growth of the thin film on the substrate surface.

In the first stage, the laser beam is focused onto the surface of the target. At sufficiently high flux densities and short pulse duration, all elements in the target are rapidly heated up to their evaporation temperature. Materials are dissociated from the target surface and ablated out with same stoichiometry as in the target. The instantaneous ablation rate is highly dependent on the fluences of the laser shining on the target. The ablation mechanisms involve many complex physical phenomena such as collisional, thermal, and electronic excitation, exfoliation and hydrodynamics.

During the second stage the emitted materials tend to move towards the substrate according to the laws of gas dynamic and show the forward peaking phenomenon. The spot size of the laser and the plasma temperature has significant effects on the deposited film uniformity. The target-substrate distance is another parameter that governs the angular spread of the ablated materials.

The third stage is important to determine the quality of thin film. The ejected high-energy species impinge onto the substrate surface and may induce various type of damage to the substrate. These energetic species sputter some of the surface atoms and a collision region is formed between the incident flow and the sputtered atoms. Film grows after a thermalized region is formed. The region serves as a source for condensation of particles. When the condensation rate is higher than the rate of particles supplied by the sputtering, thermal equilibrium condition can be reached quickly and film grows on the substrate surface at the expenses of the direct flow of the ablation particles.

The effect of increasing the energy of the adatoms has a similar effect of increasing substrate temperature on film growth [150]. Typical power densities involved in PLD are approximately 50MWcm^{-2} for a reasonable growth rate (> 1 Å/shot). If plasma is formed in vacuum or in air during laser target interaction, then an explicit laser plasma interaction occurs. Due to which ions in the plasma are accelerated to as much as 100 - 1000 eV [150]. Nucleation and growth of crystalline films depends on many factors such as the density, energy, ionization degree, and the type of the condensing material, as well as on the temperature and the physico-chemical properties of the substrate. The two main thermodynamic parameters for

the growth mechanism are substrate temperature T and supersaturation D_m. They can be related by the following equation

$$D_m = kTln(R/R_e) \qquad (2.1)$$

where k is the Boltzmann constant, R is the actual deposition rate, and R_e is the equilibrium value at the temperature T.

The nucleation process depends on the interfacial energies between the three phases present viz, substrate, the condensing material and the vapor. The critical size of the nucleus depends on the driving force, i.e., the deposition rate and the substrate temperature. For the large nuclei, a characteristic of small supersaturation, they create isolated patches (islands) of the film on the substrate, which subsequently grow and coalesce together. As the supersaturation increases, the critical nucleus shrinks until its height reaches to atomic diameter and its shape is that of a two-dimensional layer. For large supersaturation, the layer-by-layer nucleation will happen for incompletely wetted foreign substrates.

The crystalline film growth depends on the surface mobility of the adatoms (vapor atoms). Normally, the adatom will diffuse through several atomic distances before sticking to a stable position within the newly formed film. The surface temperature of the substrate determines the adatom's surface diffusion ability. High temperature favours rapid and defect free crystal growth, whereas low temperature or large supersaturation crystal growth may be overwhelmed by energetic particle impingement, resulting in disordered or even amorphous structures.

In PLD, the plume is highly directional, and its contents are propelled to the substrate where they condensed and there by forming a film. Gases (O_2,

N_2) are often introduced in to the deposition chamber to promote surface reactions or maintain film stoichiometry. Precautions are usually taken to minimise the number of gross particulates ejected as a result of splashing from being incorporated into the depositing film. Splashing of macroscopic particles during laser-induced evaporation is a significant drawback of PLD. High directionality of the plume is another major drawback, which makes it difficult to uniformly deposit films over large area.

The generation of particulates during splashing is believed to have several origins. These include the rapid expansion of gas trapped beneath the target surface, a rough target surface morphology whose mechanically weak projections are prone to fracturing during pulsed thermal shocks, and superheating of subsurface layers before surface atoms vaporize. A common strategy for dealing with splashing effects is to interpose a rapidly spinning pinwheel-like shutter between the target and substrate. The slower moving particulates can be batted back, allowing the more mobile atoms, ions, and molecules to penetrate this mechanical mass filter. Window materials, an important component in PLD systems, must generally satisfy the dual requirement of optical transparency to both visible and ultraviolet light. Relatively few materials are suitable for this demanding role, but MgF_2, sapphire, CaF_2, and UV-grade quartz have served as suitable window materials.

In the present study fourth (266 nm) harmonics of Nd:YAG laser (Spectra Physics) is used for ablation.

2.2.2   Chemical methods

Chemistry has played a major role in developing new materials with novel and important properties. The advantage of chemical method is its versa-

tility in designing and synthesizing new materials that can be refined into a final product. The primary advantage that chemical processes over other methods is good chemical homogeneity, as chemical synthesis offers mixing at the molecular level. Molecular chemistry can be designed to prepare new materials by understanding how matter is assembled on an atomic or molecular level and the consequent effects on the desired material macroscopic properties. A basic understanding on the principles of crystal chemistry, thermodynamics, and phase equilibrium and reaction kinetics is important to take advantage of the many benefits that chemical processing has to offer.

There are certain difficulties in chemical processing. In some preparations, the chemistry is complex and hazardous. Contamination can also result from the byproducts being generated or side reactions in the chemical process. This should be minimized or avoided to obtain desirable properties in the final product. Agglomeration can also be a major cause of concern at any stage in a synthetic process and it can dramatically alter the properties of the materials. Finally, although many chemical processes are scalable for economical production, it is not always straight forward for all systems.

Solution chemistry is used sometimes to prepare the precursor, which is subsequently converted to the nano phase particles by non-liquid phase chemical reactions. Precipitation of a solid from a solution is a common technique for the synthesis of fine particles. The general procedure involves reactions in the aqueous or non-aqueous solutions containing the soluble or suspended salts [144]. Once the solution becomes super saturated with the product, the precipitate is formed by either homogeneous or heterogeneous nucleation. The formation of a stable material with and without the presence of a foreign species is referred to as heterogeneous and homogeneous

nucleation respectively. The growth of the nuclei after formation usually proceeds by diffusion, in which case concentration gradients and reaction temperatures are very important in determining the growth rate of particles. For instance, to form unagglomerated particles with a very narrow size distribution, all the nuclei must be formed at nearly the same time and the subsequent growth must be occurred without further nucleation or agglomeration of particles.

Nanostructured materials are also prepared by chemical vapour deposition (CVD) or chemical vapour condensation (CVC). In these processes a chemical precursor is converted to the gas phase and it then undergoes decomposition at either low or atmospheric pressure to generate the nanostructured particles. These products are then subjected to transport in a carrier gas and collected on a cold substrate, from where they are scarped and collected. The CVC method can be used to produce a variety of powders and fibers of metals, compounds, or composites. The CVD method has been employed to synthesis several ceramic metals, intermetallics, and composite materials. Semiconductor clusters have traditionally been prepared by use of colloids, micelles, polymers, crystalline hosts, and glasses [144]. The clusters prepared by these methods have poorly defined surfaces and a broad size distribution, which is detrimental to the properties of semiconductor materials. A more detailed discussion on nanomaterial preparation and nanostructure fabrication can be found in the recent literature [144].

Hydrothermal Method

The hydrothermal processing is a non conversional method to obtain nanocrystalline inorganic materials. The hydrothermal technique is becoming one of the most important tools for advanced materials processing, particularly

owing to its advantages in the processing of nanostructure materials for a wide variety of technological applications such as electronics, optoelectronics, catalysis, ceramics, magnetic data storage, biomedical, biophotonics, etc. The hydrothermal technique not only helps in processing monodispersed and highly homogeneous nanoparticles, but also acts as one of the most attractive techniques for processing nano-hybrid and nanocomposite materials. The term hydrothermal is purely of geological origin. Hydrothermal processing can be defined as any heterogeneous reaction in the presence of aqueous solvents or mineralizers under high pressure and temperature conditions to dissolve and recrystallize (recover) materials that are relatively insoluble under ordinary conditions. Byrappa and Yoshimura [152] define hydrothermal as any heterogeneous chemical reaction in the presence of a solvent (whether aqueous or non-aqueous) above the room temperature and at pressure greater than 1 atm in a closed system. Among various technologies available today in advanced materials processing, the hydrothermal technique occupies a unique place owing to its advantages over conventional technologies. This synthesis method uses the solubility in water of almost all inorganic substances at elevated temperature and pressures, and subsequent crystallization of the dissolved material from the fluid. Water at elevated temperatures plays an essential role in the precursor material transformation. The pressure, temperature, precursor concentration and time of reaction are the principal parameters in hydrothermal processing.

The hydrothermal processing of advanced materials has lots of advantages and can be used to give high product purity and homogeneity, crystal symmetry, meta stable compounds with unique properties, narrow particle size distributions, a lower sintering temperature, a wide range of chemical compositions, single-step processes, dense sintered powders, sub-micron to

nanoparticles with a narrow size distribution using simple equipment, lower energy requirements, fast reaction times, lowest residence time, as well as for the growth of crystals with polymorphic modifications, the growth of crystals with low to ultra low solubility, and a host of other applications. The hydrothermal technique offers a unique method for coating of various compounds on metals, polymers and ceramics as well as for the fabrication of powders or bulk ceramic bodies. It has now emerged as a frontline technology for the processing of advanced materials for nanotechnology. On the whole, hydrothermal technology in the 21st century has altogether offered a new perspective.

The behavior of the solvent under hydrothermal conditions dealing with aspects like structure at critical, supercritical and sub-critical conditions, dielectric constant, pH variation, viscosity, coefficient of expansion, density, etc. is to be understood with respect to pressure and temperature. Similarly, the thermodynamic studies yield rich information on the behaviour of solutions with varying pressure temperature conditions. Some of the commonly studied aspects are solubility, stability, yield, dissolution precipitation reactions and so on, under hydrothermal conditions. Hydrothermal crystallization is only one of the areas where our fundamental understanding of hydrothermal kinetics is lacking due to the absence of data related to the intermediate phases forming in solution in the absence of predictive models; we must empirically define the fundamental role of temperature, pressure, precursor, and time on crystallization kinetics of various compounds [153].

A key limitation to the conventional hydrothermal method has been the need for time consuming empirical trial and error methods as a mean for process development. Material processing under hydrothermal conditions

requires a vessel capable of containing a highly corrosive solvent at high temperature and pressure. Ideal hydrothermal apparatus popularly known as an autoclave should have the following characteristics:

1. Inertness to acids, bases and oxidizing agents.

2. Ease of assembly and disassembly.

3. Sufficient length to obtain a desired temperature gradient.

4. Leak-proof to the required temperature and pressure

5. Rugged enough to bear high pressure and temperature experiments for long periods with no damage so that no machining or treatment is needed after each experimental run.

Figure 2.3: Hydrothermal furnace and autoclave used for the synthesis of nanostructures

The hydrothermal furnace and autoclave used in the present study for the synthesis of nanostructures are shown in the figure 2.3. In the hydrothermal synthesis, the precursor materials are taken in a container with solid to water proportion of about 1:10. The closed containers are placed

into the sealed stainless steel autoclaves and put into the furnace. Applying the desired hydrothermal synthesis temperature, an autogenous pressure is formed. The external pressure is adjusted as soon as the temperature equilibrium is achieved within the autoclave. By the installation of the hydrothermal pressure, the reaction process takes place. Temperature fluctuations of the furnace have negative consequences because a rise in the temperature leads to a higher dissolution rate disturbing the dynamic equilibrium of dissolution-crystallization, while lowering of temperature leads to higher supersaturation.

2.3 Characterization tools

2.3.1 Structural characterization

X-ray diffraction

The structural characterization was carried out by recording the x-ray diffraction (XRD) pattern of the samples. XRD pattern was taken using Rigaku D-max C x-ray diffractometer with Cu-K$_\alpha$ radiation (λ=1.5418 Å). A given substance always produces a characteristic diffraction pattern whether that substance is present in the pure state or as one constituent of a mixture. This fact is the basis for the diffraction method of chemical analysis. The particular advantage of x-ray diffraction analysis is that it discloses the presence of a substance, as that substance actually exists in the sample and not in terms of its constituent chemical elements. Diffraction analysis is useful whenever it is necessary to know the state of chemical combination of the elements involved or the particular phase in which they are present. Compared with ordinary chemical analysis the diffraction method has the

advantage that it is usually much faster, requires only very small quantity of sample and is non destructive [154, 155].

The basic law involved in the diffraction method of structural analysis is the Bragg's law. When monochromatic x-ray impinge upon the atoms in a crystal lattice, each atom acts as a source of scattering. The crystal lattice acts as series of parallel reflecting planes. The intensity of the reflected beam at certain angles will be maximum when the path difference between two reflected waves from two different planes is an integral multiple of λ. This condition is called Bragg's law and is given by the relation 2.2,

$$2dsin\theta = n\lambda \qquad (2.2)$$

where n is the order of diffraction, λ is the wavelength of the x-rays, d is the spacing between consecutive parallel planes and θ is the glancing angle (or the complement of the angle of incidence) [156].

X-ray diffraction studies give a whole range of information about the crystal structure, orientation, average crystalline size and stress in the films. Experimentally obtained diffraction patterns of the sample are compared with the standard powder diffraction files published by the inorganic crystal structure database (ICSD).

The average grain size of the film can be calculated using the Scherrer's formula 2.3 [154],

$$d = \frac{0.9\lambda}{\beta cos\theta} \qquad (2.3)$$

where, λ is the wavelength of the x-ray and β is the full width at half maximum intensity in radians. The lattice parameter for crystallographic

systems in the present study can be calculated from the following equations using the (hkl) parameters and the interplanar spacing d.

Cubic system,

$$\frac{1}{d^2} = \frac{h^2 + k^2 + l^2}{a^2} \tag{2.4}$$

Tetragonal system,

$$\frac{1}{d^2} = \frac{h^2 + k^2}{a^2} + \frac{l^2}{c^2} \tag{2.5}$$

Hexagonal system,

$$\frac{1}{d^2} = \frac{4}{3}\left(\frac{h^2 + hk + k^2}{a^2}\right) + \frac{l^2}{c^2} \tag{2.6}$$

X-ray diffraction measurements of the films and powders in the present studies were carried out using Rigaku automated x-ray diffractometer. The filtered copper K_α (λ =1.5418 Å) radiation was used for recording the diffraction pattern.

The broadening of x-ray diffraction peaks can be obtained with a diffractometer, and this information can be directly quantified. However it is important to realize that the broadening of diffraction peaks arises mainly due to three factors

1. Instrumental effects: these effects include imperfect focusing, unresolved α_1 and α_2 peaks, or the finite widths of α_1 and α_2 peaks in cases were the peaks are resolved. These extraneous sources can cause broadening in the diffraction peak.

2. Crystallite size: the peaks become broader due to the effects of small crystallite sizes, and thus an analysis of the peak broadening can be used to determine the crystallite size from 100 to 500 nm.

3. Lattice strain: lattice strain can also cause to the broadening of the diffraction peaks. If all the effects mentioned are simultaneously present in the specimen, the peaks will be very broad.

Transmission electron microscopy (TEM)

Transmission electron microscopy (TEM) is an imaging technique whereby a beam of electrons is focused onto a specimen causing an enlarged version to appear on a fluorescent screen or on a photographic film or to be detected by a CCD camera. The first practical transmission electron microscope was built by Albert Prebus and James Hillier at the University of Torondo in 1938 using concepts developed earlier by Max Knoll and Ernst Ruska. Electrons are generated by a process known as thermionic discharge in the same manner as the cathode in a cathode ray tube, or by field emission; they are then accelerated by an electric field and focused by electrical and magnetic fields onto the sample. The electrons can be focused onto the sample providing a resolution far better than that possible with light microscopes, with improved depth of vision. Details of a sample can be enhanced in light microscopy by the use of stains. Similarly with electron microscopy, compounds of heavy metals such as osmium, lead or uranium can be used to selectively deposit on the sample to enhance structural details. The electrons that remain in the beam can be detected using a photographic film, or fluorescent screen [157]. So areas where electrons are scattered appear dark on the screen, or on a positive image.

Transmission electron microscopy is a straight forward technique to determine the size and shape of the nanostructured materials as well as to obtain structural information. In TEM, electrons accelerated to 100 keV or higher, are projected on to a thin specimen by means of a condenser lens

system, and they penetrate in to the sample [158]. TEM uses transmitted and diffracted electrons which generates a two dimensional projection of the sample. The principal contrast in this projection or image is provided by diffracted electrons. In bright field images, the transmitted electrons generate bright regions while the diffracted electrons produce dark regions. In dark field image, the diffracted electrons preferentially form the image. In TEM, one can switch between imaging the sample and viewing its diffraction pattern by changing the strength of the intermediate lens. The greatest advantage that TEM offers are the high magnification ranging from 50 to 10^6 and its ability to provide both image and diffraction information of the same sample. The high magnification or resolution of TEM is given by

$$L = \frac{h}{\sqrt{2mqV}} \tag{2.7}$$

where m and q are the electron mass and charge, h the Planck's constant and V is the potential difference through which the electrons are accelerated. The schematic of a transmission electron microscope is shown in figure 2.4.

Typically a TEM consists of three stages of lensing. The stages are the objective lenses, intermediate lenses and the projector lenses. The objective lens forms a diffraction pattern in the back focal plane with electrons scattered by the sample and combines them to generate an image in the image plane (intermediate image). Thus diffraction pattern and image are simultaneously present in the TEM. It depends on the intermediate lens which appears in the plane of the second intermediate image and magnified by the projective lens on the viewing screen. Switching from a real space to a reciprocal space (diffraction pattern) is easily achieved by changing the
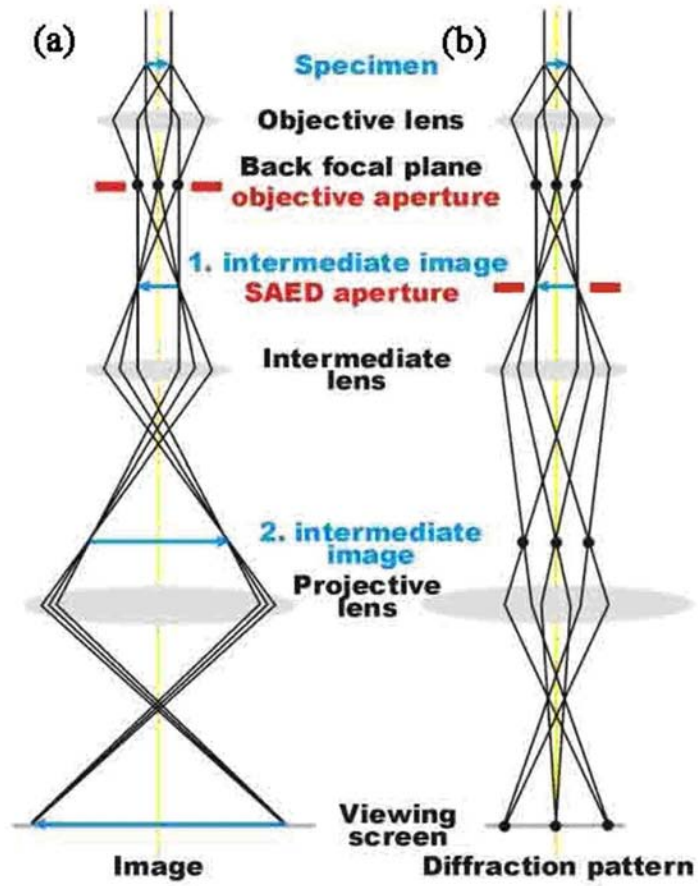
Figure 2.4: Transmission electron microscope for imaging and selected area electron diffraction pattern

strength of the intermediate lens. In imaging mode, an objective aperture can be inserted in the back focal plane to select one or more beams that contribute to the final image (Bright field (BF), Dark field (DF), High Resolution TEM (HRTEM)). The BF image is formed by effectively cutting out all the diffracted beams, leaving out only transmitted beam to form the image. The bright field image is bright only in areas that have crystalline planes that are tilted such that they do not satisfy the Bragg condition. The DF image will be obtained on the other hand if the transmitted beams are blocked instead of diffracted beams.

High-resolution TEM (HRTEM)

High resolution transmission electron microscope (HRTEM) can generate lattice images of the crystalline material allowing the direct characterisation of the samples atomic structure [159]. The resolution of the HRTEM is 1 nm or smaller. However, the most difficult aspect of the TEM technique is the preparation of samples. High-resolution TEM is made possible by using a large-diameter objective diaphragm that admits not only the transmitted beam, but at least one diffracted beam as well. All of the beams passed by the objective aperture are then made to recombine in the image-forming process, in such a way that their amplitudes and phases are preserved. When viewed at high-magnification, it is possible to see contrast in the image in the form of periodic fringes. These fringes represent direct resolution of the Bragg diffracting planes; the contrast is referred to as phase contrast. The fringes that are visible in the high-resolution image originate from those planes that are oriented as Bragg reflecting planes and that possess interplanar spacings greater than the lateral spatial resolution limits of the instrument.

Selected area electron diffraction pattern (SAED)

Selected area electron diffraction offers a unique capability to determine the crystal structure of individual nanomaterials and the crystal structure of the different parts of a sample. A small area of the specimen can be selected from a high resolution transmission image and its electron diffraction pattern (rings or spots) produced on the screen of the microscope by making appropriate arrangement in the lenses of TEM. This is an optional arrangement in HRTEM. The arrangement for taking the diffraction pattern is shown in figure 2.4(b). The SAED allows the researcher to determine lattice constant of the crystalline material which can help in species identification. Basically diffraction patterns are distinguishable as spot patterns resulting from single crystal diffraction zones or ring patterns are obtained from the randomly oriented crystal aggregates (polycrystallites). For nanocrystallites, the diffraction patterns will be a diffused ring patterns.

The d spacing of the planes corresponding to the rings can be determined by the following equation

$$Dd = L\lambda \qquad (2.8)$$

Where L is the effective camera length, λ is the de Broglie wavelength of the accelerating electrons, D is the ring diameter of a standard electron diffraction pattern and d is the interplanar spacing [157]. The term in the right hand side of the equation is referred to as the camera constant. TEM, JEOL operating at an accelerating voltage of 200 kV was used for the confirmation of the formation of nanoparticles in the present work.

2.3.2   Surface morphology

Surface morphology is an important property while studying nanostructures. Characterization tools used to study the surface morphology of the nanostructures is described below.

Scanning electron microscope (SEM)

The scanning electron microscope (SEM) is a type of electron microscope that images the sample surface by scanning it with a high-energy beam of electrons in a raster scan pattern. The electrons interact with the atoms that make up the sample producing signals which contain information about the sample's surface topography, composition and other properties such as electrical conductivity [158]. There are many advantages for using the SEM instead of a light detector [160]. The SEM has a large depth of field, which allows more of a specimen to be in focus at one time. The SEM also has much higher resolution, so closely spaced specimens can be magnified at much higher levels. Figure 2.5 shows the schematic diagram of the scanning electron microscope.

The scanning electron microscope (SEM) is a microscope that uses electrons rather than light to form an image. Preparation of the samples is relatively easy since most SEMs only require that sample should be conductive. The combination of higher magnification, larger depth of focus, greater resolution, and ease of sample observation makes SEM one of the most heavily used instruments in the research field. The electron beam comes from a filament, made of various types of materials. The most common is the tungsten hairpin gun. This filament is a loop of tungsten that functions as the cathode. A voltage is applied to the loop, causing it to heat up.
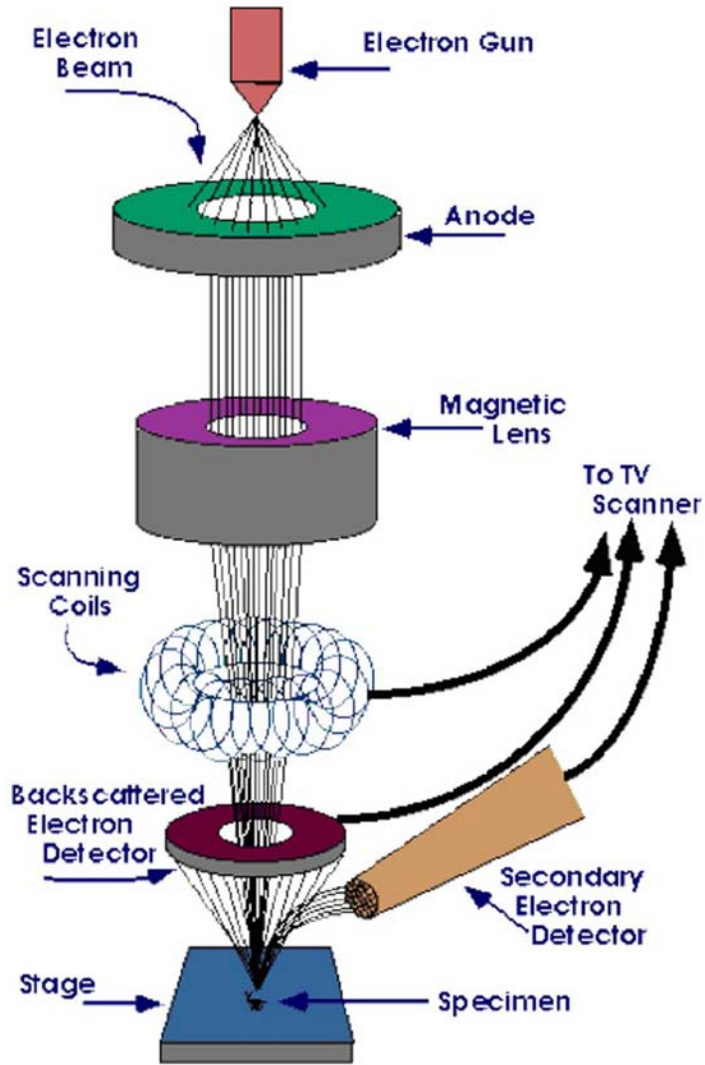
Figure 2.5: Schematic diagram of scanning electron microscope

The anode, which is positive with respect to the filament, forms powerful attractive forces for electrons. This causes electrons to accelerate toward the anode. The anode is arranged, as an orifice through which electrons would pass down to the column where the sample is held. Other examples of filaments are lanthanum hexaboride filaments and field emission guns.

In scanning electron microscopy, an electron beam with energy typically of 1-10 keV is focused by a lens system into a spot of 1-10 nm in diameter on the sample surface. The focused beam is scanned in a raster across the sample by a deflection coil system in synchronous with an electron beam of a video tube, which is used as an optical display. Both beams are controlled by the same scan generator and the magnification is just the size ratio of the display and scanned area on the sample surface. A variety of signals can be detected, including secondary electrons, backscattered electrons, x-rays, cathodoluminescence and sample current. The two dimensional map of the signal yields a SEM image. The main applications of SEM are in surface topography and elemental mapping. By appropriate choice of the detector, the signal of the electrons from a desired energy range can be monitored [161].

The streams of electrons that are attracted through the anode are made to pass through a condenser lens, and are focused to very fine point on the sample by the objective lens (figure 2.6). The electron beam hits the sample, producing secondary electrons from the sample. These electrons are collected by a secondary detector or a backscatter detector, converted to a voltage, and amplified. The amplified voltage is applied to the grid of the CRT that causes the intensity of the spot of light to change. The image consists of thousands of spots of varying intensity on the face of a CRT that correspond to the topography of the sample.
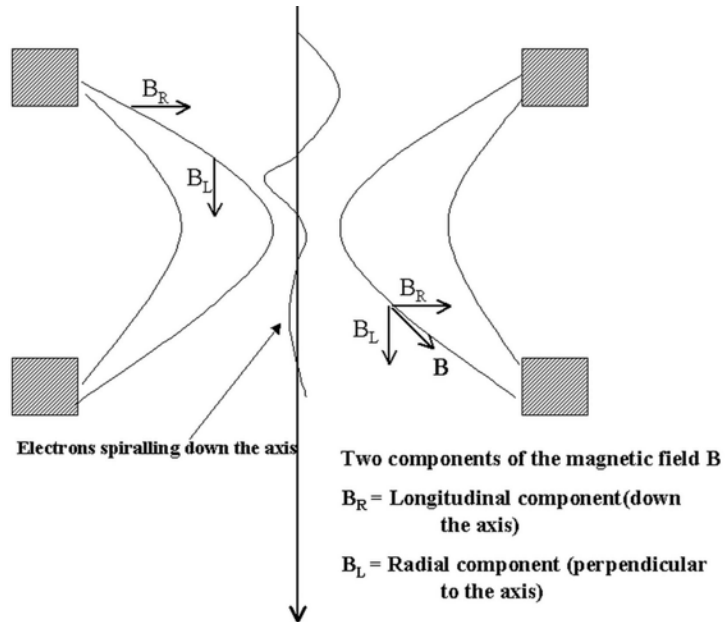
Figure 2.6: The focusing of electrons in SEM

There are three major types of electron sources: tungsten filament, LaB_6, and hot and cold field emission. In the first case, a tungsten filament is heated to allow electrons to be emitted via thermionic emission. Temperatures as high as 3000^0C are required to produce a sufficiently bright source. These filaments are easy to work with, but have to be replaced frequently because of evaporation. The material LaB_6 has a lower work function than tungsten and thus can be operated at lower temperatures, and it yields higher source brightness. However, LaB_6 filaments require much better vacuum than tungsten to achieve good stability and a longer lifetime. Field emission SEM (FESEM) is another type of SEM instrument where electrons are produced using the phenomenon of 'field emission'. In

this instrument tips are very sharp; the strong electric field created at the tip extracts electrons from the source even at low temperatures. In this case, the energy profile is sharper and less the effect of chromatic aberrations of the magnetic defocusing lenses. Although they are more difficult to work with, since they need very high vacuum, occasional cleaning and sharpening via thermal flashing, the enhanced resolution and low voltage applications of field emission tips are making them unique for high resolution scanning [162]. In the present study, JEOL Model JSM-6390LV was used for SEM analysis.

2.3.3   Compositional analysis

The composition of various elements in the nanostructures were studied using the analysis technique like energy dispersive x-ray and inductively coupled plasma.

Energy dispersive x-ray (EDX) analysis

EDX/EDAX analysis stands for energy dispersive x-ray analysis. It is sometimes referred to also as EDS or EDAX analysis. It is a technique used for identifying the elemental composition of the specimen, on an area of interest thereof. The EDX analysis works as an integrated feature of a scanning electron microscope (SEM), and cannot be operated its own without the latter [157, 160].

During EDX analysis, the specimen is bombarded with an electron beam inside the scanning electron microscope. The bombarding electrons collide with the specimen atom's own electrons, knocking some of them off in the process. A position vacated by an ejected inner shell electron is eventually

occupied by a higher-energy electron from an outer shell. To be able to do so, however, the transferring outer electron must give up some of its energy by emitting an x-ray. The amount of energy released by the transferring electron depends on which shell it is transferring from, as well as which shell it is transferring to. Furthermore, the atom of every element releases x-rays with unique amounts of energy during the transferring process. Thus, by measuring the energy of the x-rays emitted by a specimen during electron beam bombardment, the identity of the atom from which the x-ray was emitted can be established. The output of an EDX analysis is an EDX spectrum, which is a plot of how frequently x-ray is received for each energy level.
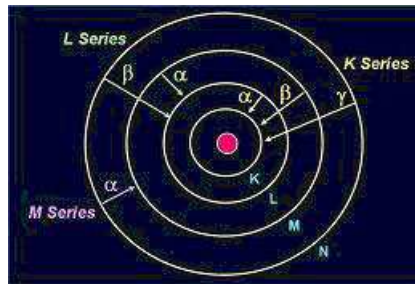
Figure 2.7: The emission of x-rays

EDX spectrum normally displays peaks corresponding to the energy levels for which the most x-rays had been received. Each of these peaks are unique to an atom, and therefore corresponds to a single element. The higher a peak in a spectrum, the more concentrated the element is in the specimen. An EDX spectrum plot not only identifies the element corresponding to each of its peaks, but the type of x-ray to which it corresponds as well. For example, a peak corresponding to the amount of energy pos-

sessed by x-rays emitted by an electron in the L-shell going down to the K-shell is identified as a K_α peak. The peak corresponding to x-rays emitted by electrons transition from upper levels to the K-shell is identified as a K_α, K_β, K_γ etc as shown in figure 2.7.

Inductively coupled plasma - Atomic emission spectroscopy (ICP-AES)

Inductively coupled plasma atomic emission spectroscopy (ICP-AES), also referred to as inductively coupled plasma optical emission spectrometry (ICP-OES), is a spectrophotometric technique, exploiting the fact that excited electrons emit energy at a given wavelength as they return to ground state [163]. This technique uses plasma called inductively coupled plasma to produce excited atoms. The fundamental characteristic of this process is that each element emits energy at specific wavelengths peculiar to its chemical character. Although each element emits energy at multiple wavelengths, in the ICP-AES technique it is most common to select a single wavelength (or a very few) for a given element. The intensity of the energy emitted at the chosen wavelength is proportional to the amount (concentration) of that element in the analyzed sample. Thus, by determining which wavelengths are emitted by a sample and by determining their intensities, the analyst can quantify the elemental composition of the given sample relative to a reference standard. ICP -AES measurement was done in the present work using Thermo Electron IRIS INTREPID II XSP DUO.

2.3.4   Thin film thickness

Thickness is one of the most important thin film parameter to be characterized since it plays an important role in the film properties unlike a bulk

material. Microelectronic applications generally require the maintenance of precise and reproducible film metrology (i.e., thickness as well as lateral dimensions). Various techniques are available to characterize the film thickness which are basically divided into optical and mechanical methods, and are usually nondestructive but sometimes destructive in nature. Film thickness may be measured either by in-situ monitoring the rate of deposition or after the film deposition.

The stylus profiler takes measurements electromechanically by moving the sample beneath a diamond tipped stylus. The high precision stage moves the sample according to a user defined scan length, speed and stylus force. The stylus is mechanically coupled to the core of a linear variable differential transformer (LVDT). The stylus moves over the sample surface. Surface variations cause the stylus to be translated vertically. Electrical signals corresponding to the stylus movement are produced as the core position of the LVDT changes. The LVDT scales an ac reference signal proportional to the position change, which in turn is conditioned and converted to a digital format through a high precision, integrating, analog-to-digital converter [164]. The film whose thickness has to be measured is deposited with a region masked. This creates a step on the sample surface. Then the thickness of the sample can be measured accurately by measuring the vertical motion of the stylus over the step.

The thicknesses of the thin films prepared for the work presented in this thesis were measured by a stylus profiler (Dektak 6M).

2.3.5 Fourier transform infrared (FTIR) spectroscopy

FTIR spectroscopy is a technique that provides information about the chemical bonding or molecular structure of materials, whether organic or

inorganic. It is used to identify unknown materials present in a specimen. The technique works on the fact that bonds and groups of bonds vibrate at characteristic frequencies. A molecule that is exposed to infrared rays absorbs infrared energy at frequencies which are characteristic of that molecule. During FTIR analysis, a spot on the specimen is subjected to a modulated IR beam. The specimen's transmittance and reflectance of the infrared rays at different frequencies is translated into an IR absorption plot consisting of reverse peaks. The resulting FTIR spectral pattern is then analyzed and matched with known signatures of identified materials in the FTIR library. FTIR spectroscopy does not require a vacuum, since neither oxygen nor nitrogen absorbs infrared rays. FTIR analysis can be applied to minute quantities of materials, whether solid, liquid, or gaseous. When the library of FTIR spectral patterns does not provide an acceptable match, individual peaks in the FTIR plot may be used to yield partial information about the specimen.

Schematic diagram of a Fourier transform infra red spectrometer is shown in the figure 2.8. A parallel beam of radiation is directed from the source to the interferometer, consisting of a beam splitter B and two mirrors M_1 and M_2. The beam splitter is plate of suitably transparent material coated so as to reflect 50% of the radiation falling on it. Thus half of the radiation goes to M_1 and half to M_2, returns from both these mirrors along the same path and is then recombined to a single beam at the beam splitter. If a monochromatic radiation is emitted by the source, the recombined beam leaving B shows constructive or destructive interference depending on the relative path lengths B to M_1 and B to M_2. As the mirror M_2 is moved smoothly towards or away from B, therefore, a detector sees radiation alternating in intensity.
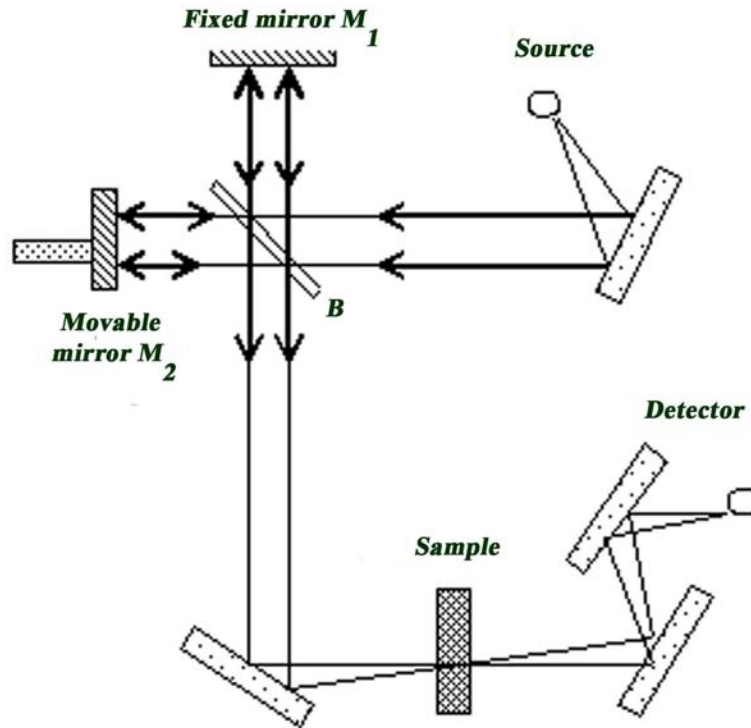
Figure 2.8: Schematic diagram of a Fourier transform infra red spectrometer

The production of spectrum is a two stage process. Firstly, without the sample in the beam, mirror M_2 is moved smoothly over a period of time through a distance of about 1 cm, while the detector signal-the interferogram-is collected into the multichannel computer; the computer carries out the Fourier transformation of the stored data to produce the background spectrum. Secondly with the sample in the beam, a inteferogram is recorded in exactly the same way. Fourier transformed and then

ratioed against the background spectrum for plotting as a transmittance spectrum. Alternatively the sample and background spectra may each be calculated in absorbance forms and the latter simply subtracted from the former [165].

2.3.6 Thermo-gravimetric analysis (TGA)

The thermal properties like heat capacities, the glass transition temperature, melting and degradation of macromolecules can be analysed using thermogravimetry and differential thermal analysis along with differential scanning calorimetry (DSC). Thermal measurements are based on the measurement of dynamic relationship between temperature and some property of a system such as mass, heat of reaction or volume when the material is subjected to a controlled temperature programme.

In thermo-gravimetric analysis, the mass of the sample is recorded continiously as a function of temperature as it is heated or cooled at a controlled rate. A plot of mass as a function of temperature, known as thermogram, provides both quantitative and qualitative information. The apparatus required for thermo-gravimetric analysis include a sensitive recording analytical balance, a furnace, a temperature controller, and a programmer that provides a plot of the mass as a function of temperature. Often an auxiliary equipment to provide an inert atmosphere for the sample is also needed. Changes in the mass of the sample occurs as a result of rapture and/or formation of various physical and chemical bonds at elevated temperature that led to the evolution of volatile products or formation of reaction products. Thus TGA curve provides information regarding the thermodynamics and kinetics of various chemical reactions, reaction mechanisms, and intermediate and final reaction products.

2.3.7 Optical studies

Transmission spectroscopy

An important technique for measuring the band gap of a semiconductor is by studying the absorption of incident photons by the material. In this, photons of selected energy are directed to the sample and the relative transmission of the various photons is observed. Since photons with energies greater than the band gap energy are absorbed while photons with energies less than band gap energy are transmitted, the experiment gives an accurate measure of band gap [166].

According to Bardeen et al. [167] for the parabolic band structure, the relation between the absorption coefficient (α) and the band gap E_g of the material is given by,

$$\alpha = [\frac{A}{h\nu}](h\nu - E_g)^{\gamma} \tag{2.9}$$

where, $\gamma = 1/2$ for allowed direct transitions, $\gamma = 2$ for allowed indirect transitions, $\gamma = 3$ for forbidden indirect transitions and $\gamma = 3/2$ for forbidden direct transitions. A is the parameter which depends on the transition probability. The absorption coefficient can be deduced from the absorption or transmission spectra using the relation,

$$I = I_0 e^{-(\alpha)t} \tag{2.10}$$

where, I is the transmitted intensity and I_0 is the incident intensity of the light and t is the thickness of the film. In the case of direct transition, $(\alpha h\nu)^2$ will show a linear dependence on the photon energy ($h\nu$). A plot of $(\alpha h\nu)^2$ against $h\nu$ will be a straight line and the intercept on energy axis

at $(\alpha h\nu)^2$ equal to zero will give the band gap. The transmission spectra of the thin film samples were recorded using JASCO V 570 spectrophotometer in the present studies.

Diffuse reflectance spectroscopy

The measurement of diffused radiation reflected from a surface constitutes the area of spectroscopy known as diffuse reflectance spectroscopy. Diffuse reflectance spectrometry concerns one of the two components of reflected radiation from an irradiated sample, namely specular reflected radiation, R_s and diffusely reflected radiation, R_d . The former component is due to the reflection at the surface of single crystallites while the latter arises from the radiation penetrating into the interior of the solid and re-emerging to the surface after being scattered numerous times. These spectra can exhibit both absorbance and reflectance features due to contributions from transmission, internal and specular reflectance components as well as scattering phenomena in the collected radiation. Based on the optical properties of the sample, several models have been proposed to describe the diffuse reflectance phenomena. The model put forward by Kubelka-Munk in 1931 is widely used and accepted in diffuse reflectance infrared spectrometry. The intensity of the reflected light depends on the scattering coefficient s and the absorption coefficient k. The reflectance data can be converted to absorbance by Kubelka-Munk equation [168, 169]. Kubelka-Munk equation is as

$$Log[(\frac{(1-r)^2}{2r}] = Logk - Logs \qquad (2.11)$$

Where r $= \frac{R(sample)}{R(standard)}$

Here the standard used is $BaSO_4$. R (standard) is taken as unity. R (sample) is the diffuse reflectance of the sample

($R= I_{sam}/I_{ref}$).

Equation 2.11 Implies,

$$\frac{(1-R)^2}{2R} = \frac{k}{s} \tag{2.12}$$

The band gap is estimated from the plot of $((k/s)h\nu)^2$ vs $h\nu$ ($h\nu$ is the photon energy) by extrapolating the graph to the x-axis. DRS was recorded using JASCO V 570 spectrophotometer in the present study.

Photoluminescence (PL)

Luminescence in solids is the phenomenon in which electronic states of solids are excited by photons from an external source and the excited states release energy as electromagnetic radiation. When short wavelength radiation illuminate a solid and results in the emission of higher wavelength, the phenomenon is called photoluminescence (PL) [170]. PL is divided into two major types: Intrinsic and extrinsic depending on the nature of electronic transition producing it.

Intrinsic luminescence are of three kinds

1. Band to band luminescence

2. Exciton luminescence

3. Cross-luminescence.

Band to band luminescence: Luminescence owing to the band-to-band transition, ie to the recombination of an electron in the conduction band

with a hole in the valance band, can be seen in pure crystal at relatively high temperature. This has been observed in Si, Ge and IIIb-Vb compounds such as GaAs.

Exciton luminescence: An exciton is a composite particle of an excited electron and a hole interacting with one another. It moves in a crystal conveying energy and produces luminescence owing to the recombination of the electron and the hole. There are two kinds of excitons: Wannier exciton and Frenkel exciton. The Wannier exciton model express an exciton composed of an electron in the conduction band and a hole in the valence band bound together by Coulomb interaction. The expanse of the wave function of the electron and hole in Wannier exciton is much larger than the lattice constant. The exciton in IIIb-Vb and IIb-VIb compounds are examples for Wannier exciton. The Frenkel exciton model is used in cases where expanse of electron and hole wave function is smaller than lattice constant. The excitons in organic molecular crystals are examples of Frenkel exciton.

Cross luminescence: Cross luminescence is produced by the recombination of an electron in the valance band with a hole created in the outer most core band. This is observed in number of alkali and alkaline-earth halides and double halides. This takes place only when the energy difference between the top of valance band and that of conduction band is smaller than the band gap energy. This type of luminescence was first observed in BaF_2.

Extrinsic luminescence: Luminescence caused by intentionally incorporated impurities, mostly metallic impurities or defects is classified as extrinsic luminescence. Most of the observed type of luminescence of practical application belongs to this category. Intentionally incorporated impurities are activators and materials made luminescent in this way are called

phosphors. Extrinsic luminescence in ionic crystals and semiconductors is classified into two types: unlocalized and localized. In the unlocalized type, the electrons and holes of the host lattice participate in the luminescence process, while in localized type the luminescence excitation and emission process are confined in a localized luminescence center.

Two types of luminescence spectra can be distinguished: excitation and emission. In the case of an excitation spectrum the wavelength of the exciting light is varied and the intensity of the emitted light at a fixed emission wavelength is measured as a function of the excitation wavelength. The excitation spectrum gives the energy levels position of the excited states just as the absorption spectrum does, except that the former reveals only the absorption bands that result in the emission of light. The observed differences between the absorption and excitation spectra can yield useful information. An emission spectrum provides information on the spectral distribution of the light emitted by a sample. The time resolved PL measurements are a powerful tool for the determination of the radiative efficiency. The radiative efficiency specifies the fraction of excited states, which de-excite by emitting photons [170].

The emission and excitation spectra for the liquid and powder samples were recorded using Fluoromax -3 spectroflurometer having a 150 W xenon lamp. For studying the PL of multiple quatum well structures, a fourth harmonic pulsed Nd: YAG laser operating at 266 nm was used as an excitation source and resulting luminescence was collected using gated CCD.

2.3.8   CIE color coordinates

Color characterization of a spectral distribution is done to gauge the quality of its chromaticity. This is accomplished using color coordinates [171].

In 1931, the Commission Internationale de l'Eclairage (CIE) established an international standard for quantifying color known as CIE color coordinates. The chromaticity coordinates map all the visible colors with respect to hue and saturation on a two dimensional chromaticity diagram. The CIE coordinates are obtained from the three CIE tristimulus values, X, Y and Z. These tristimulus values are computed by integrating the product of the spectrum of the light source, $P(\lambda)$, and standard observer functions called the CIE color matching functions, $x_\lambda(\lambda)$, $y_\lambda(\lambda)$ and $z_\lambda(\lambda)$ (shown in figure 2.9) over the entire visible spectrum using the relations,

$$X = \sum_{\lambda=380nm}^{780} x_\lambda(\lambda)P(\lambda)\Delta\lambda \tag{2.13}$$

$$Y = \sum_{\lambda=380nm}^{780} y_\lambda(\lambda)P(\lambda)\Delta\lambda \tag{2.14}$$

$$Z = \sum_{\lambda=380nm}^{780} z_\lambda(\lambda)P(\lambda)\Delta\lambda \tag{2.15}$$

Once X, Y and Z are known, the CIE color coordinates are calculated using the relations,

$$x = \frac{X}{X + Y + Z} \tag{2.16}$$

$$y = \frac{Y}{X + Y + Z} \tag{2.17}$$

$$z = \frac{Z}{X + Y + Z} \tag{2.18}$$

Being constrained by the relation $(x + y + z) = 1$, any two of the three CIE color coordinates are independent.
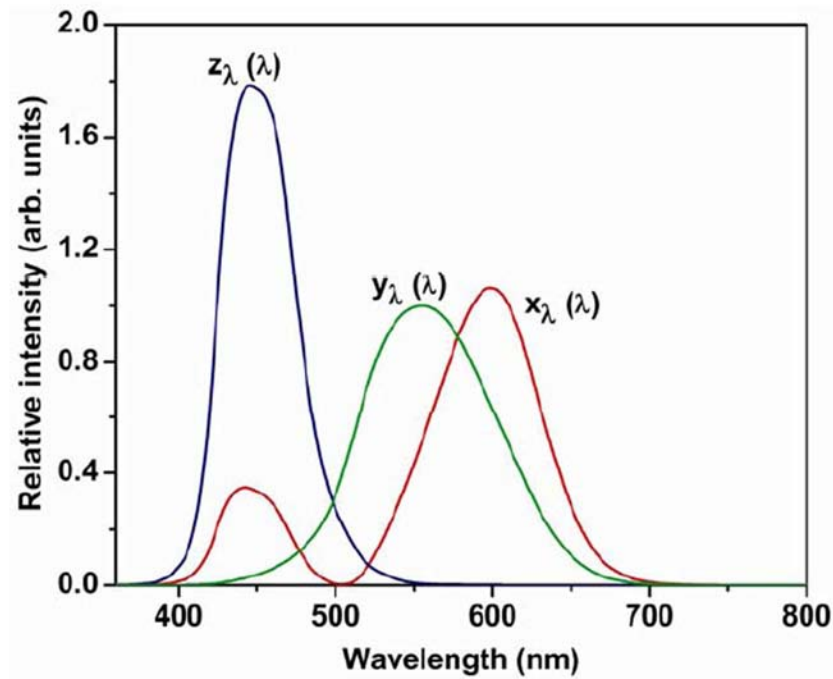
Figure 2.9: Plot of the CIE tristimulus (x, y, and z) functions

Plotting of the CIE x versus CIE y color coordinate over the visual range of light leads to a horseshoe shaped diagram known as the CIE chromaticity diagram shown in figure 2.10.
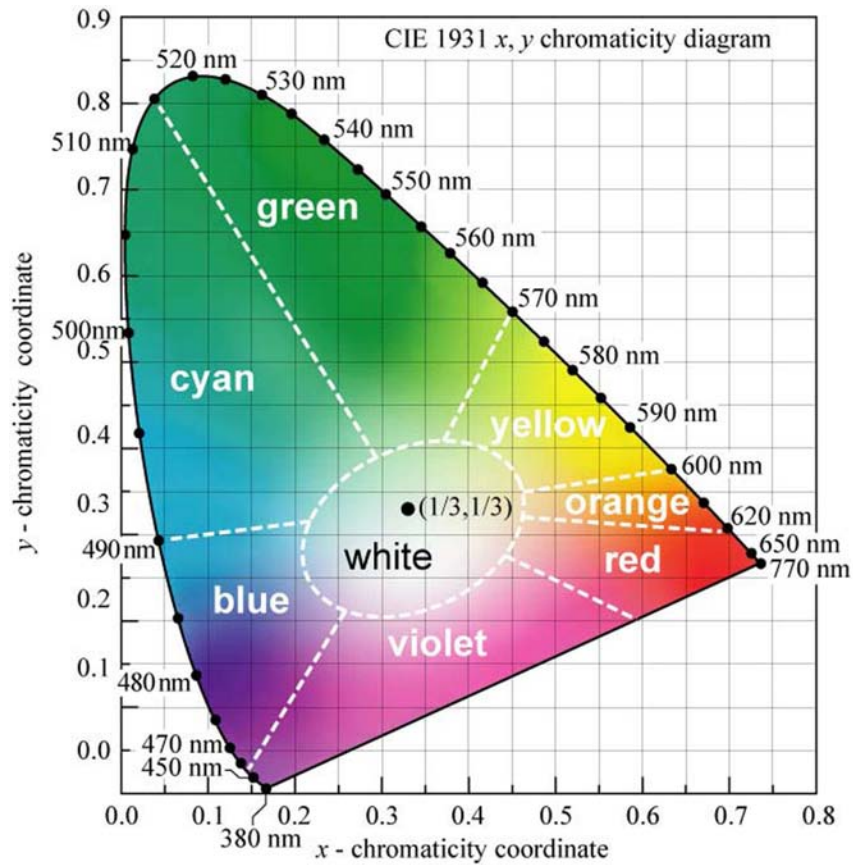
Figure 2.10: The CIE chromaticity diagram

The monochromatic spectral colors lie along the horse shoe shaped path called the spectral locus. All visible colors lie within the shape bounded by this path. The straight line from violet (400 nm) to red (700 nm) is called the purple line and cannot be produced by light of a single wavelength. The CIE coordinates for achromatic white is (x, y) = (0.33, 0.33). When the CIE coordinates of a color are specified, the dominant wavelength of

the color is the intersection of the line connecting these CIE coordinates and those of white light with the upper arc of the diagram. The CIE coordinates, therefore, is an extremely powerful concept because it allows the representation of an entire luminescent spectrum on a two dimensional plane.

2.3.9   Raman spectroscopy

Raman spectroscopy is a technique that can detect both organic and inorganic species and measure the crystallanity of solids. Raman spectroscopy is based on the Raman effect, first reported by Raman in 1928 [172]. If the incident photon imparts part of it's energy to the lattice in the form of a phonon it emerges as a lower energy photon. This down converted frequency shift is known as Stokes-shifted scattering. Anti-Stokes shifted scattering results when the photon absorbs a phonon and emerges with higher energy. The anti-Stokes mode is much weaker than the Stokes mode so the Stokes-mode scattering is usually monitored. In Raman spectroscopy a laser beam, referred to as the pump, is incident on the sample. The weak scattered light or the Raman signal is passed through a double monochromator to reject the Raleigh scattered light and the Raman shifted wavelengths are detected by a photodetector. Various properties of the semiconductors, mainly composition and crystal structure can be determined. The Stokes line shifts and broadens becomes asymmetric for microcrystalline Si with grain sizes below 10 nm [173]. The lines become very broad for amorphous semiconductors, allowing distinction to be made between single crystal, polycrystalline, and amorphous materials.

Raman spectroscopy is used to study the vibrational properties of nanostructured materials. The information about structure, phase, grain size,

phonon confinement etc can be obtained from Raman spectroscopy. The extend of phonon confinement in a material can be observed as the shift in Raman line frequencies. Acoustic modes are not observed by Raman measurements in bulk systems because of their low frequencies. But in nanostructured materials, they appear in the measurable frequency range (below 100 cm^{-1}) [174, 175]. The frequency of the acoustic mode is inversely proportional to the size of the nanoparticles and this can be used to determine the size of the particles. Confinement of optical phonons results in the frequency shift and asymmetrical broadening of longitudinal optical (LO) and transverse optical (TO) mode line shape [176]. The information about the structure and quality of the low dimensional structures can be obtained from Raman spectroscopy.

In the present work, Raman studies were carried out with micro Raman (Renishaw) with He- Ne Laser (632.8 nm) as the excitation source.

2.3.10   SQUID Magnetometer

SQUID magnetometer is the instrument used to measure extremely sensitive magnetic fields of the order of 10^{-14} T. The superconducting quantum interference device (SQUID) consists of two superconductors separated by thin insulating layers to form two parallel Josephson junctions. The great sensitivity of the SQUID devices is associated with measuring changes in magnetic field associated with one flux quantum (h/2e). The basic principle that follows in a SQUID magnetometer is that, if a constant biasing current is maintained in the SQUID device, the measured voltage oscillates with the changes in phase at the two junctions, which depends upon the change in the magnetic flux. Counting the oscillations allows to evaluate the flux change which has occurred. Hence, when the sample is moved

through the superconducting magnetic coils, a flux change is induced in the pick up coils. Highly magnetic sample should be moved slowly through the coils in order not to exceed the maximum slewing rate of the electronic system [177].

Chapter 3

Hydrothermal synthesis and characterization of undoped and Eu doped ZnGa$_2$O$_4$ nanoparticles

3.1 Introduction

Phosphors are substance that exhibits the phenomenon of luminescence. Efficient phosphors for lighting applications, flat panel displays, etc have always been a goal for researchers. Phosphor materials are generally composed of a pure host matrix and a small amount of intentionally added impurity, so-called activator [54]. If the host material and the activator concentrations are fixed, the physical properties of phosphor materials such as the surface area, the crystallinity, the phase purity, and the distribution of activator in the host matrix play crucial roles in modulating luminescence

characteristics. Those material properties can be controlled by the preparation conditions: temperature, precursor concentration, and post annealing. Especially, the preparation and annealing temperatures greatly influence the luminescence intensity of phosphor particles since it directly affects the formation of crystal structure, crystallinity, the surface area of particles, and the distribution of activator. (Y,Gd)BO$_3$:Eu [178] or Y$_2$O$_3$:Eu [179], Zn$_2$SiO$_4$:Mn [180], and BaMgAl$_{10}$O$_{17}$:Eu [181] are some phosphor materials which give red, green and blue emission respectively. Generally, most of the light emitting devices utilizes red, green, and blue colors for practical applications. The particle size of conventional phosphors are in micrometer scale, hence light scattering at grain boundaries is strong and it decreases the light output. Nanophosphors can be synthesized whose size varying from tens to hundreds of nanometers which itself are smaller than the incident light wavelength and this will reduce the scattering, thereby enhancing the luminescence efficiency. Synthesis of nanometre-size phosphors has attracted much attention owing to their size-dependent electrical and optical properties originating from the quantum confinement.

Zinc gallium oxide, ZnGa$_2$O$_4$, is a well-known low voltage oxide phosphor used in flat panel displays [182–184]. This ternary oxide compound is a self activated phosphor, crystallizing in the normal spinel structure. The spinel unit cell belongs to the cubic space group Oh7 (Fd*3m*) with eight formula units per cell and contains two kinds of cation sites. The A site (Zn^{2+}) has tetrahedral coordination with full T$_d$ symmetry, while the B site (Ga^{3+}) has six fold distorted octahedral coordination belonging to the D$_{3d}$ point group. The trigonal axis of the B site is, of course, coincident with the unit cell (111) axis, and the site has a center of inversion [185]. When undoped, ZnGa$_2$O$_4$ provides a blue emission and rare earth doping

gives the emission characteristics of rare earth ions and provides tunability over the whole visible spectra. Therefore zinc gallate is an excellent multi color phosphor material for flat panel displays. White light emitters have attracted special interest recently for a number of potential applications in cars, traffic information signs, displays and general illumination [132–134]. White LEDs can be fabricated by several methods [133]. The first lies solely on combinations of LEDs with the three primary colors to produce bright white light sources which are significantly more efficient than incandescent bulbs and are more adaptable. Multiple semiconductor LEDs will not be competitive in the larger market for residential and commercial lighting. Moreover, the directional nature of LED output makes this approach not suitable for general illumination application. Another more practical method for producing white LEDs is upon absorption of blue or UV light, the phosphors convert the energy to visible radiation depending on the type of phosphors used. White light can be achieved either through several different colored phosphors, or utilizing the blue emission of the LED as the blue part of a multichromatic source. Ce^{3+} doped $Y_3Al_5O_{12}$ nanophosphor absorbs light efficiently in the visible region of 400-500 nm, and shows single broadband emission peaking at $\sim$560 nm and hence, it can be considered as a candidate for generating white light when coupled to a blue light-emitting diode [186].

Synthesis of $ZnGa_2O_4$ spinel powders have been previously accomplished by solid state reaction between zinc oxide and gallium oxide or by flux method [106, 109, 184, 187–189]. But this method requires heat treatment at higher temperatures for several hours and subsequent grinding. This may damage the phosphor surfaces, resulting in the loss of emission intensity. Various chemical syntheses have been developed to grow nanoparticles of

such ternary oxide materials [185, 190]. Hydrothermal method offers some advantages over the other techniques, such as low temperature synthesis, low cost, less hazardous and no need for the use of metal catalysts [190–192]. Hirano *et al.* [192] studied the growth of undoped ZnGa$_2$O$_4$ nanoparticles by hydrothermal method. Tas *et al* [193] prepared pure and Mn^{2+} doped ZnGa$_2$O$_4$ nanoparticles by aging aqueous solutions of precursors and Takesada *et al.* [194] by glycothermal method. The effect of rare earth doping in the ZnGa$_2$O$_4$ spinel structure is less studied.

In the present study, undoped and Eu doped zinc gallium oxide (ZnGa$_2$O$_4$) nanoparticles were synthesized via hydrothermal route using metallic precursors. The effect of temperature, Zn/Ga precursor ratio, dopant concentration and duration of growth on the structural and optical properties of nanoparticles were studied.

3.2   Experimental

Fine powder of pure and Eu doped ZnGa$_2$O$_4$ phosphors were prepared by the hydrothermal method. High-purity metals of gallium (99.9999%, Alcan Electronic Materials) and zinc (99.995%, 5 mm dia, Qualigens) were dissolved in nitric acid (70%, Merck) separately and then diluted to appropriate concentrations with distilled water. The concentrations of the stock solutions were determined by inductively coupled plasma atomic emission spectrometric (ICP-AES) analysis (8440 PLASMALAB, LABTAM). The concentration of the gallium and zinc precursor solutions was determined to be 7.82 and 67.63 gm/litre respectively. The gallium and zinc stock solutions were mixed in the 1:2 volume ratios with constant stirring. To prepare ZnGa$_2$O$_4$:Eu^{3+} phosphor, appropriate amount of Eu$_2$O$_3$ (99.99%,

Alfa Aesar) was added to the mixed solution of parent cations. On constant stirring, a desired amount of aqueous ammonia (25%, Merck) was added to the clear solutions soon after dissolution to make pH of the solution as 8. The mixed solution was refluxed at room temperature in a magnetically stirred reactor for 30 minutes and then transferred into a teflon lined stainless steel autoclave. The tightly sealed autoclave was placed in oven and heated to a temperature of 200^0C for 3 h under autogenous pressure. The precipitates, which were formed under autogenously established hydrothermal conditions, were separated by filtering, then washed and dried in air at 50^0C in air. The samples were washed with H_2SO_4 so as to remove the residual ZnO phase, if any, present in them to obtain single phase zinc gallate spinel particles.

Phase identification of the fine white zinc gallate powders was performed by x- ray powder diffraction (XRD) (Rigaku D max-C) using Cu-K$_\alpha$ radiation (1.5418 Å). The morphology and size were examined by JEOL JEM-3100F transmission electron microscope (TEM) operating at 200 kV. The sample for TEM was prepared by placing a drop of the synthesized powder suspension in methanol onto a standard carbon coated copper grid. The grids were dried before recording the micrographs. The elemental composition of Eu in the synthesized powders was determined by using 8440 PLAS-MALAB, LABTAM inductively coupled plasma atomic emission spectrometer (ICP-AES). Thermogravimetric analysis (TGA) (Perkin Elmer) of the as prepared sample was carried out in the temperature range 50-1000^{0}C at a heating rate of 10^0C/min under nitrogen atmosphere. Horiba Jobin Yvon Fluoromax-3 spectrofluorimeter was used to investigate the photoluminescence properties of the phosphors at room temperature using Xe lamp as

the excitation source. FT-IR (Thermo Nicolet) spectra were recorded in the range 4000-400 cm^{-1}.

3.3   Results and discussion
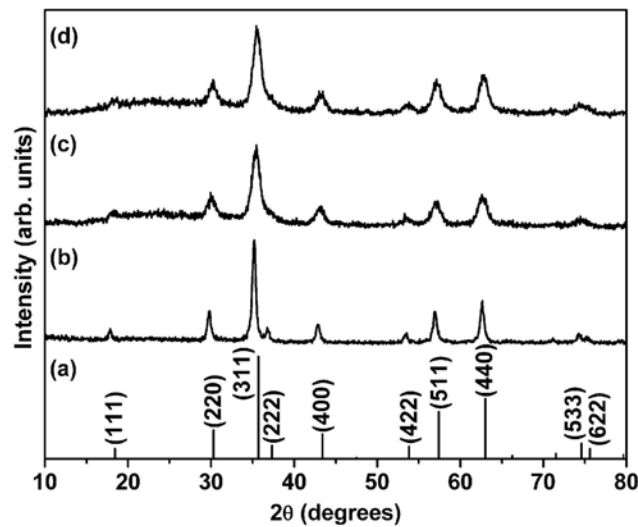
Figure 3.1: XRD pattern of (a) ICSD of ZnGa$_2$O$_4$ (ICSD Card No. 081113) (b) bulk ZnGa$_2$O$_4$ (c) ZnGa$_2$O$_4$nanoparticles (d) Eu doped ZnGa$_2$O$_4$ nanoparticles

Figure 3.1 shows the XRD pattern of the ZnGa$_2$O$_4$ bulk powder (curve (b)) synthesized via solid state reaction by firing the mixture of ZnO and Ga$_2$O$_3$ at 1200^{0}C for 12 h. Curve (c) and (d) in figure 3.1 shows the XRD patterns of pure ZnGa$_2$O$_4$ and Eu doped ZnGa$_2$O$_4$ nanoparticles synthesized by hydrothermal technique at a growth temperature of 200^{0}C for 3 h. All the peaks in the x-ray diffraction pattern could be assigned to the typical spinel structure of ZnGa$_2$O$_4$ (Figure 3.1(a)) [195]. There

are no characteristic peaks of constituent oxides regardless of the dopant concentrations. Thus the spinel structure is not modified by the addition of Eu into the $ZnGa_2O_4$ matrix. The broadening of the diffraction peaks shows that the synthesized materials are in nanometer regime.
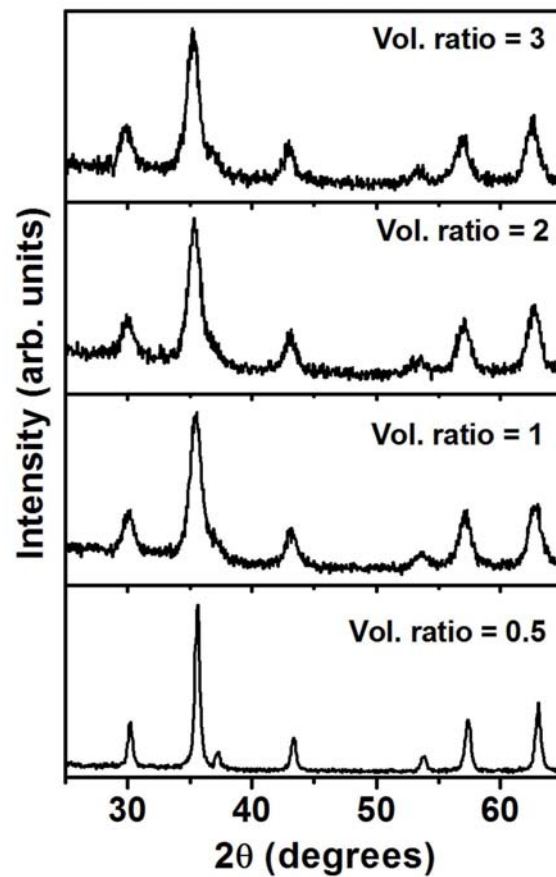
Figure 3.2: XRD pattern of Eu doped $ZnGa_2O_4$ nanoparticles synthesized at various volume ratios of Zn/Ga precursor solutions at 200^0C for 3 h
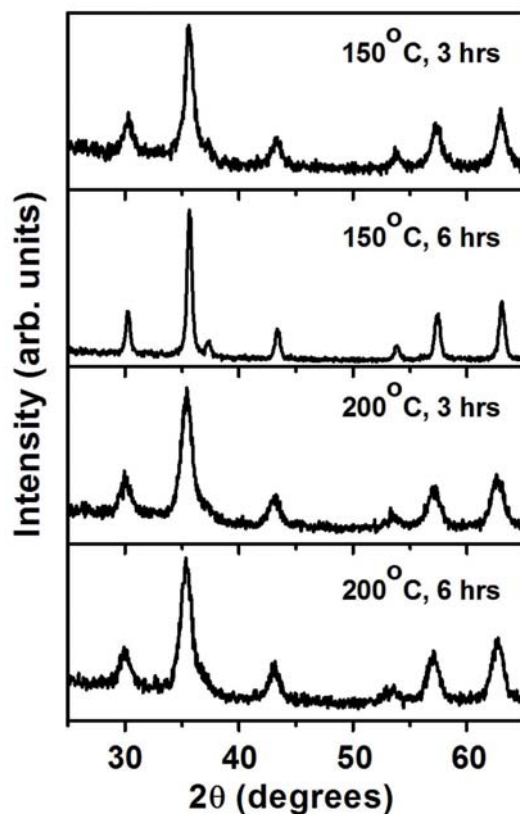
Figure 3.3: XRD pattern of Eu doped ZnGa$_2$O$_4$ nanoparticles synthesized at various temperature and duration of hydrothermal growth for a fixed volume ratio of 2 between Zn/Ga precursor solution

Figure 3.2 shows the XRD profile of ZnGa$_2$O$_4$ nanoparticles synthesized by varying the volume ratio of Zn/Ga precursor solutions at a temperature of 200^{0}C for 3 h. It is observed that the FWHM of the (311) peak increases with the volume ratio of Zn/Ga precursors. When the volume ratio of Zn/Ga precursor solution is below 0.5, ZnO and Ga$_2$O$_3$ phases were detected by XRD, but no spinel ZnGa$_2$O$_4$ phase was found. Figure 3.3

shows the XRD profile of $ZnGa_2O_4$ nanoparticles synthesized by varying the temperature and duration of growth by keeping the volume ratio of Zn/Ga precursor solutions as 2. The FWHM is found to be more or less same for hydrothermally grown samples for a duration of 3 h at 150^0C and 200^0C. The samples grown at 150^0C for a growth time of 6 h resulted in bigger particles (15.5 nm) where as at 200^0C for 6 h, the size of the particle remains almost same as that grown at 3 h. The exact mechanism of growth is not well understood. In the present study we have chosen the optimum values of volume ratio of Zn/Ga precursors, temperature and time of hydrothermal growth as 2, 200^0C and 3 h respectively. The average grain size (D) of the samples was estimated with the help of Scherrer equation [154] using the diffraction intensity of (311) peak.

$$D = \frac{0.9\lambda}{\beta cos\theta} \tag{3.1}$$

where, λ is the x-ray wavelength, β is the full width at half maximum (FWHM) of the $ZnGa_2O_4$ (311) line and θ is the diffraction angle. The grain size of the nanoparticles is in the range 8-17 nm and lattice parameter calculated were found to vary with the growth conditions and is in quite agreement with reported values.

FT-IR spectra of the nanosized $ZnGa_2O_4$ powders are shown in the figure 3.4. The peaks at 3318 cm^{-1} is due to the (O-H) vibration of H_2O absorbed by the sample. The peaks at about 584 cm^{-1} and 409 cm^{-1} represent the characteristic metal-oxygen (Zn-O and Ga-O) vibrations respectively. The sharp peak at 1382 cm^{-1} corresponds to the adsorbed nitrate ions.
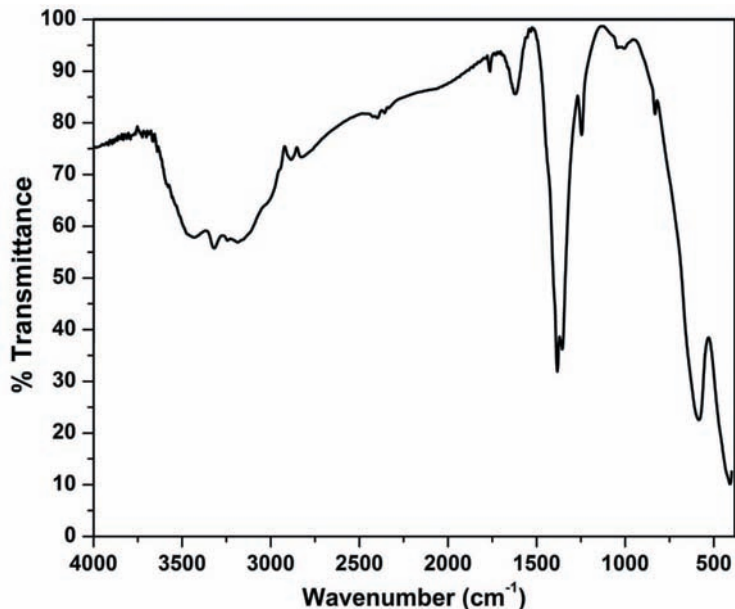
Figure 3.4: FTIR spectra of the nanoparticles of ZnGa$_2$O$_4$ synthesized by hydrothermal method

Figure 3.5 shows the TGA profile of the as-prepared undoped ZnGa$_2$O$_4$ sample with a heating rate of 10^0C/min and a nitrogen flow rate of 100 ml/min. It is observed that the powder undergoes two phase transitions in different temperature regions. The first occurs below the temperature of 125^0C which could be attributed to the loss of water molecules associated with the particles. The weight loss between 125 and 550^0C is due to the removal of nitrates. The evaporation of the adsorbed moisture contributed to the major weight loss of 8%. The pyrolytic condensation of residual metal salts or hydroxides in air involved a weight loss less than 5%.
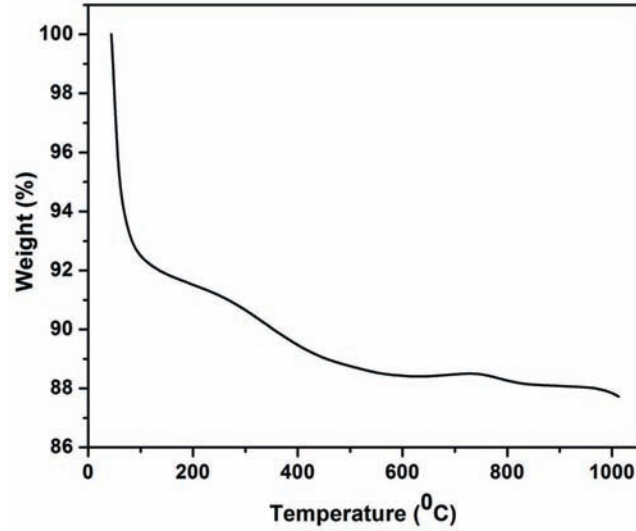
Figure 3.5: TGA spectra of the $ZnGa_2O_4$ nanoparticle synthesized by hydrothermal method

The diffuse reflectance spectrum of the bulk and nanosized $ZnGa_2O_4$ powder in the visible region is shown in Figure 3.6. The diffuse reflectance spectroscopy measurements confirm the blue shift in the band gap of nanocrystals with respect to the bulk. The absorbance was calculated from the reflectance using Kubelka-Munk equation [168, 169]. Relative diffuse reflectance was measured with $BaSO_4$ powder as reference. The band gap 4.59 eV of nano $ZnGa_2O_4$ particles was estimated from the plot of $\{(k/s)h\nu\}^2$ versus $h\nu$, [109, 168, 169] which is shown in the figure 3.7, where k and s denote absorption and scattering coefficients, $h\nu$ the photon energy. The band gap of $ZnGa_2O_4$ nanoparticles is blue shifted from that of the bulk $ZnGa_2O_4$ (4.52 eV). This increase in the band gap is due to the quantum confinement effects.
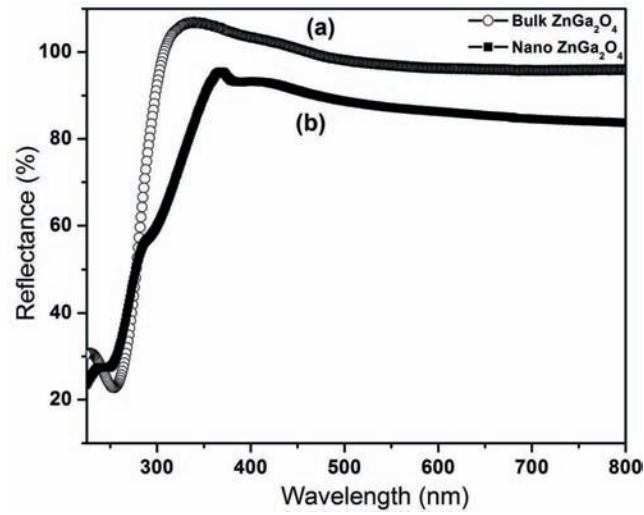
Figure 3.6: Diffuse reflectance spectra of bulk and nanosized $ZnGa_2O_4$ powder
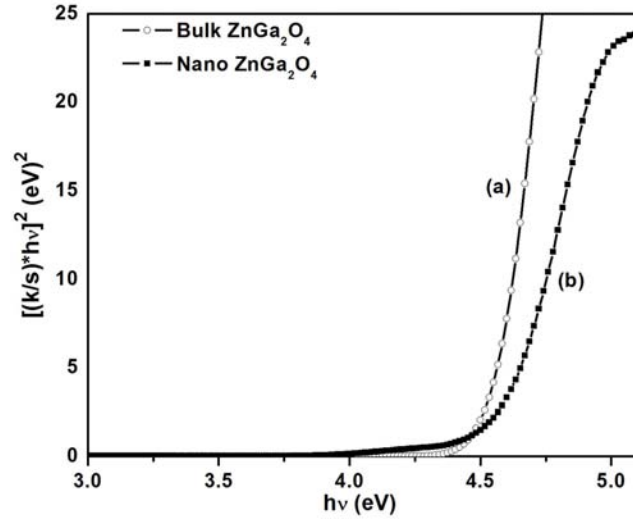
Figure 3.7: Plot of $[(k/s)h\nu]^2$ vs energy of (a) bulk and (b) nanosized $ZnGa_2O_4$ powder
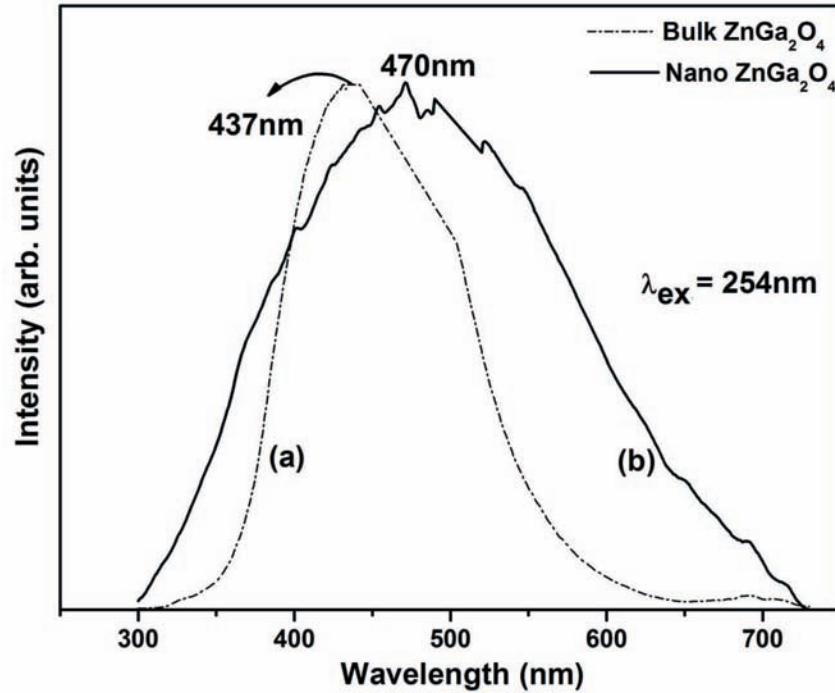
Figure 3.8: Room temperature photoluminescence emission spectra of bulk and ZnGa$_2$O$_4$ nanoparticles excited at $\lambda_{ex} = 254$ nm

Figure 3.8 shows the room temperature photoluminescence emission spectra of bulk and nano ZnGa$_2$O$_4$. The room temperature photoluminescence measurements of the nanocrystals monitored at an excitation wavelength of 254 nm gave a broad spectrum [185]. The diffuse reflectance spectra (Figure 3.6) indicates that gallium is responsible for the photoluminescence excitation of the prepared nanopowders of ZnGa$_2$O$_4$ [114]. However, the PL emission spectra shows some peaks at wavelengths of 399, 443, 453, 464, 470, 476, 484, and 493 nm when the nanophosphors were excited with the UV light of wavelength 254 nm. The excitation peak at

254 nm corresponds to the charge transfer from O^{2-} to Ga^{3+} at regular octahedral sites [196]. All the samples prepared at different volume ratio of Zn/Ga precursors exhibit broad emission spectra. These spectra exhibit certain peaks apart from the characteristic bell-shaped emission spectra of bulk $ZnGa_2O_4$ phosphors as reported in literature [110, 114]. The isolated Ga^{3+} ion exhibits spectral lines at wavelengths of 438.07, 438.18, 486.30, and 499.38 nm in air [197]. Peaks observed in the emission spectra of the prepared $ZnGa_2O_4$ nanophosphors may correspond to the electronic transitions of localized Ga^{3+} ion in the octahedral Ga-O sites which induces the electronic energy levels to split. The quantum effects in nanophosphors prepared in this study are predominant because it have much smaller particle size than those of the powder prepared by the conventional solid-state reaction. [185]. This leads to splitting of electronic energy levels of Ga^{3+} in the octahedral site of Ga-O resulting the peaks in the emission spectra. The blue emission band maximum at 470 nm corresponds to the self-activated luminescence of the host. The origin of the self activated blue emission around 437 nm in $ZnGa_2O_4$ bulk is attributed to Ga^{3+} at octahedrally coordinated site [110, 114].

Figure 3.9(a) shows the TEM image of Eu doped $ZnGa_2O_4$ prepared with 0.02 mol Eu_2O_3 in the precursor solution. TEM image confirms the formation of nanoparticles of the spinel phosphor material. The average size of the spherically shaped particles was determined to be 8 nm. This result is consistent with what we had obtained from XRD analysis. Figure 3.9(b) shows the HRTEM images of the Eu doped $ZnGa_2O_4$ nanoparticles. The d value 2.1 Å corresponds to the (400) planes of the $ZnGa_2O_4$ nanoparticles. From the diffraction rings (Figure 3.9(c)) in the selected area electron diffraction (SAED) pattern, (220), (311), (400), (422), (511)

and (440) planes of $ZnGa_2O_4$ could be identified. The particle size distribution of the Eu doped $ZnGa_2O_4$ nanoparticles by counting the number of particles from the TEM image shown in figure 3.9(d) do assert the fact that most of the nanoparticles synthesized had the dimension 6-9 nm.
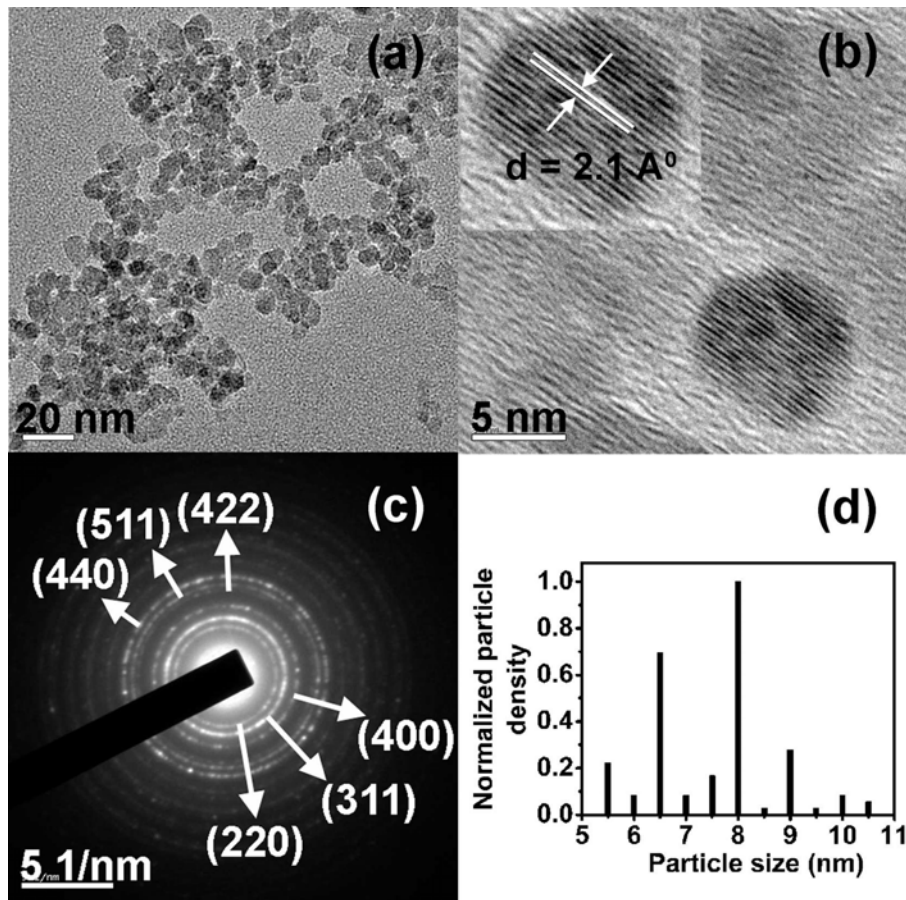
Figure 3.9: (a) TEM image (b) HRTEM image (c) SAED pattern and (d) particle size distribution from the TEM image of Eu doped $ZnGa_2O_4$ nanoparticles grown by hydrothermal method
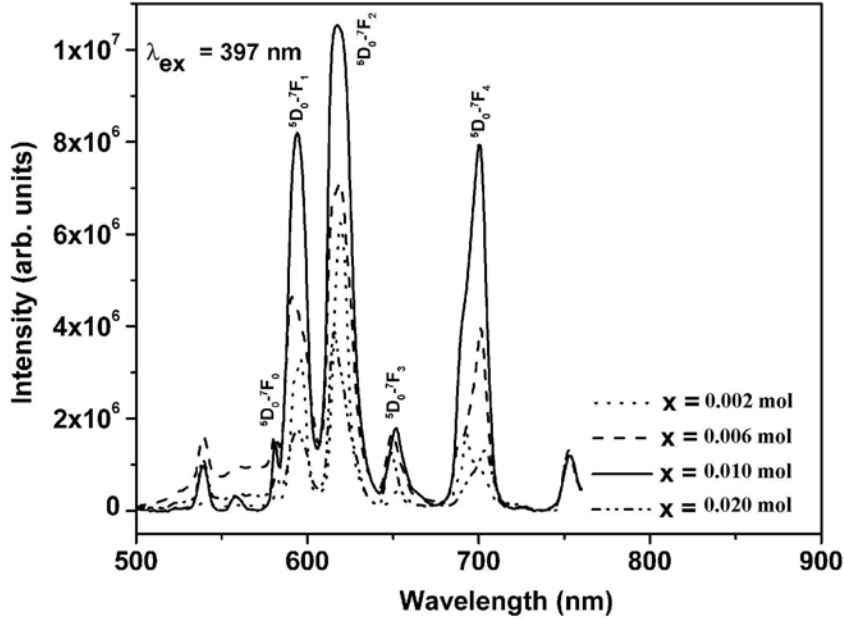
Figure 3.10: Room temperature photoluminescence emission spectra of Eu doped $ZnGa_2O_4$ nanoparticles excited at $\lambda_{ex} = 397$ nm for different amount of Eu_2O_3 in the precursor solution

From the ICP-AES results it is found that Eu/(Eu+Ga) is about 3.38%. Figure 3.10 shows the room temperature photoluminescent emission spectra of Eu doped $ZnGa_2O_4$ nanoparticles excited at 397 nm. The excitation energy almost coincides with the energy of $^7F_0 \rightarrow {}^5L_6$ transitions of Eu^{3+} ions, which is 3.147 eV [198]. Excitation at 397 nm yields the characteristic emissions of Eu^{3+} corresponding to ^5D_j (j=0, 1) $\rightarrow {}^7F_j$ (j=0, 1, 2, 3 and 4). The emission at 596 nm originates from the magnetic-dipole allowed $^5D_0 \rightarrow {}^7F_1$ transition, indicating that Eu^{3+} ions occupy a site with inversion symmetry. This is the only transition when Eu^{3+} is situated at a site coinciding with a centre of symmetry. The emission at 619 nm corresponds

to electric-dipole allowed $^5D_0 \rightarrow {}^7F_2$ transition, which results in a large transition probability in the crystal field with inversion antisymmetry. The intensity of emission corresponds to the $^5D_0 \rightarrow {}^7F_2$ transition is stronger than that of $^5D_0 \rightarrow {}^7F_1$ transition. It is suggested that the Eu^{3+} ions mainly occupy a site with inversion antisymmetry in the $ZnGa_2O_4$ host. The emission at 701 nm is from $^5D_0 \rightarrow {}^7F_4$ transition and at 653 nm is from $^5D_0 \rightarrow {}^7F_3$ transition. The emission peaks at 583 nm corresponds to $^5D_0 \rightarrow {}^7F_0$ transition. The observation of forbidden $^5D_0 \rightarrow {}^7F_0$ transition indicates that some of the Eu ions are at low symmetry site. The detection of this transition suggests that Eu^{3+} ions do not occupy a lattice site with inversion center. The emission at 543 nm is from $^5D_1 \rightarrow {}^7F_1$ transition.
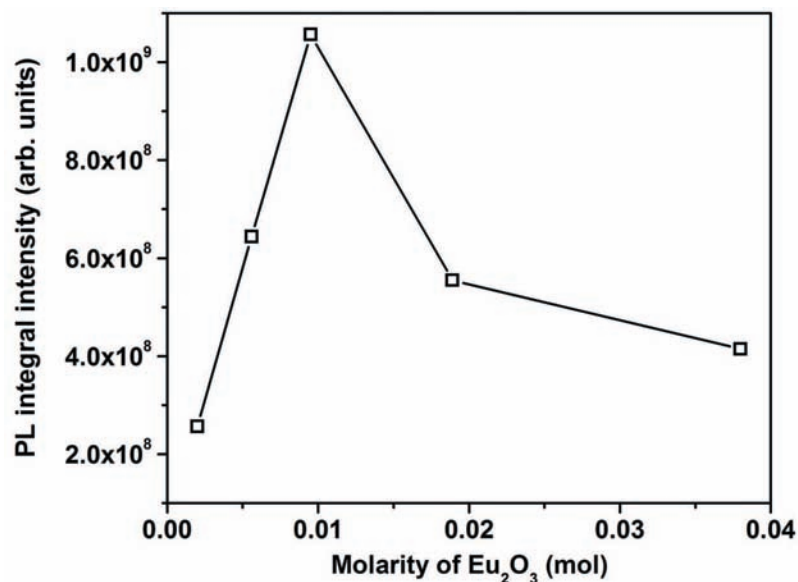
Figure 3.11: Variation of PL integral intensity of Eu doped $ZnGa_2O_4$ nanoparticles with amount of Eu_2O_3 in the hydrothermal precursor solution

The luminescent intensity of Eu doped ZnGa$_2$O$_4$ nanoparticles increases with increase of the amount of Eu$_2$O$_3$ in the precursor solution up to 0.01 mol and then it decreases which is shown in the figure 3.11. When the activator concentration increases above a certain level, luminescence begins to quench. Thus the emission intensity of ^{5}D$_0 \rightarrow ^7$F$_j$ (j=0-4) depends on the amount of Eu$_2$O$_3$. In this case, the pairing or aggregation of activator atoms at high concentration may change a fraction of the activators into quenchers and induce the quenching effect. The migration of excitation by resonant energy transfer between the Eu^{3+} activators can sometimes be so efficient that it may carry the energy to a distant killer or to a quenching centre existing at the surface of the crystal.

3.4   Conclusion

Undoped and Eu doped ZnGa$_2$O$_4$ nanophosphors were synthesized by hydrothermal method by varying the process parameters such as temperature, time of growth, volume ratio of Zn/Ga precursor solutions and the amount of Eu$_2$O$_3$ added to the precursor solution. The room temperature photoluminescence measurements of the nanocrystals monitored at an excitation wavelength of 254 nm gave a peak-shaped spectrum instead of the normally observed bell-shaped spectrum of bulk ZnGa$_2$O$_4$. The band gap of the ZnGa$_2$O$_4$ nanoparticles is blue shifted compared with the bulk material due to quantum confinement effects. XRD and SAED results show Eu doped ZnGa$_2$O$_4$ nanoparticles have spinel structure and the particle size 8 nm as confined by the TEM. Incorporation of Eu in the nanoparticles was confirmed by the ICP-AES studies. The red PL emissions from the intra-4f transition of Eu^{3+} ions are observed in Eu doped ZnGa$_2$O$_4$ nanophosphors

under an excitation of 397 nm. Luminescence quenching is observed in these nanophosphors as the amount of Eu_2O_3 increases. These nanophosphors can be used as a blue to red converter for solid state lighting applications.

Chapter 4

Hydrothermal synthesis of zinc oxide nanostructures

4.1 Introduction

Semiconductors with dimensions in the nanometer realm are important because their electrical, optical and chemical properties can be tuned by changing the size of the particles. These nanostructures have attracted much interest due to their fundamental importance in bridging the gap between bulk matter and molecular species [199, 200]. Optical properties of nanoparticles are of great interest for application in optoelectronics, photovoltaics and biological sensing.

Advances in the synthesis of highly luminescent semiconductor nanocrystals currently allow their extensive applications in different fields, ranging from optoelectronic to bio-imaging. Depending on the applications, surface modifications of semiconductor nanocrystals are essential. For example, a water soluble surface is necessary for biological labels. An electron conduc-

tive layer is important for solar cells. In recent years, one-dimensional (1D) nanostructures, such as nanorods, nanowires, nanobelts, and nanotubes, have attracted much attention due to their potential applications in a variety of novel nanodevices, such as field-effect transistors, single-electron transistors, photodiodes, and chemical sensors. Various chemical synthetic methods have been developed to prepare such nanostructures.

Zinc oxide (ZnO) is a unique material with a direct band gap (3.37 eV) and large exciton binding energy of 60 meV [201, 202], which makes the exciton state stable even at room temperature. ZnO has been widely used in near-UV emission, gas sensors, transparent conductor, thin film transistors and piezoelectric applications [203–205]. Zinc is also a very important trace element in humans [206]. The average adult body contains 3.0-4.5 x 10^{-2} mmol (2-3 g) of zinc, which is found in muscle, bone, skin and plasma. Significant amounts occur in the liver, kidney, eyes and hair etc. Zinc has been found to play an important part in many biological systems. Therefore, ZnO is environmentally friendly and suitable for in-vivo bio-imaging and cancer detection. Solid state white light emitting sources based on the existing Si-based technology is one of the challenging goals in the field of display and light emitting technology. The potential applications of solid state white light emitting sources are immense because of their distinctive properties like low power consumption, high efficiency, long lifetime, reduced operating costs and free from toxic mercury. To generate white light, a blend of phosphors that emits in blue, green and red wavelengths are required. This difficulty could be overcome by using semiconducting nanocrystalline luminescent materials, which have larger molar absorption and exhibit broadband emission in the visible spectrum without self-absorption. Since nanostructures possess an enormous

surface-to-volume ratio, they are suitable candidates for defect emission. ZnO commonly exhibits luminescence in the visible spectral range due to different intrinsic defects. This opens the possibility of use of ZnO for solid state lighting. Controlled incorporation of defects generally involves high temperature annealing [207], substitution [208], mechanical milling [209] etc. Due to its excellent stability and the defect emission, ZnO has been widely used as a phosphor in vacuum fluorescent displays (VFD).

Most of the ZnO crystals have been synthesized by traditional high temperature solid state reaction which is energy consuming and difficult to control the particle properties. ZnO [210, 211] nanoparticles can be prepared on a large scale at low cost by simple solution based methods, such as chemical precipitation [212, 213], sol-gel synthesis [214], and solvothermal/hydrothermal reaction [210, 211]. Hydrothermal technique is a promising method because of the low process temperature and very easy to control the particle size. The hydrothermal process have several advantages over other growth processes such as use of simple equipment, catalyst-free growth, low cost, large area uniform production, environmental friendliness and less hazardous. The low reaction temperatures make this method an attractive one for microelectronics and plastic electronics [215]. This method has also been successfully employed to prepare nano-scale ZnO and other luminescent materials. The particle properties such as morphology and size can be controlled via the hydrothermal process by adjusting the reaction temperature, time and concentration of precursors.

The present study focuses on the hydrothermal synthesis of ZnO nanopowder and the effect of precursors, reaction temperature, concentration of the precursors and time of growth on its properties. The hydrothermal synthesis of ZnO powder has many advantages like (1) powder with nanometer-

size can be obtained by this method (2) the reaction can be carried out under moderate conditions (3) powder with different morphologies can be grown by adjusting the reaction conditions and (4) the as-prepared powder have properties different from that of the bulk.

4.2   Experimental

ZnO nanoparticles were synthesized from $Zn(CH_3COO)_2.2H_2O$ and NaOH precursors by hydrothermal method. To the stock solution of $Zn(CH_3COO)_2.$ $2H_2O$ (0.1 M) prepared in 50ml methanol, 25 ml of NaOH (varying from 0.2 M to 0.5 M) solution prepared in methanol was added under continuous stirring in order to get the pH value of reactants between 8 and 11. These solution was transferred into teflon lined sealed stainless steel autoclaves and maintained at various temperatures in the range of 100-200^{0}C for 3 to 12 h under autogenous pressure. It was then allowed to cool naturally to room temperature. After the reaction was complete, the resulting white solid products were washed with methanol, filtered and then dried in air in a laboratory oven at 60°C.

The ZnO nanorods were synthesized from $Zn(CH_3COO)_2.2H_2O$ and NH_4OH precursors by hydrothermal method. To the stock solution of 0.1 M $Zn(CH_3COO)_2.2H_2O$, NH_4OH was added dropwise in order to get a pH value of reactants between (8-9). The final solution was transferred into teflon lined sealed stainless steel autoclaves and maintained at 100^{0}C for 3 h under autogenous pressure. After cooling white solid products of ZnO nanostructures were washed with distilled water, filtered and then dried in air.

The synthesized samples were characterized for their structure by x-ray diffraction (Rigaku D max-C) with Cu K_α radiation. Transmission electron microscopy (TEM), selected area electron diffraction (SAED) and high resolution transmission electron microscopy (HRTEM) were performed with a JEOL JEM-3100F transmission electron microscope operating at 200 kV. The sample for TEM was prepared by placing a drop of the ZnO suspension in methanol onto a 200 mesh carbon coated copper grid. The grids were dried before recording the micrographs. The optical band gap E_g was estimated from the UV-Vis-NIR diffuse reflectance spectroscopic (UV-Vis-NIR DRS) studies in a wavelength range from 190nm to 1200nm with JASCO V-570 spectrophotometer. The samples for this study were used in the form of powder and pure $BaSO_4$ used as the reference. The elemental composition of the ZnO nanoparticles were determined by using Thermo Electron IRIS INTREPID II XSP DUO inductively coupled plasma atomic emission spectrometer (ICP-AES). Room temperature photoluminescence (PL) of the samples was measured on Horiba Jobin Yvon Fluoromax-3 spectrofluorimeter using Xe lamp as the excitation source.

4.3   Results and discussion

4.3.1   Characterization of ZnO nanoparticles synthesized by hydrothermal method

The x-ray diffraction data were recorded using Cu K_α radiation (1.5418 Å). The intensity data were collected over a 2θ range of $20\text{-}80^0$. The average grain size of the samples was estimated with the help of Scherrer equation from the diffraction intensity of (101) peak.

X-ray diffraction studies confirmed that the synthesized materials were ZnO with wurtzite phase and all the diffraction peaks agreed with the reported ICSD data [216] and no characteristic peaks were observed other than ZnO.

The mean grain size (D) of the particles was determined from the XRD line broadening measurement using Scherrer equation [217].

$$D = \frac{0.9\lambda}{\beta cos\theta} \tag{4.1}$$

Where λ is the wavelength of the Cu K$_\alpha$ radiation, β is the full width at half maximum (FWHM) of the ZnO (101) peak and θ is the diffraction angle.

A definite line broadening of the diffraction peaks is an indication that the synthesized materials are in nanometer range. The grain size was found to be in the range of 7-24 nm depending on the growth condition. The lattice parameters calculated were also in agreement with the reported values.

The reaction temperature greatly influences the particle morphology of as-prepared ZnO powders. Figure 4.1 shows that the XRD patterns of ZnO nanoparticles synthesized at various temperatures with 0.3 M NaOH for reaction time of 6 h. As the reaction temperature increases, FWHM decreases. Thus the size of ZnO nanoparticles increases as the temperature for the hydrothermal synthesis increases. This is due to the change of growth rate between the different crystallographic planes.
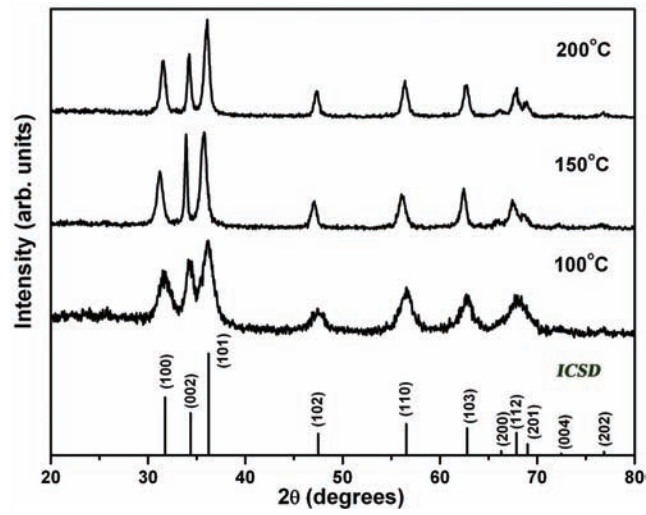
Figure 4.1: XRD patterns of ZnO nanoparticles synthesized from 0.3 M NaOH at various temperatures for 6 h
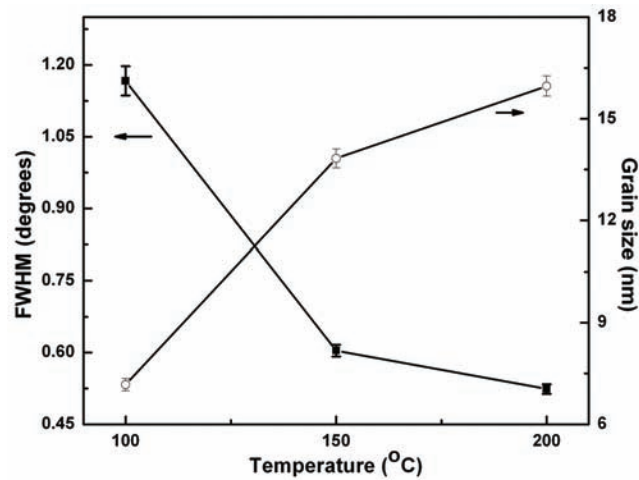
Figure 4.2: Variation of FWHM and grain size with temperature for the ZnO nanoparticles synthesized using 0.3 M NaOH for a growth time of 6 h

Figure 4.2 shows the variation of FWHM and grain size of ZnO nanoparticles synthesized from 0.3 M NaOH at different temperatures for a fixed growth time of 6 h. The average grain size calculated by Scherrer equation is observed to increases from 7 nm to 16 nm as the temperature increases from 100^0C to 200^0C [218].
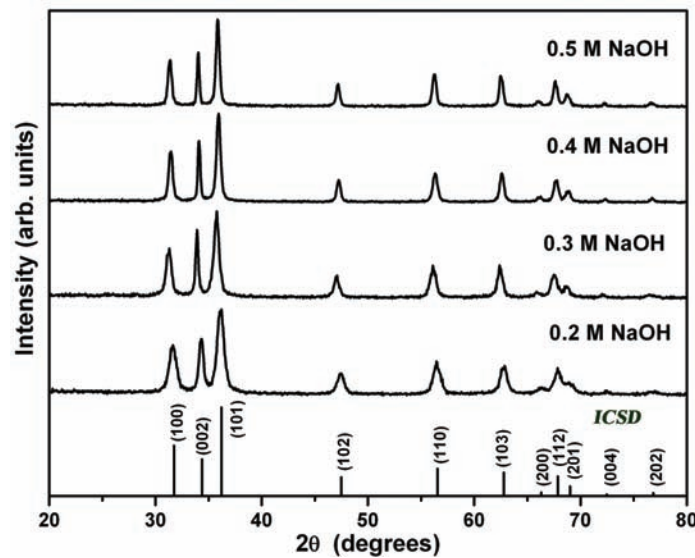
Figure 4.3: XRD patterns of ZnO nanoparticles synthesized at various concentration of NaOH (0.2 M, 0.3 M, 0.4 M and 0.5 M) at 200^0C for a duration of 12h

ZnO structures with different grain sizes can be obtained by controlling the concentration of the precursors. ZnO nanoparticles were synthesized by keeping the concentration of $Zn(CH_3COO)_2.2H_2O$ as 0.1 M in all reactions, the concentration of NaOH was varied from 0.2 M to 0.5 M at a hydrothermal growth temperature of 200^0C for a duration of 12 h. Figure 4.3 shows the XRD pattern of ZnO nanoparticles synthesized by varying the concen-

tration of precursors. All the peaks match well with the standard wurtzite structure [216] and the FWHM of the (101) diffraction peak increases with the decreasing concentration of the NaOH. These results reveal that the molar ratio of OH^- to Zn^{2+} is a dominant factor for the formation of the ZnO nanoparticles.
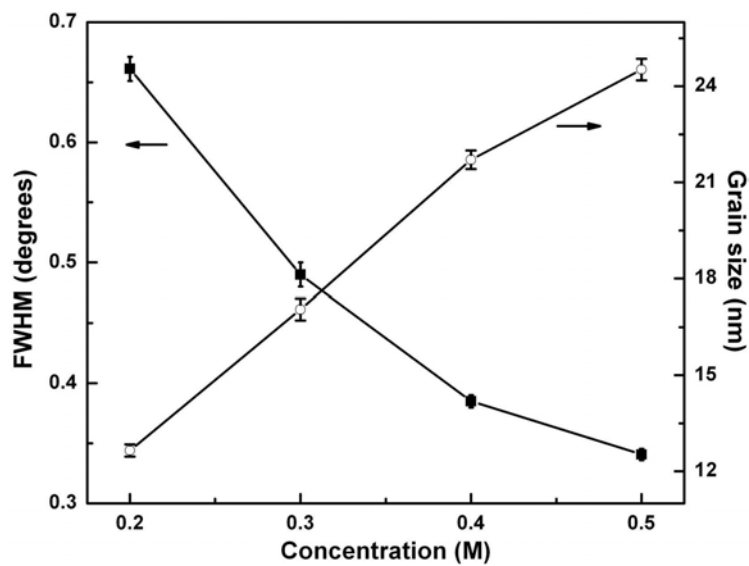
Figure 4.4: Variation of FWHM and grain size of ZnO nanoparticles with various concentration of NaOH grown at 200^0C for a growth time of 12 h

Figure 4.4 shows the variation of FWHM and grain size of ZnO nanoparticles with concentration of NaOH precursor for the samples grown at 200^0C for a reaction time 12 h. It has a linear variation with the concentration of NaOH precursor. The grain size increases from 12 nm to 24 nm as the concentration of NaOH precursors increases from 0.2 M to 0.5 M.
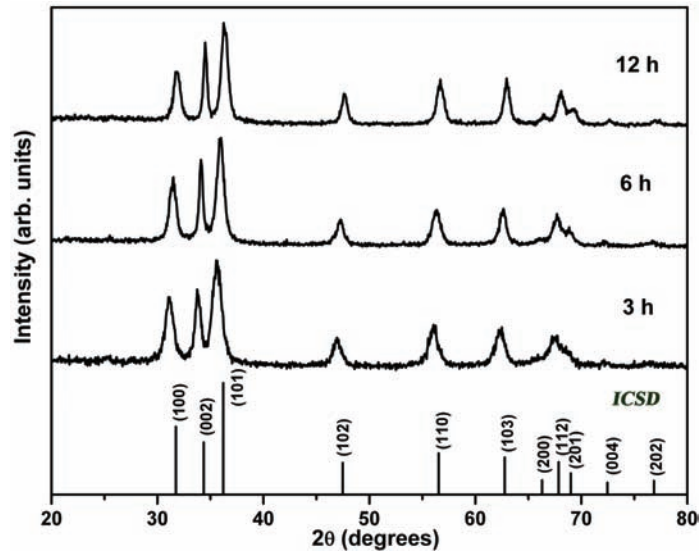
Figure 4.5: XRD patterns of ZnO nanoparticles with different time of growth for 0.2 M NaOH at 150^0C

Figure 4.5 shows the XRD pattern of the ZnO nanoparticles synthesized from 0.2 M NaOH at a growth temperature of 150^0C with different growth time. The variation of FWHM and grain size of ZnO nanoparticles obtained from Scherrer's formula with different time of growth for 0.2 M NaOH at 150^0C is shown in the figure 4.6.

The grain size of ZnO nanoparticles synthesized from 0.2 M NaOH at 150^0C increases from 9 nm to 13 nm as the time of growth increases from 3 h to 12 h. It shows that grain size has a linear dependence on time of growth [219].
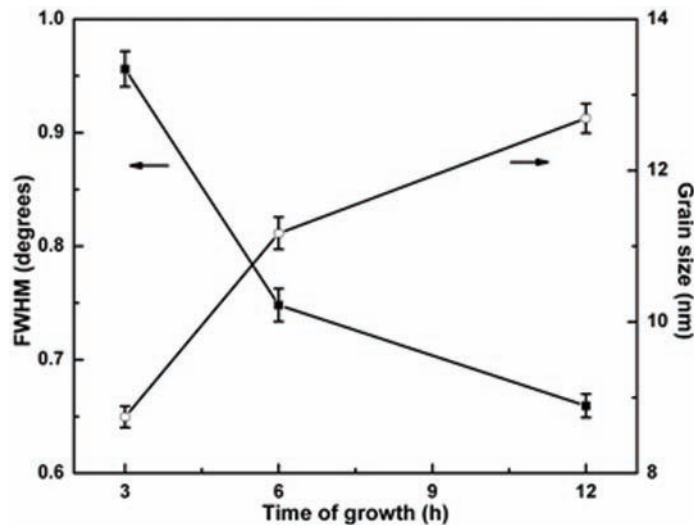
Figure 4.6: Variation of FWHM and grain size of ZnO nanoparticles obtained with different time of growth for 0.2 M NaOH at 150^0C

In the precursor solution used in the experiment, the source of Zn is in the form of $Zn(OH)_2$ precipitates and $Zn(OH)_4{}^{2-}$ species according to the stoichiometric ratio of Zn^{2+} on OH^-. The $Zn(OH)_2$ precipitates under the hydrothermal conditions will dissolve to considerable extent to form ions of Zn^{2+} and OH^-, once the product of $[Zn^{2+}]$ and OH^- exceeds a critical value which is necessary for the formation of ZnO crystals, the ZnO crystals will precipitate from the solution. The solubility of ZnO is significantly smaller than that of $Zn(OH)_2$ under the hydrothermal conditions, consequently, the $Zn(OH)_2$ precipitates strongly tended to be transformed into ZnO crystals during the hydrothermal process, by the following reactions [220, 221].

$$Zn(OH)_2 \rightarrow Zn^{2+} + 2OH^- \tag{4.2}$$

$$Zn^{2+} + 2OH^- \rightarrow ZnO + H_2O \tag{4.3}$$
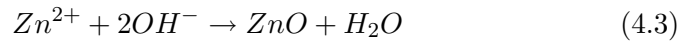
At the initial stage of the process, the concentrations of Zn^{2+} and OH^- were relatively higher so that the crystal growth in different directions was considerable [220, 222]. When the concentration of Zn^{2+} and OH^- reaches the supersaturation value of ZnO, ZnO begins to nucleate and the crystal growth begins.
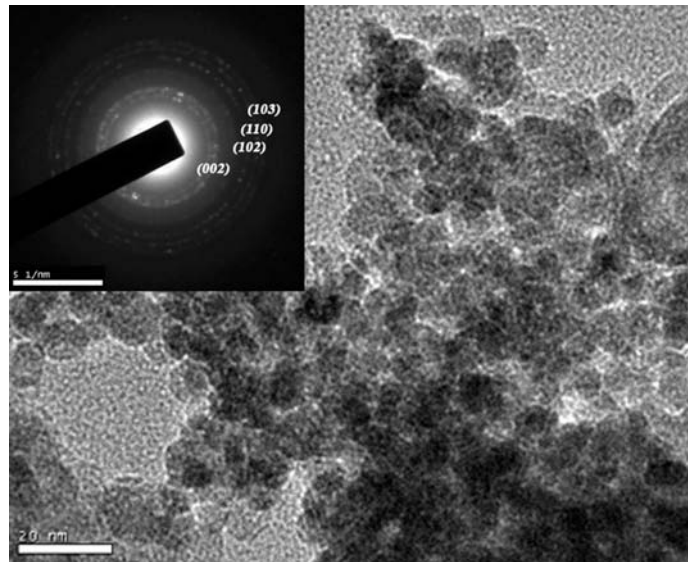
Figure 4.7: TEM image of the ZnO nanoparticles synthesized from 0.3 M NaOH at 100^oC for a growth duration of 3 h. Inset shows the SAED image

Figure 4.7 shows the TEM image and corresponding selected-area electron diffraction (SAED) pattern of the ZnO nanoparticles synthesized at 100^0C for a duration of 3 h from 0.3 M NaOH. TEM image confirms the formation of ZnO nanoparticle and it has an average size about 8 nm. From

the diffraction rings of SAED pattern shown in the inset of figure 4.7, (002), (102), (110) and (103) plane of the ZnO nanoparticles were identified.
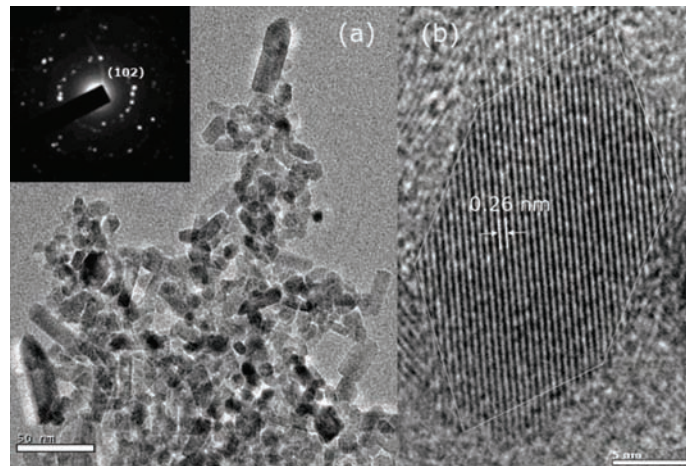
Figure 4.8: (a) TEM image of the ZnO nanoparticles synthesized from 0.3 M NaOH at 150°C for 6 h. Inset shows the SAED image (b) HRTEM of the ZnO nanoparticle

Figure 4.8(a) shows the TEM image and corresponding selected area electron diffraction (SAED) pattern of the ZnO nanoparticle synthesized at 150°C for 6 h from 0.3 M NaOH. TEM image confirms the formation of ZnO nanoparticle with an average size about 10 nm. Some ZnO nanorods with average diameter of 15nm and length of about 50 nm were also observed. From the diffraction rings of SAED pattern shown in the inset of figure 4.8(a), (102) plane of the ZnO nanoparticles were identified. Figure 4.8(b) shows the HRTEM image of the ZnO nanoparticle synthesized at 150^{0}C for 6 h from 0.3 M NaOH. HRTEM pattern indicates that the nanorods grow along the c axis and it has hexagonal structure.

The optical band gap of the synthesized nanoparticles were estimated from the diffuse reflectance spectral studies in the UV-Vis-NIR region. Figure 4.9 shows the plot for the percentage of reflection as a function of photon energy ($h\upsilon$) for the nanoparticles synthesized via hydrothermal method from 0.3 M NaOH at 100°C for a duration of 6 h. The band gap estimated for this sample is 3.42eV and that is slightly higher than that of bulk commercial ZnO powder (3.37eV). This blue shift may be attributed to quantum confinement effects.
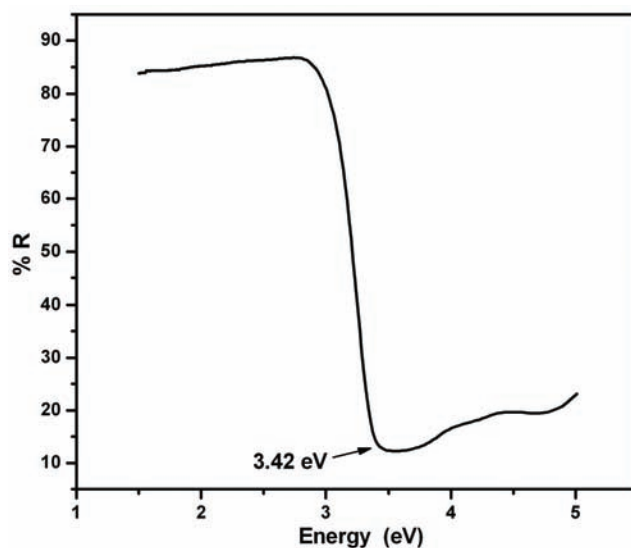
Figure 4.9: DRS of the typical ZnO nanoparticles synthesized from 0.3 M NaOH at 100^{0}C for a reaction time of 6 h

The amount of Na that is incorporated in ZnO nanoparticles was determined using ICP-AES data. The ICP-AES shows that Na incorporated into the nanoparticles is about 0.17% for lower concentration (0.2 M) and about 1.49% for higher concentration (0.5 M) of NaOH in the precursor

solution. The Na content in the ZnO nanoparticles increases with NaOH concentration. The theoretical binding energy of dopant atoms on the individual semiconductor nanocrystal surface determines its doping efficiency [223]. The binding energy for wurtzite semiconductor nanocrystal is three times less than that of zinc blend or rock salt structure on (001) faces. The low concentration of incorporated Na is likely to be a consequence of lower doping efficiency of the wurtzite ZnO nanocrystal surfaces.
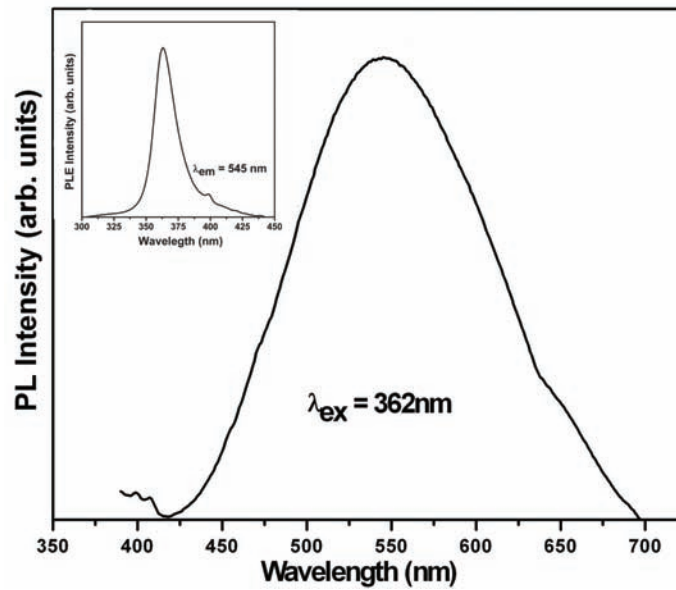
Figure 4.10: Room temperature photoluminescence spectra of ZnO nanoparticle excited at $\lambda_{ex} = 362$ nm. The inset shows the corresponding photoluminescent excitation spectra ($\lambda_{em} = 545$ nm) of ZnO nanoparticles

The luminescence of ZnO nanoparticles is of particular interest from both physical and applied aspects. Figure 4.10 shows the room temperature photoluminescence spectrum of the ZnO nanoparticles excited with 362 nm.

Green emission was observed from the hydrothermally synthesized ZnO nanoparticles. The green emission can be attributed to the transition between singly charged oxygen vacancy and photo excited hole or Zn interstitial related defects [224, 225]. The inset in the figure 4.10 shows the photoluminescent excitation spectra of the ZnO nanoparticles (λ_{em}= 545nm) which indicates that the excitation is at 362 nm. The excitation peak corresponds to the band to band transition which also confirms the blue shift in the band gap of ZnO nanoparticles.

4.3.2   Characterization of ZnO nanorods synthesized by hydrothermal method
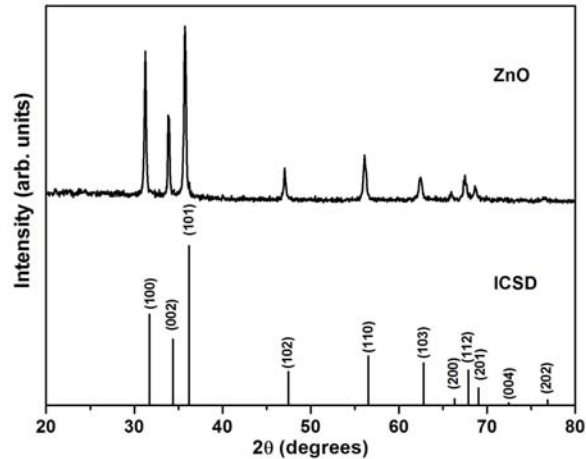
Figure 4.11: XRD pattern of ZnO nanorods synthesized by hydrothermal method

Figure 4.11 shows the x-ray diffraction (XRD) pattern of the ZnO nanostructures grown by hydrothermal method. These spectra can be indexed

for diffractions from different planes of wurtzite ZnO crystals with lattice constants a =0.325 nm and c =0.521 nm.

The SEM image of the flower like nanostructure of ZnO synthesized at 100^0C for a growth duration of 3 h from 0.3 M zinc acetate as precursor are shown in the figure 4.12. The flower like nanostructure consists of ZnO nanorods that grown at various angles from a single nucleation centre arranging them in a spherical shape exhibiting flower-like morphologies. Each nanorod has hexagonal shape at the tip and these nanorods have an average diameter of 500 nm and a length of 4 μm.
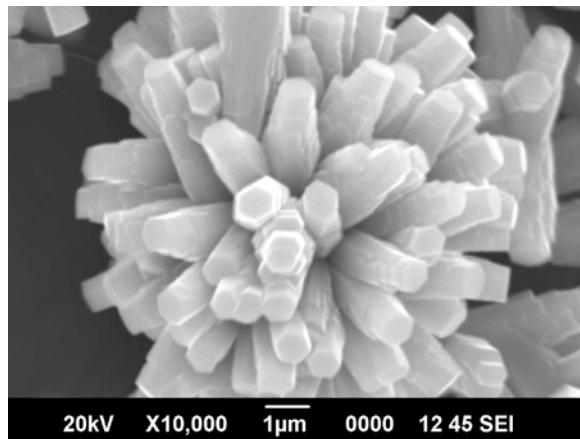
Figure 4.12: SEM image of ZnO nanorods synthesized at a temperature of 100^0C for a growth duration of 3 h by hydrothermal method

Figure 4.13 shows the SEM image of the pure ZnO nanorods synthesized at 100^0C for 6 h from 0.3 M zinc acetate as precursor. Thus the morphology of the nanostructures changes with growth parameters. Thus hydrothermal method can be used as a suitable method for obtaining different nanostructures by varying the process parameters like growth temperature, time of

growth, precursors etc.
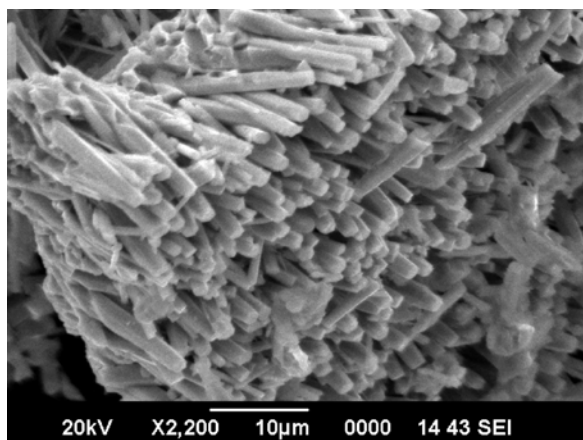
Figure 4.13: SEM image of the undoped ZnO nanorods grown at a temperature of 100^0C for 6 h by hydrothermal method
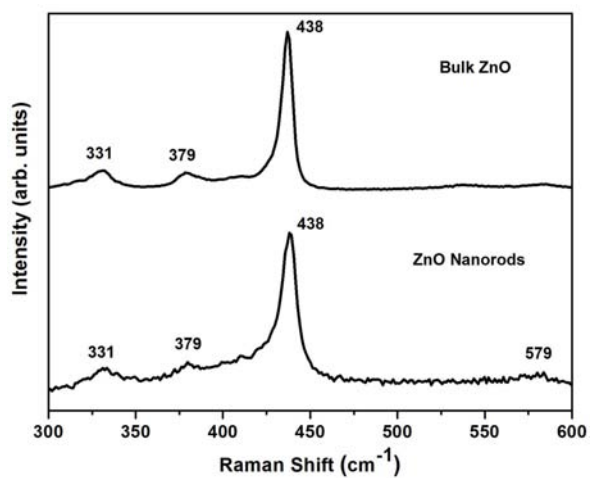
Figure 4.14: Raman spectra of ZnO nanorods synthesized by hydrothermal method

Figure 4.14 shows the Raman spectra of ZnO nanostructures synthe-sized by hydrothermal method and it confirms the formation of wurtzite ZnO. The broad peak at about 331 cm^{-1} seen in both spectra is attributed to the second-order Raman processes. The peak at 379 cm^{-1} corresponds to A_1 transverse optical(TO) and 438 cm^{-1} corresponds to transverse E_2 line. The A_1 longitudinal optical(LO) mode is absent in the bulk where as nanorods grown by hydrothermal technique shows a broad peak at 579 cm^{-1}, which can be assigned to the A_1(LO) phonon mode.

The diffuse reflectance spectroscopy measurements confirm the blue shift in the band gap of nanostructures with respect to the bulk. This increase in the band gap is due to the quantum confinement effects.
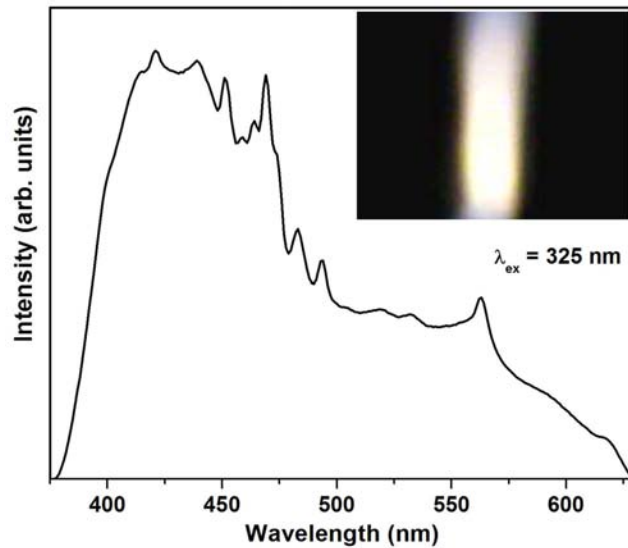
Figure 4.15: Photoluminescent emission spectra of ZnO nanorods synthesized by hydrothermal method at an excitation wavelength of 325 nm. Inset shows the white emission from ZnO nanostructures

The room temperature photoluminescence measurements of the nanorods monitored at an excitation wavelength of 325 nm gave a broad spectrum and it results in white emission from the nanostructures (Figure 4.15). The broad spectrum is assigned to the intrinsic and extrinsic defects of ZnO. The color of emission are measured and expressed by the resultant chromaticity coordinates (x, y). The Commission Internationale de l'Eclairage (CIE) diagram of ZnO nanorods synthesized by hydrothermal method is shown in the figure 4.16. The CIE color coordinates measured from the photoluminescent emission of ZnO nanostructures is found to be (0.28, 0.29) and this shows the emission close to achromatic white emission with CIE values (0.33, 0.33). Therefore, these ZnO nanostructures can be considered as a potential candidate for solid state lighting applications.
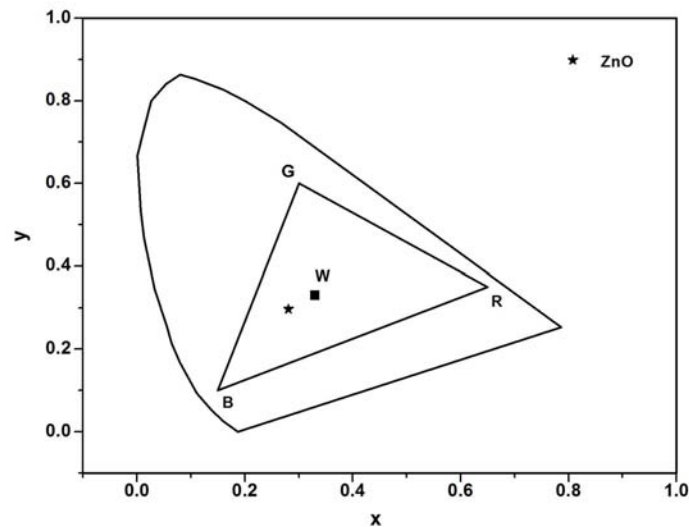
Figure 4.16: CIE coordinates of ZnO nanorods synthesized by hydrothermal method. The figure also shows the phosphor triangle and the achromatic white

In order to determine the defects and mechanism of photoluminescent emission from ZnO nanorods synthesized by hydrothermal method, the samples were annealed at 800^0C for 1 h in oxygen atmosphere and oxygen in the presence of Zn vapour. The XRD pattern of the ZnO pristine sample and that annealed in (oxygen+Zn) atmosphere and oxygen atmosphere are shown in the figure 4.17. The wurtzite structure of the ZnO were not modified by the annealing in different atmosphere.
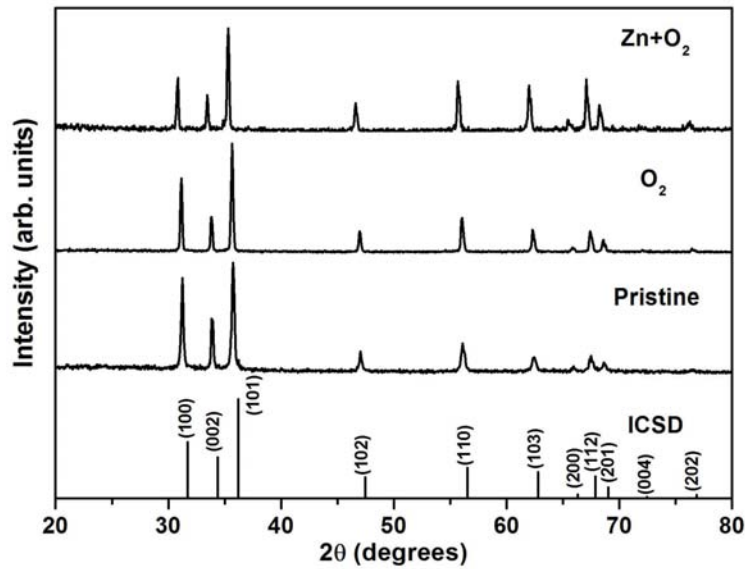
Figure 4.17: XRD pattern of the ZnO pristine sample and that annealed in oxygen atmosphere and (oxygen+Zn) atmosphere

The photoluminescence emission from ZnO nanorods annealed at different atmosphere is shown in the figure 4.18. The PL emission at 420 nm corresponds to the interstitial oxygen defects (O_i) [226]. During oxygen annealing, oxygen interstitial defects may increase and results in the increase

of PL intensity compared to that of pristine samples. During the (oxygen+Zn) annealing by the flow of oxygen in the presence of Zn granules, the oxygen in the interstitial position and the supplied oxygen combines with the Zn results in the formation of ZnO and thus the PL emission at 420 nm becomes weaker than the pristine samples.
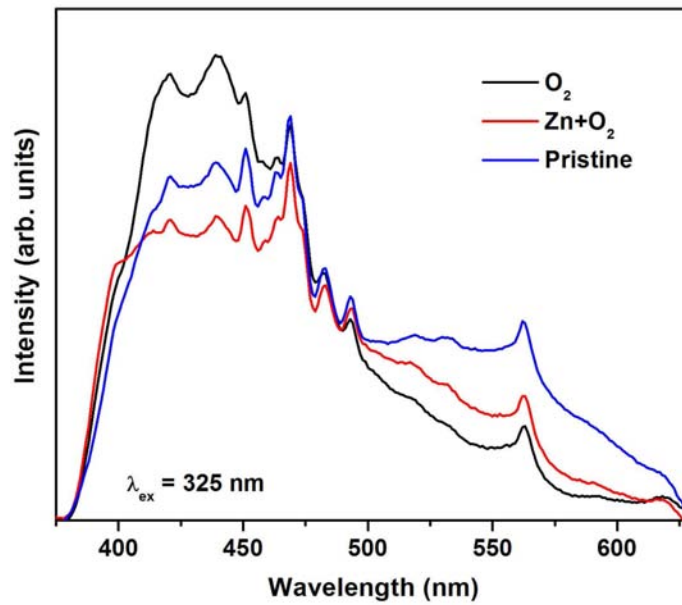
Figure 4.18: Photoluminescent emission spectra of ZnO nanorods synthesized by hydrothermal method annealed in oxygen, oxygen in the presence of Zn at an excitation wavelength of 325 nm

The PL emission at 440 nm is due to the V_{Zn} or O_i [227]. During oxygen annealing, oxygen interstitial defects may increase. The Zn vacancy defects may also increase due to the formation of ZnO. This results in the increase in the PL emission intensity during the annealing of ZnO nanorods in oxygen atmosphere. Vacancies of Zn may decrease during the annealing

of ZnO samples in (oxygen+Zn) atmosphere.

The vacancy of Zn^{2-} are responsible for the PL emission at 452 nm [228]. From the PL measurements it is found that, during oxygen annealing the PL emission intensity at this wavelength is weaker than that of pristine samples. This may be due to the formation of ZnO by the reaction of oxygen with Zn. Annealing of the samples in (oxygen+Zn) atmosphere may cause decrease in the Zn vacancy by the addition of Zn to the samples. This results in the decrease of PL emission intensity compared with that of pristine samples.

The PL emission at 470 nm is due to the interstitial defects of O^- [228], so the PL emission intensity decreases during oxygen annealing than the pristine samples. The annealing of the samples in (oxygen+Zn) atmosphere shows a decrease in the PL emission intensity as that of pristine and which is assigned to the formation of ZnO.

The PL emission at 485 nm corresponds to the transition between oxygen vacancy and oxygen interstitial defects and at 490 nm corresponds to the singly ionized oxygen vacancy [224]. Thus during oxygen annealing the oxygen vacancy decreases and results in the decrease in the PL emission intensity and during the annealing of the samples in oxygen atmosphere in the presence of Zn shows a increase in PL emission intensity than that annealed in oxygen atmosphere. This may be due to the formation of ZnO with the use of oxygen supplied during annealing.

The PL emission at 564 nm is also due to the oxygen vacancies [35]. Thus during oxygen annealing, PL emission intensity decreases due to reduction of oxygen vacancies. The PL emission from the ZnO nanorods annealed in (oxygen+Zn) atmosphere is found to be higher than that annealed in oxygen atmosphere and weaker than that of pristine samples.

This may be due to the formation of ZnO by diffusion between Zn and oxygen.

Based on the above mechanism, a schematic of the energy levels that contributes to the PL emission of ZnO nanorods can be suggested. Generally oxygen vacancies (V_O) and zinc interstitials (Zn_i) are donors and zinc vacancies (V_{Zn}) and antisite oxygen (O_{Zn}) are acceptors [228]. Figure 4.19 shows a schematic representation of the main energy levels identified in the studied samples.
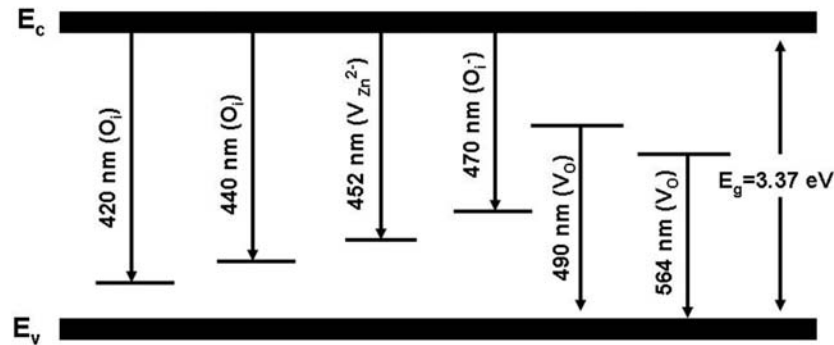
Figure 4.19: Simplified energy diagram of ZnO nanorods

4.4   Conclusion

ZnO nanoparticles were synthesized by hydrothermal method using NaOH precursor. The effect of concentration of the precursors, temperature and time of growth on the structure, grain size, band gap energy and PL were investigated. The XRD analysis demonstrates that the nanoparticles have the hexagonal wurtzite structure and the particle size increases with growth temperature and time while it decreases with concentration of the pre-

cursors. Due to quantum confinement effects, the band gap of the ZnO nanoparticles is blue shifted compared with the bulk material. The green PL emission observed for the synthesized ZnO nanoparticles is due to the oxygen vacancy or Zn interstitial defects. Flower like nanostructures of ZnO have been synthesized by hydrothermal method using NH_4OH precursor. These nanostructures have photoluminescent emission across the visible region of the electromagnetic spectrum which is due to the intrinsic and extrinsic defects of ZnO. CIE color coordinates measured from the PL spectra confirms the white emission from these nanostructures. The outstanding white emission from these nanostructures will find application for solid state lighting.

Chapter 5

Doped ZnO nanostructures grown by hydrothermal method

5.1 Introduction

Methods for introducing new magnetic, optical, electronic, photophysical or photochemical properties to semiconductor nanocrystals are attracting intense interest as prospects for nanotechnological applications emerge in the areas of spintronics, optoelectronics, quantum computing, photocatalysis and luminescence labeling. Introduction of impurity atoms into semiconducting materials is the primary method for controlling the properties of the semiconductors, such as band gap, electrical conductivity etc. II-VI and III-V semiconductors that have been doped with transition metals are currently generating much research interest, principally for their novel magnetic properties. These semiconductors are commonly called as di-

lute magnetic semiconductors (DMS) and are envisioned to be the suitable candidate for spintronic devices. Materials for spintronics (spin based electronics) combine complementary properties of ferromagnetic material and semiconductor structures. In DMS, a stoichiometric fraction of the host semiconductor atoms is randomly replaced by magnetic atoms and resulting solid solution is semiconducting, but can possess well defined magnetic properties (paramagnetic, antiferromagnetic, ferromagnetic) that conventional semiconductor do not have. Dilute magnetic semiconductor based on ZnO have attracted a great deal of attention because their application in magnetic semiconductor devices. To date, the origin of ferromagnetism in oxide DMSs remain controversial topic. For ZnO based DMSs, oxygen vacancies (V_O) and zinc vacancies (V_{Zn}) play important roles in the magnetic origin.

The optical properties of doped semiconductor nanoparticles has given rise to intriguing science in nanoresearch in the new millennium. With emerging interest in the field emission display (FED) as one of the promising candidates for flat panel display devices, extensive research on the low voltage phosphors for FED have been carried out. In particular, the use of oxide phosphors has been preferred for LED application due to higher stability in a high vacuum environment and less emission of contaminating gases. Much attention has been paid to the optical properties of II-VI semiconductor nanocrystals such as CdSe, CdS and ZnS because their optical properties depend strongly on the nanocrystal size and shape. But sulfide based phosphor is known to easily degrade at high current densities. High quality II-IV semiconductor nanocrystals also become materials for doping of optically active impurities. The II-VI semiconductor nanocrystals doped with luminescent centers exhibit efficient luminescence even at room

temperature. There are many reports on the synthesis and optical properties of II-VI semiconductor nanocrystals doped with luminescence centers such as transition metals, rare earth ions and donor acceptor pair. Rare earth ions are good luminescence centers due to their narrow and intense emission lines originating from 4f intrashell transitions. These rare earth doped nanocrystals have wide variety of applications including phosphors, display monitors, x-ray imaging, scintillators, optical communications and fluorescence imaging.

This chapter is divided into two parts: first part deals with the synthesis and characterization of cobalt doped ZnO nanostructures for magnetic applications and the synthesis and characterization of europium doped ZnO nanostructures for the luminescent applications are discussed in the second part of the chapter.

5.2 Co^{2+} doped ZnO nanoflowers grown by hydrothermal method

Dilute magnetic semiconductors (DMS) have become a new area of research interest due to its potential application in the field of spintronics [229, 230]. The basic requirement for practical applications is to achieve Curie temperature (T_c) well above the room temperature [231]. Transition metal doped semiconductors, namely ZnO, SnO_2 etc., have attracted a great research interest due to the prediction of room temperature ferromagnetism (RTFM) in them [232, 233]. However the origin of RTFM is not yet clearly understood. The preparation method and growth conditions play an important role in determining the magnetic behaviour of ZnO based DMS materials.

Zinc oxide (ZnO) is a wide band gap (3.3 eV) II-VI compound semiconductor and having an exciton binding energy of 60 meV. The magnetic studies of the pure ZnO shows well known diamagnetic behavior [234, 235]. Hydrothermal method is one of the most cost effective methods and flexible in terms nature of substrates due to its significantly low growth temperature employed. The low growth temperature prevents the diffusion of dopants to form metal clusters.

This chapter deals with the synthesis of undoped and Co^{2+} doped ZnO nanostructures by hydrothermal method and their structural, morphological, optical properties and magnetic properties were studied using x-ray diffraction (XRD), scanning electron microscopy (SEM), photoluminescence (PL), diffuse reflectance (DRS) measurements and superconducting quantum interference device (SQUID) magnetometery.

5.2.1   Experimental

Undoped ZnO and cobalt doped ZnO nanostructures were grown by hydrothermal method. An appropriate quantity of ammonium hydroxide was added to the mixture of zinc acetate (1M-0.3M) and cobalt nitrate (0.01M-0.001M) solution to adjust the pH value between 9 and 11. The Co content was changed by altering the molar ratio of zinc acetate and cobalt nitrate. The mixture was stirred vigorously for 20 min to form a homogeneous solution with the colour changing from pink to brown. The resulting solution was then transferred into a teflon-lined autoclave, which was sealed and maintained at 100^{0}C for 3 to 6 h, before being left to cool to room temperature naturally. A light green precipitate was obtained. After washing with distilled water several times, these samples were finally dried at 60^{0}C

for 2 h for further characterization. The experiment is repeated by varying process parameters such as duration of growth, molar concentration of precursors and growth temperature. The undoped ZnO nanoparticles were also synthesized in a similar manner described above but without adding $Co(NO_3)_2$.

The synthesized nanostructures were structurally characterized by x-ray diffraction technique using Rigaku D max-C x-ray diffractometer with Cu K_α radiation (1.5418 Å). Morphology of the samples was analyzed using scanning electron microscopy (SEM) using JEOL model JSM - 6390LV. The exact amount of cobalt that is incorporated in the ZnO nanostructures was determined using inductively coupled plasma- atomic emission spectra (ICP-AES) obtained using thermo electron IRIS INTREPID II XSP DUO. The optical band gap E_g was estimated from the UV-Vis-NIR diffuse reflectance spectra (DRS) recorded with JASCO V-570 spectrophotometer. The samples for this study were used in the form of powder and pure $BaSO_4$ used as the reference. Room temperature photoluminescence (PL) of the samples was measured on Horiba Jobin Yvon Fluoromax-3 spectrofluorimeter using Xe lamp as the excitation source. Magnetic measurements were taken with superconducting quantum interference device (SQUID) magnetometer (QD MPMS-XL)

5.2.2 Results and discussion
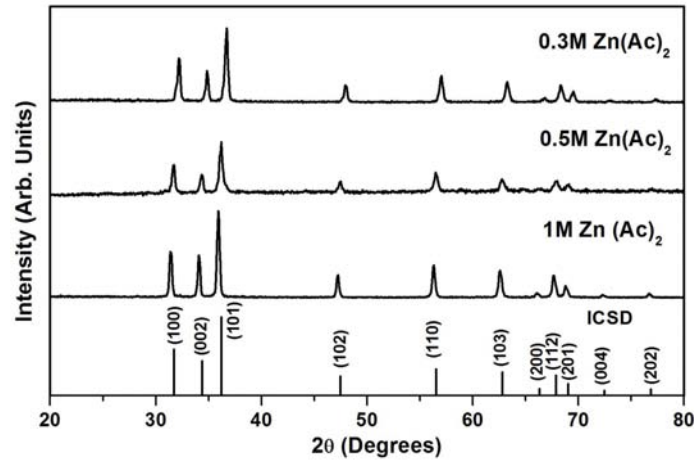
Figure 5.1: XRD patterns of Co doped ZnO nanostructures grown by hydrothermal method with different concentration of Zn (Ac)$_2$, the Co(NO$_3$)$_2$ concentration fixed at 0.01 M and the growth temperature as 100°C for 3 h

Figure 5.1 shows the powder x-ray diffraction patterns of cobalt doped ZnO nanostructures prepared at different molarity of zinc acetate and a growth temperature of 100^{0}C for 3 h with a fixed cobalt nitrate concentration of 0.01M. Figure 5.2 shows the XRD pattern of cobalt doped ZnO nanostructures prepared at different molarity of cobalt nitrate, the zinc acetate was fixed at 1 M and the growth temperature being 100^{0}C and for a duration of 3 h. All the peaks in the x-ray diffraction profile could be assigned to the typical wurtzite structure of ZnO [216]. There are no characteristic peaks of impurity phases regardless of the dopant concentrations. Thus the wurtzite structure is not modified by the addition of Co into the ZnO matrix. The wurtzite structure of the ZnO is not obtained as the concen-

tration of the $Co(NO_3)_2$ precursor increases beyond 0.1 M. With increase of dopant concentration, the peak positions of cobalt doped ZnO shift towards high angles because Co ions have the smaller ionic radius (0.72 $\mathring{A}$) than Zn ions (0.74 $\mathring{A}$) [236]. It is found that the lattice parameters of Co doped ZnO nanostructures increases with molar concentration of cobalt nitrate. The increase in the lattice parameters is attributed to the cobalt substitution in zinc site of zinc oxide nanostructures.
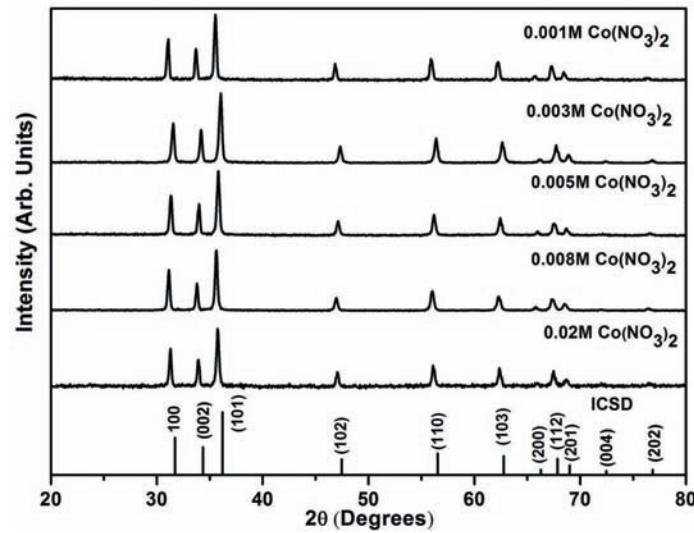
Figure 5.2: XRD patterns of Co doped ZnO nanostructures grown by hydrothermal method with different concentration of $Co(NO_3)_2$, $Zn(Ac)_2$ concentration fixed at 1 M and the growth temperature is 100^oC for 3 h

Figure 5.3 shows the SEM image of the cobalt doped ZnO nanostructures synthesized at 100^0C for a duration of 6 h from 0.3 M zinc acetate and 0.01M cobalt nitrate. SEM image confirms the formation of hexagonal shaped rods and the rods assemble like a flower. The cobalt doped

ZnO structures has an average diameter of about 0.56 μm and a length of about 13 μm. Figure 5.4 shows the SEM image of the cobalt doped ZnO nanostructures synthesized at 100^0C, but for a duration of 3 h from 0.3 M zinc acetate and 0.001M cobalt nitrate.It confirms that the width of the nanorods decreases as the time of growth decreases from 6 h to 3 h, however there is not much change in the length of these rods which is about 13 μm. Thus the doping of cobalt in ZnO matrix may generate some active sites around the circumference of ZnO nuclei, so that ZnO will preferentially grow on the active sites. Flower like ZnO nanostructures can be grown by varying the process parameters such as time of growth, temperature, pH etc [237].
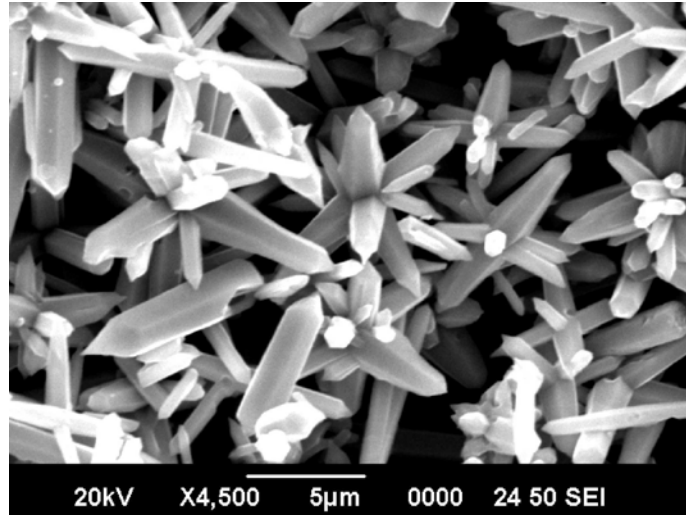
Figure 5.3: SEM image of the cobalt doped ZnO nanorods grown by hydrothermal method at a growth temperature of 100^0C for 6 h
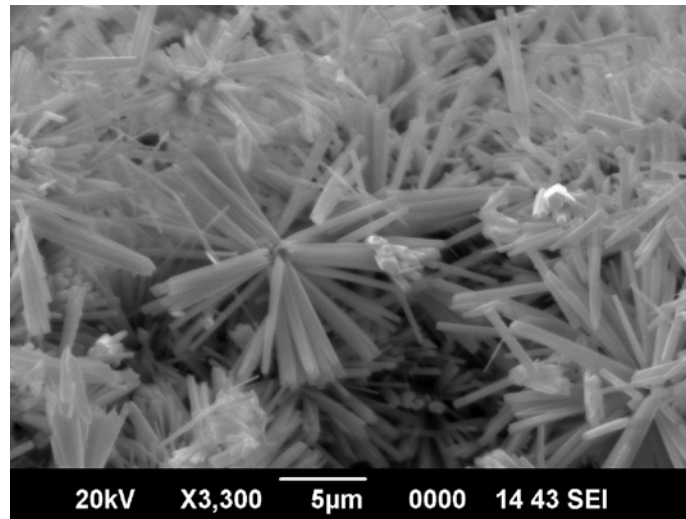
Figure 5.4: SEM image of the cobalt doped ZnO nanorods grown by hydrothermal method at a growth temperature of 100^0C for 3 h

The exact amount of cobalt that is incorporated in the ZnO nanostructures was determined using ICP-AES data. The ICP-AES shows that cobalt incorporated into the nanostructures is about 0.11 atomic % for lower concentration of cobalt nitrate (0.001M) and about 1.06 atomic % for higher concentration (0.01M) of cobalt nitrate in the precursor solution. It is found that the Co content in the ZnO nanostructures increases with cobalt nitrate concentration.

The successful incorporation of Co^{2+} on Zn sites in the ZnO nanostructures is further confirmed by electron paramagnetic resonance (EPR) studies. A broad spectrum observed for these nanostructures due to their random orientation with respect to the magnetic field. The measured spectrum is broader for several reasons. First, Co^{2+} located near the surface of the nanostructures will see a different crystal field compared to Co^{2+}

core of the nanostructures. Furthermore Co-Co interactions can also cause a broadening of the spectrum. The g value of Co^{2+} doped ZnO nanostructures, g = 4.6109 is comparable with reported values [238]. The EPR spectrum of ZnO:Co^{2+} samples are shown in figure 5.5.
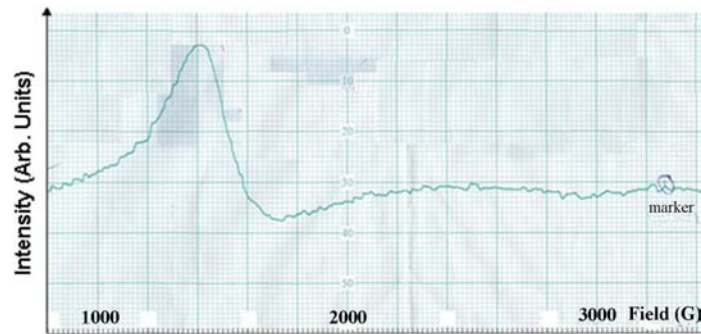
Figure 5.5: EPR spectra of Co doped ZnO nanostructures grown by hydrothermal method at 100^0C for 6 h

Figure 5.6 shows the room temperature photoluminescence emission spectra of ZnO nanostructures and cobalt doped ZnO nanostructures prepared at 100^0C using 0.3 M zinc acetate for a growth duration of 6 h. Blue emission at 437 nm was observed for an excitation wavelength of 350 nm in the ZnO nanostructures and it may be due to Zn interstitial related defects [224, 225]. The dominant transition at 1.88 eV due to the d-d transitions of Co^{2+} in tetrahedral crystal fields is not seen in the room temperature PL spectra. Low temperature PL studies are necessary to observe the d-d transitions of Co^{2+} ions [239].
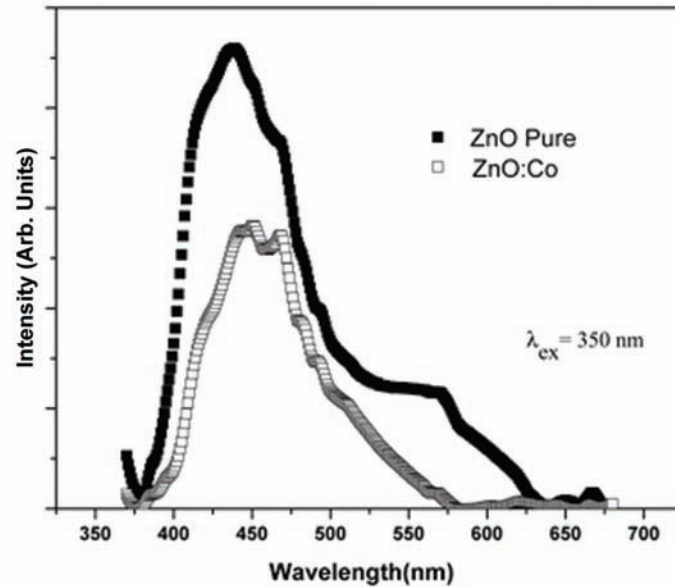
Figure 5.6: Room temperature photoluminescence emission spectra of ZnO and Co doped ZnO nanostructures grown by hydrothermal method at 100^0C for a duration of 6 h

Figure 5.7 shows the diffuse reflectance spectra (DRS) of undoped ZnO and cobalt doped ZnO nanostructures synthesized by hydrothermal method at a growth temperature of 100^0C for 3 h. Figure 5.7(a) corresponds to the DRS of undoped ZnO synthesized from 0.3 M $Zn(Ac)_2$ and figure 5.7(b), (c) and (d) corresponds to that of Co doped ZnO synthesized from 0.3 M, 0.5 M and 1 M $Zn(Ac)_2$ respectively for a particular concentration of $Co(NO_3)_2$ of 0.01 M. Two bands of absorption are observed for the Co doped ZnO samples: an intense absorption peak in the ultraviolet region and a weak band in the visible region (1.8-2.3 eV). The absorption at high energies is due to the band to band transition of ZnO and the visible band is due to

the Co^{2+} d-d internal transitions. The three peaks observed at positions 1.89 eV, 2.03 eV, 2.19 eV have been identified as the internal transitions $^{4}A_{2}$ to $^{2}T_{1}(G)$, $^{4}T_{1}(P)$ and $^{2}A_{1}(G)$ of substitution of Co^{2+} on Zn sites in ZnO, respectively [225]. The band gap of the material can be obtained from the figure 5.7 and it shows that the band gap of the Co doped ZnO nanostructures increases from 3.32 eV to 3.44 eV as the concentration of zinc acetate precursor decreases from 1 M to 0.3 M while other growth parameters were kept constant. The band gap of undoped ZnO is found to be 3.42 eV. This blue shift in the band gap of undoped ZnO and Co doped ZnO nanostructures are due to the quantum confinement effects.
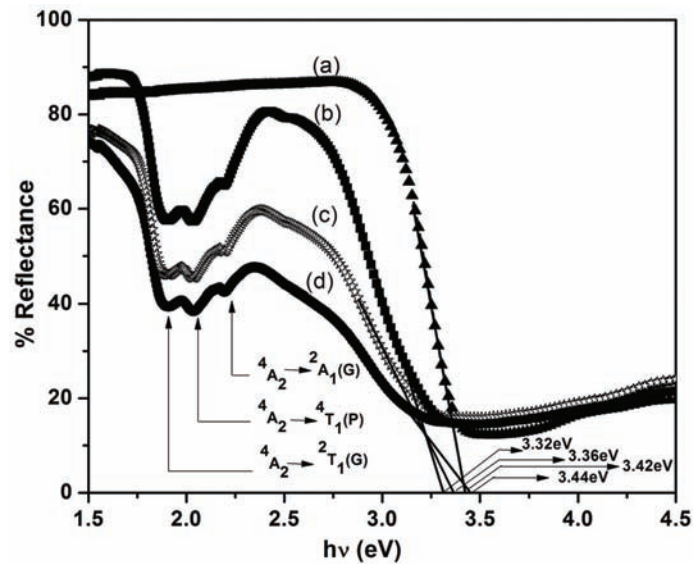
Figure 5.7: Diffuse reflectance spectra of (a) undoped ZnO and cobalt doped ZnO nanostructures grown by hydrothermal method at a growth temperature of $100^{0}C$ for 3 h using $Zn(Ac)_{2}$ precursors of various molarity (b) 0.3 M (c), 0.5 M (d) and 1 M

The magnetic moment of Co doped ZnO nanostrutures, synthesized from 0.01 M cobalt nitrate, measured in the field range 0 to $\pm$ 20 kOe at 5 K is shown in the figure 5.8. The hydrothermally synthesized Co doped ZnO nanostructures were showing paramagnetic behaviour since the curve do not show any hysteresis and no remanence. According to Blasco *et. al* [240] the ferromagnetism at room temperature is always due to the presence of secondary phases and not due to the doping of ZnO, whereas single phases behave as paramagnetic semiconductors. XRD patterns of Co doped ZnO nanostructures synthesized by hydrothermal method shows no significant peaks of secondary phases which may explain the absence of ferromagnetism in Co doped Zno nanostructures.
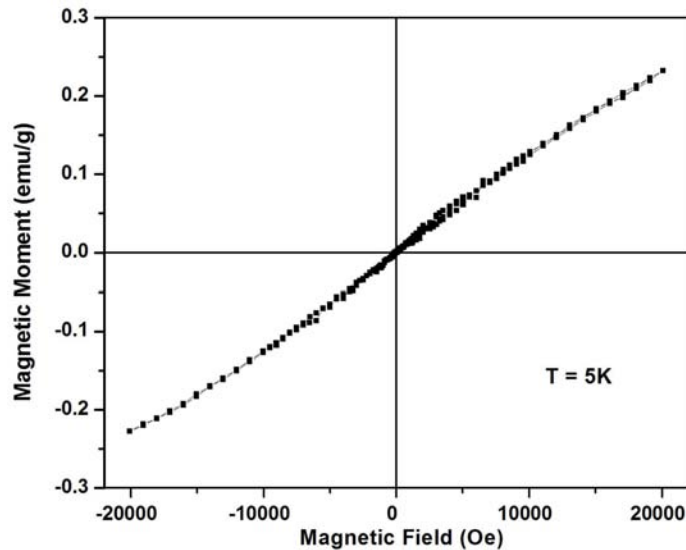
Figure 5.8: Magnetic hysteresis loop of Co doped ZnO nanostructures synthesized from 0.01 M cobalt nitrate at 5 K

The ferromagnetism in dilute magnetic semiconductors is originated from the exchange interaction between free delocalized carriers and localized d spins of the cobalt ions [241]. So the presence of free carriers is essential for the appearance of ferromagnetism in DMS. Free carriers can be induced either by doping or by defects or by cobalt ions in another oxidation state like Co^{3+}. The samples prepared by hydrothermal method have limited number of impurities or defects, which may explain the absence of free carriers and consequently the ferromagnetism.
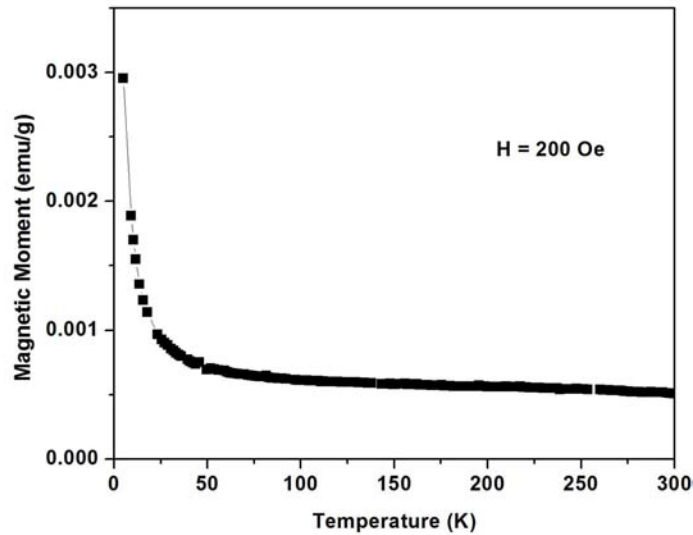
Figure 5.9: Temperature dependant magnetic moment of Co doped ZnO nanostructures synthesized from 0.01 M cobalt nitrate in a magnetic field of 200 Oe

The steep increase in the magnetic moment with decreasing temperature below 50 K as shown in the figure 5.9 is a characteristics of all DMS materials and probably related to the defects structure and possible fraction of Co atoms which are not participating in the long range ferromagnetic

ordering [242]. As the temperature falls below 50 K, the paramagnetic properties dominates and the magnetization increases.

Figure 5.10 shows the inverse susceptibility (χ^{-1}) of Co doped ZnO nanostructures synthesized from 0.01 M cobalt nitrate as a function of temperature. The result is consistent with the Curie- Weiss equation [243]

$$\chi = \frac{C}{(T + \Theta)} \tag{5.1}$$

where χ is the magnetic susceptibility, C is the paramagnetic Curie constant and Θ is the Curie- Weiss temperature. It can be observed from the figure that the curve passes through the origin indicating nanostructures are paramagnetic in nature, giving no evidence for antiferromagnetic coupling.
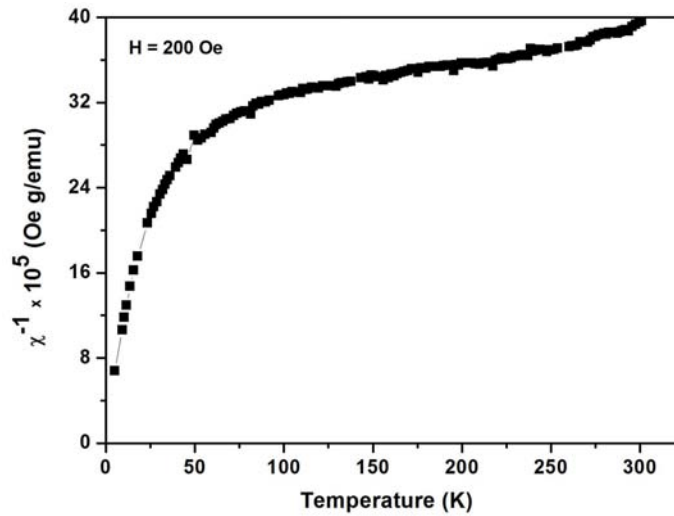
Figure 5.10: Temperature dependent inverse susceptibility of Co doped ZnO nanostructures synthesized from 0.01 M cobalt nitrate under a magnetic field of 200 Oe

5.2.3 Conclusion

Cobalt doped zinc oxide (ZnO) and undoped ZnO nanostructures were synthesized by low temperature hydrothermal method by varying the process parameters such as molarity of precursors and time of growth. The structural studies of these Co doped ZnO and undoped ZnO nanostructures were characterized by x-ray diffraction technique. SEM images show that width of the nanorods decreases with decrease in the duration of hydrothermal growth. Blue PL emission at 437 nm were observed from the ZnO nanostructures at an excitation wavelength of 350 nm which corresponds to Zn interstitial related defects. Three peaks observed at positions 1.89 eV, 2.03 eV, 2.19 eV in DRS spectrum confirms the presence of substitutional incorporation of Co^{2+} on the Zn site in the ZnO matrix. The spectrum also shows that the band gap of ZnO nanostructures is blue shifted from that of bulk ZnO powder due to quantum confinement effects. ICP AES studies confirm the incorporation of cobalt in the ZnO nanostructures. The g value obtained from the EPR measurements is comparable with theoretical values which confirm the Co^{2+} incorporation in ZnO matrix. The magnetic studies of Co doped ZnO nanostructures shows paramagnetic behaviour and is attributed to the absence of secondary phases.

5.3 Red luminescence from hydrothermally synthesized Eu doped ZnO nanoparticles under visible excitation

Phosphor which has high efficiency and low degradation is required for the development of lighting technology and for flat panel displays such as field

emission displays (FEDs) and plasma display panels (PDPs) [244, 245]. The use of oxide phosphors in place of conventional sulfide phosphors has been preferred for FED applications due to higher stability in high vacuum environment and less emission of contaminating gases [105].

High quality II-VI semiconductor nanocrystals and their luminescence properties have been studied recently both experimentally and theoretically [246–248]. The II-VI semiconductor nanomaterial are unique host materials for doping optically active impurities, and these semiconductor doped with luminescence centers exhibit efficient luminescence even at room temperature [101, 249].

In recent years, rare earth (RE) doped wide band gap semicoducting nanomaterials finds various applications such as thin-film electroluminescent (TFEL) devices [250], optoelectronic or cathodoluminescent devices [251]. RE-doped insulators are used in telecommunications, lasers and amplifiers [252], medical analysis and phosphors [244], etc.

CdSe and CdS are the most widely studied among the II-VI semiconductor nanoparticles [246–248, 253, 254]. However these materials contain toxic elements such as Cd and Se. Zinc oxide (ZnO) is a wide band gap (3.3 eV) *II-VI* compound semiconductor with large exciton binding energy (60 meV). ZnO is an environmentally friendly material and is one of the suitable candidates for practical use as a nanodevices. It has a stable wurtzite structure with lattice spacing a= 0.325 nm and c= 0.521 nm. Most of the ZnO: RE^{3+} crystals have been synthesized by traditional high temperature solid state reaction [250, 255] which is energy consuming and difficult to control the particle properties.

Rare-earth (RE) ions are better luminescent centers than the transition metal elements because their 4f intrashell transitions originate narrow and

intense emission lines. The synthesize of Eu doped ZnO nanoparticles by low temperature hydrothermal method and their photoluminescence emission characteristics were discussed in this chapter.

5.3.1   Experimental

The Eu doped ZnO nanoparticles were synthesized from the stock solutions of $Zn(CH_3COO)_2.2H_2O$ (0.1 M) prepared in 50 ml methanol under stirring. To this solution Eu_2O_3 varying from 0.005 gm to 0.03 gm was added. This leads to europium concentration variation from 1.2 at.% to 5.27 at.% in the ZnO nanoparticle. 25 ml of NaOH (0.3 M) solution prepared in methanol was mixed with the above solution under continuous stirring in order to get the pH of reactants between 8 to 11. These solutions was transferred into teflon lined sealed stainless steel autoclaves and maintained at 150^oC for 12 h under autogenous pressure. It was then allowed to cool naturally to room temperature. After the reaction was complete, the resulting white solid products were washed with methanol, filtered and then dried in air in a laboratory oven at 60^0C. The undoped ZnO nanoparticles were also synthesized in similar manner described above but without adding Eu_2O_3.

The synthesized samples were characterized for their structure by x-ray diffraction (Rigaku D max-C) with Cu K_α radiation (1.5418 Å). Transmission electron microscopy (TEM), selected area electron diffraction (SAED) and high resolution transmission electron microscopy (HRTEM) were performed with a JEOL JEM-3100F transmission electron microscope operating at 200 kV. The sample for TEM was prepared by placing a drop of the ZnO suspension in methanol onto a 200 mesh carbon coated copper grid. The grids were dried before recording the micrographs. The elemental composition of the Eu doped ZnO nanoparticles were determined using

energy dispersive x-ray spectroscopy (EDX). Room temperature photoluminescence (PL) of the samples was measured using the Horiba Jobin Yvon Fluoromax-3 spectrofluorimeter with Xe lamp as the excitation source.

5.3.2 Results and discussion

The x-ray diffraction pattern were recorded with Cu K_α radiation (1.5418 Å). The intensity data were collected over a 2θ range of $20\text{-}80^o$.
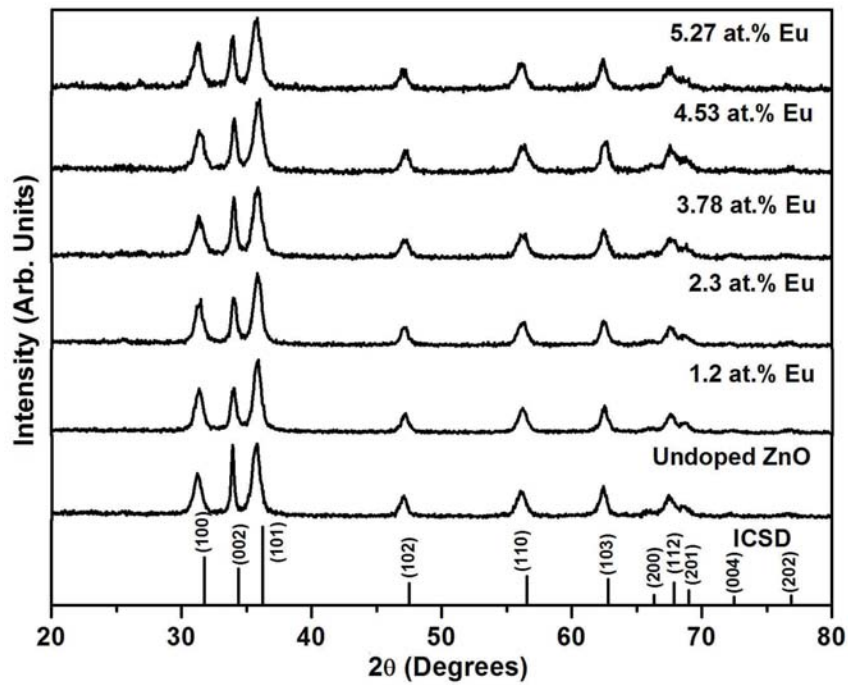
Figure 5.11: XRD pattern of undoped ZnO and Eu doped ZnO nanoparticles of varying Eu dopant concentration

All the peaks in the x-ray diffraction pattern (Figure 5.11) can be assigned to the typical wurtzite structure of ZnO [216]. There are no char-

acteristic peaks of Eu_2O_3 regardless of the Eu dopant concentration. Thus the wurtzite structure is not modified by the addition of Eu into the ZnO matrix. The average grain size (D) of the samples was estimated with the help of Scherrer equation using the diffraction intensity of (101) peak [217].

$$D = \frac{0.9\lambda}{\beta cos\theta} \tag{5.2}$$

Where λ is the wavelength (Cu K_{α}), β is the full width at half maximum (FWHM) of the ZnO (101) line and θ is the diffraction angle.

The broadening of the diffraction peaks is an indication that the synthesized materials are in nanometer regime. The grain size was found to be in the range of 8-12 nm depending on the growth condition. The lattice parameters calculated were also in agreement with the reported values.

EDX results shows that the elemental percentage of the Eu ions incorporated in the Eu doped ZnO nanoparticles are 1.2, 2.3, 4.53 and 5.27 at.% as 0.005, 0.01, 0.02 and 0.03 gm Eu_2O_3 were used in the precursor solution.

Figure 5.12(a) shows the TEM image and corresponding SAED pattern (inset of figure 5.12(a)) of 2.3 at.% Eu doped ZnO synthesized by hydrothermal method. TEM image confirms the formation of nanoparticles and it has an average size of 8 nm and they are spherical in shape. This result is consistent with what we had obtained from XRD analysis. From the diffraction rings of the SAED pattern, (002), (102) and (110) planes of ZnO were identified.

Figure 5.12(b) shows the TEM image and corresponding SAED pattern of 3.78 at.% Eu doped ZnO grown by hydrothermal method. TEM image confirms the size of the particles is in the nanoregime. These are not spherical in shape and it has a length of 20 nm and diameter of 7 nm. From

the diffraction rings in the SAED pattern, (002), (102) and (110) planes of ZnO were identified.
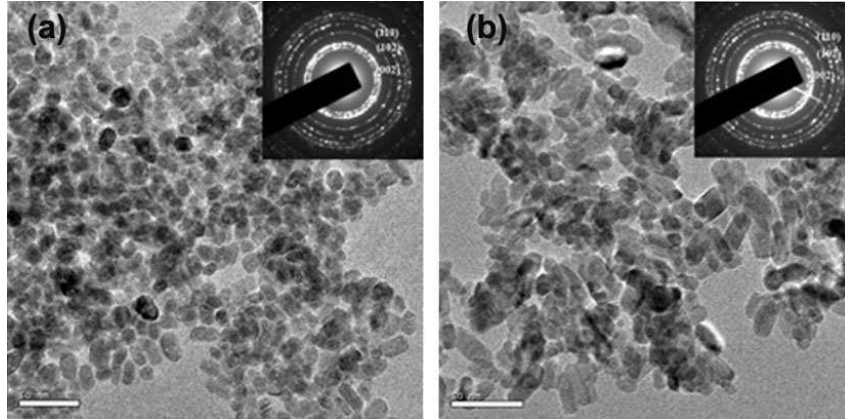
Figure 5.12: TEM image of Eu doped ZnO nanoparticles with (a) 1.2 at.% and (b) 3.78 at.% Eu dopant concentration. SAED pattern of the ZnO:Eu with (a) 1.2 at.% and (b) 3.78 at.% Eu dopant concentration are shown in the inset.

Figure 5.13 shows the photoluminescent emission spectra of Eu doped ZnO nanoparticles at an excitation wavelength (λ_{ex}) of 397 nm. The excitation energy almost coincides with the energy of $^7F_0 \rightarrow {}^5L_6$ transitions of Eu^{3+} ions, which is 3.147 eV [198]. Excitation at 397nm yields the characteristic emissions of Eu^{3+} corresponding to ^5D_j(j=0, 1) $\rightarrow {}^7F_j$ (j=0, 1, 2, 3 and 4). The direct excitation of Eu^{3+} enhances the PL due to Eu^{3+} ions. The emission at 596 nm originates from the magnetic- dipole allowed $^5D_0 \rightarrow {}^7F_1$ transition, indicating that Eu^{3+} ions occupy a site with inversion symmetry and 617 nm from electric- dipole allowed $^5D_0 \rightarrow {}^7F_2$transition, which results in a large transition probability in the crystal field with inversion antisymmetry. The intensity of emission corresponds to the $^5D_0 \rightarrow {}^7F_2$transition is stronger than that of $^5D_0 \rightarrow {}^7F_1$ transition. It is suggested

that the Eu^{3+} ions mainly take a site with inversion antisymmetry in the ZnO host. The emission at 701 nm is from $^5D_0 \rightarrow {}^7F_4$ transition and at 653 nm is from $^5D_0 \rightarrow {}^7F_3$ transition. The emission peaks at 583 nm corresponds to $^5D_0 \rightarrow {}^7F_0$ transition. The observation of forbidden $^5D_0 \rightarrow {}^7F_0$ transition indicates that some of the Eu ions are at low site symmetry. The emission at 543 nm is from $^5D_1 \rightarrow {}^7F_1$ transition.
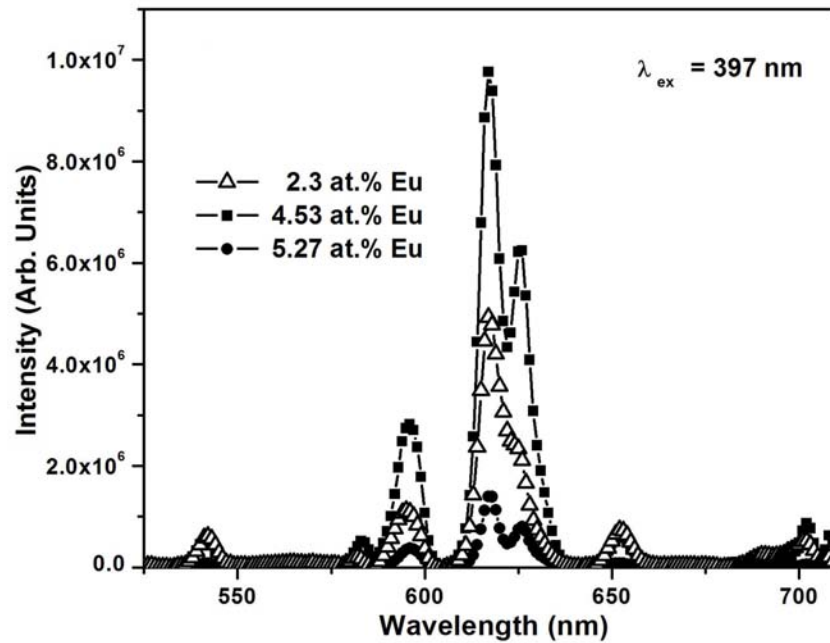
Figure 5.13: Room temperature photoluminescence emission spectra of Eu doped ZnO nanoparticles excited for various Eu dopant concentrations at an excitation wavelength of 397 nm

The luminescent intensity of Eu doped ZnO nanoparticles increases with increase in the Eu dopant concentration at first and then it decreases. When the activator concentration increases above a certain level, luminescence be-

gins to quench. Thus the emission intensity of $^5D_0 \rightarrow {}^7F_j$ (j=0-4) depends on Eu dopant concentration. In this case, the pairing or aggregation of activator atoms at high concentration may change a fraction of the activators into quenchers and induce the quenching effect. The migration of excitation by resonant energy transfer between the Eu^{3+} activators can sometimes be so efficient that it may carry the energy to a distant killer or to a quenching centre existing at the surface of the crystal.
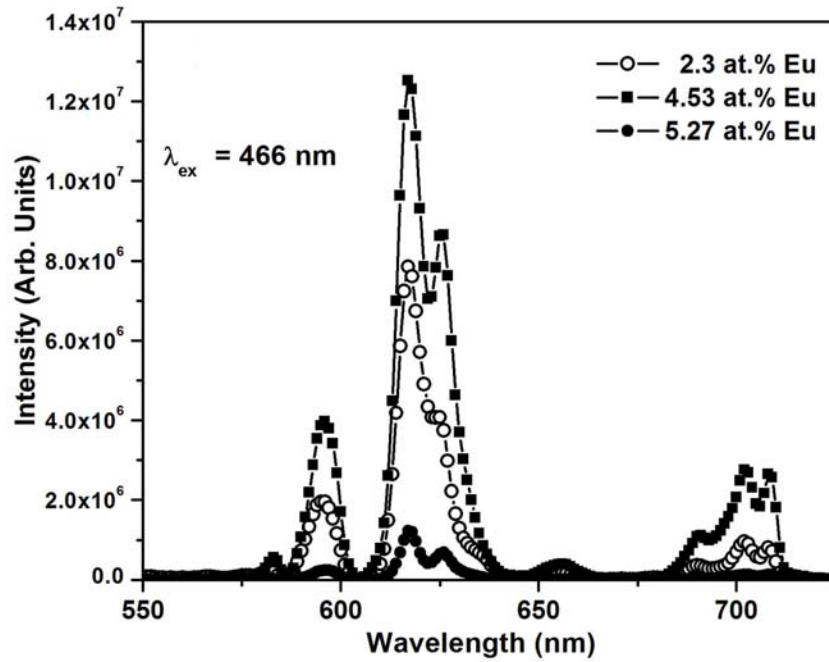
Figure 5.14: Room temperature photoluminescence emission spectra of Eu doped ZnO nanoparticles excited for various Eu dopant concentrations at an excitation wavelength of 466nm

Figure 5.14 shows the photoluminescent emission spectra of Eu doped

ZnO nanoparticles excited at 466 nm. The peaks at 583, 596, 617, 653 and 701 nm corresponding to the $^5D_0 \rightarrow {}^7F_j$ (j=0-4) transitions of Eu^{3+} ions which is dominated by the $^5D_0 \rightarrow {}^7F_2$ transition at 617 nm. In addition, the emission intensity increases with increasing Eu dopant concentration up to 4.53 at.% and then it decreases due to the concentration quenching.
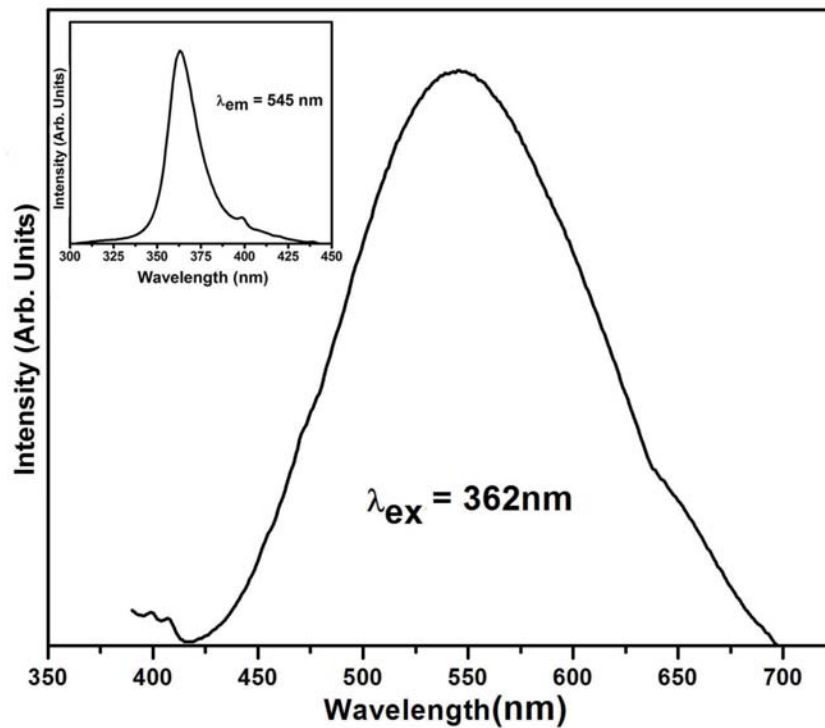
Figure 5.15: Room temperature photoluminescence spectra of ZnO nanoparticle excited at λ_{ex} = 362 nm. The inset shows the corresponding photoluminescent excitation spectra

Figure 5.15 shows the room temperature photoluminescence spectrum of the undoped ZnO nanoparticles excited at 362 nm. Green emission at

545 nm was observed from the hydrothermally synthesized ZnO nanoparticles. It can be attributed to the transition between singly charged oxygen vacancy and photo excited hole or Zn interstitial related defects [191, 224, 225]. The inset in the figure 5.15 shows the photoluminescent excitation spectra of the ZnO nanoparticles (λ_{em}= 545nm) which indicates that the excitation is at 362 nm. The excitation peak corresponds to the band to band transition which shows a blue shift in the band gap of ZnO nanoparticles due to quantum confinement effects.
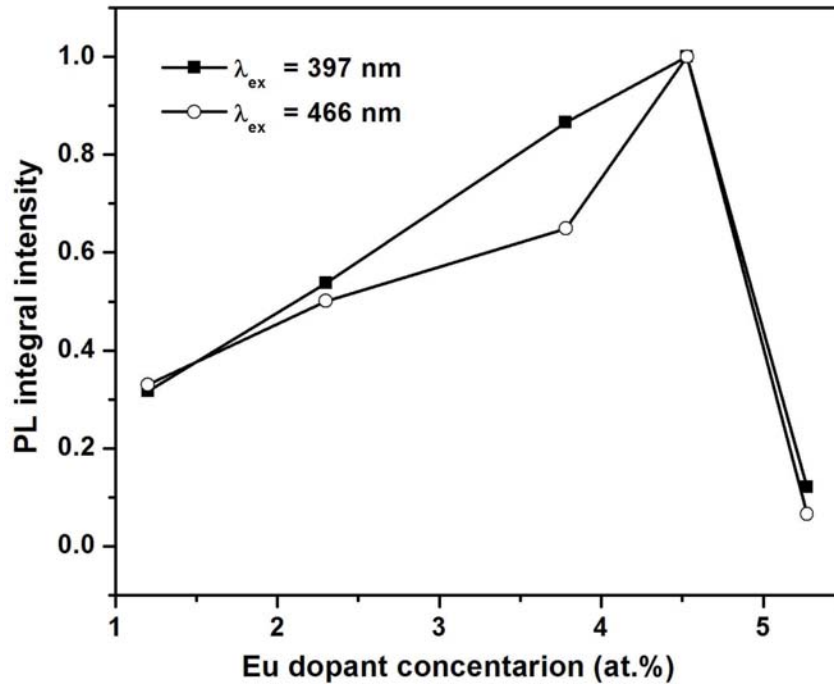
Figure 5.16: Variation of PL integral intensity with amount of Eu dopant concentration under 397 nm and 466 nm excitation

Figure 5.16 shows the variation of PL integral intensity, at an excitation

wavelength of 397 nm and 466 nm, as the Eu dopant concentration in ZnO increases from 1.2 at.% to 5.27 at.%. The PL integral intensity increases with increasing amount of Eu dopant concentration up to 4.53 at.% and then it decreases due to the concentration quenching.

When the nanoparticles are excited with wavelength of 325 nm, no intra- $4f^6$ Eu^{3+} related emission is observed. The disappearance of the red emission excited at 325 nm wavelength is probably related to the shielding effect due to the existence of the $Eu_{Zn}*$ level [256]. Thus 325 nm photon is not in resonance with any transitions of Eu^{3+} ions.
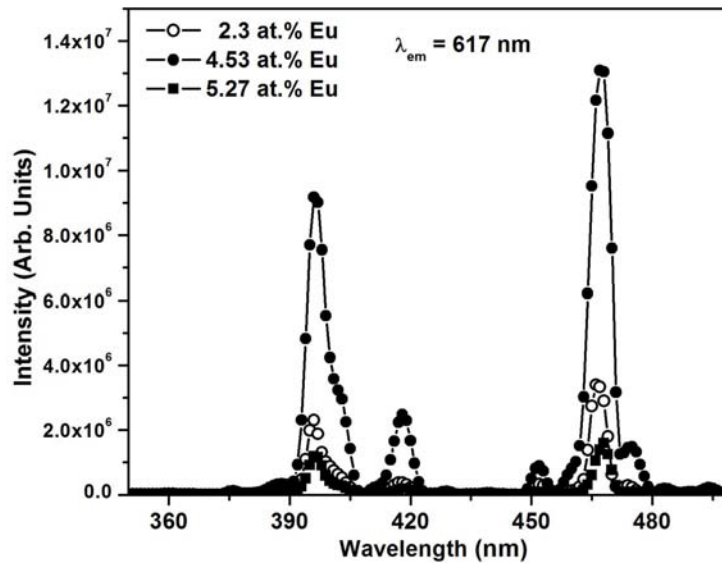
Figure 5.17: Room temperature photoluminescent excitation spectra of Eu doped ZnO nanoparticles (λ_{em} = 617 nm)

Figure 5.17 shows the photoluminescent excitation (PLE) spectra of the Eu doped ZnO nanoparticles (λ_{em}= 617nm) which indicates that the

excitation is at 397 and 466nm. The excitation peaks at 397 nm and 466 nm corresponds to the $^7F_0 \rightarrow {}^5L_6$ and $^7F_0 \rightarrow {}^5D_2$ transitions of Eu^{3+} ions. The peak at 418nm corresponds to the 4f-5d transition of Eu^{2+} ion [257]. It also shows that the PLE intensity increases with increase in the Eu dopant concentration up to 4.53 at.% and then it decreases. Figure 5.18 shows a schematic representation of the main energy levels identified in the studied samples [198].
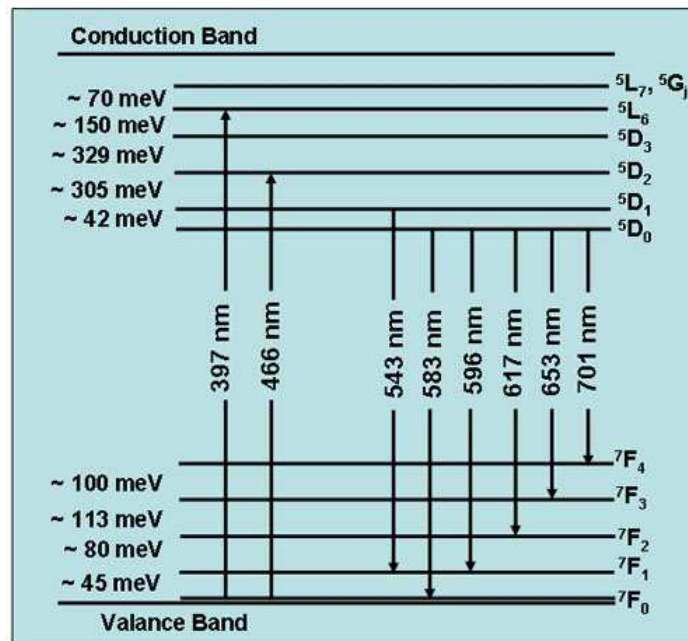
Figure 5.18: Simplified energy diagram of Eu^{3+}in Eu doped ZnO nanoparticles. The energies of absorption and emission lines are also shown

The CIE color coordinates measured from the photoluminescent emission of Eu doped ZnO nanoparticles by varying the Eu dopant concentration

are shown in the figure 5.19. For the case of the Eu doped ZnO nanoparticles with Eu dopant concentration of 1.2 at.%, 2.3 at.%, 4.53 at.% and 5.27 at.%, the CIE coordinates are (0.43, 0.54), (0.46, 0.52), (0.49, 0.49) and (0.47, 0.51) respectively and these show the colors in yellowish-orange and yellow region.
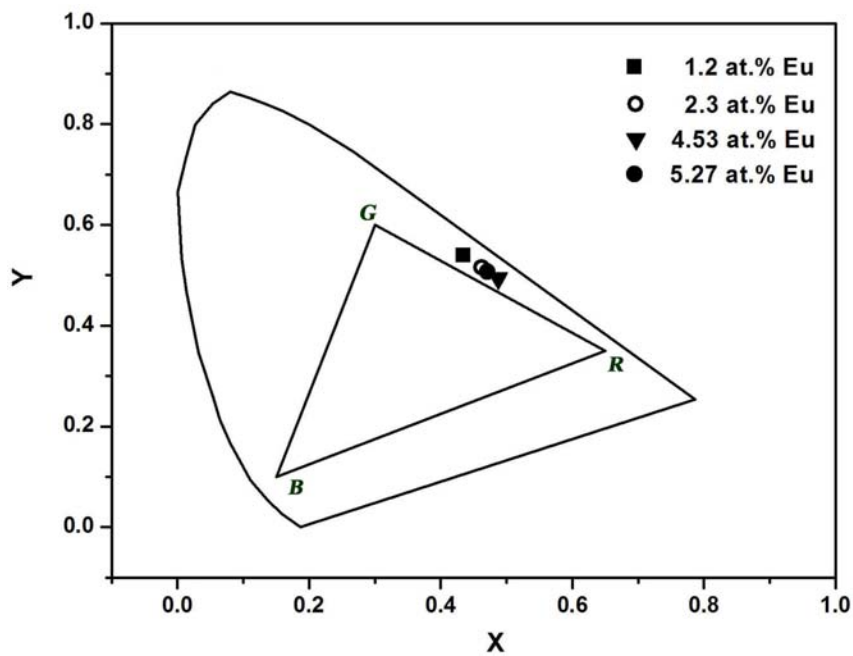
Figure 5.19: CIE diagram of Eu doped ZnO nanoparticles synthesized by varying the Eu dopant concentration (1.2 at.% to 5.27 at.%)

5.3.3   Conclusion

Europium doped ZnO nanoparticles were synthesized by hydrothermal method by varying the Eu dopant concentration. XRD and SAED results show these nanoparticles have wurtzite structure and the particle size distribu-

tions were studied from the TEM. The red PL emissions from the intra-4f transition of Eu^{3+} ions are observed under an excitation of 397 and 466 nm. Luminescence quenching is observed in the nanoparticles as the Eu dopant concentration increases. Incorporation of Eu in the nanoparticles was confirmed by the EDX studies. Thus Eu doped ZnO nanostructures can be used in UV to red converting applications.

Chapter 6

Synthesis of nanoparticles by liquid phase pulsed laser ablation

6.1 Introduction

In the last few decades, research interest in nanostructured materials has arised due to their unusual properties which are different from their bulk materials, such as their electronic, optical, magnetic and chemical properties. In recent years great efforts have been made on the synthesis of nanoparticle colloids because of their special properties and their promising application in various fields of research like drug delivery [258], imaging [259, 260], diagnostics [261, 262] and for nanocomposites with special optical, mechanical, or bioactive properties [263, 264].

Pulsed laser ablation (PLA) was first developed in the 1960s, shortly after the invention of the pulsed ruby laser. Since then, laser ablation in

a vacuum or dilute gas has been studied by many researchers. By using different target materials and background gases, and varying parameters such as the laser wavelength, fluence, and pulse duration, it is possible to produce a wide variety of thin films [265]. These include high temperature superconductors [266], metals, semiconductors, oxides, diamond-like carbon [267] and other ceramics [268].

Pulsed laser ablation also has appeared to be the most flexible and promising technique because of its ability to ablate almost all kinds of materials due the ultra-high energy density and control over the growth process by manipulating the process parameters like irradiation time, duration, energy density, wavelength, etc [269].

The introduction of pulsed laser ablation at the solid-liquid interface was first reported by Patil and co-workers in 1987, who used a pulsed laser to ablate a pure iron target in water to form iron oxides with metastable phases [270]. This method is known as liquid phase pulsed laser ablation (LP-PLA), in which a solid target is immersed in a liquid medium and the laser beam is focused through the liquid onto the target surface.This pioneering work opened new routes for materials processing based on the PLA of solids in various liquids. Since then, the LP-PLA method has been used to produce a wide range of novel materials, such as nanodiamond and related nanocrystals, metallic nanocrystals, nanocrystal alloys, and metal oxides. Formation of nanoclusters under laser ablation in liquid environment has been much less studied.

LP-PLA techniques has become a successful material fabrication technique, allowing versatile design through choosing suitable solid targets and confining liquids. Compared to the other conventional physical methods

such as pulsed laser ablation in vacuum, sputtering etc and chemical methods, LP-PLA technique has many advantages. It is a chemically simple and clean process. The final product is usually obtained without any byproducts and therefore no need for further purification. It requires only inexpensive equipment for controlling the ablation atmosphere and easy to control the parameters. It requires minimum amount of chemical species for synthesis compared to the conventional chemical process. The extreme confined conditions and induced high temperature and high pressure region in this techniques favours the formation of metastable phases. Thus nanostructures of metals and semiconductors can be easily grown by this technique.

Commercial colloids are usually derived from sol-gel or salt precipitation processes, for which a precursor, additive and surfactant system need to be designed for each type of nanoparticle. Suitable chemical precursors like metal acetates and carbonates are a requirement for every synthesis process in nano-chemistry. Oxidation of metal or hydroxylation of ceramic nanoparticles is often unavoidable, and unreacted precursors and additives tend to remain in the final colloidal product [271, 272]. Today, huge efforts are being made for an efficient purification of these impurities [272]. Despite advances in the field of wet chemistry, the possibilities of sol-gel processes, especially with regard to product diversity, have not been exploited sufficiently [273]. In addition, the products are often restricted to thermodynamically stable crystal structures, which complicates the generation of hard ceramics like alpha aluminium oxide and tetragonal zirconium dioxide. Nanoparticles from such hard materials cannot be gained by mechanical milling, as the required forces increase exponentially with smaller particle size. In addition, milling may introduce impurities from grinding media [274]. But LP-PLA technique enables the development and supply of

new nanomaterials with comparably little effort. Still, the yield is mostly restricted to about (0.01-0.1) μg min^{-1} [275], and there are knowledge deficits on the physical and chemical processes involved.

LP-PLA involves focusing a high power laser beam onto the surface of a solid target, which is submerged beneath a liquid. The interaction of the laser with the target causes the surface to vaporise in the form of an ablation plume, which contains species such as atoms, ions, and clusters, travelling with high kinetic energy. The species in the plume collide and react with molecules of the surrounding liquid, producing new compounds containing atoms from both the original target and the liquid. Due to the intensity of the laser and the nanosecond timescales, the instantaneous temperatures and pressures within the reaction volume can be extreme (many thousands of K at tens of GPa). Such high temperature, high pressure, and high density conditions results in the synthesis of novel materials which are not possible by other conventional techniques.

Melting of the solid is a necessary condition for the formation of nanoparticles under ablation in liquid environment. This is gained under sufficiently high laser fluence depending on the absorptivity of the material at the laser wavelength.

Formation of nanoparticles (NPs) using laser ablation of solids, either in gas or in vacuum, has been extensively explored during the last decade. Understanding the mechanisms of cluster formations is needed to control the process of pulsed laser ablation now widely used for the deposition of a large variety of compounds. LP-PLA can be seen as the extension of this concept. Therefore, the process of laser interaction with the target is similar for both laser ablation in a vacuum and ablation at the solid-liquid interface. Both produce plasma and create a strong confinement of

the emission species, resulting in an efficient electron-ion recombination. The difference is that the expansion of plasma occurs freely in vacuum in normal PLA, where as it is confined by a liquid layer in LP-PLA. The liquid delays the expansion of the plasma, leading to a high plasma pressure and temperature, which allows the formation of novel materials. Another advantage of LP-PLA is that both the solid target and the liquid are vaporized, so the product can contain atoms from the target material and the liquid. The generation of various NPs by LP-PLA is an alternative to the well-known chemical vapour deposition (CVD) method. Moreover, NPs produced by laser ablation of solid targets in a liquid environment are free of any counter-ions or surface-active substances [276]. This method combines the advantages of pulsed laser deposition (PLD) and those of chemical routes. As with the soft chemical routes, the product obtained is a stable colloidal dispersion of nanoparticles in a liquid medium but the ablation process allows the growth of materials with complex stoichiometries. Moreover, using pulsed laser ablation in a liquid medium gives access to materials which can only be synthesized at high pressure. Briefly, when a target is irradiated with fluences over 0.1 GWcm^{-2}, material is ejected and evaporated. According to Fabbro et al [277], a laser power density of several GWcm^{-2} ensures a maximum pressure of several GPa generated by shock waves.

The mechanisms involved in the nucleation and phase transition of nanocrystals upon LP-PLA are not well understood. A recent review by Yang [278] gives an understanding of some of the nucleation thermodynamics, the phase transition, and the growth kinetics of nanocrystals by laser ablation of liquids.

LP-PLA is very fast and far-from-equilibrium process, so that all metastable and stable phases forming at the initial, intermediate and final stages of the conversion could be reserved in the final products, especially, for any metastable intermediate phases [278]. In other words, the quenching times in LP-PLA are so short that the metastable phases which form during the intermediate stage of the conversion can be frozen in, and form the synthesized final products.

According to Barther and co-workers [279], at the very initial stage of interaction of the high energy laser with the interface between the solid and the liquid, species ejected from the solid target surface have a large initial kinetic energy. Due to the covering effect of the liquid, these ejected species form a dense region in the vicinity of the solid-liquid interface. This stage is similar to that which occurs in vacuum or low pressure gas, where the laser generates a plasma plume. In LP-PLA, since the plasma is confined in the liquid, it expands adiabatically at supersonic velocity creating a shock-wave in front of it. This shock-wave will induce an extra, instantaneous pressure as it passes through the liquid. This laser-induced pressure will result in the increase of temperature in the plasma [280, 281]. Therefore, compared with a PLA plasma formed in gas or vacuum, the plasma formed in LP-PLA is at higher pressure and higher density. Another effect of the localized high temperature is that a small amount of the surrounding liquid is vaporized to form bubbles within the liquid. As more material is vaporized, the bubbles expand, until, at a certain critical combination of temperature and pressure, they collapse [282]. It is believed that when the bubbles collapse, the nearby species are subjected to temperatures of thousands of Kelvin (K) and pressures of several gigapascals (GPa), and that these extreme conditions allow novel materials to be created [283].

LP-PLA has been used to produce nanoparticles of many different metal elements including titanium [284], silicon [285], cobalt [286], zinc [287], copper [288], silver [289] and gold [290]. This technique can also be used to prepare NPs of compound materials such as TiO_2 [291], TiC [292] and CoO [286] in water, and ZnSe and CdS in various solvents, including water [293]. The use of this method opens up the possibility of studying new materials at the nanoscale range and therefore to envision new applications.

Only very recently has LP-PLA gained intensive attention for its ability to form more complex, higher dimensional nanostructures, and instigated the study of the dynamical process among laser-solid-liquid interactions.

6.2 Synthesis of ZnO nanoparticles by liquid phase pulsed laser ablation

Zinc oxide (ZnO) is a wide band gap (3.37eV) promising semiconductor having large exciton binding energy (60 meV) at room temperature and has important applications in electroluminescent displays [294], optoelectronics [295, 296], sensors [297], lasers [122] etc. Because zinc is an important trace element for humans [206], ZnO is environment friendly and is suitable for in vivo bioimaging and cancer detection.

There have been reports on synthesis of ZnO nanoparticles by LP- PLA techniques from metal target [287, 298]. This chapter discusses the synthesis of highly luminescent, transparent, chemically pure and crystalline ZnO nanoparticles by LP- PLA technique from sintered ZnO mosaic target and Zn metal target without using any surfactant. The dependence of oxygen and nitrogen bubbling during ablation and pH of the medium on the properties of the ZnO nanoparticles were also investigated. The surfactant free

nanoparticles were grown by LP-PLA in acidic and basic medium. The surface charge of the nanoparticles provided the repulsive force between nanoparticles which suppressed the growth through coagulation.

6.2.1   Experimental

A ZnO (99.99%) mosaic target sintered at 1000^0C for 5 h was used for the synthesis of ZnO nanoparticles. The ZnO target immersed in 15 mL of the liquid media having different pH was ablated at room temperature by third harmonic of Nd: YAG laser (355 nm, repetition frequency of 10 Hz, pulse duration of 9 ns). The experimental arrangement is shown in figure 6.1. The laser beam was focused using a lens and the ablation was done at a laser fluence of 15 mJ/ pulse. The spot size of the laser beam is about 1 mm. The duration of ablation was 1 h in all the media. This simple room temperature method produced a highly transparent ZnO nanoparticles well dispersed in the liquid media.

Zinc nanoparticles were produced by pulsed laser ablation of a piece of zinc granules in water. Zn granules in 15 mL water was ablated at room temperature using third harmonic of Nd: YAG laser (355 nm, repetition frequency of 10 Hz, pulse duration of 9 ns). During the ablation, oxygen was bubbled in the water media and the ablation was carried out at different laser fluence and different time duration. This results in the formation of highly transparent colloidal solution of Zn nanoparticles well dispersed in water.

The formation of ZnO and Zn nanoparticles was confirmed by transmission electron microcopy (JEOL, TEM) operating at an accelerating voltage of 200 kV. The sample for TEM was prepared by placing a drop of nanoparticle colloidal solution onto a standard carbon coated copper grid.

The grids were dried before recording the micrographs. Photoluminescence (PL) spectra were recorded using Jobin Yvon Fluoromax-3 spectrofluorimeter equipped with 150 W xenon lamp.
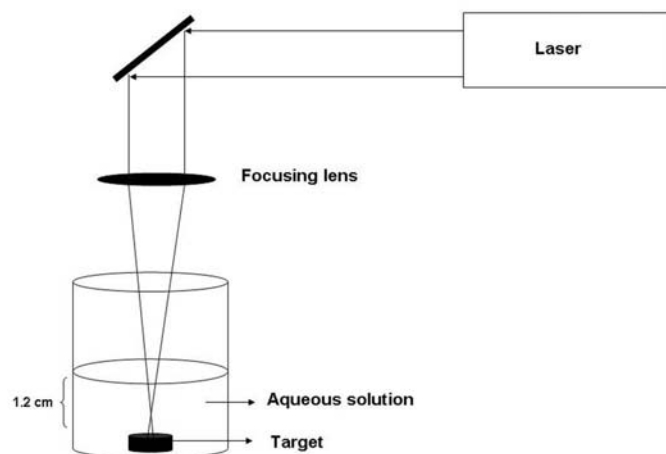
Figure 6.1: Experimental setup for the LP-PLA technique

6.2.2 Results and discussion

Transmission electron microscopic (TEM) studies confirm the resulting product after laser ablation in different media consisted of particles in the nanoregime. The selective area electron diffraction (SAED) pattern shows concentric rings corresponding to the hexagonal ZnO. This clearly shows the growth of crystalline ZnO nanoparticles. From these studies, the formation of other species like $Zn(OH)_2$ or ZnO/Zn core shell structure is not found. Because the ejected molten material from the target normally reacts with medium only at the outer surface [299], the ejected plasma readily cools, thereby forming ZnO itself. Because there are many surface oxygen

deficiencies, these nanoparticles will be charged. The ZnO nanoparticles grown by LP-PLA in pure water is usually charged because the isoelectronic points of ZnO ($\sim$9.3) is well above the pH 7.0 of pure water [300]. This surface charge provides a shield, preventing further agglomeration and forming self stabilized particles even in the absence of surfactant.

The preliminary studies carried out in this laboratory [35] shows that higher laser fluence results in bigger size and wide size distribution. The larger duration of LP-PLA at lower fluence does not increase the size of the nanoparticles but increase the particle density.

The size of the particle is found to increase when the experiment is done with oxygen bubbling into the water during laser ablation of ZnO targets while size remains the same as that grown in pure water when ZnO nanoparticles were grown in nitrogen atmosphere. Figure 6.2(a) and (b) shows the TEM images of the ZnO nanoparticles prepared in oxygen atmosphere and nitrogen atmosphere. The TEM image of nanoparticles grown in nitrogen atmosphere keeping the other parameters of the experiment the same has same size as those grown in neutral demonized water (figure 6.2(b) and 6.2(c)). The oxygen bubbling during the ablation increases the amount of dissolved oxygen and promotes the growth of ZnO. This leads to bigger ZnO nanoparticles, where as nitrogen bubbling through the solution does not provide any extra oxygen other than the oxygen in the plasma produced by the laser interaction with the ZnO target. Thus the size of the particle is same as those obtained by LP-PLA in pure water.
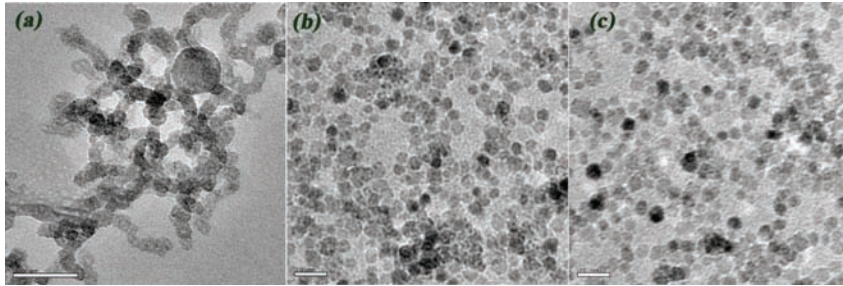
Figure 6.2: TEM image of the ZnO NPs prepared in (a) oxygen atmosphere, (b)nitrogen atmosphere and (c)in water

The growth of ZnO nanoparticles by LP-PLA can be modeled as follows. The plasma consisting of ionic and neutral species of Zn and oxygen [301] along with water vapor is produced at the solid-liquid interface on interaction between the laser beam and the ZnO target. Due to the high intensity of the laser beam in the nano second scales, high temperature (10^4-10^5K) and pressure of few GPa [302] in the volume is produced. The adiabatic expansion of the plasma leads to formation of ZnO. The ZnO thus formed interact with the solvent water forming a thin layer of $Zn(OH)_2$ since ZnO is extremely sensitive to H_2O environment [303]. Thus the ZnO nanoparticles prepared by LP-PLA may have a thin passivation layer of $Zn(OH)_2$. The oxygen bubbling during the ablation increases the amount of dissolved oxygen and promotes the growth of ZnO. This leads to bigger ZnO nanoparticles, where as nitrogen bubbling through the solution does not provide any extra oxygen other than the oxygen in the plasma produced by the laser interaction with the ZnO target. Thus the size of the particle is same as those obtained by LP-PLA in pure water. The ZnO nanoparticles grown by LP-PLA in the acidic medium pH=5 shows relatively bigger size in comparison with those grown in pure water under identical experimental

conditions. The very thin passivation layer of $Zn(OH)_2$ during the cooling of laser plasma interacting with the liquid medium may be slower owing to higher dissolution of hydroxide in acidic medium. Hence this favours the growth of bigger ZnO nanoparticles. Where as the ablation in alkali medium favours growth of $Zn(OH)_2$ by providing hydroxyl group and hence result in smaller nanoparticles.
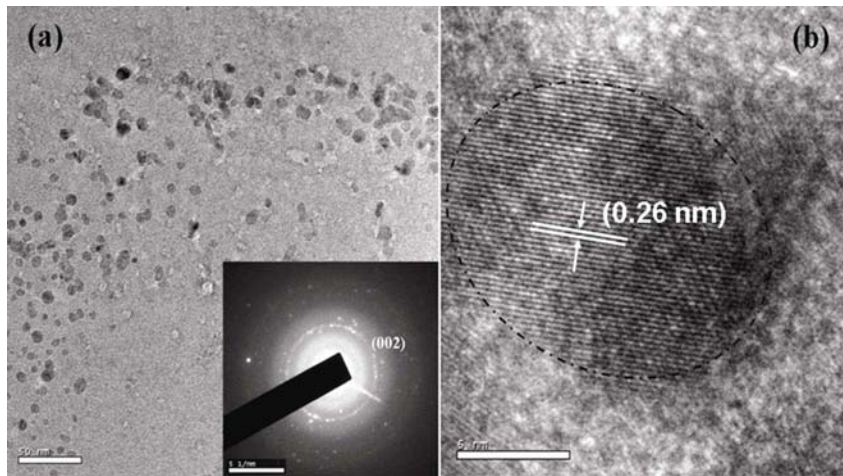
Figure 6.3: (a) TEM image and (b) HRTEM image of ZnO NPs synthesized in acid media by LP-PLA method. Inset of (a) shows the corresponding SAED pattern

Figure 6.3(a) shows TEM and figure 6.3(b) is the high resolution transmission electron microscopic (HRTEM) image. The SAED pattern of the ZnO NPs prepared in acid media (pH∼5) keeping all other experimental parameters the same shows the ring pattern corresponding to the (002) plane of ZnO. The particles have an elliptical shape with 15 nm size along the elongated region (semi major axis) and 11 nm along the compressed region (semi minor axis) is observed from the HRTEM image. From the

diffraction rings in the SAED pattern, (002) plane of the wurtzite ZnO was identified.
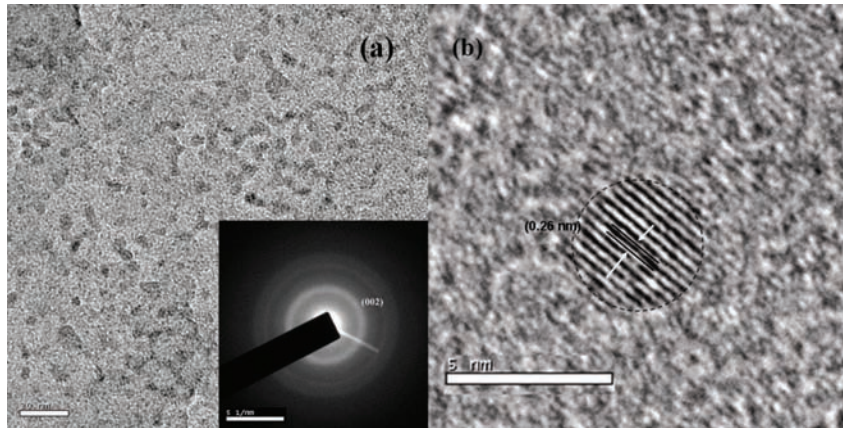
Figure 6.4: (a) TEM image and (b) HRTEM image of ZnO NPs synthesized in basic media by LP-PLA method. Inset of (a) shows the corresponding SAED pattern

Figure 6.4(a) shows the TEM and the SAED pattern (inset) of ZnO nanoparticles prepared by pulsed laser ablation in basic media (pH∼9). Spherical particles were observed in the HRTEM image (Figure 6.4(b)) having a size about 4 nm. The (002) plane of wurtzite ZnO is observed in the SAED pattern. This confirms the formation of crystalline ZnO nanoparticles by pulsed laser ablation in liquid.

The thermodynamic conditions created by the laser ablation plume in the liquid are localized to a nano meter scale which is not much influenced by the pH of the solution. The increase of laser energy for the ablation results in increase of size of the nanoparticles due to ablation of more material. The hydroxide passivation layer formation is much influenced by the

pH of the aqueous solution which may affect the growth and size of the particles. All the particles grown in acidic, alkali and neutral medium are well dispersed and no agglomeration of the particles are observed as in the case of ablation of zinc metal targets in aqueous solution [304]. In the present study the particles grown with oxygen bubbling during LP-PLA leads to the formation of bigger particles and there by causing agglomeration. This suggests that surface charge of ZnO nanoparticles arise mainly from oxygen deficiency and pH of the medium has less pronounced effect.
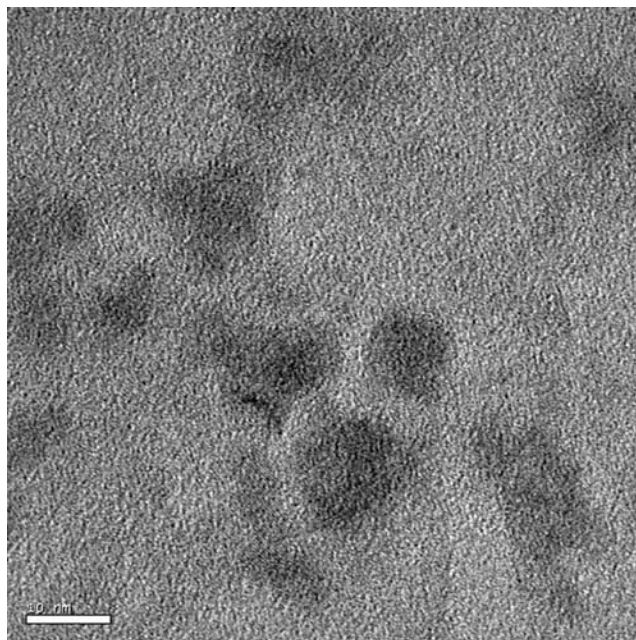
Figure 6.5: TEM image of Zn nanoparticles synthesized by LP-PLA method

TEM image of the Zn nanoparticles synthesized by liquid phase pulsed laser ablation of Zn target with oxygen bubbling is shown in the figure

6.5. These nanoparticles have an average size about 8 nm. The inductively coupled atomic emission spectroscopic (ICP-AES) studies confirms the presence of Zn in the colloidal solution and the Zn content increases as the laser fluence and time of ablation increases. This may be due to the increased particle size and number density. The Zn content in the colloidal solution increases as the pH of the medium changes from basic to acidic.
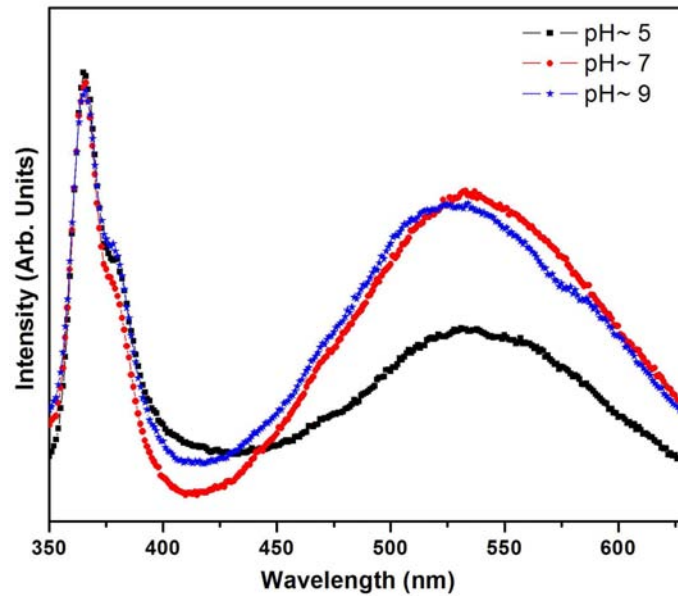
Figure 6.6: Room temperature PL emission of ZnO nanoparticles synthesized by LP-PLA technique in basic, neutral and acidic medium

The room temperature photoluminescence measurements of these nanoparticles were carried out at an excitation wavelength of 325 nm. PL studies of ZnO nanoparticles synthesized in basic, neutral and acidic medium shows a emission at 379 nm which corresponds to the band to band transition of ZnO (Figure 6.6). In addition to the peak corresponding to band edge,

Raman peak of water and broad peak centered at 540 nm were observed in the PL spectra of ZnO nanoparticles synthesized by LP-PLA technique. This luminescence emission at 540 nm originates from the native oxygen defects of the prepared ZnO nanoparticles [35]. This emission at 540 nm corresponds to the transition between the photo excited holes and singly ionized oxygen vacancy.
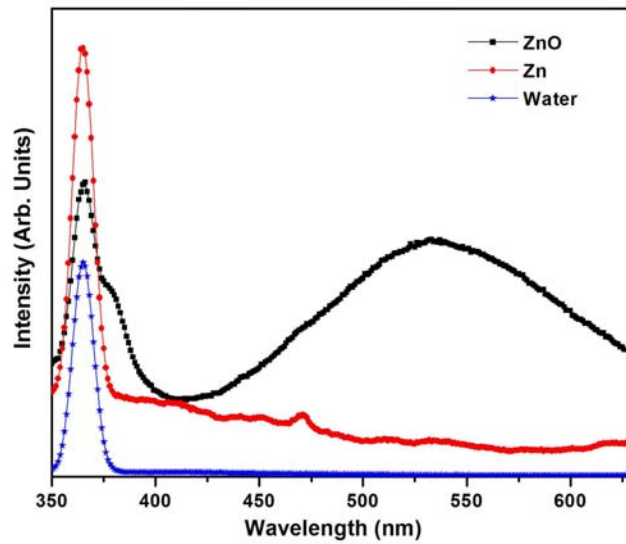
Figure 6.7: Room temperature PL emission spectra of ZnO and Zn nanoparticles synthesized by LP-PLA technique

Room temperature PL emission of water, ZnO and Zn nanoparticles synthesized by LP-PLA of ZnO and Zn targets at 15mJ/pulse for 1 h were shown in the figure 6.7. It shows that only ZnO nanoparticles have PL emission at 379 nm and 540 nm in addition to the Raman peak of water. The PL spectra of Zn nanoparticles in water contains only the Raman peak of water.

6.2.3 Conclusion

Highly transparent, luminescent, bio-compatible ZnO nanoparticles were prepared in basic, neutral and acidic medium using LP-PLA technique without using any surfactant. Transmission electron microscopic study confirms the formation of crystalline ZnO and Zn nanoparticles. The size of the ZnO nanoparticles increases when oxygen is bubbled, where as it remains same when nitrogen is bubbled during the LP-PLA. The size of the ZnO nanoparticles is found to be smaller when prepared in basic medium and larger when prepared in acidic medium compared to those synthesized in pure water. The room temperature PL emission studies of ZnO nanoparticles shows peaks corresponding to band edge at 379 nm and yellow emission due to oxygen native defects at 540 nm in addition to the Raman peak of water. PL spectra of Zn nanoparticles shows only the Raman peak of water.

6.3 Liquid phase pulsed laser ablation of ZnS and ZnS:Mn nanoparticles

Synthesis of nanoparticles has been the focus of an ever increasing number of researchers worldwide, mainly due to their unique optical and electronic properties [122, 305], which make them ideal for a wide spectrum of applications ranging from displays and lasers [306, 307] to invivo biological imaging. A variety of preparation methods to produce nanoparticles, such as magnetic liquids [308], metals [309, 310], metal-polymer nanocomposites [311], semiconductors [312] and colloidal systems [313] have been reported. Over the past decade liquid-phase pulsed laser ablation (LP-PLA) technique has aroused immense interest [314, 315]. LP-PLA involves the firing

of laser pulses on to the target surface through the liquids transparent to incident laser wavelength. The ablation plume interacts with the surrounding liquid media, creating cavitation bubbles that, upon their collapse, give rise to extremely high pressure and temperature. These conditions are, however, localized and exist across the nanometer scale. LP-PLA has proven to be an effective method for preparation of many nanostructured materials, including nanocrystalline diamond, cubic boron nitride, and nanometer-sized particles of Ti, Ag, Au and TiC. Zinc sulfide is a wide band gap (E_g = 3.6 eV at 300 K) semiconductor, which is considered important for applications such as ultraviolet-light-emitting diodes, electroluminescent devices, flat-panel displays, sensors and injection lasers [316, 317]. Under ambient conditions, ZnS has two types of polymorphs: zinc blende (cubic) and wurtzite (hexagonal). The cubic ZnS is stable at room temperature, whereas the hexagonal ZnS is stable at temperatures higher than 1020^0C. When doped with some metal cations (including transition metal ions and rare-earth elements), ZnS is an excellent luminescent phosphor exhibiting photoluminescence (PL), electroluminescence (EL), thermoluminescence and triboluminescence [318–320].

Among these elements, Mn doping in ZnS attracts a great deal of interest since Mn doping can not only enhance its optical transition efficiency, but can also induce the material to exhibit interesting optical properties [321, 322] which is obviously an effective way to enhance the luminescent properties of ZnS for practical application.

Efficient phosphors for lighting applications, flat panel displays, target identitification etc have always been a goal for researchers. The particle size of conventional phosphors are in micrometer scale, hence light scattering at grain boundaries is strong and it decreases the light output. Nanophosphors

can be prepared from tens to hundreds of nanometers that are smaller than the visible light wavelength and it will reduce the scattering, thereby enhancing the luminescence efficiency. Manzoor et al [104] reported the growth of Cu^+-Al^{3+} and Cu^+-Al^{3+}-Mn^{2+} doped ZnS nanoparticles by wet chemical method for electroluminescent applications. The high fluorescent efficiency and dispersion in water makes ZnS:Mn nanoparticles an ideal candidate for biological labelling. Since ZnS is an environment friendly material; it will eliminate potential toxicology problems. The growth of doped systems of II- VI semiconductor by LP-PLA is not yet reported to our knowledge. In the present study the growth, structural and luminescent characteristics of undoped and Mn doped ZnS nanoparticles were discussed.

6.3.1   Experimental

Target Preparation

ZnS target was prepared from commercially available ZnS (99.99%, Alfa Aesar) powder, weighed to an accuracy of 0.001 mg, hand mixed thoroughly in methanol medium using an agate mortar and pestle and allowed to dry in an oven. The dried mixture was then pressed into a 4 mm thick disk of diameter 13 mm by using a press applying a force of 3 tons. The pellet is placed in an alumina boat and introduced into the hot temperature zone of a horizontal tube furnace equipped with a proportional integral differential (PID) controller. The sintering was performed at 550^0C for 6 h in H_2S atmosphere. The temperature was raised slowly to completely remove moisture from the target. Moisture, if trapped inside the target, leads to cracking during firing. Normally, the outer part of a target heats up faster than the inner part. If the temperature were increased too quickly from

room temperature to the high processing temperature, the outer part of the target would become dense before the moisture in the inner part escapes.

A ZnS:Mn target with 2% Mn was synthesized in the laboratory by high temperature solid state reaction between ZnS (99.99%, Alfa Aesar) and MnO (99.99%, Alfa Aesar). ZnS:Mn target of 4 mm thick and diameter 13 mm were obtained after sintering the pressed ZnS:Mn pellet at 550^0C for 6 h in H_2S atmosphere.

Liquid phase pulsed laser ablation (LP-PLA)

The sintered ZnS and ZnS:Mn targets were used for the preparation of nanoparticles by liquid phase ablation. These targets, immersed in 15 mL of distilled water, was ablated at room temperature by the fourth harmonics (266nm) of Nd:YAG laser with repetition frequency of 10 Hz and pulse duration of 7 ns. The experimental arrangement is shown in the figure 6.1. The spot size of the laser beam was 2 mm after focusing by a lens of focal length 20 cm which is placed above the target, and the ablation was done at laser fluences of 20 and 25 mJ/pulse. The duration of laser ablation was 1, 2 and 3 h. This simple technique produced doped and undoped ZnS nanoparticles at room-temperature, well dispersed in liquid media.

The synthesized targets were characterized for their structure by x-ray diffraction (Rigaku D max-C) with Cu K_α radiation. The particle size, distribution, and crystallinity of ZnS nanoparticles were investigated by transmission electron microcopy (JEOL, TEM) operating at an accelerating voltage of 200 kV. The sample for TEM was prepared by placing a drop of the ZnS nanoparticle colloidal solution onto a standard carbon coated copper grid. The grids were dried before recording the micrographs. The absorption spectra of the nanoparticle colloidal solution were measured by

JASCO V-570 spectrophotometer. Photoluminescence (PL) spectra were recorded using Jobin Yvon Fluoromax-3 spectrofluorimeter equipped with 150 W Xenon lamp.

6.3.2 Results and discussion

The crystalline structure of the target was analyzed by x-ray diffraction (XRD) with Cu K_α radiation (wavelength =1.5418 Å). The XRD pattern of undoped and doped ZnS pellet is shown in figure 6.8.
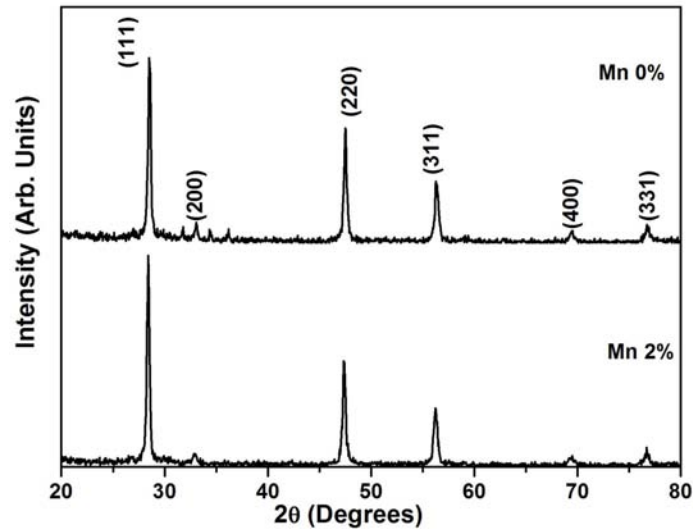
Figure 6.8: The XRD pattern of ZnS:Mn target synthesized by solid state reaction

The XRD pattern shows the cubic structure of ZnS:Mn (0 and 2%) targets. It can be seen that the Mn incorporation has not changed the structure of ZnS. The lattice constant of pure ZnS is 5.345 and that of ZnS:Mn is 5.438. The Mn^{2+} ions may have replaced the Zn^{2+} considering

the similar ionic radii of Zn (74pm) and Mn (67pm) in the ZnS:Mn lattice
with out any structural change.

The formation of nanoparticles of undoped ZnS was confirmed by trans-
mission electron microscopy (TEM). TEM analysis revealed that the result-
ing product after laser ablation for 1 h with energy of 25 mJ/pulse in water
is spherical in shape and particles are in the nano regime, as shown in fig-
ure 6.9. From TEM analysis, the formation of other molecules or core shell
structure was not observed.
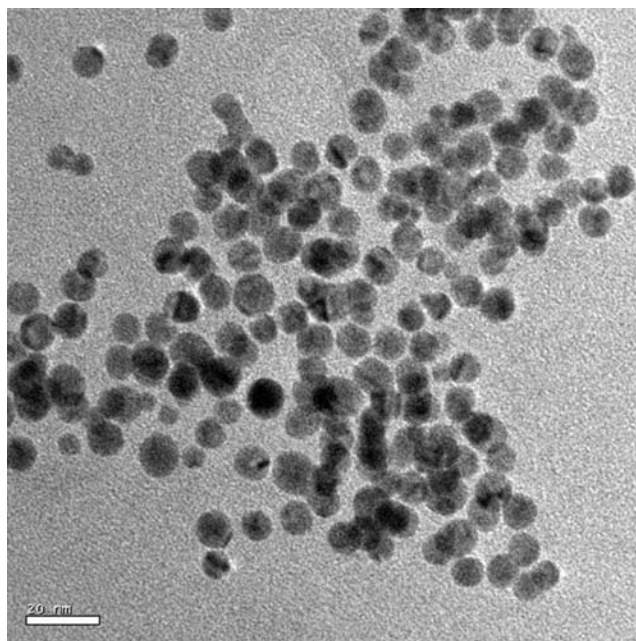
Figure 6.9: The TEM image of ZnS nanoparticles in liquid medium
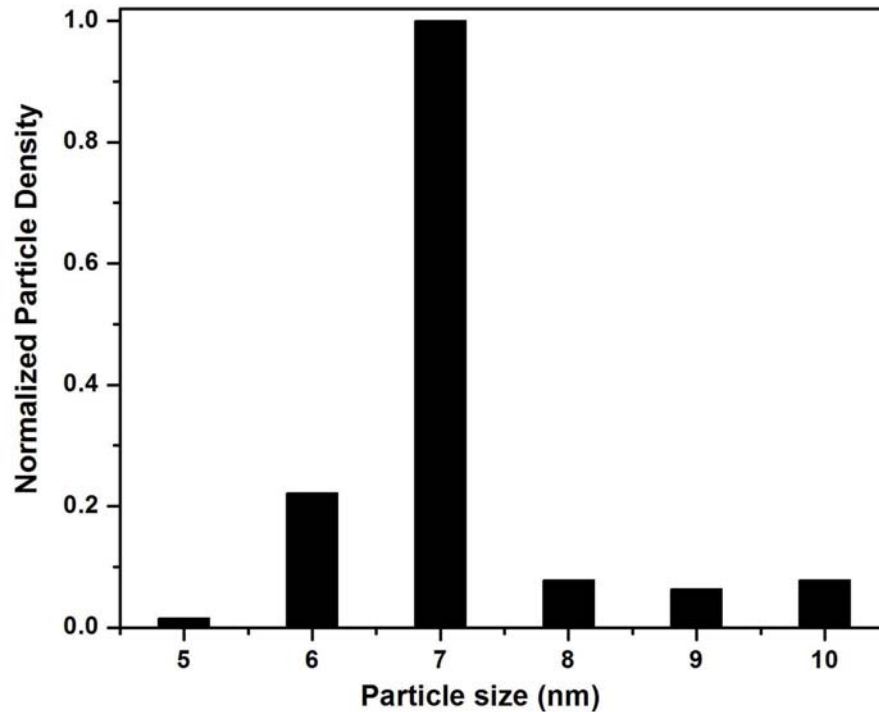
Figure 6.10: The particle size distribution of ZnS nanoparticles at laser fluence 25mJ/pulse ablated for 1 h

Statistical size analysis (figure 6.10) shows almost uniform particle-size distribution with a particle size of 7 nm for ZnS nanoparticles grown at laser fluence 25mJ/pulse ablated for 1 h.

Figure 6.11 shows the high-resolution TEM (HRTEM) images of ZnS nanoparticles showing parellel lines of atoms. The interplanar spacing of ZnS as seen from the figure is 0.26 nm which corresponds to (200) plane.
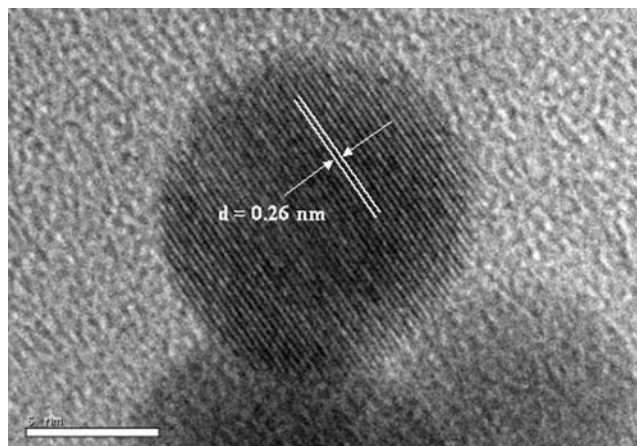
Figure 6.11: The high-resolution TEM (HRTEM) images of ZnS nanoparticles
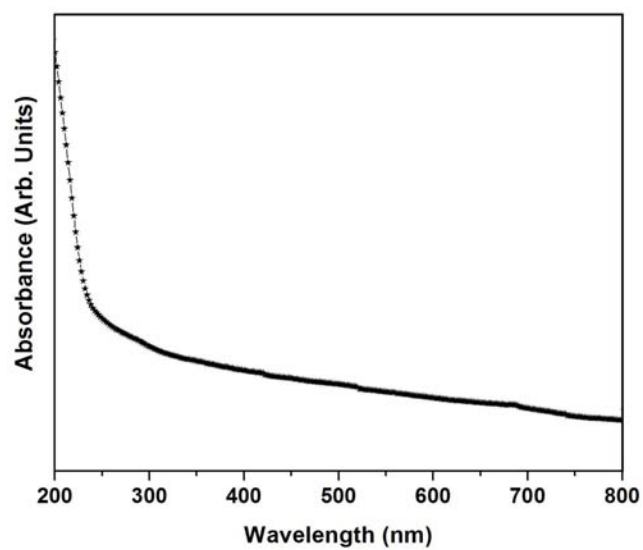
Figure 6.12: UV-visible spectra of ZnS nanoparticles in aqueous medium ablated at 20mJ/pulse laser fluence for a duration of 2 h

UV-Vis-NIR absorption spectra of the ZnS nanoparticles in water were measured over the wavelength range of 200-800 nm. Figure 6.12 shows the absorption spectra of ZnS nanoparticles in aqueous medium ablated at 20 mJ/pulse laser fluence for a duration of 2 h. The absorption edge is around 300 nm which correspondence to band gap energy of about 4 eV. This increase in the band gap compared with that of the bulk value (3.7 eV) is due to quantum confinement effects.
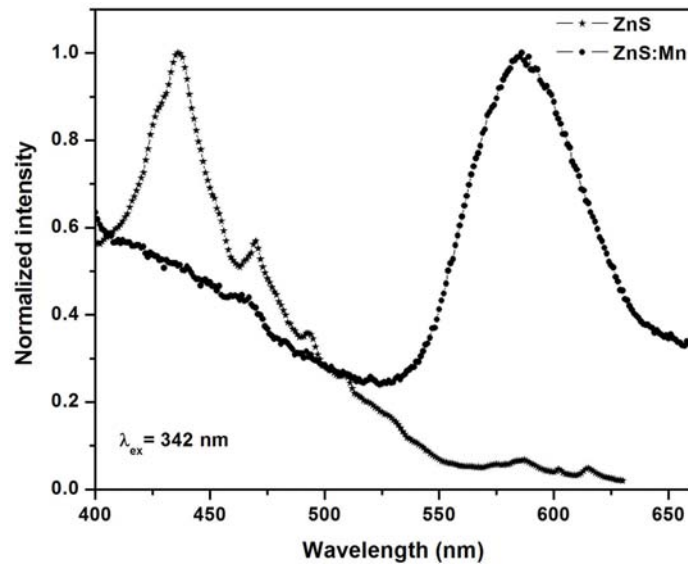
Figure 6.13: Room temperature PL emission spectra (λ_{ex}= 342 nm) of ZnS and ZnS:Mn nanoparticles ablated at 20mJ/pulse for 3 h

Room temperature photoluminescence emission (PL) and excitation spectra (PLE) of ZnS and Mn doped ZnS nanoparticles were studied for its luminescent applications. Figure 6.13 shows the PL emission spectra (λ_{ex}= 342 nm) of ZnS and Mn doped ZnS nanoparticles ablated at 20mJ/pulse

for 3 h. The emission spectra of ZnS nanoparticles show a peak at 436 nm. The emission at 436 nm can be attributed to the sulfur vacancy. This agrees well with the peak values reported by Becker and Bard [323].

The ZnS:Mn nanoparticles showed yellow emission at 585 nm. The emission at 585nm can be attributed to the radiative transition between $^4T_1$ and $^6A_1$ levels within the $3d^5$ orbital of Mn^{2+}, indicating the doping effect of Mn^{2+} in the ZnS nanostructures [324]. The emission corresponding to sulfur vacancy is absent in the Mn doped ZnS nanoparticles.

Mn^{2+} ions occupy Zn^{2+} lattice sites in the ZnS host lattice. In the PL process, an electron from the ZnS valence band is excited across the band gap and the photoexcited electron subsequently decays by a normal recombination process to some surface defects or defect states. Now on Mn doping, it occupies the tetrahedral cationic site with T_d symmetry and the electron may be captured by the Mn^{2+} ion in the $^4T_1$ level, from which it decays radiatively to the $^6A_1$ level. Mn doping actually reduces the nonradiative recombination and radiative transition takes place between Mn $^4T_1$ and $^6A_1$ levels [320].

The room temperature PLE spectra of ZnS:Mn monitored at 585 nm is shown in figure 6.14. The figure clearly shows the excitation wavelength at 342 nm. Inset of figure 6.14 shows the schematic representation of the main energy levels identified in the studied samples.
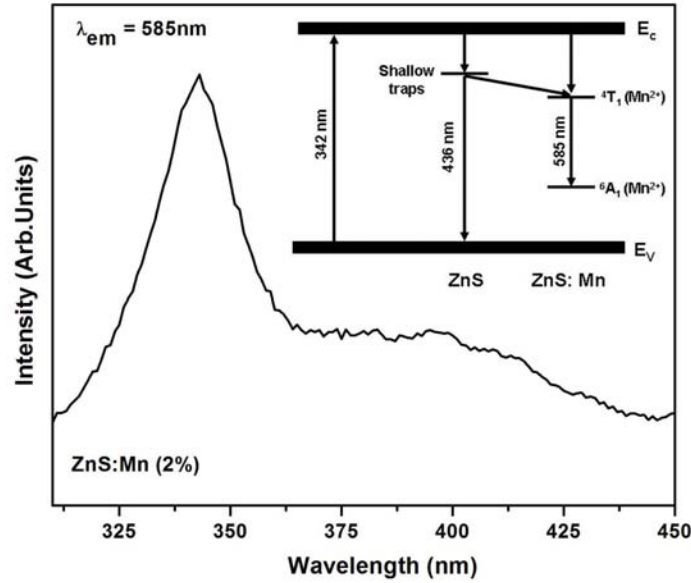
Figure 6.14: Room temperature PLE spectra of ZnS:Mn nanoparticles. Inset shows simplified energy diagram of ZnS and Mn doped ZnS nanoparticles. The energies of absorption and emission lines are also shown

Color characterization of a spectral distribution is carried out to gauge the quality of its chromaticity. This is accomplished using color coordinates [171]. In 1931, the Commission Internationale de l'Eclairage (CIE) established an international standard for quantifying color known as CIE color coordinates. The chromaticity coordinates map all the visible colors with respect to hue and saturation on a two-dimensional chromaticity diagram. The CIE coordinates are obtained from the three CIE tristimulus values, X, Y and Z. These tristimulus values are computed by integrating the product of the spectrum of the light source, $P(\lambda)$, and standard observer functions called the CIE color matching functions, $x_\lambda(\lambda)$, $y_\lambda(\lambda)$ and $z_\lambda(\lambda)$ over the

entire visible spectrum.

The CIE color coordinates measured from the photoluminescent emission of ZnS and Mn doped sample was calculated by above-mentioned method and it was (0.17, 0.12) and (0.54, 0.45) respectively. These coordinates can be represented inside a gamut drawn from the standard x, y values (Figure 6.15). This clearly indicates the purity of the yellow color of the Mn doped ZnS while the undoped sample shows blue emission.
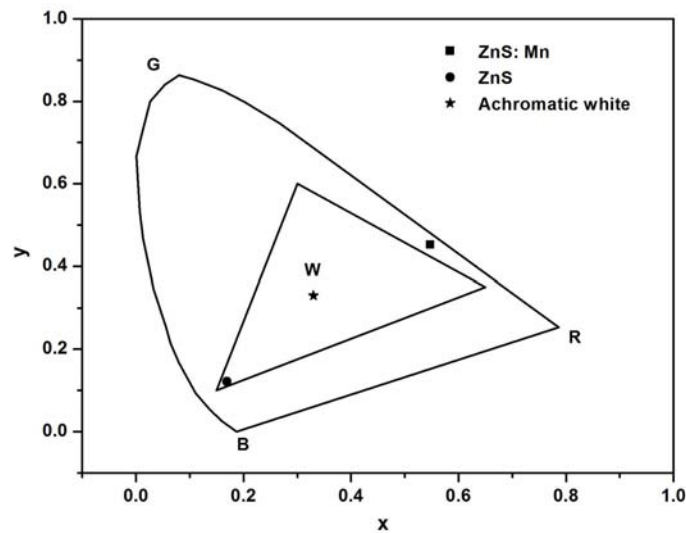
Figure 6.15: CIE coordinates of PL emission spectra of pure and Mn doped ZnS nanoparticles

6.3.3   Conclusion

ZnS and ZnS:Mn nanoparticles were prepared by LP-PLA. The targets for LP-PLA were synthesized by the solid-state reaction. The cubic structure of ZnS:Mn (0, 2%) targets were confirmed by XRD. Mn has been successfully

incorporated into the ZnS host lattice as evident from the increase in lattice constant. The structural characterization of laser ablated nanoparticles is obtained from the TEM measurements. The TEM analysis confirms the average particle size of the ZnS samples to be 7 nm. The absorption spectra show band edge around 300 nm. The blue shift in the band edge is due to the quantum confinement effects. The PL spectrum of the pure sample shows an emission in the blue region at 436 nm corresponding to the sulfur vacancy for an excitation wavelength of 342 nm. The PL spectra of ZnS:Mn shows a yellow emission at 585 nm under same excitation. This can be attributed to the radiative transition between $^4T_1$ and $^6A_1$ levels within the $3d^5$ orbital of Mn^{2+}. The CIE color coordinates calculated from the PL spectrum confirms the yellow emission of ZnS:Mn nanoparticles.

LP-PLA is a suitable method to grow nanoparticles of semiconductors, doped semiconductors and metals without any capping agents. The particle properties can easily tuned by varying the laser fluence, time of ablation, pH of the medium, etc. These surfactant free nanoparticles synthesized in water can be used in biological application by utilizing the luminescence emission from these nanoparticles.

Chapter 7

Room temperature photoluminescence from symmetric and asymmetric multiple quantum well structures

7.1 Introduction

The optical characteristics of semiconductor bulk materials are mainly determined by the inherent band structure of the material, but utilization of quantum well structures restricts carrier motion to quasi-two-dimensions and the confinement of carriers at the nanometer scale gives rise to various quantum effects on optical characteristics. The quantum well (QW) structures have a small volume. Therefore, when carriers are injected into a QW

structure, the free carrier concentration in QW will be high. At high free carrier concentrations, non-radiative deep-level transitions are less likely to occur which results in high radiative efficiency in QW structures. The carrier density required to achieve population inversion in QW lasers is small because of the small volume of QW structures. Thus the threshold current density of the QW structures is low. Surface recombination is less important in QW structures as compared to bulk material. In QW structures, carriers are trapped by the QW and, therefore, cannot reach the surface. Band gap engineering is an important research field for further ZnO applications. Together with high thermal conductivity, high luminous efficiency, and mechanical and chemical robustness, ZnO and its alloys have great prospects in optoelectronics applications in the wavelength range from the ultraviolet to the red [325]. Moreover, excitons in ZnO-based quantum well (QW) heterostructures exhibit high stability compared to bulk semiconductors or III-V QWs due to the enhancement of the binding energy [326, 327] and the reduction of the exciton-phonon coupling [328] caused by quantum confinement and thus excitons are expected to play an important role in ZnO based quantum wells. An important step in order to design high performance ZnO-based optoelectronic devices is the realization of band gap engineering to create barrier layers and quantum wells in heterostructure devices.

The ternary alloy semiconductor, $Zn_{(1-x)}Mg_xO$, is considered to have larger fundamental band gap energy than ZnO, while the lattice parameter exactly matching that of ZnO, making it an appropriate candidate as a barrier material for ZnO quantum wells. Multiple quantum well (MQW) consists of more than one well so that more carriers can be injected into the MQW. Band filling is one of the problem associated with single QW

structures. That means if the QW is filled with carriers, luminescence saturation occur at high current densities. MQW structure preserves the advantages of single QW structures. However MQW structure has a larger volume of active region and thus allows for higher light powers. Recently, much effort has been devoted toward the investigation and fabrication of ZnO/ZnMgO multiple quantum wells (MQWs) for UV light emitting applications [74, 295, 329–332]. Ohtomo et al. have grown ZnO/ZnMgO MQWs on lattice mismatched sapphire substrates using laser molecular beam epitaxy but no photoluminescence was observed above 150 K [329, 333]. In addition, the quantum confinement effects could not be observed in their MQWs through optical absorption spectroscopy [333] presumably due to the inadequate quality of the grown structures. Krishnamoorthy et al. [334] have reported size dependent quantum confinement effects at 77 K using pulsed PL measurements in ZnO/ZnMgO single quantum well samples grown on sapphire substrates using the pulsed laser deposition. However, a significant improvement in the structural and optical characteristics of ZnO MQWs was accomplished when a lattice-matched substrate ScAlMgO$_4$ (SCAM) was used instead of sapphire, which was evident from their efficient photoluminescence [325, 330, 335] and distinct photoabsorption features [336] at room temperature. But the ScAlMgO$_4$ substrates are scarce and expensive compared to abundantly available sapphire substrates. It was therefore imperative to improve the method of growing ZnO MQWs on sapphire to the level that one could get efficient room temperature PL for making them versatile. As demonstrated by the practical light emitting devices, many semiconductor devices must take advantage of multiple quantum well structures for improved device performance. Many efforts must be devoted toward the understanding, design, and fabrication of ZnO/ZnMgO

MQWs for light-emitting applications. One of the important considerations in the design and fabrication of these MQW structures is to obtain maximum quantum efficiency, i.e., to maximize the optical emission from the confined states in the well regions and to minimize the optical losses outside the well regions. It has been demonstrated recently that the optical and structural properties of ZnO/ZnMgO MQWs were greatly improved by the employment of lattice-matched substrates.

Use of asymmetric quantum well heterostructures is a new concept of band gap engineering for semiconductor optoelectronics. Initial conception of the asymmetric multiple quantum well heterostructure lasers was described early in 1991. In recent years, there has been considerable interest in asymmetrical multiple quantum well systems, because many new optical devices based on inter subband transitions are being developed. This feature could fulfil the need for efficient sources of coherent mid infrared radiation for application in several branches of science and technology, such as communications, radar, and optical electronics. Application of quantum wells with varying widths and compositions gives additional degrees to stipulate required laser regimes. Asymmetric multiple quantum well heterostructures are also used to study the carrier distribution across the active region of the lasers and to examine dependence of the carrier relaxation and transport process on the quantum well parameters and laser structure design.

This chapter deals with the fabrication of ten-period $Zn_{0.9}Mg_{0.1}O/ZnO/Zn_{0.9}Mg_{0.1}O$ symmetric MQW and ten-period $CuGaO_2/ZnO/Zn_{0.9}Mg_{0.1}O$ asymmetric MQW on Al_2O_3 substrates by pulsed laser deposition (PLD). It is known that good crystalline and optical quality of ZnO films on sapphire are obtained at a growth temperature of 750^0C or higher [337, 338] through

domain epitaxy [339], but the ZnO/ZnMgO heterointerfaces and ZnMgO alloy are chemically stable only below 650^0C [340]. To accomplish these contradictory growth requirements, a buffer assisted growth methodology has been used [337]. ZnO buffer layer of (50 nm) in thickness was first grown on sapphire substrate at 700^0C and the subsequent growth of barrier and well layers was carried out on this ZnO template at a lower substrate temperature of 600^0C. This ensured a high crystalline quality of the barrier and well layers along with the physically and chemically sharp interfaces. The room temperature (RT) photoluminescent emission was observed from these MQW structures.

7.2   Experimental

Ceramic targets of ZnO, $Zn_{0.9}Mg_{0.1}O$ and $CuGaO_2$ were used for pulsed laser deposition of $Zn_{0.9}Mg_{0.1}O/ZnO/Zn_{0.9}Mg_{0.1}O$ and $CuGaO_2$ /ZnO/ $Zn_{0.9}Mg_{0.1}O$ MQW structure. The $Zn_{0.9}Mg_{0.1}O$ target was prepared by mixing 10 at.% of high purity MgO and ZnO powders and sintered at 1300^0C. The ZnO target was prepared by sintering its high purity powder at 1300^0C for 5 hours in air. The $CuGaO_2$ target was prepared by mixing CuO and Ga_2O_3 powders and sintered at 1100^0C in argon atmosphere. The fourth harmonics of a Q-switched Nd:YAG laser (266 nm) was used for ablation. The repetition frequency was 10 Hz with a pulse width of 6-7 ns. Laser beam was focused to a spot size 2 mm on the surface of the target and the target was kept in rotation to avoid pitting. The growth chamber was evacuated to a base pressure of 10^{-6} mbar by using turbo molecular pump backed with diaphragm pump, and then O_2 (99.99% purity) was introduced as working gas, with a pressure of 10^{-3} mbar. The target to

substrate distance was kept as 6 cm and the substrate temperature was kept at 600^0C. The ablation was carried out at a constant laser energy of 2 J/cm^2/pulse for all the depositions. ZnO, ZnMgO and CuGaO$_2$ targets were laser ablated individually and the deposited film thickness was measured using stylus profiler. From these measured thicknesses, the growth rate was found to be 0.08 nm/s for ZnO, 0.03 nm/s for ZnMgO and 0.06 nm/s for CuGaO$_2$ films. Knowing the growth rates, the deposition time was adjusted to get the desired barrier and well layer thickness. To eliminate the lattice mismatch-induced effects, 50 nm ZnO buffer layer was first grown on Al$_2$O$_3$ substrate at 700^0C by pulsed laser ablation. Then, the ten periods of Zn$_{0.9}$Mg$_{0.1}$O/ZnO/Zn$_{0.9}$Mg$_{0.1}$O layer was grown on this ZnO template at a substrate temperature of 600^0C keeping all the other deposition parameters the same. The Zn$_{0.9}$Mg$_{0.1}$O barrier layer thickness was 8 nm. The quantum well structures with well layer thickness (ZnO layer) ranging from 2 to 6 nm were grown by pulsed laser deposition. All the layers were deposited sequentially without breaking the vacuum. Similarly for growing asymmetric MQW structure, 50 nm ZnO buffer layer was first grown on Al$_2$O$_3$ substrate at 700^0C by pulsed laser ablation. Then, 10 periods of CuGaO$_2$/ZnO/Zn$_{0.9}$Mg$_{0.1}$O layer was grown on this ZnO buffer layer keeping all the deposition parameters the same, except the substrate temperature as 600^0C. The thickness of Zn$_{0.9}$Mg$_{0.1}$O and CuGaO$_2$ barrier layer was kept at 8 nm and that of ZnO confinement layer was varied from 2 to 6 nm.

The crystallinity of thin films was determined by x-ray diffraction (XRD) using Cu K$_\alpha$ radiation ($\lambda = 1.5418$ Å). The thickness of the samples was measured using a Dektak 6 M stylus profiler. For studying the photoluminescence (PL), a fourth harmonic pulsed Nd:YAG laser operating at 266 nm

was used as an excitation source and resulting luminescence was collected using gated CCD at room temperature.

7.3   Results and discussion

ZnMgO/ZnO/ZnMgO symmetric MQW structure were grown on Al_2O_3 substrate by fourth harmonic Nd:YAG laser with 2 nm as the confinement layer (ZnO layer) thickness.A schematic of the ZnMgO/ZnO/ZnMgO symmetric MQW structure grown on Al_2O_3 substrate is shown in figure 7.1. The band structure of ZnMgO/ZnO/ ZnMgO symmetric MQW structures are shown in the figure 7.2.
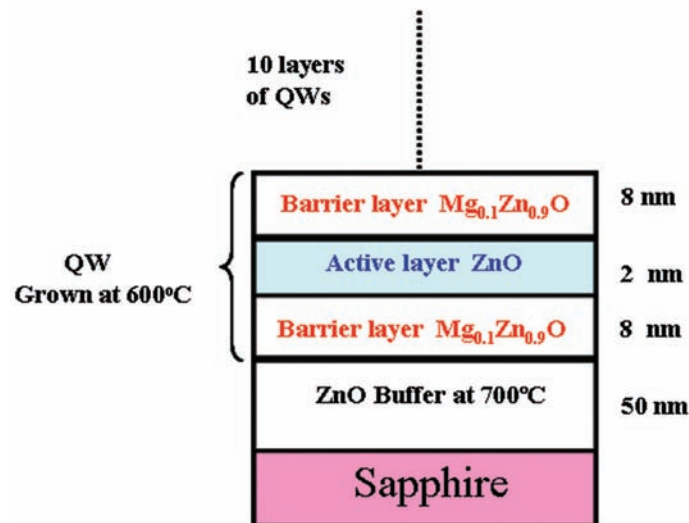
Figure 7.1: Schematic of the ZnMgO/ZnO/ZnMgO symmetric MQW structures grown by PLD
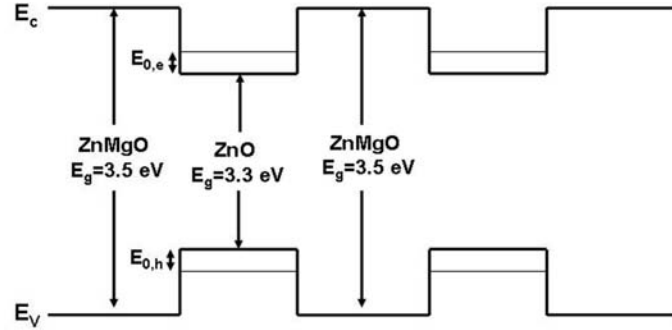
Figure 7.2: Band structure of ZnMgO/ZnO/ZnMgO symmetric MQW structures grown by PLD

Luminescence emission measurements allows one to determine the energy shift due to the quantum size effects. The band-edge photoluminescence has been studied extensively in ZnO bulk, films, quantum wells and other nanostructures, and the origin of the PL spectra in the near band-gap region has been proposed [328, 341, 342]. At low temperatures, the PL spectra near the band gap consists of transitions of free and bound excitons, followed by their longitudinal optical phonon replica on the low-energy side as a shoulder [343].

The near-band-edge PL band becomes broad at room temperature due to strong inhomogeneous broadening and thermal broadening. The band-edge PL of ZnO multiple quantum wells was studied by Makino and colleagues, who found that the room-temperature photoluminescence spectrum is dominated by exciton recombination [330]. The weak PL spectrum due to thermal annihilation suggests that non radiative recombination, rather than radiative recombination, is dominant at room temperature.

Earlier studies carried out in our laboratory on the room temperature

PL emission of ZnMgO/ZnO/ ZnMgO symmetric MQW grown by third harmonic Nd:YAG laser (λ=355 nm) shows a broad peak with small spikes. Figure 7.3 shows the room temperature PL emission at an excitation wavelength of 266 nm from ZnMgO/ZnO/ ZnMgO symmetric MQW grown by third harmonic Nd:YAG laser with 2 nm as the confinement layer (ZnO layer) thickness. The large FWHM ($\sim$39 nm) and small spikes in the PL spectra is due to the interface roughness and fluctuations in the well layer thickness [344].

Figure 7.3: Room temperature PL emission from ZnMgO/ZnO/ZnMgO symmetric MQW grown by third harmonics of Nd:YAG laser (λ=355 nm)

The PL emission from the MQW structure can be improved with the barrier and confinement layer quality and the better interface between these layers. The layer properties can be improved by using fourth harmonic Nd:YAG laser (λ=266 nm). The large absorption coefficient of the target material at lower wavelength results in the ablation of a thin surface layer of the material. This can be observed from the lower growth rate of materials during the ablation with fourth harmonic of Nd:YAG laser than with third harmonic Nd:YAG laser. The growth rate was found to be 0.18 nm/s for ZnO and 0.14 nm/s for ZnMgO films during the ablation with third harmonic Nd:YAG laser [344]. The lower laser wavelength, ie., at higher incident photon energy results in the highly energetic ablated particles, which improves the crystallinity of the layers.

ZnMgO/ZnO/ZnMgO symmetric MQW were grown on Al_2O_3 substrate by fourth harmonic Nd:YAG laser (λ=266 nm) with 2 nm as the confinement layer thickness. The deposition parameters of the pulsed laser ablation for growing each layer have optimized before growing the MQW structures.

Figure 7.4(a) shows the XRD pattern of the ZnO thin film grown on quartz substrate by pulsed laser ablation at 600^0C by fourth harmonic Nd:YAG laser. A sharp and dominant peak at 34.2^0 was observed which corresponds to the (0002) plane of ZnO. The (0002) peak is related to the crystal plane of wurtzite ZnO with [0001] growth direction. Moreover, the strong intensity of the (0002) reflection with narrow width also shows that the c-axis of ZnO are well oriented along the normal direction of the substrate surface.

Figure 7.4(b) shows the XRD pattern of the ZnMgO thin films grown by pulsed laser deposition at 600^0C on quartz substrate by fourth harmonic

Nd:YAG laser. The appearance of only the (0002) diffraction peak indicated that the film is highly c-axis oriented and corresponds to the hexagonal wurtzite structure of ZnMgO. No other secondary phase was observed in the XRD pattern.
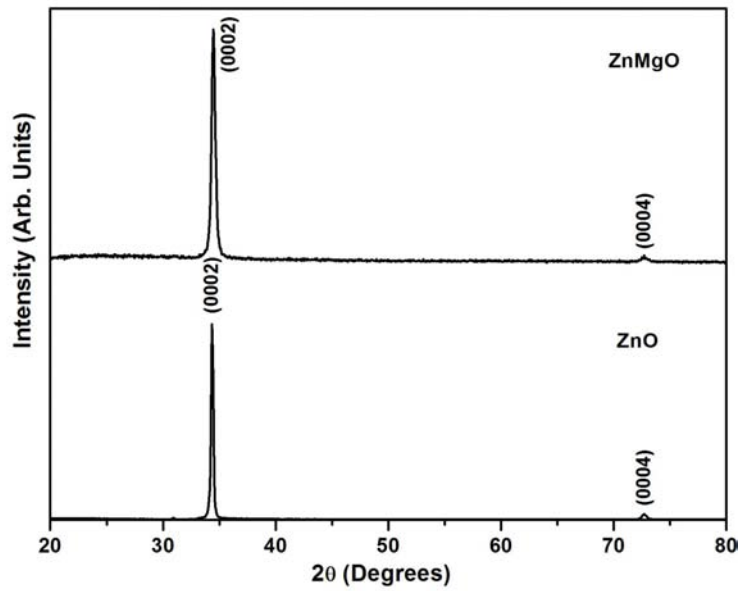
Figure 7.4: XRD pattern of the (a) ZnO and (b) ZnMgO thin films grown on quartz substrate by pulsed laser ablation at 600^0C

XRD pattern of the ZnO thin film and ZnMgO/ZnO/ZnMgO symmetric MQW grown on Al_2O_3 substrate by pulsed laser ablation at 600^0C by fourth harmonic Nd:YAG laser is shown in the figure 7.5. The peaks in the XRD pattern corresponds to the crystal plane of wurtzite ZnO with [0001] growth direction.
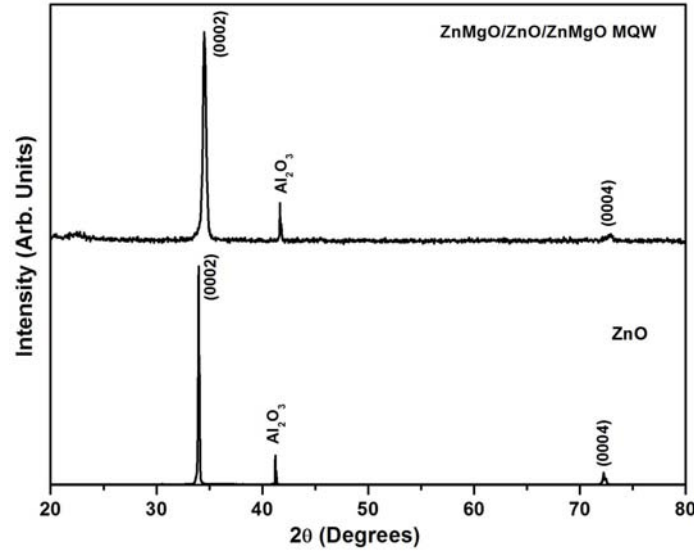
Figure 7.5: XRD pattern of the (a) ZnO thin film and(b) ZnMgO/ZnO/ZnMgO symmetric MQW grown on Al_2O_3 substrate by pulsed laser ablation at 600^0C

The room temperature PL emission at an excitation wavelength of 266 nm from the ZnMgO/ZnO/ZnMgO symmetric MQW with confinement layer thickness of 2 nm grown on Al_2O_3 substrate by fourth harmonic Nd:YAG laser is shown in the figure 7.6. It shows a sharp PL emission peak centered at 362 nm which corresponds to the band edge of the ZnO. The PL peak have smaller FWHM ($\sim$20 nm) compared to MQW grown by ablating with 355 nm and spikes are absent in the spectrum which indicates the improvement in the layer qualities. There is a blue shift in the PL peak position with respect to the bulk which is assigned to the quantum confinement effects. These studies confirms that fourth harmonics of the Nd:YAG laser is better than third harmonics for growing the multiple quantum well structures. So the remaining studies on the multiple quantum

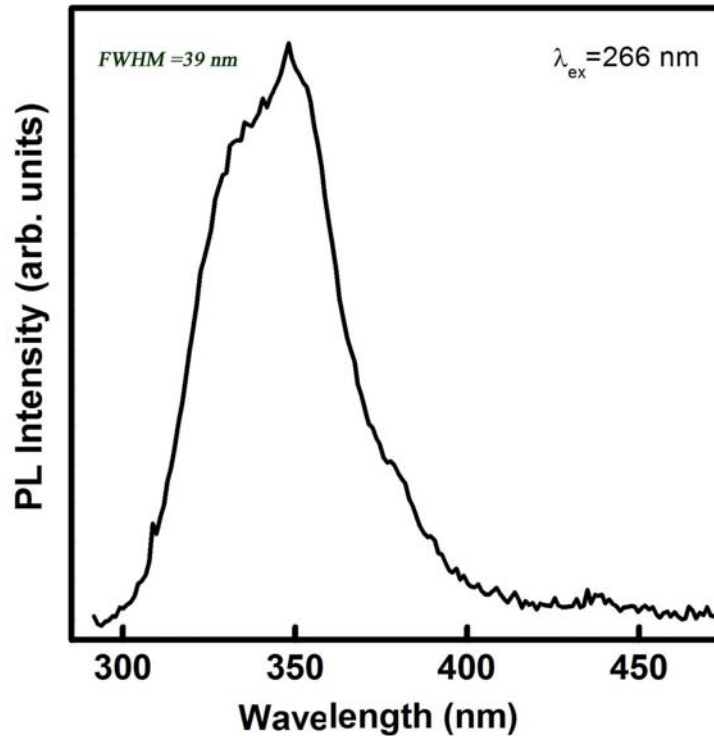well structures were carried out with fourth harmonic Nd:YAG laser.
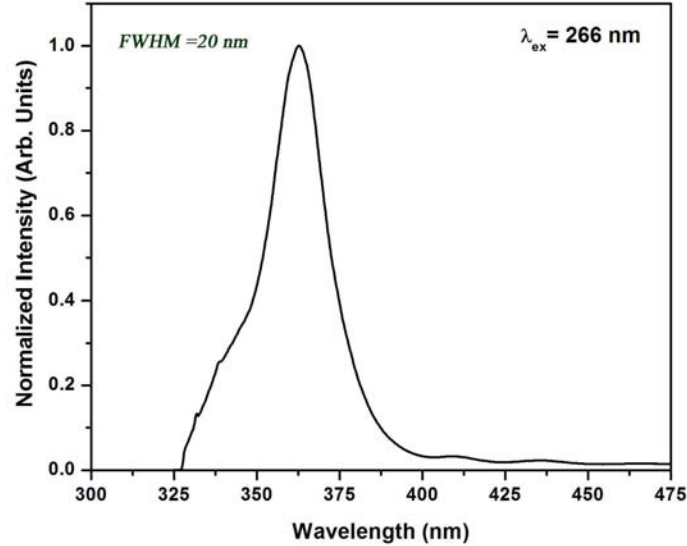
Figure 7.6: Room temperature PL emission from ZnMgO/ZnO/ZnMgO symmetric MQW grown by fourth harmonics of Nd:YAG laser (λ=266 nm)

The dependance of confinement layer thickness of ZnMgO/ZnO/ZnMgO symmetric MQW on the room temperature PL emission were studied. This shows a blue shift in the PL peak position with decrease in the confinement layer thickness from 6 nm to 2 nm. This is due to the increase in the quantum confinement effects as the thickness of the layer decreases. The small PL peak at 345nm corresponds to the band edge of ZnMgO. Figure 7.7 shows the room temperature PL emission from ZnMgO/ZnO/ZnMgO symmetric MQW with varying confinement layer thickness (2, 4 and 6 nm). The full width at half maximum (FWHM) of the PL peaks increases with decreasing the confinement layer thickness. This can be attributed to the fluctuations in well layer thickness and dominance of the interface rough-

ness in thinner wells. Further studies are required to investigate the exact mechanism for the small emission peaks at higher wavelength region in the PL spectra of MQW structures with 4 nm as the confinement layer thickness.
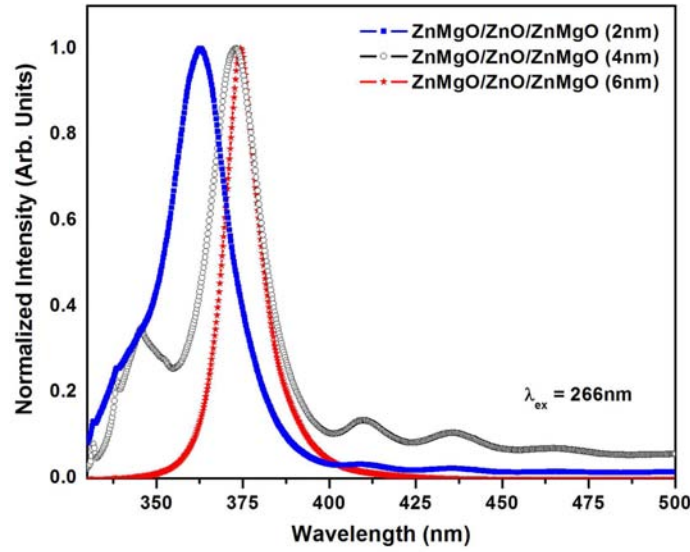
Figure 7.7: Room temperature PL emission from ZnMgO/ZnO/ZnMgO symmetric MQW with varying confinement layer thickness (2, 4 and 6 nm)

Quantum well structure consists of a thin layer of a narrow band gap semiconductor between thicker layers of a wide band gap semiconducting material. The emission energies of the QW is different from either band gap energies of the two semiconductors. The absorption edge of the QW structure is given by

$$E_{g,QW} = E_{g,bulk} + E_{0,e} + E_{0,h} \qquad (7.1)$$

where, $E_{0,e}$ and $E_{0,h}$ are the quantized electron and hole energies as shown in the band diagram as shown in the figure 7.8.
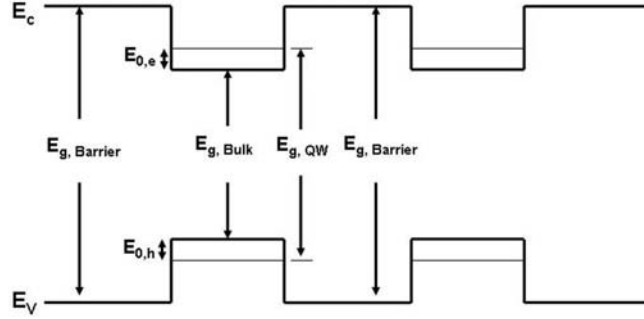
Figure 7.8: Band structure of symmetric MQW structures

The infinite well approximation is the simplest method to calculate the quantum energy of carriers in the valance band well and the conduction band well. The quantum energies in the infinite well approximation are given by

$$E_n = \frac{\hbar^2}{2m^*}[\frac{(n+1)\pi}{L_{QW}}]^2 \qquad (7.2)$$

n=0,1,2,...

where m^* and L_{QW} are the effective mass and the confinement layer thickness respectively.

The energy of the lowest state or ground state energy is given by

$$E_0 = \frac{\hbar^2}{2m^*}[\frac{\pi}{L_{QW}}]^2 \qquad (7.3)$$

The theoretical value of the confinement layer thickness were measured from the PL peak position. The thickness of the symmetric MQW struc-

tures with 2 nm as the confinement layer thickness as calculated from the rate of growth have a thickness of 4 nm as obtained theoretically. Thus there is a discrepancy of the layer thickness measurements from the rate of growth and that obtained theoretically. The small blue shift in the PL peak position for the higher active layer thickness in comparison with the bulk is attributed to the less quantum confinement effects as the confinement layer thickness is larger. The symmetric MQW structures grown with 4, 6 nm as the confinement layer thickness measured from the rate of growth are found to have 8 and 10 nm thickness from the theoretical calculations based on the PL peak position. This may be the reason for only a slight variation of PL peak position from that of the bulk because the quantum confinement effects is less prominent in that region. The quantum confinement effects in nanostructures are only expected for the structures having one dimension is comparable to the he exciton Bohr radius. The exciton Bohr radius of ZnO is only $\sim$2 nm [345].

Since development of semiconductor injection lasers the considerable improvement of their characteristics has been achieved. It widens the use of laser diodes in different fields of science and technology. QW injection lasers differ from traditional laser diodes in a series of positive virtues, as extremely small power consumption, low noise level, small threshold currents, weak sensitivity to ambient temperature fluctuations, sufficiently great values of lasing radiation power and efficiency, additional resources in control of emission characteristics. From this point of view, laser heterostructures with varied QWs in the active region being called asymmetric systems have big prospects. There are several ways of deriving the asymmetric multiple-quantum-well (AMQW) heterostructures. The active layers can differ in

the width, component composition, and in the order of location relative to each other or to emitters.

In a semiconductor, electrons are not normally in the conduction band, but they can be excited using optical radiation to form exciton pairs, which consist of an electron that is excited into the conduction band and a hole that the electron leaves behind in the valence band. After the creation of an exciton from a photon, if the photon had more energy than required, the excess energy will be released as a phonon (heat). Normally, the ground state energies in each well are degenerate. However, if an electric field is applied across the layers of the MQW, the degeneracy is lost and the potential appears as a slanted step function. In this case, when a photon has more energy than is required to excite an electron, the excess energy can be used to cause the electron to jump to a neighboring well with a higher potential from the electric field. Similarly, if the photon has less energy than required for the formation of an exciton, it can still form an exciton as long as the electron subsequently jumps to a well with a lower ground state potential. This carrier injection will be more as in the case of asymmetric multiple quantum well structures with p and n type barrier layers.

The delafossite structure has high p-type conductivity. It have the formula $A^{II}B^{IV}O_2^{VI}$, where A is a monovalent cation (Cu, Ag, Pd, Pt) and B is a trivalent transition metal cation (Al, Co, Cr, Ga, In etc). The band structure of delafossites is such that the valance band maximum is at a low symmetry point. Thus the intra-valence band optical absorption is quantum mechanically allowed which results in the decrease in optical transparency in delafossites. $CuMO_2$ (M= Ga, Al) are p-type conducting transparent oxides of significant interest for transparent electronics [346, 347]. $CuGaO_2$

is a wide band gap semiconductor with direct bad gap of 3.4-3.6 eV and having p type conductivity. In $CuGaO_2$ structure, layers of A cations are linearly coordinated to two oxygen atoms, are alternatively stacked between layers of edge sharing $B^{3+}O_6$ octahedra oriented perpendicular to c-axis. In these $B^{3+}O_6$ octahedra, the oxygen atom is in pseudo-tetragonal coordination as B_3AO. Depending on the stacking, $B^{3+}O_6$ octahedral layers can lead to either rhombohedral or hexagonal structures. The material have reasonable transparency in the visible region. Band structure calculations indicate that there is also an indirect gap at 0.95 eV [348]. The p-type conductivity originates from the +1 valence of the Cu cation within the delafossite structure. Phase formation, crystallinity and orientation of $CuGaO_2$ thin films is reported in which hydrogen gas is utilized as a reducing reactant during growth to drive the valence state of Cu to +1. Cu vacancies or oxygen interstitials are the dominant acceptor defect species which determine the hole density. At relatively low growth temperatures, the films are a mixture of $CuGaO_2$, Cu_2O and $CuGa_2O_4$. At higher temperatures, the majority phase is $CuGaO_2$. One of the challenges in the growth of $CuGaO_2$ thin films is in minimizing the formation of secondary phases, in particular Cu_2O and $CuGa_2O_4$, driven by the variable valence state of Cu cations.

$CuGaO_2/ZnO/ZnMgO$ asymmetric MQW were grown on Al_2O_3 substrate. A schematic of the $CuGaO_2/ZnO/ZnMgO$ asymmetric MQW structure are given in figure 7.9. Band structure of $CuGaO_2/ZnO/ZnMgO$ asymmetric MQW structures are shown in the figure 7.10.
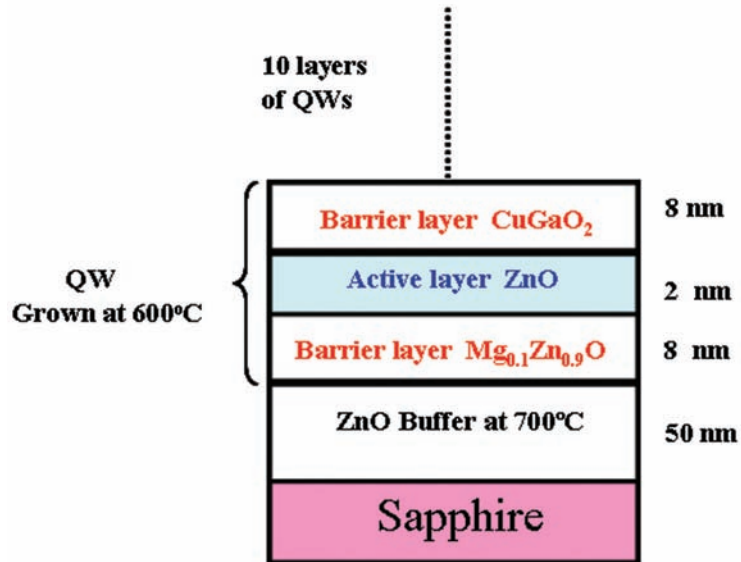
Figure 7.9: Schematic of the $CuGaO_2/ZnO/ZnMgO$ asymmetric MQW structures grown by PLD
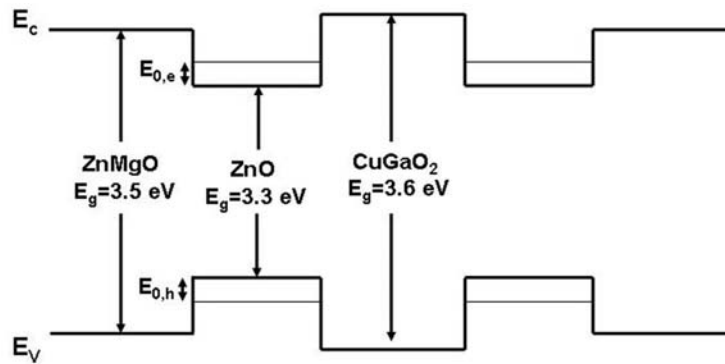
Figure 7.10: Band structure of $CuGaO_2/ZnO/ZnMgO$ asymmetric MQW structures grown by PLD
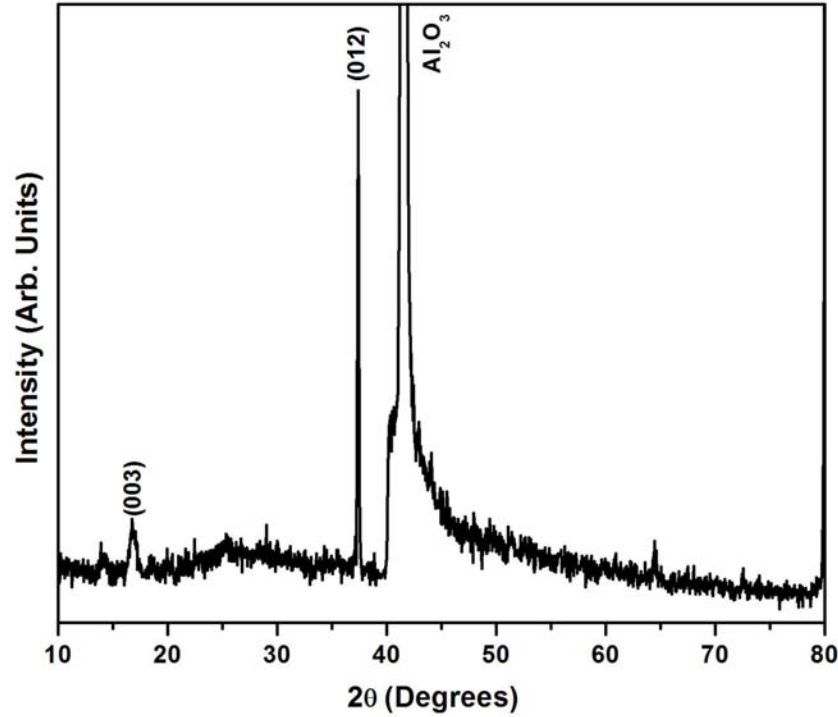
Figure 7.11: XRD pattern of the $CuGaO_2$ thin film grown on Al_2O_3 substrate by pulsed laser ablation at 600^0C

The conditions for growing the MQW structures were optimized by depositing the individual layer by pulsed laser ablation. Figure 7.11 shows the XRD pattern of the PLD grown $CuGaO_2$ thin film on Al_2O_3 substrate at 600^0C with an oxygen pressure of 10^{-3} mbar by ablating with 266 nm. The (003) and (012) planes of $CuGaO_2$ identified from the XRD pattern confirms the formation of delafossite structure. The peaks of secondary phases, such as Cu_2O and $CuGa_2O_4$ were not detected in the XRD pattern.
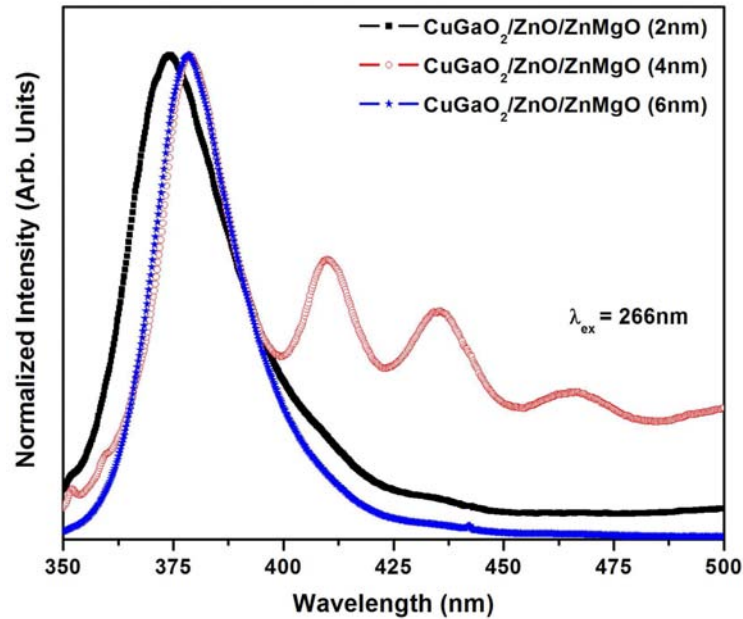
Figure 7.12: Room temperature PL emission from $CuGaO_2$/ZnO/ZnMgO asymmetric MQW with varying confinement layer thickness (2, 4 and 6 nm)

$CuGaO_2$/ZnO/ZnMgO asymmetric MQW structures were grown with varying thickness (2, 4 and 6 nm) of confinement layer (ZnO layer). Figure 7.12 shows that the room temperature photoluminescent emission from the $CuGaO_2$/ZnO/ZnMgO asymmetric MQW structures grown by pulsed laser ablation with various thickness of the confinement layer. The PL peak is blue shifted as the active layer thickness decreases from 6 to 2 nm. This shift is attributed to the quantum confinement effects. Small peaks were observed in the PL spectra at longer wavelength region of asymmetric MQW structures with 4 nm confinement layer thickness and further studies are required for identify the exact reason. The confinement layer thickness

were estimated from the PL peak position using the equation 7.3 and found that the thickness of the asymmetric MQW structures with 2 nm as the confinement layer thickness as calculated from the rate of growth have 8 nm thickness. Similarly the asymmetric MQW structures grown with 4, 6 nm as the confinement layer thickness measured from the rate of growth in fact have larger thickness as estimated from the PL peak positions. The relatively very small blue shift in the PL peak positions with bulk may be attributed to the larger thickness of the confinement layer where quantum confinement effects are less prominent.
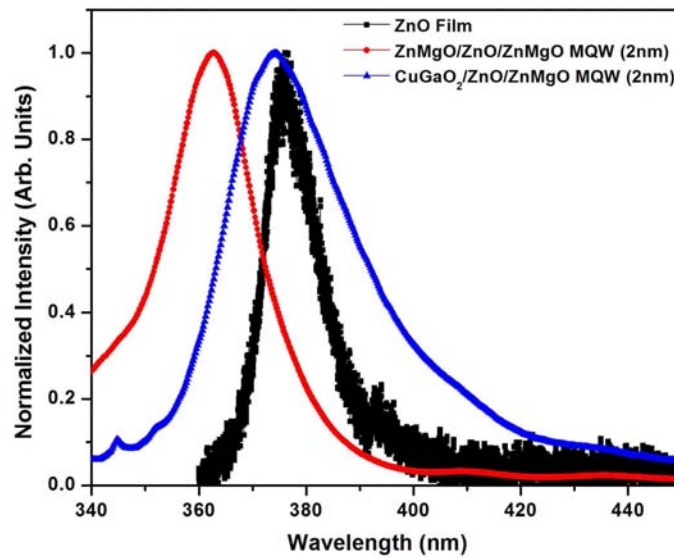
Figure 7.13: Room temperature PL emission from ZnO thin film, Zn-MgO/ZnO/ZnMgO symmetric and CuGaO$_2$/ZnO/ZnMgO asymmetric MQW grown by PLD

150 nm thick ZnO thin films were grown on Al$_2$O$_3$ substrate at 600^{0}C by pulsed laser ablation. The room temperature PL emission of this ZnO thin

film is compared with ZnMgO/ZnO/ZnMgO symmetric and CuGaO$_2$/ZnO/ ZnMgO asymmetric MQW having 2 nm thick confinement layer which is calculated from the rate of growth. Figure 7.13 shows the room temperature PL emission from ZnO thin film, ZnMgO/ZnO/ZnMgO symmetric and CuGaO$_2$/ZnO/ZnMgO asymmetric MQW grown by PLD. It shows the blue shift in the PL peak position of MQW structures from that of ZnO thin film. This is attributed to quantum confinement effects. The blue shift in the ZnMgO/ZnO/ZnMgO symmetric MQW is larger than that of CuGaO$_2$/ZnO/ZnMgO asymmetric MQW. This is due to the fact that the larger confinement layer thickness in asymmetric MQW structures than symmetric MQW structures.

7.4 Conclusion

ZnMgO/ZnO/ZnMgO symmetric and CuGaO$_2$/ZnO/ZnMgO asymmetric multiple quantum well structures grown by buffer assisted pulsed laser ablation using fourth harmonic Nd:YAG laser. The XRD pattern confirms the wurtzite structure of ZnO and ZnMgO and delafossite structure of CuGaO$_2$. Room temperature photoluminescence emission was observed from the symmetric and asymmetric MQW structures excited at a wavelength of 266 nm. The PL emission of symmetric and asymmetric MQW structures was blue shifted with decrease in the confinement layer thickness from 6 to 2 nm and this is attributed to quantum confinement effects. The thickness of the confinement layer calculated from the rate of growth was found to be different from theoretical measurements using the PL peak position. The PL emission from symmetric and asymmetric MQW structures is blue shifted from that of 150 nm thick ZnO thin film grown by pulsed

laser ablation and which is due to the quantum confinement effects. The thickness of the confinement layer found out from the deposition rate may not be the correct thickness of the confinement layer. This is reflected in the PL peak positions also. A more accurate in-situ method is required to have precise control of the confinement layer thickness.

Chapter 8

Summary and Scope for further study

8.1 Summary of the present study

Nanotechnology is a collective definition referring to the science and technology which operates on a nanoscale that includes the scientific principles and new properties that can be found and mastered when operating in this regime. Royal Society defines nanotechnology as the design, characterization, production and application of nanostructured devices and systems by controlling their size and shape at nanometer scale. In the nanoscale (size below 100 nm), the materials show properties that are very different from those at larger (bulk) scale. A nanometer (nm) is one thousand millionth of a meter $(10^{-9}m)$. In certain aspects, nanoscience and nanotechnologies are not new. Chemists have been making polymers, which are large molecules made up of nanoscale subunits, for many decades technologies in the nanoscale have been used to create the tiny features on computer chips.

However recent advances in the tools that allow atoms and molecules to be examined and probed with great precision have enabled the expansion and development of nanoscience and nanotechnology.

Earlier people believed that material characteristics can be changed only by varying its chemical composition or by mixing materials in different conditions. But recently a different approach for synthesizing materials has been introduced in which material characteristics could also be changed by changing the particle size keeping the chemical composition intact. However the variation of the material characteristics with size was feasible only in a specific size regime, called the quantum confinement regime. There are two principal ways of manufacturing nanoscale materials; the top-down nanofabrication starts with a large structure and proceeds to make it smaller through successive cuttings while the bottom-up nanofabrication starts with individual atoms and builds them up to a nanostructure. In the present thesis, bottom up process like hydrothermal method, liquid phase pulsed laser ablation and pulsed laser deposition were used for the growth of nanostructures. When we bring constituents of materials down to the nanoscale, their properties change. Some materials used for electrical insulations can become conductive and other materials can become transparent or soluble in the nanoregime. Nano gold does not look like bulk gold, the nanoscale particles can be orange, purple, red or greenish depending on the size of the particle [349]. Nonluminescent ZnO can be made luminescent by playing the intrinsic defects [35]. All these new properties that open up when bringing the material down to nanoregime is of great interest for the industry and society as it enables new applications and production.

The properties of materials will be different at the nanoscale due to two main reasons. First, nanomaterials have a relatively larger surface area when compared to the same mass of material produced in the bulk form. This will increase the chemical reactivity of materials (in some cases materials that are inert in their bulk form are reactive when produced in their nanoscale form), and affect their strength and electrical properties. Secondly when quantum effects begin to dominate the behaviour of matter at the nanoscale, it will affect the optical, electrical and magnetic behaviour of materials.

Nanostructured materials are the materials in which quantum confinement occurs when the carriers are trapped in one or more dimensions within the nanometer regime. If the carriers are trapped in one dimension while it can move freely in other two dimensions, such structures are called quantum well structures. In the present study one dimensional confinement has been achieved by fabricating ZnMgO/ZnO/ZnMgO symmetric and $CuGaO_2$/ZnO/ZnMgO asymmetric multiple quantum well structures by pulsed laser deposition. If the confinement of the carriers is in two directions so that the carriers have free motion only in one direction, such structures are called as quantum wires. Nanorods of ZnO grown by hydrothermal method discussed in the present thesis is an example for confinement in two dimensions. Confinement in all the three directions will result in no free motion of electrons or holes in any direction. Such structures are called quantum dots. Liquid phase pulsed laser ablation has been used for the growth of quantum dots in the present study. The density of states also get modified with the reduction in the size of the material.

Alternatives to silicon-based electronics are already being explored through nanoscience and nanotechnologies, for example plastic electronics for flex-

ible display screens. Other nanoscale electronic devices currently being developed are sensors to detect chemicals in the environment. Much interest is also given to quantum dots, that can be tuned to emit or absorb particular light colours for use in solar energy cells or fluorescent biological labels.

The semiconductor nanocrystals show a variety of unique optical, electronic and chemical properties which originate mainly due to two reasons, i.e., quantum confinement effects and large surface to volume ratio. Materials that convert absorbed energy to visible light without going to high temperatures are known as luminescent materials and are also referred as phosphors. Such materials find applications in cathode ray tubes (CRT), plasma display panels (PDP), electroluminescent (EL) displays and field emission displays, detectors for x-rays, temperature and pressure. Phosphors are generally in crystalline powder form with size ranging from 1-100 μm. Phosphors with one dimension <100 nm are called nanophosphors which possess different absorption and emission characteristics with improved efficiency and life times [101]. In recent years, the luminescent nanocrystals, also termed as nanophosphors, attracted considerable interest after the observation of enhanced luminescence efficiency and shortening of radiative lifetime by orders of magnitude from milliseconds to nanoseconds as compared to the bulk counterparts. These promising properties along with the possibility of synthesizing such materials by simple low temperature methods will bear a great potential for their applications in a number of high technology areas such as high density displays, bio-markers, lasers, sensors, etc.

The focus of the study presented in the thesis is the growth and characterization of nanophosphors as well as the nanostructures of various wide

band gap semiconductors for optoelectronic applications. Undoped and europium doped zinc gallium oxide ($ZnGa_2O_4$) nanophoshors were synthesized by hydrothermal method for solid state lighting applications. Undoped and manganese doped zinc sulfide (ZnS) nanophoshors were grown by low temperature liquid phase pulsed laser ablation method and their luminescent properties were studied. Various nanostructures of doped and undoped zinc oxide were grown for optoelectronic applications. ZnO based symmetric and asymmetric multiple quantum well structures were grown by pulsed laser deposition techniques.

In the present study $ZnGa_2O_4$ nanophosphors were grown by hydrothermal method and emission colour is tuned from blue to red by doping $ZnGa_2O_4$ with europium that find application in solid state white lighting. White light can be achieved by the combinations of three primary colors or by using the blue excitation source and the red phosphor [350] and it will effectively reduce the number of phosphor components. Various nanostructures of ZnO were grown by hydrothermal method by varying the process parameters such as precursors, time of growth, temperature etc. White luminescence were obtained from ZnO nanorods by utilizing the intrinsic and extrinsic defects of ZnO. Cobalt and europium doped ZnO nanostructures were grown by hydrothermal method for magnetic and luminescent applications. The Eu doped ZnO nanostructures can act as UV to red and blue to red converter. Highly transparent, luminescent, bio-compatible ZnO and ZnS nanoparticles were synthesized by LP-PLA technique without using any surfactant and studied its luminescent and structural properties. Room temperature photoluminescent emission were observed from $ZnMgO/ZnO/ZnMgO$ symmetric and $CuGaO_2/ZnO/ZnMgO$ asymmetric multiple quantum well structures which can act as UV emitters.

8.2   Scope for further study

ZnO nanorods were synthesized in the present study by low temperature hydrothermal method. These nanorods can be grown on various substrates like glass, silicon, plastics etc by buffer assisted hydrothermal method. These vertically aligned nanorods can be used for dye sensitized solar cells and sensor applications. The white luminescence emission from the ZnO nanorods can be utilized for lighting application. Highly transparent, luminescent, bio-compatible ZnO and ZnS nanoparticles were synthesized in the present study by LP-PLA technique without using any surfactant. Toxicity studies of these ZnO and ZnS nanoparticles are essential before they could be used in invivo cancer imaging applications.

Appendix A

Abbreviations used in the thesis

Abbreviation	Expansion
AFM	Atomic Force Microscope
BF	Bright Field
CCD	Charge Coupled Device
CdS	Cadmium Sulfide
CdSe	Cadmium Selenide
CGO	Copper Gallium Oxide
CIE	Commission Internationale de lEclairage
CRT	Cathode Ray Tube
CVC	Chemical Vapor Condensation
CVD	Chemical Vapour Deposition
DF	Dark Field
DMS	Diluted Magnetic Semiconductor
DNA	Deoxyribonucleic Acid
DOS	Density of States
DRS	Diffuse Reflectance Spectroscopy
DSC	Differential scanning calorimetry
EDAX	Energy Dispersive X-ray Spectroscopy

Abbreviation   Expansion

Abbreviation	Expansion
ELD	Electroluminescent Device
EPR	Electron Paramagnetic Resonance
FED	Field Emission Display
FESEM	Field Emission Scanning Electron Microscope
FET	Field Effect Transistor
FM	Ferromagnetism
FT-IR	Fourier Transform Infrared Spectroscopy
FWHM	Full Width at Half Maximum
GMR	Giant Magnetoresistance
HRTEM	High Resolution Transmission Electron Microscope
ICP-AES	Inductively Coupled Plasma Atomic Emission Spectroscopy
ICP-OES	Inductively Coupled Plasma Optical Emission Spectroscopy
ICSD	Inorganic Crystal Structure Database
LED	Light Emitting Diode
LP-PLA	Liquid Phase Pulsed Laser Ablation
LO	Longitudinal Optical
LVDT	Linear Variable Differential Transformer
MBE	Molecular Beam Epitaxy
MEMS	Micro Electro Mechanical Systems
MOCVD	Metal Organic Chemical Vapour Deposition
MOVPE	Metalorganic Vapour Phase Epitaxy
MQW	Multiple Quantum Well
MWCNT	Multi Walled Carbon Nanotube
Nd:YAG	Neodymium Yttrium Aluminium Garnet
nm	nanometer
NP	Nanoparticle
PDP	Plasma Display Panel
PECVD	Plasma Enhanced Chemical Vapour Deposition
PID	Proportional Integral Derivative
PL	Photoluminescence
PLA	Pulsed Laser Ablation
PLD	Pulsed Laser Deposition
PLE	Photoluminescence Excitation
PVD	Physical Vapor Deposition

Abbreviation	Expansion
QD	Quantum Dot
QW	Quantum Well
RE	Rare Earth
RF	Radio Frequency
RT	Room Temperature
RTFM	Room Temperature Ferromagnetism
SAED	Selected Area Electron Diffraction
SEM	Scanning Electron Microscopic
SQUID	Superconducting Quantum Interference device
SWCNT	Single Walled Carbon Nanotube
TCO	Transparent Conducting Oxide
TEM	Transmission Electron Microscope
TFEL	Thin Film Electroluminescence
TGA	Thermogravimetric Analysis
TO	Transverse Optical
UV	Ultraviolet
VFD	Vacuum Fluorescent Display
XRD	X-ray Diffraction
ZGO	Zinc Gallium Oxide
ZnMgO	Zinc Magnesium Oxide
ZnO	Zinc Oxide
ZnS	Zinc Sulfide

Bibliography

[1] H. Zhao and Y. Ning. *Gold Bull*, 33:103, 2000.

[2] M. Faraday. *Philosophical Transactions*, 147:145, 1857.

[3] R. P. Feynman. *Philosophical Transactions*. Reinhold, New York, 1961.

[4] H. W. C. Postma, T. Teepen, Z. Yao, M. Grifoni, and C. Dekker. *Science*, 293:76, 2001.

[5] S. J. Tans, M. H. Devoret, H. Dai, A. Thess, R. E. Smalley, L. J. Geerligs, and C. Dekker. *Nature*, 386:474, 1997.

[6] K. Keren, R. S. Berman, E. Buchstab, U. Sivan, and E. Braun. *Science*, 302:1380, 2003.

[7] S. J. Tans, A. R. M. Verschueren, and C. Dekker. *Nature*, 393:49, 1998.

[8] R. Martel, T. Schmidt, H. R. Shea, T. Hertel, and A. Ph. *Appl. Phys. Lett.*, 73:2447, 1998.

[9] J. H. Davies. *The Physics of Low-Dimensional Semiconductors.* Cambridge University Press, Cambridge, 1998.

[10] T. Numai. *Fundamentals of Semiconductor Lasers.* Springer, New York, 2004.

[11] M. A. Zimmler, J. Bao, F. Capasso, S. Mller, and C. Ronning. *Appl. Phys. Lett.*, 93:051101, 2008.

[12] A. Javey, S. Nam, R. S. Friedman, H. Yan, and C. M. Lieber. *Nano Lett.*, 7:773, 2007.

[13] L. Tsakalakos, J. Balch, J. Fronheiser, B. A. Korevaar, O. Sulima, and J. Rand. *Appl. Phys. Lett.*, 91:233117, 2007.

[14] S. M. Tanner, J. M. Gray, C. T. Rogers, K. A. Bertness, and N. A. Sanford. *Appl. Phys. Lett.*, 91:203117, 2007.

[15] Z. Y. Fan and J. G. Lu. *Appl. Phys. Lett.*, 86:123510, 2005.

[16] M. Haruta, S. Tsubota, T. Kobayashi, H. Kageyama, M. J. Genet, and B. Delmon. *J. Catal.*, 144:175, 1993.

[17] E. C. Garnett, W. Liang, and P. Yang. *Adv. Mater*, 19:2946, 2007.

[18] J. Wang, J. Polleux, J. Lim, and B. Dunn. *J. Phys. Chem. C*, 111:14925, 2007.

[19] C. Mah, I. Zolotukhin, T. J. Fraites, J. Dobson, C. Batich, and B. J. Byrne. *Mol Therapy*, 1:S239, 2000.

[20] M. Pereiro, D. Baldomir, J. Botana, J. E. Arias, K. Warda, and L. Wojtczak. *J. Appl. Phys.*, 103:07A315, 2008.

[21] G. Cao. *Nanostructures & Nanomaterials: Synthesis, Properties & Applications.* Imperial College Press, London, 2004.

[22] H. Ogawa, M. Nishikawa, and A. Abe. *J. Appl. Phys.*, 53:4448, 1982.

[23] H. Luth. *Surfaces and Interfaces of Solid Materials.* Springer, Heidelberg, 1995.

[24] L. E. Brus. *J. Chem. Phys.*, 80:4403, 1984.

[25] Al. L. Efros and M. Rosen. *Annu. Rev. Mater Sci.*, 30:475, 2000.

[26] Al. L. Efros and A. L. Efros. *Sov. Phys. Semicond.*, 16:772, 1982.

[27] S.D. Hersee, B. DeCremoux, and J.P. Duchemin. *Appl. Phys. Lett.*, 44:476, 1984.

[28] J. Westwater, D. P. Gosain, S. Tomiya, S. Usui, and H. Ruda. *J. Vac. Sci. Technol. B*, 15:554, 1997.

[29] Y.F. Zhang, Y.H. Tang, C. Lam, N. Wang, C.S. Lee, I. Bello, and S.T. Lee. *J. Crystal Growth*, 212:115, 2000.

[30] Y. Lei, L. D. Zhang, G. W. Meng, G. H. Li, X. Y. Zhang, C. H. Liang, W. Chen, and S. X. Wang. *Appl. Phys. Lett.*, 78:1125, 2001.

[31] C. H. Liang, G. W. Meng, Y. Lei, F. Phillipp, and L. D. Zhang. *Adv. Mater.*, 13:1330, 2001.

[32] P. Nguyen, H. T. Ng, J. Kong, A. M. Cassell, R. Quinn, J. Li, J. Han, M. McNeil, and M. Meyyappan. *Nano. Lett.*, 3:925, 2003.

[33] T. Ono, S. Tsukamoto, and K. Hirose. *Appl. Phys. Lett.*, 82:4570, 2003.

[34] H. Qi, C. Y. Wang, and J. Liu. *Adv. Mater.*, 15:411, 2003.

[35] R. S. Ajimsha, G. Anoop, Arun Aravind, and M. K. Jayaraj. *Electrochem. and Solid-State Lett.*, 11:K14, 2008.

[36] S. Iijima. *Nature*, 354:56, 1991.

[37] M. G. Bawendi, P. J. Carroll, W. L. Wilson, and L. E. Brus. *J. Chem. Phys.*, 96:946, 1992.

[38] W.C. Chan and S. Nie. *Science*, 281:2016, 1998.

[39] M. Bruchez Jr., M. Moronne, P. Gin, S. Weiss, and A. P. Alivisatos. *Science*, 281:2013, 1998.

[40] X. Li, Y. Wu, D. Steel, D. Gammon, T. H. Stievater, D. S. Katzer, D. Park, C. Piermarocchi, and L. J. Sham. *Science*, 301:809, 2003.

[41] A. P. Alivisatos. *Science*, 271:933, 1996.

[42] C. Herring and J. K. Galt. *Phys. Rev.*, 85:1060, 1952.

[43] S. Veprek and A. S. Argon. *Surface and Coatings Technology*, 146:175, 2001.

[44] S. W. Stanislaus, T. W. Adam, O. Teri Wang, H. Jin-Lin, K. Philip, V. V. Dimitri, and M. L. Charles. *Appl. Phys. Lett.*, 73:3465, 1998.

[45] G. C. David, K. F. Wayne, E. G. Kenneth, D. M. Gerald, M. Arun, J. M. Humphrey, M. Roberto, and R. P. Simon. *J. Appl. Phys.*, 93:793, 2003.

[46] M. S. Dresselhaus, G. Dresselhaus, and P. Avouris. *Carbon Nanotubes Synthesis, Structure, Properties, and Applications.* Springer, Berlin, 2001.

[47] M. N. Baibich, J. M. Broto, A. Fert, F. Nguyen Van Dau, F. Petroff, P. Eitenne, G. Creuzet, A. Friederich, and J. Chazelas. *Phys. Rev. Lett.*, 61:2472, 1988.

[48] A.J. Nozik and R. Memming. *J. Phys. Chem.*, 100:13061, 1996.

[49] Y. Wang and N. Herron. *J. Phys. Chem.*, 95:525, 1991.

[50] M. H. Huang, Y. Y. Wu, H. Feick, N. Tran, E. Weber, and P. D. Yang. *Adv. Mater.*, 13:113, 2001.

[51] M. Kerker. *The Scattering of Light and Other Electromagnetic Radiation.* Academic Press, New York, 1969.

[52] C.F. Bohren and D.R. Huffman. *Adsorption and Scattering of Light by Small Particles.* Wiley, New York, 1983.

[53] U. Kreibeg and M. Vollmer. *Optical Properties of Metal Clusters.* Springer- Verlag, Berlin, 1995.

[54] S. Shionoya and W. Yen. *Phosphor Handbook.* CRC Press, Boca Raton, FL, 1998.

[55] C. Feldmann, T. Justel, C. R. Ronda, and P. J. Schmidt. *Adv. Funct. Mater.*, 13:511, 2003.

[56] L. E. Brus. *J. Chem. Phys.*, 79:5566, 1983.

[57] L. E. Brus. *Appl. Phys. A*, 53:465, 1991.

[58] C. Burda, X. Chen, R. Narayanan, and M. A. El-Sayed. *Chem. Rev.*, 105:1025, 2005.

[59] K. K. Kim, H. S. Kim, D. K. Hwang, J. H. Lim, and S. J. Park. *Appl. Phys. Lett*, 83:63, 2003.

[60] Y. R. Ryu, T. S. Lee, and H. W. White. *Appl. Phys. Lett*, 83:87, 2003.

[61] M. Joseph, H. Tabata, H. Saeki, K. Ueda, and T. Kawai. *Physica B*, 140:302, 2001.

[62] E. Senthil Kumar, S. Venkatesh, and M. S. R. Rao. *Appl. Phys. Lett*, 96:232504, 2010.

[63] W. B. Pearson. *A Handbook of Lattice Spacings and Structures of Metals and Alloys.* Pergamon Press, New York, 1967.

[64] D. C. Look. *Mater. Sci. Eng. B*, 80:383, 2001.

[65] H. Zeng, Z. Li, W. Cai, B. Cao, P. Liu, and S. Yang. *J. Phys. Chem. B*, 111:14311, 2007.

[66] S. Baruah, C. Thanachayanont, and J. Dutta. *Sci. Technol. Adv. Mater.*, 9:025009, 2008.

[67] Y. Huang, Y. Zhang, X. Bai, J. He, J. Liu, and X. Zhang. *J. Nanosci. Nanotechnol.*, 6:2566, 2006.

[68] W. L. Hughes and Z. L. Wang. *Appl. Phys. Lett.*, 86:043106, 2005.

[69] X. Y. Kong and Z. L. Wang. *Nano Lett.*, 3:1625, 2003.

[70] W. L. Hughes and Z. L. Wang. *J. Am. Chem. Soc.*, 126:6703, 2004.

[71] T. Sun, J. Qiu, and C. Liang. *J. Phys. Chem. C*, 112:715, 2008.

[72] M. Snure and A. Tiwari. *J. Nanosci. Nanotechnol.*, 7:485, 2007.

[73] G. Bajaj and R.K. Soni. *Appl. Surf. Sci.*, 256:6399, 2010.

[74] P. Misra, T. K. Sharma, S. Porwai, and L. M. Kukreja. *Appl. Phys. Lett.*, 89:161912, 2006.

[75] Z. L. Wang. *J. Phys.: Condens. Matter*, 16:R829, 2004.

[76] B. Gil and A. V. Kavokin. *Appl. Phys. Lett.*, 81:748, 2002.

[77] E. Wong and P. C. Searson. *Appl. Phys. Lett.*, 74:2939, 1999.

[78] W.I. Park, G.C. Yi, M.Y. Kim, and S.J. Pennycook. *Adv. Mater.*, 15:526, 2003.

[79] K. Maejima, M. Ueda, S. Fujita, and S. Fujita. *Jpn. J. Appl. Phys.*, 42:2600, 2003.

[80] S. Hashimoto and A. Yamaguchi. *J. Am. Ceram. Soc.*, 79:1121, 1996.

[81] Z. W. Pan, Z. R. Dai, and Z. L. Wang. *Science*, 291:1947, 2001.

[82] D. Wang, X. Chu, and M. Gong. *Nanotechnology*, 18:185601, 2007.

[83] A. Ishizumia, Y. Taguchia, A. Yamamotoa, and Y. Kanemitsu. *Thin Solid Films*, 486:50, 2005.

[84] J. Cui, Q. Zeng, and U. J. Gibson. *J. Appl. Phys.*, 99:08M113, 2006.

[85] N. W. Emanetoglu, C. Gorla, Y. Liu, S. Liang, and Y. Lu. *Mater. Sci. Semicond. Process*, 2:247, 1999.

[86] Y. Chen, D. Bagnall, and T. Yao. *Mater. Sci. Eng. B*, 75:190, 2000.

[87] S. Liang, H. Sheng, Y. Liu, Z. Huo, Y. Lu, and H. Shen. *J. Crystal Growth*, 225:110, 2001.

[88] N. Saito, H. Haneda, T. Sekiguchi, N. Ohashi, I. Sakaguchi, and K. Koumoto. *Adv. Mater.*, 14:418, 2002.

[89] J. Y. Lee, Y. S. Choi, J. H. Kim, M. O. Park, and S. Im. *Thin Solid Films*, 403:533, 2002.

[90] A. Mitra, A. P. Chatterjee, and H. S. Maiti. *Mater. Lett.*, 35:33, 1998.

[91] M. H. Koch, P. Y. Timbrell, and R. N. Lamb. *Semicond. Sci. Technol.*, 10:1523, 1995.

[92] M. Gratzel. *MRS Bull.*, 30:39374, 2005.

[93] Y. Lin, Z. Zhang, Z. Tang, F. Yuan, and J. Li. *Adv. Mater. Opt. Electron.*, 9:205, 1999.

[94] N. Padmavathy and R. Vijayaraghavan. *Sci. Technol. Adv. Mater.*, 9:035004, 2008.

[95] C. Ma, D. Moore, J. Li, and Z.L. Wang. *Adv. Mater.*, 15:228, 2003.

[96] D. Moore, C. Ronning, C. Ma, and Z. L. Wang. *Chem. Phys. Lett.*, 385:8, 2004.

[97] D. Moore, Y. Ding, and Z.L. Wang. *J. Am. Chem. Soc.*, 126:14372, 2004.

[98] Y. Q. Li, J. A. Zapien, Y. Y. Shan, Y. K. Liu, and S. T. Lee. *Appl. Phys. Lett.*, 88:013115, 2006.

[99] J. A. Zapien, Y. Jiang, X. M. Meng, W. Chen, F. C. K. Au, Y. Lifshitz, and S. T. Lee. *Appl. Phys. Lett.*, 84:1189, 2004.

[100] C.N. King. *J. Vac. Sci. & Tech. A*, 14:1736, 1996.

[101] R. N. Bhargava, D. Gallagher, X. Hong, and A. Nurmikko. *Phys. Rev. Lett.*, 72:416, 1994.

[102] X. P. Shen, M. Han, J. M. Hong, Z. l. Xue, and Z. Xu. *Chemical Vapor Deposition*, 11:250, 2005.

[103] S. S. Nath, D. Chakdar, G. Gope, J. Kakati, B. Kalita, A. Talukdar, and D. K. Avasthi. *J. Appl. Phys*, 105:094305, 2009.

[104] K. Manzoor, S. R. Vadera, N. Kumar, and T. R. N. Kutty. *Appl. Phys. Lett*, 84:284, 2004.

[105] S. Itoh, H. Toki, Y. Sato, K. Morimoto, and T. Kishino. *J. Electrochem. Soc.*, 138:1509, 1991.

[106] T. Omata, N. Ueda, K. Ueda, and H. Kawazoe. *Appl. Phys. Lett.*, 64:1077, 1994.

[107] K. E. Sickafus, J. M. Wills, and N. W. Grimes. *J. Am. Chem. Soc.*, 82:3279, 1999.

[108] A.F. Wells. *Structural Inorganic Chemistry*. Clarendon Press, Oxford, 5 edition, 1984.

[109] R. Reshmi, K. Mini Krishna, R. Manoj, and M.K. Jayaraj. *Surface & Coatings Technology*, 198:345, 2005.

[110] I. K. Jeong, H. L. Park, and S. I. Mho. *Solid State Commun.*, 105:179, 1998.

[111] M. Yu, J. Lin, Y. H. Zhou, and S. B. Wang. *Mater. Lett.*, 56:1007, 2002.

[112] C. F. Yu and P. Lin. *J. Appl. Phys.*, 79:7191, 1996.

[113] I. J. Hsieh, M. S. Feng, K. T. Kudo, and P. Lin. *J. Electrochem. Soc.*, 14:1617, 1994.

[114] L. E. Shea, R. K. Datta, and J. J. Brown Jr. *J. Electrochem. Soc.*, 141:1950, 1994.

[115] K. H. Hsu, M. R. Yang, and K. S. Chen. *J. Mater. Sci. Mater. Electron.*, 9:283, 1998.

[116] Z. Xu, Y. Li, Z. Liu, and D. Wang. *J. Alloys and Compds.*, 391:202, 2005.

[117] T. Abritta and F.H. Blak. *J. Lumin.*, 48:558, 1991.

[118] P. D. Rack, J. J. Peterson, M. D. Potter, and W. Park. *J. Mater. Res.*, 16:1429, 2001.

[119] M. Yu, J. Lin, Y. H. Zhou, and S. B. Wang. *Mater. Lett.*, 56:1007, 2002.

[120] T. M. Chen and Y. W. Chen. *J. Solid State Chem.*, 150:204, 2000.

[121] H. I. Kang, J. S. Kim, M. Lee, J. H. Bahng, J. C. Choi, H. L. Park, G. C. Kim, T. W. Kim, Y. H. Hwang, S. I. Mho, S. H. Eom, Y. S. Yu, H. J. Song, and W. T. Kim. *Solid State Commun.*, 122:633, 2002.

[122] M. H. Huang, S. Mao, H. Feick, H. Yan, Y. Wu, H. Kind, E. Weber, R. Russo, and P. Yang. *Science*, 292:1897, 2001.

[123] H. Yan, R. He, J. Johnson, M. Law, R. J. Saykally, and P. Yang. *J. Am. Chem. Soc.*, 125:4728, 2003.

[124] J. C. Johnson, H. Yan, R. D. Schaller, L. H. Haber, R. J. Saykally, and P. Yang. *J. Physical Chem. B*, 105:11387, 2001.

[125] L.A. Kolodziejski, R.L. Gunshor, and A.V Nurmikko. *Ann. Rev. Muter. Sci.*, 25:711, 1995.

[126] J. Ding, M. Hagerott, P. Kelkar, A.V Nurmikko, D.C. Grillo, L. He, J. Han, and R.L. Gunshor. *Phys. Rev.*, B50:5787, 1994.

[127] M. Hagerott, J. Ding, H. Jeon, A. V. Nurmikko, Y. Fan, L. He, J. Han, J. Saraie, R.L. Gunshor, C.G. Hua, and N. Otsuka. *Appl. Phys. Lett.*, 62:2108, 1993.

[128] E.T. Yu, M.C. Phillips, J.O. McCaldin, and T.C. McGill. *Appl. Phys. Lett.*, 61:1962, 1992.

[129] Y. Liu, C. R. Gorla, S. Liang, N. Emanetoglu, Y. Lu, H. Shen, and M. Wraback. *J. Electron. Mater.*, 29:69, 2000.

[130] H. Kind, H. Yan, B. Messer, M. Law, and P. Yang. *Adv. Mater.*, 14:158, 2002.

[131] R. J. Collins and D. G. Thomas. *Phys. Rev.*, 112:388, 1958.

[132] S. Lee and S. Y. Seo. *J. Electrochem. Soc.*, 149:J85, 2002.

[133] S.J. Pearton, C.R. Abernathy, M.E. Overberg, G.T. Thaler, A.H. Onstine, B.P. Gila, F. Ren, B. Lou, and J. Kim. *Materials Today*, 6:24, 2002.

[134] G. Zorpette. *IEE spectrum*, 9:70, 2002.

[135] G. A. Hirata, J. McKittrick, J. Siquerios, O. A. Lopez, T. Cheeks, O. Contreras, and J. Y. Yi. *J. Vac. Sci. Technol. A*, 14:791, 1996.

[136] C. J. Lee, T. J. Lee, S. C. Lyu, Y. Zhang, H. Ruh, and H. J. Lee. *Appl. Phys. Lett.*, 81:3648, 2002.

[137] Y. W. Zhu, H. Z. Zhang, X. C. Sun, S. Q. Feng, J. Xu, Q. Zhao, B. Xiang, R. M. Wang, and D. P. Yu. *Appl. Phys. Lett.*, 83:144, 2003.

[138] M. S. Arnold, P. Avouris, Z. W. Pan, and Z. L. Wang. *J. Phys. Chem. B*, 107:659, 2003.

[139] W.J. Parak, D. Gerion, T. Pellegrino, D. Zanchet, C. Micheel, S.C. Williams, R. Bourdreau, M.A. Le Gros, C.A. Larabell, and A.P. Alivisatos. *Nanotechnology*, 14:R15, 2003.

[140] T. A. Taton. *Nature Mater.*, 2:73, 2003.

[141] M. Han, X. Gao, J.Z. Su, and S. Nie. *Nature Biotechnol.*, 19:631, 2001.

[142] J. J. Storhoff, R. Elghanian, R.C. Mucic, C.A. Mirkin, and R.L. Letsinger. *J. Am. Chem. Soc.*, 120:1959, 1998.

[143] K. R. Babu, M. S. Mohan, M. Deepa, and K. G. Nair. In M. K. Jayaraj, editor, *Proc. of International Conference on Optoelectronic Materials and Thin film for Advanced Technology*, page 87. Allied Publishers, 2005.

[144] K. E. Gonsalves, S. P. Rangarajan, and J. Wang. *Nanostructured Materials and Nanotechnology*. Academic Press, 2002.

[145] K. Wasa, M. Kitabatake, and H. Adachi. *Thin Film Materials Technology*. Springer-Verlag GmbH & Co. KG, Germany, 2004.

[146] L. I. Maissel and R. Glang. *Handbook of Thin Film Technology*. McGraw-Hill, New York, 1970.

[147] M. Ohring. *Materials Science of Thin Films: Deposition and Structure*. Academic Press, New York, 2001.

[148] A. Rahm, M. Lorenz, T. Nobis, G. Zimmermann, M. Grundmann, B. Fuhrmann, and F. Syrowatka. *Appl. Phys. A*, 88:31, 2007.

[149] H. B. Zeng, W. P. Cai, B. Q. Cao, J. L. Hu, Y. Li, and P. S. Liu. *Appl. Phys. Lett.*, 88:181905, 2006.

[150] D. B. Chrisey and G. K. Hubler. *Pulsed laser deposition of thin films*. John Wiley and Sons, New York, 1994.

[151] R.Venkatesan and S.M.Green. *The Industrial Physicist*, 2:22, 1996.

[152] K. Byrappa, I. Yoshimura, and M. Yoshimura. *Handbook of Hydrothermal Technology*. William Andrew Publishing, New York, 2001.

[153] K. Byrappa and T. Adschiri. *Progress in Crystal Growth and Characterization of Materials*, 53:117, 2007.

[154] B. D. Cullity and S.R. Stock. *Elements of X ray diffraction*. Prentice Hall, New Jersey, 3 edition, 2001.

[155] M. J. Buerger. *X-ray Crystallography*. John Wiley and Sons, New York, 3 edition, 1962.

[156] C.Kittel. *Introduction to solid state Physics*. Wiely Eastern Limtd, 1996.

[157] P. E. J. Flewitt and R. K. Wild. *Physical methods for materials characterisation*. IOP Publishing Ltd, 2003.

[158] M. Watt. *The principle and practise of electron microscopy*. Cambridge Uni. Press, Cambridge, 1997.

[159] A. Subramanian and L. D. Marlcs. *Ultramicroscopy*, 98:151, 2004.

[160] D. K. Schroder. *Semiconductor material and device charecterisation*. Wiley Interscience, New York, 1998.

[161] K. Oura, V. G. Lifshits, A. A. Saranin, A. V. Zotov, and M. Katayama. *Surface science, an introduction*. Springer-Verlag, Heidelberg, Germany, 2003.

[162] C. R. Brundle, C. A. Evans, and S. Wilson. *Encyclopedia of materials characterisation.* Reed Publishing, USA, 1992.

[163] A. Stefnsson, I. Gunnarsson, and N. Giroud. *Anal. Chim. Acta,* 582:69, 2007.

[164] *Veeco Dektak 6M,* 2004.

[165] C. N. Banwell and E. M. McCash. *Fundamentals of molecular spectroscopy.* Tata McGraw Hill, 4 edition, 1994.

[166] B. G. Streetman. *Solid state electronic devices.* Prentice Hall of India Pvt Ltd, New York, 1995.

[167] J.Bardeen, F.J.Blatt, and L.H.Hall, editors. *Proc. of Photoconductivity Conf.*, Atlantic city, 1954. J.Wiley and Sons.

[168] P. Kubelka. *J. Opt. Soc. Am.*, 38:448, 1948.

[169] P.Kubelka and F.Munk. *Zh. Tekh. Fiz,* 12:593, 1931.

[170] D. R. Vij. *Luminescence of solids.* Plenum Press, New York, 1998.

[171] G. Wyszecki and W. S. Stiles. *Color Science: Concepts and Methods, Quantitative Data and Formulae.* John Wiley and Sons Inc., New York, 2 edition, 1982.

[172] C. V. Raman and K. S. Krishna. *Nature,* 121:501, 1928.

[173] H. Richter, Z. P. Wang, and L. Ley. *Solid State Commun.*, 39:625, 1981.

[174] M. Rajalakshmi, T. Sakunthala, and A. K. Arora. *J. Phys.: Condens. Matter*, 9:9745, 1997.

[175] A. Tanaka, S. Onari, and T. Arai. *Phys. Rev. B*, 47:1237, 1993.

[176] A. Tanaka, S. Onari, and T. Arai. *Phys. Rev. B*, 45:6587, 1992.

[177] K. Gramm, L. Lundgren, and Beckman. *Physica Scripta.*, 13:93, 1976.

[178] D. S. Kim and R. Y. Lee. *J. Mater. Sci.*, 35:4777, 2000.

[179] S. B. Park, Y. C. Kang, I. W. Lenggoro, and K. Okuyama. *J. Aerosol. Sci.*, 29:S909, 1998.

[180] Y. C. Kang and S. B. Park. *Mater. Res. Bull.*, 35:1143, 2000.

[181] Y. C. Kang, S. B. Park, and I. W. Lenggoroand K. Okuyama. *J. Electrochem. Soc.*, 146:2744, 1999.

[182] M. Flynn and A. H. Kitai. *J. Electrochem. Soc.*, 148:H149, 2001.

[183] T. Minami, T. Maeno, Y. Kuroi, and S. Tanaka. *J. Vac. Sci. Technol. A*, 14:1736, 1996.

[184] T. K. Tran, W. Park, J. W. Tomm, B. K. Wagner, S. M. Jacobsen, C. J. Summers, P. N. Yocom, and S. K. McClelland. *J. Appl. Phys.*, 78:5691, 1995.

[185] S. H. Wu and H. C. Cheng. *J. Electrochem. Soc.*, 151:H159, 2004.

[186] D. Haranath, H. Chander, P. Sharma, and S. Singh. *Appl. Phys. Lett.*, 89:173118, 2006.

[187] S.K. Sampsth and J.F. Cordaro. *J. Am. Ceram. Soc.*, 81:649, 1998.

[188] Z. Yan and H. Takei. *J. Cryst. Growth*, 171:131, 1997.

[189] Z. Yan, H. Takei, and H. Kawazoe. *J. Am. Ceram. Soc.*, 81:180, 1998.

[190] M. Hirano. *J. Mater. Chem.*, 10:469, 2000.

[191] P.M. Aneesh, K.A. Vanaja, and M.K. Jayaraj. *Proc. SPIE*, 6639:66390J, 2007.

[192] M. Hirano, M. Imai, and M. Inagaki. *J. Am. Ceram. Soc.*, 83:977, 2000.

[193] A. C. Tas, P. J. Majewski, and F. Aldinger. *J. Mater.Res.*, 17:1425, 2002.

[194] M. Takesada, T. Isobe, H. Takahashi, and S. Itoh. *J. Electrochem.Soc.*, 154:J136, 2007.

[195] *ICSD.* Number 081113.

[196] J. S. Kim, H. I. Kang, W. N. Kim, J. I. Kim, J. C. Choi, H. L. Park, G. C. Kim, T. W. Kim, Y. H. Hwang, S. I. Mho, M. C. Jung, and M. Han. *Appl. Phys. Lett*, 82:2029, 2003.

[197] J. Reader and C. H. Corliss. *CRC Handbook of Chemistry and Physics.* CRC Press Inc., 1993.

[198] M. Peres, A. Cruz, S. Pereira, M.R.. Correia, M.J. Soares, A. Neves, M.C. Carom, T. Monteiro, S. Pereira, M.A. Martins, T. Trindade, E. Alves, S.S. Nobre, and R. A. Sa Ferreira. *Appl. Phys. A*, 88:129, 2007.

[199] R. Rossetti, S. Nakahara, and L. E. Brus. *J. Chem. Phys.*, 79:1086, 1983.

[200] A. P. Alivisatos. *J. Phys. Chem.*, 100:13226, 1996.

[201] G. C. Yi, C. Wang, and W. II. Park. *Semicond. Sci. Technol*, 20:S22, 2005.

[202] Z. Qiuxiang, Y. Ke, B. Wei, W. Qingyan, X. Feng, Z. Ziqiang, D. Ning, and S. Yan. *Mater. Lett.*, 61:3890, 2007.

[203] L. Yuzhen, G. Lin, X. Huibin, D. Lu, Y. Chunlei, W. Jiannong, G. Weikun, Y. Shihe, and W. Ziyu. *J. Appl. Phys.*, 99:114302, 2006.

[204] A. Hachigo, H. Nakahata, K. Higaki, S. Fujii, and S-I. Shikata. *Appl. Phys. Lett.*, 65:2556, 1994.

[205] H. Morkoc, S. Strite, G. B. Gao, M. E. Lin, , B. Sverdlov, and M. Burns. *J. Appl. Phys.*, 76:1363, 1994.

[206] G. Thomas. *Chemistry for Pharmacy and Life Sciences: Including Pharmacology and Biomedical Science.* Ellis Horwood Ltd., London, 1996.

[207] S. Dutta, M. Chakrabarti, S. Chattopadhyay, D. Jana, D. Sanyal, and A. Sarkar. *J. Appl. Phys.*, 98:053513, 2005.

[208] S. Chattopadhyay, S. Dutta, A. Banerjee, D. Jana, S. Bandyopadhyay, S. Chattopadhyay, and A. Sarkar. *Physica B*, 404:59, 2009.

[209] S. Dutta, S. Chattopadhyay, D. Jana, A. Banerjee, S. Manik, S. K. Pradhan, M. Sutradhar, and A. Sarkar. *J. Appl. Phys.*, 100:114328, 2006.

[210] Z. Hui, Y. Deren, M. Xiangyang, J. Yujie, X. Jin, and Q. Duanlin. *Nanotechnology*, 15:622, 2004.

[211] J. Zhang, L. D. Sun, J. L. Yin, H. L. Su, C. S. Liao, and C. H. Yan. *Chem. Mater.*, 14:4172, 2002.

[212] Q. P. Zhong and E. Matijevic. *J. Mater. Chem*, 3:443, 1996.

[213] W. Lingna and M. Mamoun. *J. Mater. Chem*, 9:2871, 1999.

[214] D. W. Bahnemann, C. Kormann, and M. R. Hoffmann. *J.Phys. Chem.*, 91:3789, 1987.

[215] C. Y. Lee, T. Y. Tseng, S. Y. Li, and P. Lin. *J. Appl. Phys.*, 99:024303, 2006.

[216] *ICSD*. Number 086254.

[217] H. P. Klug and L. E. Alexander. *X-ray diffraction Procedures for polycrystalline and Amorphous Materials*, volume 9. Wiley, New York, 1 edition, 1954.

[218] W. Zhijian, Z. Haiming, Z. Ligong, Y. Jinshan, Y. Shenggang, and W. Chunyan. *Nanotechnology*, 14:11, 2003.

[219] J. Flor, S. A. Marques, de.Lima, and M. R. Davolos. *Surface and Colloid Science*, 128:239, 2004.

[220] Q. Ahsanulhaq, A. Umar, and Y. B. Hahn. *Nanotechnology*, 18:115603, 2007.

[221] M. Xiangyang, Z. Hui, J. Yujie, X. Jin, and Y. Deren. *Mater. Lett.*, 59:3393, 2005.

[222] A. I. Y. Tok, F. Y. C. Boey, S. W. Du, and B. K. Wong. *Materials Science and Engineering: B*, 130:114, 2006.

[223] C.E. Steven, Z. Lijun, I. H. Michael, L. E. Alexander, A. K. Thomas, and J. N. David. *Nature*, 436:91, 2005.

[224] K. Vanheusden, W. L. Warren, C. H. Seager, D. R. Tallant, J. A. Voigt, and B. E. Gnade. *J Appl Phys*, 79:7983, 1996.

[225] W. Q. Peng, S.C. Qu, G. W. Cong, and Z.G. Wang. *Materials Science in Semiconductor Processing*, 9:156, 2006.

[226] M. Ahmad, C. Pan, J. Zhao, J. Iqbal, and J. Zhu. *Materials Chemistry and Physics*, 120:319, 2010.

[227] Y. Zhang, D. Lan, Y. Wang, and F. Wang. *Front. Chem. China*, 3:229, 2008.

[228] J. Liu, S. Lee, Y. H. Ahn, J. Y. Park, and K. H. Koh. *J. Phys. D: Appl. Phys.*, 42:095401, 2009.

[229] S. A. Wolf, D. D. Awschalom, R. A. Buhrman, J. M. Daughton, S. von. Molnar, M. L. Roukes, A. Y. Chtchelkanova, and D. M. Treger. *Science*, 294:1488, 2001.

[230] J. J. Liu, M. H. Yu, and W. L. Zhou. *Appl. Phys. Lett.*, 87:172505, 2005.

[231] T. Dietl, H. Ohno, F. Matsukura, J. Cibert, and D. Ferrand. *Science*, 287:1019, 2000.

[232] K. Ueda, H. Tabata, and T. Kawai. *Appl. Phys. Lett.*, 79:988, 2001.

[233] K. R. Kittilstved, N. S. Norberg, and D. R. Gamelin. *Phys. Rev. Lett.*, 94:147209, 2005.

[234] A. Quesada, M. A. Garca, M. Andrs, A. Hernando, J. F. Fernndez, A. C. Caballero, M. S. Martn-Gonzlez, and F. Briones. *J. Appl. Phys*, 100:113909, 2006.

[235] E. Schlenker, A. Bakin, H. Schmid, W. Mader, H. Bremers, A. Hangleiter, H. H. Wehmann, M. Al-Suleiman, J. Ludke, M. Albrecht, and A. Waag. *Appl. Phys. A*, 91:375, 2008.

[236] Y. X. Wang, X. Ding, Y. Cheng, Y. J. Zhang, L. L. Yang, H. L. Liu, H. G. Fan, Y. Liu, and J. H. Yang. *Cryst. Res. Technol.*, 44:517, 2009.

[237] H. Zhang, D. Yang, X. Ma, Y. Ji, J. Xu, and D. Que. *Nanotechnology*, 15:622, 2004.

[238] N. Jedrecy, H.J. von Bardeleben, Y. Zheng, and J. L. Cantin. *Phys. Rev. B*, 69:041308, 2004.

[239] N. Volbers, H. Zhou, C. Knies, D. Pfisterer, J. Sann, D. M. Hofmann, and B.K. Meyer. *Appl. Phys. A*, 88:153, 2007.

[240] J. Blasco, F. Bartolom, L.M. Garca, and J. Garca. *J. Magnetism and Magnetic Materials*, 316:e177, 2007.

[241] M. Bouloudenine, N. Viart, S. Colis, J. Kortus, and A. Dinia. *Appl. Phys. Lett.*, 87:052501, 2005.

[242] O. D. Jayakumar, I. K. Gopalakrishnan, R. M. Kadam, A. Vinu, A. Asthana, and A. K. Tyagi. *J. Crystal Growth*, 300:358, 2007.

[243] B. D. Cullity and C. D. Graham. *Introduction to Magnetic Materials.* Addison- Wesley, Reading, MA, 1972.

[244] G. Blasse and B. C. Grabmaier. *Luminescent Materials.* Springer, New York, 1994.

[245] W.M. Yen and S. Shionoya. *Phosphor Handbook.* Number 9. CRC Press, Boca Raton, FL, 1 edition, 1998.

[246] C. B. Murray, D. J. Norris, and M. G. Bawendi. *J. Am. Chem. Soc.*, 115:8706, 1993.

[247] D. Matsuura, Y. Kanemitsu, T. Kushida, C. W. White, J. D. Budai, and A. Meldrum. *Appl. Phys. Lett.*, 77:2289, 2000.

[248] N. Nirmal, B. O. Dabbousi, M. G. Bawendi, J. I. Macklin, J. K. Trautman, T. D. Harris, and L. E. Brus. *Nature (London)*, 383:802, 1996.

[249] A. A. Bol and A. Meijerink. *Phys. Rev. B*, 58:R15997, 1998.

[250] J. Kossanyi, D. Kouyate, J. Pouliquen, J. C. Ronfard-Haret, P. Valat, D. Oelkrug, U. Mammel, G.P. Kelly, and F. Wilkinson. *J. Luminesc.*, 46:17, 1990.

[251] M. Leskela. *J. Alloys Compds.*, 275:702, 1998.

[252] B. Jacquier, E. Lebrasseur, S. Guy, A. Belarouci, and F. Menchini. *J. Alloys Compds.*, 303:207, 2000.

[253] J. Hu, L.S. Li, W. Yang, L. Manna, L.W. Wang, and A. P. Alivisatos. *Science*, 292:2060, 2001.

[254] X. Peng, L. Manna, W. Yang, J. Wickham, E. Scher, A. Kadavanich, and A. P. Alivisatos. *Nature (London)*, 404:59, 2000.

[255] S. Bachir, K. Azuma, J. Kossanyi, P. Valat, and J. C. Ronfard-Haret. *J. Luminesc.*, 75:35, 1997.

[256] C. C. Yang, S. Y. Cheng, H. Y. Lee, and S. Y. Chen. *Ceramic International*, 32:37, 2006.

[257] X. Zhang, J. Wang, J. Zhang, and Q. Su. *Mater. Lett.*, 61:761, 2007.

[258] P. H. Yang, X. Sun, and J.-F. Chiu. *Bioconjugate Chem.*, 16:494, 2005.

[259] J. Chen, F. Saeki, B. J. Wiley, H. Chang, M. J. Cobb, Z. Y. Li, L. Au, H. Zhang, M. B. Kimmey, X. Li, and Y. Xia. *Nano Lett.*, 5:473, 2005.

[260] X. Gao, Y. Cui, M. Levenson, L. W. K. Chung, and S. Nie. *Nature Biotechnol.*, 22:969, 2004.

[261] J. Chen, B. Wiley, D. Campbell, F. Saeki, L. Chang, L. Au, J. Lee, X. Li, and Y. Xia. *Adv. Mater.*, 17:2255, 2005.

[262] I. Brigger, C. Dubernet, and P. Couvreur. *Adv. Drug Delivery Rev.*, 54:631, 2002.

[263] S. Barcikowski, M. Hustedt, and B. N. Chichkov. *Polimery*, 53:657, 2008.

[264] G. Compagnini, A. A. Scalisi, and O. Puglisi. *Phys. Chem. Chem. Phys.*, 4:2787, 2002.

[265] S. J. Henley, M. N. R. Ashfold, and D. Cherns. *Surf. Coat. Tech.*, 177:271, 2004.

[266] D. Dijkkamp, T. Venkatesan, X. D. Wu, S. A. Shaheen, N. Jisrawi, Y. H. Minlee, W. L. Mclean, and M. Croft. *Appl. Phys. Lett.*, 51:619, 1987.

[267] D. L. Pappas, K. L. Saenger, J. Bruley, W. Krakow, J. J. Cuomo, T. Gu, and R. W. Collins. *J. Appl. Phys.*, 71:5675, 1992.

[268] G. Radhakrishnan and P. M. Adams. *Appl. Phys. A*, 69:S33, 1999.

[269] V. Dureuil, C. Ricolleau, M. Gandais, C. Grigis, J. P. Lacharme, and A. Naudon. *Journal of Crystal Growth*, 233:737, 2001.

[270] P. P. Patil, D. M. Phase, S. A. Kulkarni, S. V. Ghaisas, S. K. Kulkarni, S. M. Kanetkar, S. B. Ogale, and V. G. Bhide. *Phys. Rev. Lett.*, 58:238, 1987.

[271] G. W. Scherer. *J. Non-Cryst. Solids*, 73:661, 1985.

[272] J. A. Dahl, B. L. Maddux, and J. E. Hutchison. *Chem. Rev.*, 107:2228, 2007.

[273] S. Hartmann, D. Brandhuber, and N. Husing. *Acc. Chem. Res.*, 40:885, 2007.

[274] S. Mende, F. Stenger, W. Peukert, and J. Schwedes. *J. Mater. Sci.*, 39:5223, 2004.

[275] S. Besner, A. V. Kabashin, F. M. Winnik, and M. Meunier. *Appl. Phys. A*, 93:955, 2008.

[276] J. B. Wang, C. Y. Zhang, X. L. Zhong, and G. W. Yang. *Chem. Phys. Lett.*, 361:86, 2002.

[277] R. Fabbro, J. Fournier, P. Ballard, D. Devaux, and J. Virmont. *J. Appl. Phys.*, 68:775, 1990.

[278] G. W. Yang. *J. Prog. Mater. Sci.*, 52:648, 2007.

[279] L. Barther, R. Fabbro, P. Peyre, L. Tollier, and E. Bartinicki. *J. Appl. Phys.*, 89:2836, 1997.

[280] S. Zhu, Y. F. Lu, M. H. Hong, and X. Y. Chen. *J. Appl. Phys.*, 89:2400, 2001.

[281] S. Zhu, Y. F. Lu, and M. H. Hong. *Appl. Phys. Lett.*, 79:1396, 2001.

[282] O. Yavas, A. Schilling, J. Bischof, J. Boneberg, and P. Leiderer. *Appl. Phys. A*, 64:331, 1997.

[283] S. J. Shaw, W. P. Schiffers, T. P. Gentry, and D. C. Emmony. *J. Phys. D*, 32:1612, 1999.

[284] A. V. Simakin, V. V. Voronov, N. A. Kirichenko, and G. A. Shafeev. *Appl. Phys. A*, 79:1127, 2004.

[285] N. Takada, T. Sasaki, and K. Sasaki. *Appl. Phys. A*, 93:833, 2008.

[286] T. Tsuji, T. Hamagami, T. Kawamura, J. Yamaki, and M. Tsuji. *Appl. Surf. Sci.*, 243:214, 2005.

[287] S. C. Singh and R. Gopal. *Bull. Mater. Sci.*, 30:291, 2007.

[288] M. S. Yeh, Y. S. Yang, Y. P. Lee, H. F. Lee, Y. H. Yeh, and C.S. Yeh. *J. Phys. Chem. B*, 103:6851, 1999.

[289] G. A. Shafeev, E. Freysz, and F. Bozon-Verduraz. *Appl. Phys. A*, 78:307, 2004.

[290] J. P. Sylvestre, S. Poulin, A. V. Kabashin, E. Sacher, M. Meunier, and J. H. T. Luong. *J. Phys. Chem. B*, 108:16864, 2004.

[291] M. Sugiyama, H. Okazaki, and S. Koda. *Jpn. J. Appl. Phys.*, 41:4666, 2002.

[292] S. I. Dolgaev, A. V. Simakin, V. V. Voronov, G. A. Shafeev, and F. Bozon-Verduraz. *Appl. Surf. Sci.*, 186:546, 2002.

[293] K. V. Ankin, N.N. Melnik, A.V. Simakin, G.A. Shafeev, V.V. Voronov, and A.G. Vitukhonovsky. *Chem. Phys. Lett.*, 366:357, 2002.

[294] R. Konenkamp, R. C. Word, and C. Schlegel. *Appl. Phys. Lett.*, 85:6004, 2004.

[295] T. Gruber, C. Kirchner, R. Kling, and F. Reuss. *Appl. Phys. Lett.*, 84:5359, 2004.

[296] C. W. Sun, P. Xin, Z. W. Liu, and Q. Y. Zhang. *Appl. Phys. Lett.*, 88:221914, 2006.

[297] K. S. Weissenrieder and J. Muller. *Thin Solid Films*, 300:30, 1997.

[298] H. Usui, Y. Shimizu, T. Sasaki, and N. Koshizaki. *J. Phys. Chem. B*, 109:120, 2005.

[299] W. T. Nichols, T. Sasaki, and N. Koshizaki. *J. Appl. Phys.*, 100:114913, 2006.

[300] F. Kooli, I. C. Chsem, and W. Vucelic. *Chem. Mater.*, 8:1969, 1996.

[301] N. V. Joshy, K. J. Saji, and M. K. Jayaraj. *J. Appl. Phys.*, 104:053307, 2008.

[302] L. Berthe, R. Fabbro, P. Peyre, L. Tollier, and E. Bartnicki. *J. Appl. Phys.*, 82:2826, 1997.

[303] M. Nakagawa and H. Mitsudo. *Surf. Sci.*, 175:157, 1986.

[304] C. He, T.Saski, H.Usui, Y.Shimizu, and N.Koshizaki. *J. Photochem and Photobiology A: Chemistry*, 191:66, 2007.

[305] Y. Cui, Q. Wei, H. Park, and C. M. Leiber. *Science*, 293:1298, 2001.

[306] J. T. Andrews and P. Sen. *J. Appl. Phys.*, 91:2827, 2002.

[307] L. V. Asryana, M. Grundmann, N. N. Ledentsov, O. Stier, and D. Bimberg. *J. Appl. Phys.*, 90:1666, 2001.

[308] K. V. P. M. Shafi, S. Wizel, T. Prozorov, and A. Gedanken. *Thin Solid Films*, 318:38, 1998.

[309] R. M. Pattabi, K. R. Sridhar, S. Gopakumar, B. Vinayachandra, and M. Pattabi. *Int. J. Nanoparticles*, 3:53, 2010.

[310] A. Mathew, N. Munichandraiah, and G.M. Rao. *Mater. Sci. Engg. B*, 158:7, 2009.

[311] S. P. Gubin and J. D. Kosobudskii. *Russ. Chem. Rev.*, 52:776, 1983.

[312] J. Shi, S. Gilder, K. Babcock, and D. D. Awschalom. *Science*, 271:937, 1996.

[313] A. Henglein. *J. Phys. Chem.*, 97:5457, 1993.

[314] G. W. Yang and J. B. Wang. *Appl. Phys. A*, 71:343, 2000.

[315] C. H. Liang, Y. Shimizu, M. Masuda, T. Sasaki, and N. Koshizaki. *Chem. Mater.*, 16:963, 2004.

[316] Y. F. Zhu, D. H. Fan, and W. Z. Shen. *J. Phys. Chem. C*, 112:10402, 2008.

[317] Z. Quan, D. Yang, C. Li, D. Kong, P. Yang, Z. Cheng, and J. Lin. *Langmuir*, 25:10259, 2009.

[318] S. Hou, Y. Yuen, H. Mao, J. Wang, and Z. Zhu. *J. Phys. D: Appl. Phys.*, 42:215105, 2009.

[319] S. S. Kumar, M. A. Khadar, S. K. Dhara, T. R. Ravindran, and K. G. M. Nair. *Nuclear Instruments and Methods in Physics Research Section B: Beam Interactions with Materials and Atoms*, 251:435, 2006.

[320] R. Maity and K. K. Chattopadhyay. *Nanotechnology*, 15:812, 2004.

[321] V. Wood, J. E. Halpert, M. J. Panzer, M. G. Bawendi, and V. Bulovic. *Nano Lett.*, 9:2367, 2009.

[322] S. Kar and S. Biswas. *ACS Appl. Mater. Interfaces*, 1:1420, 2009.

[323] W. G. Becker and A. J. Bard. *J. Phys. Chem*, 87:4888, 1983.

[324] J. J. Kelly J. F. Suyver, S. F. Wuister and A. Meijerink. *Nano Lett.*, 1:429, 2001.

[325] T. Makino, Y. Segawa, M. Kawasaki, and H. Koinuma. *Semicond. Sci. Technol.*, 20:S78, 2005.

[326] H. D. Sun, T. Makino, N. T. Tuan, Y. Segawa, Z. K. Tang, G. K. L. Wong, M. Kawasaki, A. Ohtomo, K. Tamura, and H. Koinuma. *Appl. Phys. Lett.*, 77:4250, 2000.

[327] H. D. Sun, T. Makino, Y. Segawa, M. Kawasaki, A. Ohtomo, K. Tamura, and H. Koinuma. *J. Appl. Phys.*, 91:1993, 2002.

[328] U. Ozgur, Y. I. Alivov, A. Teke C. Liu, M. A. Reshchikov, S. Dogan, V. Avrutin, S. J. Cho, and H. Morkoc. *J. Appl. Phys.*, 98:041301, 2005.

[329] A. Ohtomo, M. Kawasaki, I. Ohkubo, H. Kojinuma, T. Yasuda, and Y. Segawa. *Appl. Phys. Lett.*, 75:980, 1999.

[330] T. Makino, C. H. Chia, Nguen T. Tuan, H. D. Sun, Y. Segawa, M. Kawasaki, A. Ohtomo, K. Tamura, and H. Koinuma. *Appl. Phys. Lett.*, 77:975, 2000.

[331] A. Ohtomo, K. Tamura, M. Kawasaki, T. Makino, Y. Segawa, Z. K. Tang, G. K. L. Wong, Y. Matsumoto, and H. Kojinuma. *Appl. Phys. Lett.*, 77:2204, 2000.

[332] B. P. Zhang, N. T. Binh, K. Wakatsuki, C. Y. Liu, Y. Segawa, and N. Usami. *Appl. Phys. Lett.*, 86:032105, 2005.

[333] A. Ohtomo and A. Tsukazaki. *Semicond. Sci. Technol.*, 20:S1, 2005.

[334] S. Krishnamoorthy, A. A. Iliadis, A. Inumpudi, S. Choopun, R. D. Vispute, and T. Venkatesan. *Solid-State Electron.*, 46:1633, 2002.

[335] T. Makino, N. T. Tuan, H. D. Sun, C. H. Chia, Y. Segawa, M. Kawasaki, A. Ohtomo, K. Tamura, T. Suemoto, H. Akiyama, M. Baba, S. Saito, T. Tomita, and H. Koinuma. *Appl. Phys. Lett.*, 78:1979, 2001.

[336] H. D. Sun, T. Makino, N. T. Tuan, Y. Segawa, M. Kawasaki, A. Ohtomo, K. Tamura, and H. Koinuma. *Appl. Phys. Lett.*, 78:2464, 2001.

[337] P. Misra and L. M. Kukreja. *Thin Solid Films*, 485:42, 2005.

[338] I.Ohkubo, Y. Matsumoto, A. Ohtomo, T. Ohnishi, A. Tsukazaki, M. Lippmaa, H. Koinuma, and M. Kawasaki. *Appl. Surf. Sci.*, 159:514, 2000.

[339] J. Narayan and B. C. Larson. *J. Appl.Phys.*, 93:278, 2003.

[340] A. Ohtomo, R. Shiroki, I. Ohkubo, H. Koinuma, and M. Kawasaki. *Appl. Phys. Lett.*, 75:4088, 1999.

[341] S. Monticone, R. Tufeu, and A. V. Kanaev. *J. Phys. Chem. B*, 102:2854, 1998.

[342] W. Shan, W. Walukiewicz, J. W. Ager, K. M. Yu, H. B. Yuan, H. P. Xin, G. Cantwell, and J. J. Song. *Appl. Phys. Lett.*, 86:191911, 2005.

[343] C. K. Sun, S. Z. Sun, K. H. Lin, K. Y. J. Zhang, H. L. Liu, S. C. Liu, and J. J. Wu. *Appl. Phys. Lett.*, 87:023106, 2005.

[344] R. S. Ajimsha. *Growth and Characterization of ZnO based Hetero-junction diodes and ZnO Nanostructures by Pulsed Laser Ablation.* PhD thesis, Cochin University of Science and Technology, Kochi, India, 2008.

[345] R. T. Senger and K. K. Bajaj. *Phys. Rev. B*, 68:045313, 2003.

[346] K. Ueda, T. Hase, H. Yanagi, H. Kawazoe, , H. Hosono, H. Ohta, M. Orita, and M. Hirano. *J. Appl. Phys.*, 89:1790, 2001.

[347] A.N. Banerjee, S. Kundoo, and K.K. Chattopadhyay. *Thin Solid Films*, 440:5, 2003.

[348] V. Varadarajan and D. P. Norton. *Appl. Phys. A*, 85:117, 2006.

[349] M. Ratner and D. Ratner. *Nanotechnology. A Gentle Introduction to the Next Big Idea.* Prentice Hall, New Jersey, 2003.

[350] P. M. Aneesh, K. Mini Krishna, and M. K. Jayaraj. *J. Electrochem. Soc.*, 156:K33, 2009.